RECURSIVE ESTIMATION USING THE BILINEAR OPERATOR WITH APPLICATIONS TO SYNCHRONOUS MACHINE PARAMETER IDENTIFICATION

by

Richard W. Merchant, BE(Hons)

Thesis submitted for the degree of

Doctor of Philosophy

in

The University of Adelaide

Department of Electrical and Electronic Engineering

Faculty of Engineering

August, 1992

Contents

Abstract

Due to the speed, memory capacity, and processing power of modern digital computing, most general signal processing is now performed in the discrete-time domain. As far as system modeling or estimation is concerned, this has resulted in the widespread use of discrete-time models for representing systems which are continuous-time in nature.

This thesis describes the development of a new method for estimating the coefficients of a continuous-time, Laplace-transform transfer function model of a system from sampled input-output signals. The method employs a recursive estimation algorithm to identify the coefficients of a discrete-time bilinear-operator model. The coefficients of the discrete-time bilinear-operator model, for a reasonably high sampling frequency, closely approximate those of the corresponding continuous-time Laplace transform transfer function.

To demonstrate the practicality of the proposed estimation method, it is applied to the problem of estimating various transfer functions of a 5 kV.A laboratory synchronous machine.

In the first application, the recursive estimation method is used to perform standstill tests on the machine. These tests are conventionally performed by measuring the magnitude and phase response of the machine in various standstill configurations when excited by a sinusoidal test signal. Some advantages of the bilinear-operator recursive estimation method in this application are that it allows the coefficients of the machine transfer function to be estimated quickly and accurately, directly from the sampled input-output signals. Moreover, any frequency-rich test signal can be used to excite the machine. The operational impedance parameters of the machine are directly evaluated from the estimated machine transfer functions.

The second application involves estimation of the small-signal field-to-terminal-voltage transfer function of the synchronous machine operating online in a Single Machine Infinite Bus (SMIB) arrangement. To perturb the machine for estimation, a low-level test signal is superimposed on the field excitation voltage, resulting in a 1% variation in terminal voltage. To calculate the operational impedance parameters of the machine from the estimated transfer function coefficients, the set of non-linear

equations derived for the small-signal SMIB system model is solved iteratively. The advantage of the machine parameters calculated from the estimated online transfer function is that they are representative of the synchronous machine under actual operating conditions. The recursive estimation method performs well in this online application, despite the low level of terminal voltage variation.

These practical applications demonstrate the effectiveness of the proposed recursive estimation method employing the discrete-time bilinear-operator model.

Statement of Originality

This work contains no material which has been accepted for the award of any other degree of diploma in any university or other tertiary institution and, to the best of my knowledge and belief, contains no material previously published or written by another person, except where due reference has been made in the text.

I give consent to this copy of my thesis, when deposited in the University Library, being available for loan and photocopying.

SIGNED: DATE: 26/8/92

Acknowledgements

I wish to express my gratitude to my supervisor, Dr. M.J. Gibbard, for his guidance throughout this work, and his assistance in the preparation of this thesis. Helpful discussions with Dr. A.M. Parker and Dr. C.C. Lim during a period of study leave by Dr. M.J. Gibbard are also gratefully acknowledged.

Thanks must also go to the workshop staff in the department, in particular, Mr. P. Roberts and Mr. P. Hunter for their help with the assembly of the synchronous machine apparatus, and advice on the design and construction of the test electronics.

The assistance of Mr. Tim Pattison for his help in deciphering the intricacies of the departmental computer facilities is greatly appreciated.

The financial support of the Australian Defence Science and Technology Organisation, by way of a research fellowship, is gratefully acknowledged, along with the funds made available by the Australian Research Council for equipment purchases.

List of Principal Symbols.

a	–	amplitude of the pseudo random binary sequence
$a(.)$, $b(.)$, $A(.)$, $B(.)$, $A'(.)$, $B'(.)$, $A''(.)$, $B''(.)$	–	polynomials
a_i, b_i, A_i, B_i, A'_i, B'_i, A''_i, B''_i	–	polynomial coefficients
$\hat{A}(w)$, $\hat{B}(w)$	–	estimated bilinear-operator polynomials
$\hat{a}_i^0$, $\hat{b}_i^0$	–	initial estimate of the coefficients of $\hat{A}(w)$, $\hat{B}(w)$
B_1, B_2	–	shaft damping constants
B'	–	total damping constant
B''	–	total damping constant including effects of stator core losses
e_k	–	prediction error for recursive estimation
$E(\hat{\theta})$	–	general weighted least-squares error criterion
$error_k$	–	general prediction error
$E\{.\}$	–	expectation
f_s	–	sampling frequency ($f_s = 1/\Delta$)
f	–	frequency
$F(s)$	–	signal conditioning filter for attenuating high frequencies in the pseudo random binary sequence excitation signal
f_c	–	cut-off frequency of a filter
G_0	–	d-axis field-to-stator gain
$H(s)$	–	continuous-time Laplace transform transfer function
$H_{equiv}(z)$	–	hold-equivalent discrete-time model of a continuous-time model
$H_{TH}(.)$	–	triangle-hold-equivalent discrete-time model of a continuous-time model
$\hat{h}_k$	–	parameter estimate vector for SAGARA-RLS
$H(w)$	–	bilinear-operator parameterisation of $Q(q^{-1})$
$H_\eta(s)$	–	coloured noise filter
$\hat{H}_{OP1}(\beta)$, $\hat{H}_{OP2}(\beta)$, $\hat{H}_{OP3}(\beta)$	–	estimated w-domain models for online operating conditions OP1, OP2, OP3
I	–	identity matrix
i_d, i_q, i_f, i_D, i_Q	–	machine currents (subscripts d, q, f, D, Q define the relevant machine windings)

$i_{md}(k)$	–	simulated output signal for simulation-mode test
J	–	polar moment of inertia of system rotor
$J(w)$	–	filter polynomial for the recursive estimation algorithms
j_i	–	coefficients of the $J(w)$ filter polynomial
k	–	'bit' length of a pseudo random binary sequence in sample periods, i.e. $\Delta_p = k\Delta$
$k(\tau)$	–	cross correlation measure
L	–	machine winding self inductances
$\mathcal{L}\{.\}$	–	Laplace transform
$L_d(s)$	–	d-axis operational inductance
$L_q(s)$	–	q-axis operational inductance
L_d, L_{d0}	–	d-axis self inductance
L_q, L_{q0}	–	q-axis self inductance
L'_d, L''_d	–	d-axis transient and subtransient inductances
L''_q	–	q-axis subtransient inductance
L_{dd}, kM_{fd}, kM_{df}, L_{ff}, L_{qq}, A, B, C, D	–	small-signal incremental mutual inductances
M, kM	–	mutual inductance between windings on the same machine axes
$M1$, $M2$, $M3$, $M4$	–	single-machine infinite-bus matrices
n, m	–	order of the denominator and numerator polynomials of a model
N	–	'bit' length of a pseudo random binary sequence
Op_0, Known_0, Param_k	–	labels assigned to groups of variables in evaluating machine parameters from the estimated coefficients of the field-to-terminal voltage transfer function
P_k	–	estimation covariance matrix
$\mathrm{Pre}(\beta)$	–	w-domain transfer function of the estimation prefilter $\mathrm{Pre}(w)$
P, Q	–	parks modified transform and parks transform
P_{mech}	–	prime mover power
P_{elec}	–	total electrical power
P_e	–	total losses
P_{t0}, Q_{t0}, v_{t0}, v_{b0}	–	steady-state real power output, reactive power output, terminal voltage and infinite-bus voltage

P_{iron}	–	core losses of the synchronous machine stator
$Q(q^{-1})$	–	digital low-pass filter
$R(s)$	–	continuous-time transfer function of a general reconstruction circuit
$R_{ZOH}(s)$, $R_{TH}(s)$	–	continuous-time transfer function of a zero-order-hold and triangle-hold reconstruction circuit
$R_{eu}(\tau)$	–	cross correlation between e_k and u_k
$R_{yu}(\tau)$	–	cross correlation between y_k and u_k
$r_e + j\omega L_e$	–	external reactance in single-machine infinite-bus system (Ω per phase) ($X_e = \omega_0 L_e$)
r_a, r_f, r_D, r_Q	–	machine winding resistances
s	–	Laplace transform complex variable
s_{di}, s_{ni}	–	continuous-time poles and zeros
$sG(s)$	–	field-to-stator transfer function
T'_d, T''_d	–	d-axis short-circuit-transient and short-circuit-subtransient time constants
T'_{d0}, T''_{d0}	–	d-axis open-circuit-transient and open-circuit-subtransient time constants
T''_q, T''_{q0}	–	q-axis short-circuit-subtransient and open-circuit-subtransient time constants
T_{kd}	–	d-axis damper time constant
$u(t)$, $y(t)$	–	continuous-time input and output signals
$u(k\Delta)$, $y(k\Delta)$, u_k, y_k	–	sampled input and output signals
$U(s)$, $Y(s)$	–	Laplace transform of $u(t)$ and $y(t)$
$U(z)$, $Y(z)$	–	z transform of u_k and y_k
$U(\gamma)$, $Y(\gamma)$	–	δ transform of u_k and y_k
$U(\beta)$, $Y(\beta)$	–	w transform of u_k and y_k
$v_{md}(k)$, $v_{mt}(k)$	–	simulated output signals for simulation-mode test
v_d, v_q, v_f	–	machine d-axis, q-axis and field voltages
v_{d0}, v_{q0}, v_{t0}, i_{d0}, etc	–	steady-state values of v_d, v_q, v_t, i_d, etc
$V(\hat{\theta})$	–	least-squares error criterion
$\bar{V}(\hat{\theta})$	–	limit of $V(\hat{\theta})$ as N tends to infinity
$v_d(s)$, $v_q(s)$, $v_f(s)$	–	Laplace transform of v_d, v_q, v_f
v_t	–	line-to-line terminal voltage of the synchronous machine
v_b	–	line-to-line voltage of the infinite bus

v_{PRBS}	–	pseudo random binary sequence voltage generated by the real-time system
v_{PRBSf}	–	low-pass filtered v_{PRBS}
V_{PhaseA}, V_{PhaseB}, V_{PhaseC}	–	line-to-neutral terminal voltage of the synchronous machine
v_{ag}	–	synchronous machine air-gap voltage
v_{agd}, v_{agq}	–	d- and q-axis components of v_{ag}
v_{ag0}, v_{agd0}, v_{agq0}	–	steady-state values of v_{ag}, v_{agd}, v_{agq}
x_k	–	instrumental variable
X_d	–	d-axis synchronous reactance, $X_d = \omega_0 L_d$
X_q	–	q-axis synchronous reactance, $X_q = \omega_0 L_q$
$X_{d_{unsat}}$, $X_{q_{unsat}}$, $\omega_0 k M_{f_{unsat}}$	–	unsaturated values of X_d, X_q, $\omega_0 k M_f$
X_l	–	d- and q-axis leakage reactance
$\hat{y}_k$	–	estimate of y_k
$\hat{y}_k^c$	–	bootstrap instrumental variable
y_k^c	–	'idealized' instrumental variable
$\mathcal{Z}\{.\}$	–	z transform
z_k	–	instrumental variable vector
z, γ, β	–	z-, δ- and w-transform complex variables
z_{di}, z_{ni}	–	q-domain poles and zeros
β_{di}, β_{ni}	–	w-domain poles and zeros
$\beta(t,k)$	–	weighting sequence for weighted least-squares estimation
γ_{di}, γ_{ni}	–	δ-domain poles and zeros
Δ	–	sampling period
Δ_p	–	'bit' length in seconds of the pseudo random binary sequence
$\delta(f)$	–	unit impulse
δ	–	angle between infinite-bus voltage and q-axis of the synchronous machine
δ_{t0}, δ_{e0}, δ_0	–	steady-state angles between the terminal voltage and machine q-axis, infinite-bus voltage and terminal voltage and infinite-bus voltage and machine q-axis
ϵ_k	–	prediction error for SAGARA-RLS
ζ_k	–	'idealized' instrumental variable vector
η_k	–	additive system output noise
λ_k	–	forgetting factor for recursive estimation

θ	–	true parameter vector
$\hat{\theta}_t$	–	estimate at time t of the parameter vector θ
$\xi_{iu}(k)$, $\xi_{iy}(k)$	–	filtered input and output signals for SAGARA-RLS
ρ, q, δ, w	–	differential, shift, delta, bilinear operators
τ	–	time delay
$\Phi(f)$	–	power spectral density of the pseudo random binary sequence
$\Phi_e(f,\hat{\theta})$	–	power spectral density of the prediction error e_k
$\Phi_u(f)$	–	power spectral density of the input signal u_k
$\Phi_\eta(f)$	–	power spectral density of the additive system noise η_k
$\Phi_{uy}(j\omega)$	–	cross spectral density of the input (u_k) and output (y_k) signals
ϕ_k	–	estimation regression vector
ψ_{ag}	–	resultant synchronous machine air-gap flux
ψ_k	–	regression vector for SAGARA-RLS
ψ_d, ψ_q, ψ_f, ψ_D, ψ_Q	–	machine flux linkages (subscripts d, q, f, D, Q define the relevant machine windings)
ω	–	rotor speed, electrical radians per second
ω_m	–	rotor speed, mechanical radians per second ($\omega_m = \omega/2$)
ω_c	–	angular cut-off frequency of a filter ($\omega_c = 2\pi f_c$)
ω_0	–	synchronous speed (100π rad/s)
$\omega_0 k M_f$	–	d-axis mutual reactance

List of Abbreviations

A/D	–	analogue to digital
BPF	–	block pulse function
D/A	–	digital to analogue
FIR	–	finite impulse response
FOH	–	first-order hold
IIR	–	infinite impulse response
IV	–	instrumental variable
PCBF	–	piecewise-constant basis function
PRBS	–	pseudo random binary sequence
PSS	–	power system stabiliser
PWM	–	pulse width modulation
RBS	–	random binary sequence
RIV	–	recursive instrumental-variable
RIV-BO	–	recursive instrumental-variable bilinear operator
RLS	–	recursive least-squares
RLS-BO	–	recursive least-squares bilinear operator
RTS	–	real time system
SMIB	–	single-machine infinite-bus
SNR	–	signal-to-noise ratio
SSFR	–	standstill frequency response
SSSFR	–	small-signal sinusoidal frequency response
SVF	–	state variable filter
TF	–	transfer function
TH	–	triangle hold
ZOH	–	zero-order hold
d-axis	–	direct-axis
q-axis	–	quadrature-axis

Chapter 1

Introduction

1.1 Models and Model Estimation

Mathematical models of dynamical systems provide a method for extracting information about, or quantifying the behaviour of such systems. The mathematical model representation of the system may be required for many reasons. One possible reason is for the purpose of predicting the response of the system to certain input signals. A model which is able to accurately represent the response of a system may be employed in simulation studies to investigate the behaviour of the system over a wide range of operating conditions. For example, given models that can accurately represent the response of the components of an interconnected power system, simulation studies may be conducted to predict the effects of system faults on the security of the overall power system. These studies may highlight certain 'weaknesses' in the system, and help define operating conditions in which the dynamic response of the system is unsatisfactory. Models may also be used for the purpose of control. For example, given an accurate model of a system it may be possible to design suitable controllers which feedback various signals from the overall system to improve the response. In the context of power system operation, power system stabilisers (PSS), which employ a stabilising signal such as the speed of the shaft of the synchronous machine, are used to improve the damping of rotor oscillations in the multi-machine power system [1].

For both the control and accurate prediction of a systems response, the form of the model used may not need to accurately represent the physical nature of the

actual system, its sole purpose may only be to provide an accurate model for the system response [2]. For other applications however, the system model may also be required to accurately represent the physical relationships which govern the behaviour of the system. This may be helpful in gaining a better understanding of the true physical processes involved in the system. In the design and analysis of synchronous machines for example, a model containing parameters representative of the physical parameters of the machine may help the power system designer to understand the effects of saturation in the machine iron on the various machine parameters. This may also prove useful in assessing the validity of simplifying assumptions made when deriving models for synchronous machines [3]. A model which contains parameters representative of those of the physical system may also be beneficial for fault diagnosis on the system [4].

The form of a system model can be many and varied. For example, the model can be as simple as a table of input-output values for the system, or a complex nonlinear, time-varying model which is described mathematically. The form of the model employed is dependent on many factors, including the characteristics of the system being modeled, the intended application of the model, and it also may be limited by the methods available for deriving the model.

Models can generally be classified as either parametric or nonparametric. Nonparametric models are basically the response of the dynamical system to some form of excitation. For example, the impulse or step response of a system are nonparametric models. In contrast to this, for a parametric model a form of the model must first be selected, such as an n-th order differential equation or a transfer function. The system is then described by the coefficients or parameters of this model. One benefit of the parametric model is that, providing the model form is selected wisely with respect to the actual system it represents, the parametric model may provide a concise, compact representation of the system [2]. A class of parametric model commonly employed for representing dynamical systems is the linear, lumped parameter, time invariant, finite-order model [2]. This class of model has the advantages that it is relatively easily analysed and characterised, as well as being representative of many common dynamical systems. Because of these many advantages, this thesis

deals with parametric models. Of course, for some special applications, it is possible that a nonparametric model may offer benefits over the parametric model [5].

Parametric models can further be subdivided into either discrete- or continuous-time models. The physical systems encountered in engineering are commonly continuous-time in nature. However, as the data measured from these systems is generally in the form of discrete samples, and because of the speed, memory capacity and processing power of modern digital computing, it is common to use discrete-time model representations for continuous-time systems. The discrete-time model representation for continuous-time systems may be suitable for applications involving simulation studies or control system design, in which there may be no requirement for the model to reflect the physical laws governing the actual continuous-time system. However, for cases in which the requirement of the (parametric) model is to provide insight into the physical behaviour of the underlying system, discrete-time model representations may be unsuitable, because in general the discrete-time model does not resemble the corresponding continuous-time model. Another possible disadvantage of using a conventional shift-operator discrete-time model representation for a continuous-time system is that, for high sampling frequencies (relative to the bandwidth of the continuous-time system), computations with the discrete-time model become numerically ill-conditioned [6,7], a problem highlighted with self-tuning control [8].

Having introduced a few of the many benefits of using a model for representing the characteristics of a system, the method by which these models are derived or how the parameters are calculated for parametric models, must be considered. For systems which describe known physical processes, it may be possible to derive the system model from first principles. For example, the differential equations of an RLC network can readily be derived from knowledge of the R, L and C network elements and their interconnections [9]. These parametric differential equations can be rearranged to form the nonparametric impulse- or step-response model of the network, or even converted to an equivalent discrete-time parametric model of the network.

Deriving models from first principles is a useful approach when the system is relatively simple, and the physical behaviour of the elements is well understood.

However, when the system is a large, complex interconnected system, in which the physical behaviour of several of the elements is not fully understood, it may not be possible to derive mathematically an accurate model of the system from first principles. This leads to another method for deriving a model for representing the system, namely *system identification* [10]. In system identification, input and output signals measured from the unknown system are used to infer a model for the system. System identification, for a parametric model, entails the selection of the form of the system model, the determination of the order of the model, as well as the identification of the values of the parameters of the model. In many practical situations, there is a certain level of prior knowledge about the system under test, such as the form of the system model, and even its order. When these characteristics of the system are assumed known, the system identification task reduces to the task of *parameter estimation* [10].

Because of the suitability of digital computers for performing computationally intensive tasks, extensive research has been conducted in the area of system identification and parameter estimation using discrete-time system models. There are many useful texts on this subject, for example [2,10,11,12]. In contrast, the identification and parameter estimation of *continuous-time* system models has received less attention, which is disappointing considering the widespread use of continuous-time system models. The system models considered in this thesis are continuous-time models. Specifically, this thesis deals with the parameter estimation of continuous-time differential equation or transfer function models.

The task of parameter estimation of continuous-time system models can be broadly separated into two distinct methods, namely indirect and direct methods. In the indirect methods, the identification may consist of estimating firstly a nonparametric impulse response, or frequency response model of the continuous-time system [2,13, 14]. The parameters of the continuous-time model of the system can then be evaluated by 'fitting' the response of the selected model to the measured system response. An alternative indirect method is to estimate the parameters of a discrete-time difference-equation model of the system, and then perform the transformation from the discrete- to the continuous-time model [15,16]. These indirect methods however are unsuitable

for estimation of the continuous-time parametric models 'online' in real-time, due to their indirect nature.

The primary difficulty associated with the direct methods of estimation, is that the terms in the continuous-time differential-equation model contain derivatives of the system input-output signals. These derivative terms cannot in general be measured directly from the system, and calculating their values directly from the measured input-output signals accentuates greatly any noise present on these signals.

One approach for avoiding the time derivatives in the system differential equation is to operate on the differential equation with a suitable filter. With this approach, the original system differential equation is converted to an equivalent equation containing filtered derivative terms. These filtered derivatives can be readily measured as the output of analogue *state variable filters* (SVF), which have as inputs either the input or output signals of the continuous-time system [17,18]. The outputs of these SVFs can be sampled and used directly in a discrete-time recursive estimation scheme to estimate the parameters of the continuous-time differential equation. The method does not require knowledge of the initial conditions of the differential equation.

Another approach for avoiding the derivative terms is to employ the modulating function technique [19,20]. In this technique, a set of modulating functions are defined, which are well-behaved continuous functions with the property that their derivatives and function values tend to zero at the ends of some known time interval. By virtue of these zero boundary conditions, the original system differential equation can be converted into an algebraic equation, in which the noise accentuating derivatives of the input-output signals have been transferred to the well-behaved modulating functions. This method is not well-suited to online calculation, because it requires the evaluation of time integrals involving the measured input-output signals and the modulating functions [19]. However, by selecting the modulating functions such that they are related to the impulse responses of continuous-time filters, the time integrals involving the input-output signals and modulating functions are simply the output of the continuous-time filters, with the system input and output signals as inputs to the filters. Thus this estimation method may be used for online estimation [19]. This form of real-time implementation is similar to the SVF approach described above.

Another approach to removing the time derivative terms from the original system differential equation is to perform multiple integration operations on the differential equation [21,22]. This converts the original equation, containing the derivatives of the system input-output signals, into an integral equation. The one major disadvantage of this method is that multiple integrations generally introduce extra unknowns into the system of equations, in the form of initial conditions. These initial conditions must either be known, or estimated together with the unknown differential equation parameters. Several of the common parameter estimation methods belong to this multiple integration technique, including the method of orthogonal functions. Orthogonal function methods evaluate the multiple integration operations using operational matrices for integration. These methods include the continuous orthogonal function methods, such as Laguerre polynomials [23], shifted Legendre polynomials [24], as well as the piecewise constant basis function (PCBF) methods such as Walsh functions, Haar functions, and the popular block-pulse functions (BPF) [19,25,26]. In [27], these orthogonal function methods have been referred to as rather abstract and arbitrary function expansions.

A recent advance with the multiple integration technique, labelled the linear integral filter, is to perform the integrations over a finite time interval [27,28]. The linear integral filter performs the multiple integrations on the system differential equation via numerical integration methods. The linear integral filter approach enables the differential equation to be formulated as an algebraic equation suitable for estimation, without the disadvantage of the unknown initial conditions. The method does not require the initial conditions to be known, nor does it require they be estimated. In recent papers by Sagara *et al.* [29,30], the linear integral filter approach has been interpreted as a finite impulse response, low-pass filtering of the system differential equation. By choice of the length of the time interval over which the numerical integration is performed, the bandwidth of the low-pass filtering effect of the linear integral filter can be controlled.

In [30,31], the linear integral filter approach has been broadened to explicitly filtering the original differential equation with digital low-pass filters. In [30], the digital filter is time-varying and consists of the denominator polynomial of the estimated

continuous-time transfer function. In [31], this digital filter is further generalised to use a 'standard' infinite or finite impulse response low-pass filter, with possibly a Butterworth or Chebyshev type response. It is possible to view these digital filtering techniques as basically discrete-time versions of the originally proposed SVFs.

In this thesis, an estimation method is developed for estimating the coefficients of a parametric continuous-time differential-equation model or transfer function model of a continuous-time system, using the sampled input-output signals in recursive estimation. The method employs a discrete-time bilinear-operator model representation of the continuous-time system model. Depending on the sampling period, the coefficients of the discrete-time bilinear-operator model closely approximate those of the equivalent continuous-time model. The estimation method is implemented in a recursive formulation, potentially suitable for real-time applications. It does not estimate, nor require knowledge of the system initial conditions. The method is developed from the work of Middleton and Goodwin on the use of the delta operator for general discrete-time control and estimation [6]. Middleton and Goodwin introduce the delta-operator representation of a discrete-time model to overcome several of the basic problems with the conventional shift-operator parameterisation. These problems include the fact that there is no apparent connection between the coefficients of the discrete-time shift-operator model and those of the corresponding continuous-time model. Another problem is the numerical ill-conditioning associated with the shift-operator implementation at high sampling frequencies [6]. The discrete-time bilinear-operator parameterisation is introduced in this thesis to develop a discrete-time model representation the coefficients of which, for a given sampling period, more closely resembles those of the continuous-time model than do those of the delta-operator model. The bilinear-operator representation retains the numerical superiority over the conventional shift-operator representation.

The work in this thesis on the development of the recursive estimation method using the bilinear-operator model is original work. It is however very similar to the current work of Sagara *et al.* [31]. The similarities and differences between the approach in this thesis and that of [31] are further expanded in section 3.4.

As stated, this thesis deals with the derivation of a recursive estimation method

for estimating the coefficients of a continuous-time differential equation or transfer function model of a system. As well as the development of the estimation method, the thesis also covers the practical application of the method to the task of identifying the parameters of a synchronous machine.

1.2 Synchronous Machine Parameter Identification

In the area of power system operation, a matter of primary concern with a large interconnected power system is that of system stability and dynamic performance. System stability can be divided into transient stability and small-signal dynamic stability [32,33]. Small-signal dynamic stability, which is concerned with the small-signal performance of the system about a steady-state operating condition, is a fundamental requirement for the satisfactory operation of power systems [33]. In recent times, as the size of the interconnected power systems have increased and as the systems are operated closer to their stability limit, the requirement for well-damped small-signal dynamic performance of power systems has increased.

Because of the importance of the small-signal dynamic performance of power systems, it is imperative that accurate simulation studies are performed to investigate this dynamic performance. The simulation studies may be used to help assess the performance of various synchronous machine control strategies, as well as power system stabiliser design. To perform accurate simulation studies, accurate models of the elements of the power system are required. These elements include the synchronous generators, prime movers, control systems, loads, and the transmission system. In conjunction with the requirement for accurate models, is the need for accurate parameters for these models. The derivation of parameters for some of these power system elements is not a simple task. Consider for example, the synchronous machine. The synchronous machine is an inherently nonlinear device, converting mechanical energy to electrical energy. The flux paths in a synchronous machine are constructed mainly of iron. The cross-sectional areas of these flux paths within the iron vary, and result in varying levels of iron saturation throughout the machine [34]. For this and

other reasons, the synchronous machine is a nonlinear device, with certain physical parameters that vary in a complicated way with machine flux levels, and hence with operating conditions.

To model a synchronous machine, the conventional d-q-axis representation of the machine is generally used [35]. In this representation, the three-phase rotating system is converted to a two orthogonal axis (d-q-axis) model, containing stationary conducting coils on both axes. There exist many variations in the number, and combination of d-q-axis coils (see [36]). The resulting set of d- or q-axis coils may be represented by a coupled-circuit model which consists of inductive and resistive elements, or an operational impedance formulation containing inductances and time constants. Because of saturation, these inductances vary with machine operating conditions. There are a number of techniques for modeling the variation of machine parameters due to saturation. These include modeling separately the saturation of both the d- and q-axes, or alternately using a 'total' air-gap flux as a measure of saturation [3,37,38].

As mentioned, for synchronous machine models to be employed for simulation studies, values for the machine parameters must be supplied. Usually a set of parameters representative of the synchronous machine are provided by the manufacturer of the machine. These parameters are generally derived from calculations performed when designing the machine, or measured from sudden short circuit and other tests [39]. It is often found, however, when using manufacturer-supplied parameters, the behaviour of the actual machine and that predicted by simulation differ significantly [40]. Thus it is important for accurate simulation studies that the machine parameter values be either measured or calculated from tests, or calculated by numerical techniques. Finite-element analysis appears to be a promising numerical technique for calculating the parameters of a synchronous machine at the desired operating conditions [41,42]. This method is however very computationally intensive, requires detailed knowledge of the machine iron dimensions and of experimentally determined values of the (incremental) permeability of the machine rotor iron.

The most common method for obtaining the values of machine parameters is to calculate or measure the values from tests on the machine. Some of the conventional machine tests include open- and short-circuit tests, zero power factor tests,

slip tests, load rejection tests, field and stator decrement tests, sudden short-circuit tests, etc, [43]. These tests allow several of the large-signal machine parameters to be identified (saturated and unsaturated). Another test method that has been gaining acceptance is the standstill frequency response (SSFR) test [39,44]. In the SSFR tests, a sinusoidal excitation signal is used to measure, at discrete frequencies, the frequency response of the various machine transfer functions with the machine at standstill. These frequency response measurements are performed on both the d and q axes of the machine. Parametric models of the d-q-axis machine transfer functions can then be calculated by iteratively fitting the desired transfer function model to the measured frequency response. The machine parameters may then be calculated from the transfer function coefficients. One of the benefits of this method is that the machine parameters can be identified for both the d and q axes, as the excitation is applied to both machine axes independently. Also, the tests can be performed over a large frequency range, revealing the effects of damper windings which predominantly occur at high frequencies. The advantages and disadvantages of standstill frequency response tests are further discussed in chapter 5.

Whilst the sinusoidal excitation test may provide an accurate frequency response model of the desired machine transfer functions, the method is time consuming. An alternative method of deriving the parameters at standstill is to measure the step response of the various standstill machine configurations [45]. Using the measured step response signals, the differential equations representing the synchronous machine can be converted to a set of algebraic equations using low-pass functionals. The resulting equations may then be solved using a linear least-squares method to yield the operational impedance machine parameters.

In [46], difficulties are experienced when using a simple step excitation for identifying the d-axis parameters of a high-order synchronous machine model. A random binary sequence (RBS) excitation signal proves superior for identifying the d-axis parameters. In [46], the synchronous machine is configured in the desired standstill configuration and excited by a RBS excitation signal. Measurements are made of the machine responses and excitation. Using an iterative routine, the estimated resistance and reactance parameters of the machine model are recursively adjusted to minimise

the error between the measured and calculated standstill responses.

To demonstrate the practicality of the proposed estimation method derived in this thesis, the method is applied to the task of performing standstill tests on a laboratory synchronous machine. With the machine at standstill, the various configurations of the machine are excited with a pseudo random binary sequence (PRBS) excitation signal. From the sampled excitation and response signals, the bilinear-operator estimation method is employed to estimate *directly* the coefficients of the continuous-time transfer functions of the standstill synchronous machine. From these estimated continuous-time coefficients, the operational impedance parameters of the synchronous machine can be directly evaluated.

Whilst the parameters identified from both the conventional synchronous machine tests and the standstill tests may provide reasonably accurate values for the machine parameters, the parameters are only really applicable for representing the synchronous machine under the conditions of which the tests are performed [47]. This is primarily because the parameters of a synchronous machine vary with saturation. Tests performed with different steady-state flux levels result in different machine parameter values. Also, tests performed with perturbations of different magnitudes yield different values of machine parameters. For example, small-signal standstill tests yield machine parameters representative of the 'incremental permeability' of the machine iron at a zero steady-state flux level [48]. The machine parameters may also vary between standstill and online tests due to rotational affects. For machines with rotor slot wedges, the conduction path through these wedges is dependent on the contact resistance between the rotor iron and the wedge. This contact resistance is dependent on the contract pressure, and hence will vary between tests conducted with the machine rotor at standstill and rotating [36]. Ideally, therefore, machine parameters should be measured or calculated from tests performed on the synchronous machine under operating conditions.

Several attempts have been made at evaluating the parameters of a synchronous machine under actual operating conditions [39,49,50,51,52,53]. The benefits of parameters derived under operating conditions include: (i) The parameters can be derived under the operating conditions for which they will be used in simulation studies. De-

rived online small-signal machine parameters are directly applicable to small-signal dynamic stability studies. (ii) The machine does not need to be offline for testing, a problem with the majority of test methods. (iii) The parameters may provide information as to the true effects of saturation, proving useful in machine design as well as the derivation of accurate machine models.

Several online test investigations have employed small-signal sinusoidal frequency response techniques to measure the frequency response of the desired machine transfer functions. In [39,49], small-signal sinusoidal frequency response measurements are made of the field-to-terminal-voltage and field-voltage-to-rotor-speed transfer functions. Taking the values of the machine parameters derived from standstill tests as an initial estimate, these parameters are iteratively modified to minimise the difference between the measured and computed frequency responses for the machine transfer functions. In these papers, only the rotor parameters of the machine are modified. In [50], small-signal sinusoidal tests are performed to evaluate several transfer functions of a synchronous generator operating online. The measured terminal voltage and current quantities are resolved into their d- and q-axis components to allow the required d- and q-axis transfer functions to be evaluated.

Another approach for deriving the parameters of the synchronous machine operating online is to use an extended Kalman filter [52,53]. In these papers, a step change in the external network connected to the synchronous machine is used to excite a small transient in the system. An iterative technique is used to improve an original estimate of the machine parameters, such that the measured system transient and that predicted by the system model closely agree. In [52], the method is applied to estimating the parameters of a low-order d-q-axis machine model excluding damper windings. In [53], the method is extended, with limited success, to employ a synchronous machine model including damper windings.

In [51], the parameters of a small-signal linearised machine model are calculated from small perturbation transient response tests on an online synchronous machine. The d- and q-axis voltage and current responses are measured during the transient and converted via the Laplace transform to their equivalent Laplace domain signals. Numerical curve-fitting is then used to derive the parametric d-q-axis operational

impedance transfer functions from which the machine parameters are evaluated.

The applicability of the estimation method proposed in this thesis to the online parameter identification task is demonstrated by identifying the small-signal parameters of a laboratory synchronous generator operating online in a single-machine infinite-bus (SMIB) arrangement. With the synchronous machine operating online, a small-signal PRBS perturbation is superimposed on the field voltage supply. This results in a terminal voltage perturbation of between $\pm 1\%$. Measurements are taken of the field- and terminal-voltage perturbations and are used in the proposed estimation method to estimate directly the coefficients of the continuous-time small-signal field-to-terminal-voltage transfer function of the SMIB system. Model validation tests confirm the estimated model accurately represents the field-to-terminal-voltage response of the system. In comparison with conventional small-signal sinusoidal frequency response measurements performed on the system, the estimated model provides a superior estimate of the system response, especially in the frequency region of the complex poles and zeros of the system transfer function. From the coefficients of the estimated system transfer function, the small-signal linearised equations of the SMIB system are solved to evaluate several parameters of the synchronous machine model.

1.3 Outline of the Thesis

This thesis is concerned with the estimation of the parameters of continuous-time system models from sampled input-output signals. An estimation method is developed which employs a discrete-time bilinear-operator model representation of the continuous-time model. The coefficients of the discrete-time bilinear-operator model closely approximate those of the equivalent continuous-time model for sampling frequencies which are high relative to the frequency range of interest for the continuous-time system. The estimation method is implemented in a recursive formulation, potentially suitable for real-time applications.

In chapter 2, various discrete- and continuous-time operator models are introduced, as well as their corresponding transform domain transfer functions. The discrete-time operator models considered are the conventional shift-operator model,

and the delta- and bilinear-operator models. The numerical superiority of both the delta- and bilinear-operator formulations with respect to finite word-length calculations is demonstrated. Using the hold-equivalent technique, a discrete-time model which closely approximates the relationship between the sampled input-output signals of a continuous-time system is derived. Using the hold-equivalent model, the suitability of using the coefficients of the various discrete-time model parameterisations as direct approximations to the coefficients of the continuous-time model is investigated. These investigations highlight the ability of the coefficients of the discrete-time bilinear-operator model to closely approximate those of the equivalent continuous-time model.

Having demonstrated the advantages of the discrete-time bilinear-operator model, it is applied to the task of discrete-time recursive estimation. In chapter 3, the bilinear-operator model is arranged into a linear regression form suitable for use in recursive least-squares estimation. This is done by introducing a discrete-time bilinear-operator filter polynomial $J(w)$, which is used to filter the approximate discrete-time system differential equation, removing the problem of direct evaluation of the sampled input-output signal derivatives. This chapter discusses the effects of noise on estimation, as well as the effects of the prefilter and $J(w)$ filter polynomial. The recursive least-squares estimation algorithm using the bilinear-operator model is not suitable for estimation when the sampled continuous-time system output signal is contaminated by either coloured or a high level of white additive output noise. To cope with these situations, a recursive instrumental-variable estimation algorithm using the bilinear-operator model is formulated.

To demonstrate the effectiveness of the proposed estimation method, simulation studies are conducted in chapter 4. For all simulation studies, and practical applications of the proposed estimation method discussed in later chapters, a pseudo-random binary sequence (PRBS) excitation signal is used to excite the dynamics of the continuous-time system under test. In this chapter, the salient features of a PRBS are discussed, such that the PRBS parameters can be selected appropriately for each estimation task. The simulation studies conducted include the effects of unmodeled dynamics, and both white and coloured additive output noise. The effects

of prefiltering and the choice of $J(w)$ filter polynomial on estimation are examined.

In chapter 5, the proposed estimation method is applied to the practical task of performing standstill tests on a laboratory synchronous machine. With these tests, a PRBS excitation signal is applied to the required synchronous machine configuration at standstill. The sampled excitation and response signals are used in the proposed estimation method to estimate the coefficients of the continuous-time transfer function of the synchronous machine configuration. The unknown machine parameters can then be evaluated from the estimated transfer function coefficients, using the relevant machine equations. The proposed estimation method is particularly well suited to performing standstill tests. The method estimates directly the coefficients of the continuous-time transfer function from the sampled input-output signals. The time required for testing is significantly less than that required for conventional standstill frequency response testing employing sinusoidal excitation signals. It is possible to use any persistently exciting excitation signal with the proposed estimation method, allowing the possible use of high-powered excitation signals. This may overcome one of the problems associated with small-signal standstill tests, namely, the evaluated machine parameters are representative of the small-signal incremental permeability of the machine iron. Several model validation tests which prove useful in the practical estimation tasks are introduced in this chapter.

Machine parameters derived from small-signal standstill tests may not accurately represent the parameters of a machine under actual operating conditions. Therefore, in chapter 6, the proposed estimation method is applied to the task of identifying the parameters of a synchronous machine operating online in a single-machine infinite-bus (SMIB) arrangement. At a specified operating condition a small PRBS perturbation signal is superimposed on the machine field excitation voltage. The field and terminal voltage perturbations are sampled and used in the proposed estimation method to *directly* estimate the coefficients of the small-signal field-to-terminal-voltage transfer function of the system. From the estimated online transfer function coefficients, the small-signal linearised SMIB equations are solved to evaluate several unknown synchronous machine parameters. In this application, the proposed estimation method estimates the coefficients of a model which accurately represents the small-signal re-

sponse of the SMIB system. The accuracy is confirmed by several model validation tests, as well as independent, small-signal sinusoidal frequency response measurements.

From the simulation studies and practical estimation tasks conducted in this thesis, conclusions regarding the performance of the proposed estimation method are drawn in chapter 7. The practical advantages of using the proposed estimation method for both standstill and online synchronous machine parameter identification tasks are also discussed.

The work in this thesis concerning the development of the recursive least-squares estimation method and its application to synchronous machine standstill tests (chapters 3 and 5) is published in [54]. The development and application of the method to standstill tests and online operating tests are also published in conference proceedings [55] and [56], respectively.

In summary, the major theoretical and practical contributions of this thesis are as follows:

- The development of a discrete-time recursive estimation method for estimating the coefficients of a continuous-time model from sampled input-output signals.
  - The estimation method is implemented in a recursive formulation employing the discrete-time bilinear-operator model.
  - The discrete-time bilinear-operator parameterisation shows numerical advantages over the conventional discrete-time shift-operator parameterisation.
  - As the sampling period tends to zero, the discrete-time bilinear-operator model converges to the corresponding continuous-time model.
  - In contrast to many continuous-time model estimation methods, knowledge of the system initial conditions are not required, nor are they estimated.
- Simulation studies investigating the operation of the proposed estimation method.
  - The method can accurately estimate the coefficients of a continuous-time system model.

  - The studies investigate various possible selections of the $J(w)$ filter polynomial for improving the accuracy of the coefficient estimates.

- The frequency domain analysis of the effects of the filter polynomial $J(w)$ on estimation.

  - This analysis allows the $J(w)$ filter polynomial to be selected for estimation based on the characteristics of the continuous-time system under test.

- The application of the proposed estimation method to standstill tests on synchronous machines.

  - The estimation method is well suited to the practical standstill estimation task.

  - The time required for testing is significantly less than that required for conventional sinusoidal frequency response testing.

  - The proposed estimation method estimates the coefficients of the continuous-time machine transfer functions directly from the measured input-output signals.

- The application of the proposed estimation method to the task of estimating the coefficients of the small-signal field-to-terminal-voltage transfer function of a synchronous generator operating online in a SMIB arrangement.

  - The proposed estimation method provides an accurate, efficient and rapid method for directly estimating the coefficients of the online small-signal SMIB transfer function.

  - Techniques are developed for evaluating the machine parameters from the estimated transfer function coefficients.

  - The proposed estimation method provides a useful tool for research in machine modeling and the evaluation of machine parameters under operating conditions.

Chapter 2

The Discrete-Time Bilinear-Operator Model

2.1 Introduction.

With digital computing continually increasing in speed, memory capacity, and processing power, it seems inevitable that most conventional signal processing will eventually be performed in the discrete-time digital domain. The discrete-time nature of this processing is in contrast to the continuous-time nature of most physical systems. To successfully model continuous-time systems in the discrete-time domain, one must be able to sample the continuous-time signals and hypothesise suitable discrete-time models which accurately represent the relationship between the sampled continuous-time input and output signals.

The most common linear discrete-time model form is that of the forward-shift or q-operator model, or its associated z-transform model. Several problems exist with the discrete-time q-operator representation, these include [6] : (i) numerical ill-conditioning as the sampling frequency increases, and (ii) the discrete-time model coefficients bear no resemblance to those of the underlying continuous-time model it represents.

The discrete-time delta operator (δ) was introduced to address problems with the q operator [6]. The δ operator is a simple linear reparameterisation of the q operator, with the benefits, (i) numerical conditioning is superior for high sampling

frequencies and (ii), the discrete-time δ-operator model coefficients approach those of the continuous-time model as the sampling period approaches zero. The δ operator provides an alternative discrete-time operator parameterisation which is suitable for general use in discrete-time theory.

The discrete-time bilinear operator (w) is another simple reparameterisation of the q operator. The primary benefit of this parameterisation is the close approximation of the discrete-time w-operator model coefficients to those of the underlying continuous-time model. The w-operator parameterisation also displays the superior numerical properties of the δ-operator parameterisation.

In section 2.2, some common continuous- and discrete-time operator-model representations, as well as the corresponding transform-transfer function models, are introduced. These include the differential-operator continuous-time model, as well as the q-, δ-, and w-operator discrete-time models. The corresponding transform transfer functions are also introduced.

In section 2.3, the hold-equivalents technique [57] is used to derive discrete-time model equivalents of continuous-time models. Using the triangle-hold discrete-time equivalent, the suitability of employing the coefficients of either the q-, δ-, or w-operator models as direct approximations to the coefficients of the corresponding continuous-time models is investigated.

Section 2.4 concludes the work in this chapter.

2.2 Continuous- and Discrete-Time Models

2.2.1 Operator Models

Continuous-Time Model

A Linear, Time-Invariant (LTI), continuous-time system can be written as an input-output model (differential equation) of the form [6]

$$\begin{aligned} a_n\rho^n y(t) + a_{n-1}\rho^{n-1}y(t) + \cdots + a_0 y(t) \\ = b_m\rho^m u(t) + b_{m-1}\rho^{m-1}u(t) + \cdots + b_0 u(t) \end{aligned} \tag{2.1}$$

In this equation, ρ is the differential operator $\rho = d/dt$; a_i, b_j are constant coefficients ($i = 0 \ldots n$, $j = 0 \ldots m$, $m \leq n$); and $u(t), y(t)$ are respectively the continuous-time input and output signals.

Eqn. 2.1 can be rewritten in the form

$$a(\rho)y(t) = b(\rho)u(t)$$

where $a(\rho)$ and $b(\rho)$ are polynomials in the differential operator ρ.

Discrete-Time Models

Discrete-time models are generally characterised by linear difference equations of the form [58]

$$\begin{aligned} &A_n y((k+n)\Delta) + A_{n-1} y((k+n-1)\Delta) + \cdots + A_0 y(k\Delta) \\ &\quad = B_m u((k+m)\Delta) + B_{m-1} u((k+m-1)\Delta) + \cdots + B_0 u(k\Delta) \end{aligned} \quad (2.2)$$

where A_i, B_j are constant coefficients ($i = 0 \ldots n$, $j = 0 \ldots m$, $m \leq n$); and $u(i\Delta), y(i\Delta)$ are respectively the sampled input and output signals at time $t = i\Delta$ (Δ is the sampling period). These input-output signals can either be sampled continuous-time signals, or inherently discrete-time signals.

A more convenient way of writing eqn. 2.2 is to define the forward-shift operator q, where

$$qu(k\Delta) \triangleq u((k+1)\Delta)$$

Using this operator notation, eqn. 2.2 becomes

$$\begin{aligned} &A_n q^n y_k + A_{n-1} q^{n-1} y_k + \cdots + A_0 y_k \\ &\quad = B_m q^m u_k + B_{m-1} q^{m-1} u_k + \cdots + B_0 u_k \end{aligned} \quad (2.3)$$

where the notation $y_k = y(k\Delta)$ has been adopted for simplicity. Eqn. 2.3 can be rewritten in the form

$$A(q)y_k = B(q)u_k$$

where $A(q)$ and $B(q)$ are polynomials in the operator q.

One disadvantage with using the discrete-time q-operator model is that the q operator is not at all like the continuous-time differential operator ρ. There is no correspondence between the discrete- and continuous-time models. On the other hand, a discrete-time difference-operator, which is more like a derivative, would lead to discrete-time models more like continuous-time models in ρ [6]. Both the delta and bilinear operators are such discrete-time operators.

The delta operator, which is a forward difference operator, is defined by [6]

$$\delta \triangleq \frac{q-1}{\Delta} \tag{2.4}$$

The δ operator is an Euler approximation to the differential operator ρ and is linearly related to the conventional q operator. Thus, given any discrete-time q-operator model, the substitution

$$q = 1 + \Delta\delta \tag{2.5}$$

can be used to derive the corresponding δ-operator model. For example, the q-operator model (eqn. 2.3) yields, on substitution of eqn. 2.5, the δ-operator model

$$\begin{aligned} &A'_n\delta^n y_k + A'_{n-1}\delta^{n-1}y_k + \cdots + A'_0 y_k \\ &\quad = B'_m\delta^m u_k + B'_{m-1}\delta^{m-1}u_k + \cdots + B'_0 u_k \end{aligned} \tag{2.6}$$

Note that the orders of both the $A'(\delta)$ and $B'(\delta)$ polynomials in the δ-operator model are the same as for the q-operator model (eqn. 2.3). This is due to the linear relationship between δ and q.

The δ operator has recently gained acceptance in the discrete-time control field as an alternative to the q operator [6,59].

The bilinear operator, defined by [57]

$$w \triangleq \frac{2}{\Delta}\left(\frac{q-1}{q+1}\right) \tag{2.7}$$

is another discrete-time approximation to the differential operator ρ. In contrast to the δ operator, the w operator is a *nonlinear* reparameterisation of the q operator. For

many years the w operator has been used for transforming between the discrete- and continuous-time domains. The transformation is known as the 'trapezoidal rule' or 'Tustin's method'. As with the δ operator, given any discrete-time q-operator model, the substitution

$$q = \frac{2 + \Delta w}{2 - \Delta w} \tag{2.8}$$

can be used to determine the corresponding w-operator model. For example, the discrete-time w-operator model is derived from eqn. 2.3 using eqn. 2.8

$$\begin{aligned} &A''_n w^n y_k + A''_{n-1} w^{n-1} y_k + \cdots + A''_0 y_k \\ &\quad = B''_n w^n u_k + B''_{n-1} w^{n-1} u_k + \cdots + B''_0 u_k \end{aligned} \tag{2.9}$$

Note the order of both the $A''(w)$ and $B''(w)$ polynomials in the w-operator model is n. The order of the q-operator polynomial $B(q)$ (eqn. 2.3) is m. The possible increase in order from m to n in the polynomials $B(q)$ to $B''(w)$ is due to the nonlinear relationship between w and q.

The three discrete-time operator model parameterisations, namely the q-, δ- and w-operator models (eqns. 2.3, 2.6 and 2.9), are merely different parameterisations of *exactly* the same discrete-time model, and thus they are all equivalent. The advantage of the δ- and w-operator parameterisations is that, because these operators are approximations to the continuous-time differential operator ρ, the resulting coefficients of the discrete-time models show some correspondence to those of the continuous-time model. In particular, the coefficients of the δ- and w-operator models approach those of the continuous-time model as the sampling period tends to zero. This is discussed further in section 2.3.2.

2.2.2 Implementation of Discrete-Time Operators

Having introduced the three discrete-time operator model parameterisations, it is desirable to be able to implement these models directly in their operator form.

Shift Operator

The basic building block of the q-operator model is the backward-shift operation q^{-1}. This is a delay of one sample period, and is thus very easy to implement.

Delta Operator

For implementing the δ-operator model directly, the basic building block is the δ^{-1} operation. Given the relationship

$$y_k = \delta^{-1} u_k,$$

δ^{-1} can be replaced using eqn. 2.4 to yield

$$y_{k+1} = y_k + \Delta u_k$$

Thus the δ^{-1} operation, whilst being relatively simple, is a little more complex than the simple backward-shift operation q^{-1}.

Bilinear Operator

The basic building block for direct implementation of the w-operator model is the operation w^{-1}. Given the relationship

$$y_k = w^{-1} u_k,$$

the w^{-1} operation can be replaced using eqn. 2.7 to yield

$$y_{k+1} = y_k + \frac{\Delta}{2}(u_{k+1} + u_k) \tag{2.10}$$

This relationship can be represented by the block diagram, shown in Figure 2.1. The w^{-1} operation is relatively simple to implement, however, there is a small increase in the number of additions/multiplications required, relative to the q^{-1} and δ^{-1} operations. The implementation of the w^{-1} building block in a state-space filter is given in the next section.

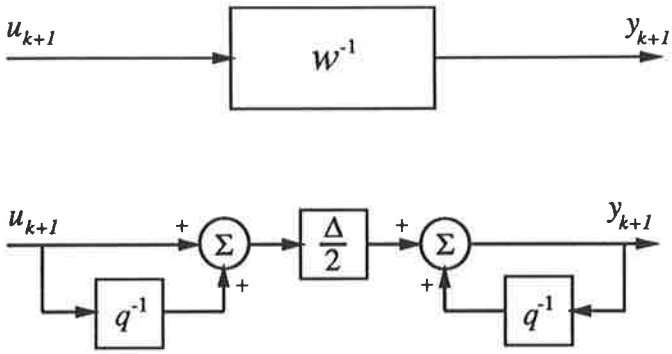

Figure 2.1: Implementation of w^{-1} operation.

2.2.3 Numerical Properties

The primary benefit of both the δ- and w-operator model parameterisations is that their coefficients approximate those of the continuous-time model. However, another advantage of these discrete-time parameterisations over the conventional q-operator parameterisation is that they are numerically superior for finite word-length computation.

Consider a normalised, fourth-order, Butterworth, low-pass filter, given by the continuous-time ρ-operator model [6, page 44]

$$(\rho^4 + 2.6131\rho^3 + 3.4142\rho^2 + 2.6131\rho + 1.0)y(t) = u(t) \tag{2.11}$$

This is converted to the corresponding q-, δ- and w-operator models by taking the z-transform with zero-order hold (see sections 2.2.4 and 2.3.1). The sampling period is chosen as $\Delta = 0.2$ s.

The evaluated q-operator model is:

$$\begin{aligned}(q^4 - 3.4788q^3 + 4.5680q^2 - 2.6809q + 0.5930)y_k \\ = 10^{-3}(0.06q^3 + 0.5936q^2 + 0.5347q + 0.0438)u_k\end{aligned} \tag{2.12}$$

The δ-operator model is found by substituting eqn. 2.5 into eqn. 2.12 :

$$(\delta^4 + 2.6059\delta^3 + 3.2882\delta^2 + 2.3269\delta + 0.77)y_k$$

$$= (0.0003\delta^3 + 0.0193\delta^2 + 0.2377\delta + 0.77)u_k \tag{2.13}$$

The w-operator model is found by substituting eqn. 2.8 into eqn. 2.12 :

$$(w^4 + 2.6167w^3 + 3.4237w^2 + 2.6218w + 1.00)y_k$$
$$= (3.47 \times 10^{-6}w^4 + 0.0006w^3 - 0.0075w^2 - 0.0913w + 1.00)u_k \tag{2.14}$$

For implementation, each input-output model is converted to a state space form. The q-operator model (eqn. 2.12) becomes [6] :

$$x_{k+1} = \begin{bmatrix} 3.4788 & -4.5680 & 2.6809 & -0.5930 \\ 1 & 0 & 0 & 0 \\ 0 & 1 & 0 & 0 \\ 0 & 0 & 1 & 0 \end{bmatrix} x_k + \begin{bmatrix} 1 \\ 0 \\ 0 \\ 0 \end{bmatrix} u_k \tag{2.15a}$$

$$y_k = 10^{-3}[\ 0.06 \quad 0.5936 \quad 0.5347 \quad 0.0438\ ]x_k \tag{2.15b}$$

The δ-operator model (eqn. 2.13) becomes [6] :

$$x_{k+1} = \begin{bmatrix} -2.6059\Delta + 1 & -3.2882\Delta & -2.3269\Delta & -0.77\Delta \\ \Delta & 1 & 0 & 0 \\ 0 & \Delta & 1 & 0 \\ 0 & 0 & \Delta & 1 \end{bmatrix} x_k + \begin{bmatrix} \Delta \\ 0 \\ 0 \\ 0 \end{bmatrix} u_k \tag{2.16a}$$

$$y_k = [\ 0.0003 \quad 0.0193 \quad 0.2377 \quad 0.77\ ]x_k \tag{2.16b}$$

where the state vector is given by

$$x_k^T = [\ \tfrac{\delta^3 u_k}{A'(\delta)} \quad \tfrac{\delta^2 u_k}{A'(\delta)} \quad \tfrac{\delta u_k}{A'(\delta)} \quad \tfrac{u_k}{A'(\delta)}]$$

To derive a w-operator state-space implementation, a state vector x_k is selected with the same form as the δ-operator state vector, namely

$$x_k^T = \left[\frac{w^4 u_k}{A''(w)} \quad \frac{w^3 u_k}{A''(w)} \quad \frac{w^2 u_k}{A''(w)} \quad \frac{w u_k}{A''(w)} \quad \frac{u_k}{A''(w)} \right] \tag{2.17}$$

where $A''(w)$ is the polynomial (from eqn. 2.14)

$$A''(w) = w^4 + 2.6167w^3 + 3.4237w^2 + 2.6218w + 1$$

This form of the state vector also happens to closely resemble the form of the regression vector (eqn. 3.9) for the recursive estimation algorithms developed independently in section 3.2.

The elements of the state vector (eqn. 2.17) can be expressed in the form

$$\frac{w^i u_k}{A''(w)} = w^{-1} \frac{w^{i+1} u_k}{A''(w)}$$

which, using eqn. 2.10, can be expanded to yield

$$\frac{w^i u_{k+1}}{A''(w)} = \frac{w^i u_k}{A''(w)} + \frac{\Delta}{2} \left(\frac{w^{i+1} u_{k+1}}{A''(w)} + \frac{w^{i+1} u_k}{A''(w)} \right)$$

The state vector elements thus become

$$\begin{aligned}
\frac{w^3 u_{k+1}}{A''(w)} &= \frac{w^3 u_k}{A''(w)} + \frac{\Delta}{2} \left(\frac{w^4 u_{k+1}}{A''(w)} + \frac{w^4 u_k}{A''(w)} \right) \\
\frac{w^2 u_{k+1}}{A''(w)} &= \frac{w^2 u_k}{A''(w)} + \frac{\Delta}{2} \left(\frac{w^3 u_{k+1}}{A''(w)} + \frac{w^3 u_k}{A''(w)} \right) \\
\frac{w u_{k+1}}{A''(w)} &= \frac{w u_k}{A''(w)} + \frac{\Delta}{2} \left(\frac{w^2 u_{k+1}}{A''(w)} + \frac{w^2 u_k}{A''(w)} \right) \\
\frac{u_{k+1}}{A''(w)} &= \frac{u_k}{A''(w)} + \frac{\Delta}{2} \left(\frac{w u_{k+1}}{A''(w)} + \frac{w u_k}{A''(w)} \right)
\end{aligned} \tag{2.18}$$

On further equation can be obtained by expanding out the term u_{k+1}

$$\begin{aligned}
u_{k+1} &= A''(w) \frac{u_{k+1}}{A''(w)} \\
&= \frac{w^4 u_{k+1}}{A''(w)} + A_3'' \frac{w^3 u_{k+1}}{A''(w)} + A_2'' \frac{w^2 u_{k+1}}{A''(w)} + A_1'' \frac{w u_{k+1}}{A''(w)} + A_0'' \frac{u_{k+1}}{A''(w)}
\end{aligned} \tag{2.19}$$

Rearranging eqns. 2.18 and 2.19 by collecting common terms in k and $k+1$ yields the matrix relationship

$$Nx_{k+1} = Mx_k + \begin{bmatrix} 1 \\ 0 \\ 0 \\ 0 \\ 0 \end{bmatrix} u_{k+1}$$

where

$$N = \begin{bmatrix} 1 & A_3'' & A_2'' & A_1'' & A_0'' \\ -\Delta/2 & 1 & 0 & 0 & 0 \\ 0 & -\Delta/2 & 1 & 0 & 0 \\ 0 & 0 & -\Delta/2 & 1 & 0 \\ 0 & 0 & 0 & -\Delta/2 & 1 \end{bmatrix}$$

$$M = \begin{bmatrix} 0 & 0 & 0 & 0 & 0 \\ \Delta/2 & 1 & 0 & 0 & 0 \\ 0 & \Delta/2 & 1 & 0 & 0 \\ 0 & 0 & \Delta/2 & 1 & 0 \\ 0 & 0 & 0 & \Delta/2 & 1 \end{bmatrix}$$

A rearrangement provides the state-space implementation of the w-operator model

$$x_{k+1} = N^{-1}Mx_k + N^{-1} \begin{bmatrix} 1 \\ 0 \\ 0 \\ 0 \\ 0 \end{bmatrix} u_{k+1} \qquad (2.20a)$$

$$y_k = [\ B_4''\ \ B_3''\ \ B_2''\ \ B_1''\ \ B_0''\ ]x_k \qquad (2.20b)$$

Note that B_i'' are the coefficients of the polynomial $B''(w)$ from eqn. 2.14,

$$B''(w) = B_4''w^4 + B_3''w^3 + B_2''w^2 + B_1''w + B_0''$$

$$= 3.47 \times 10^{-6} w^4 + 0.0006 w^3 - 0.0075 w^2 - 0.0913 w + 1.00$$

To compare the numerical properties of these three state-space implementations of the filter (eqn. 2.15, 2.16 and 2.20), the step response of each is calculated. To simulate finite precision calculations, each multiplication and addition operation is rounded to the nearest floating point number with an n-bit mantissa. The resulting step response of each state-space operator formulation of the filter is displayed in Figures 2.2, 2.3 and 2.4, for several values of the mantissa length n. For n=32 bits, the step response for all implementations is virtually identical to the true step response of the continuous-time filter.

From these figures it is clear that both the δ- and w-operator parameterisations have superior numerical properties concerning finite word-length effects, compared to the conventional q-operator formulation.

2.2.4 Transform Transfer Functions

The four operator models introduced so far, describe the behaviour of a system in the time domain; the operators ρ, q, δ and w all represent an operation on a time sequence.

A convenient technique for analysing the behaviour of these time domain models is by means of transform techniques. Such techniques transform the time-domain differential or difference equations into linear, algebraic equations in the complex frequency domain. These algebraic equations can often be solved relatively easily in the complex frequency domain, then transformed back to the time domain to provide the solution to the original time-domain equations.

As well as providing a method of solution for the time-domain equations, the transform domain also introduces many useful concepts to help analyse and characterise the behaviour of the system. For example, the transform-domain transfer function introduces techniques such as Routh's criterion, or the root-locus technique, for examining the stability and dynamic performance of a system.

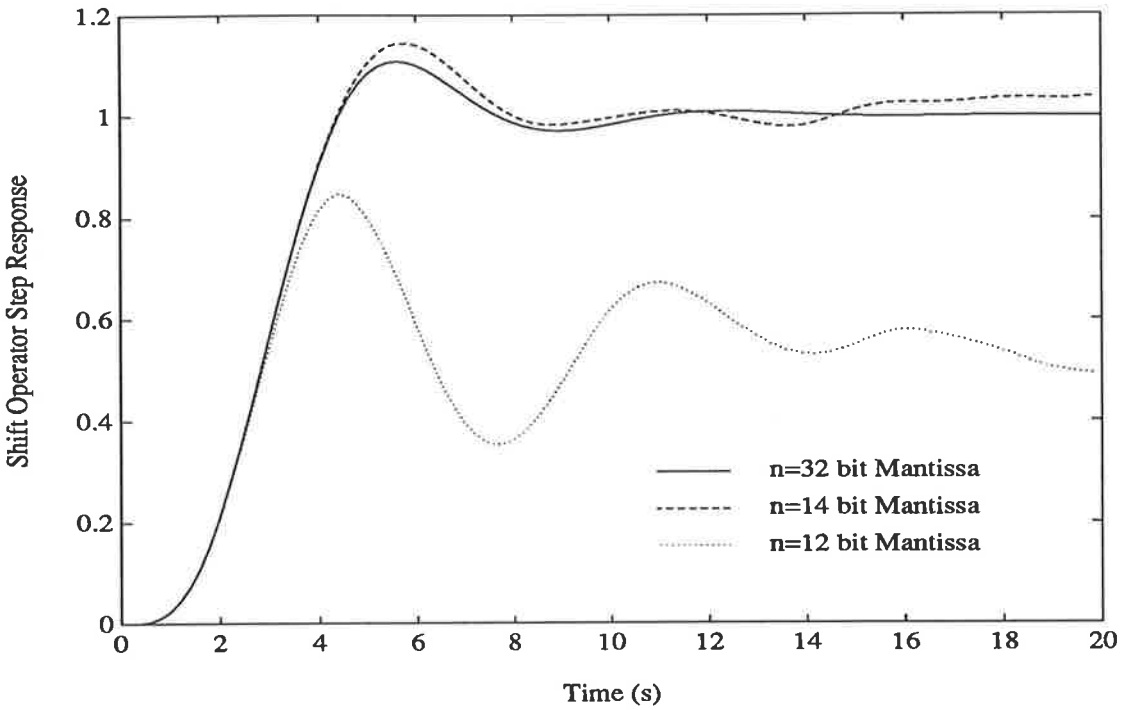

Figure 2.2: The step response for the state-space q-operator implementation, eqn. 2.15.

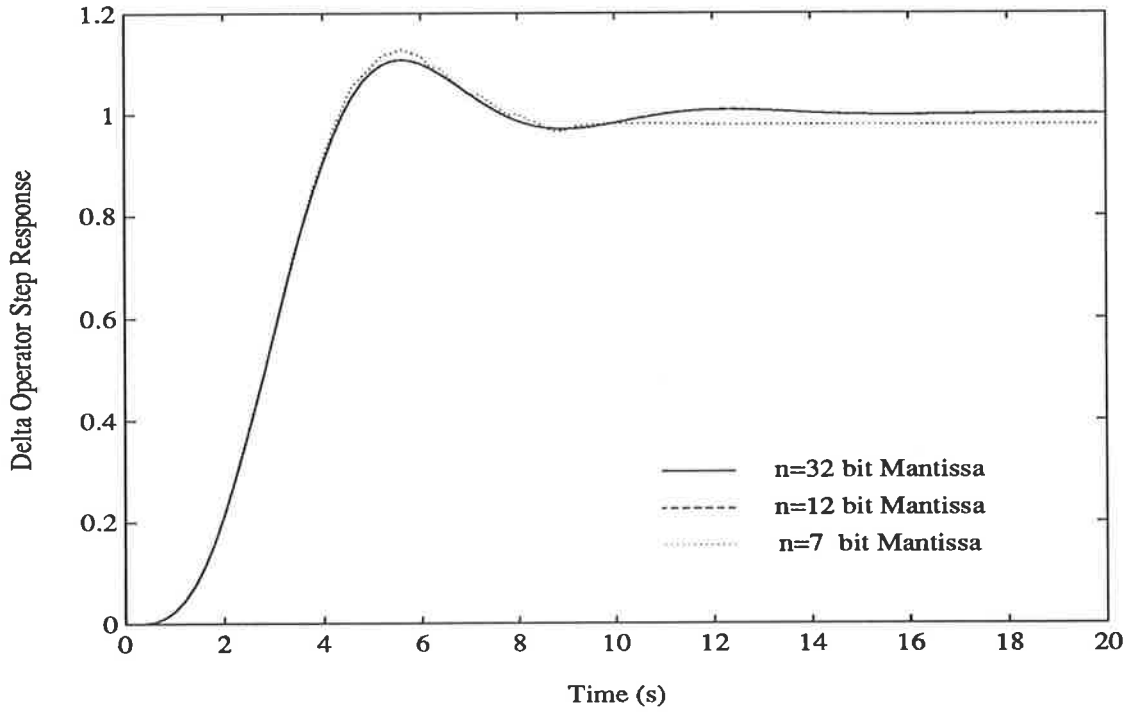

Figure 2.3: The step response for the state-space δ-operator implementation, eqn. 2.16.

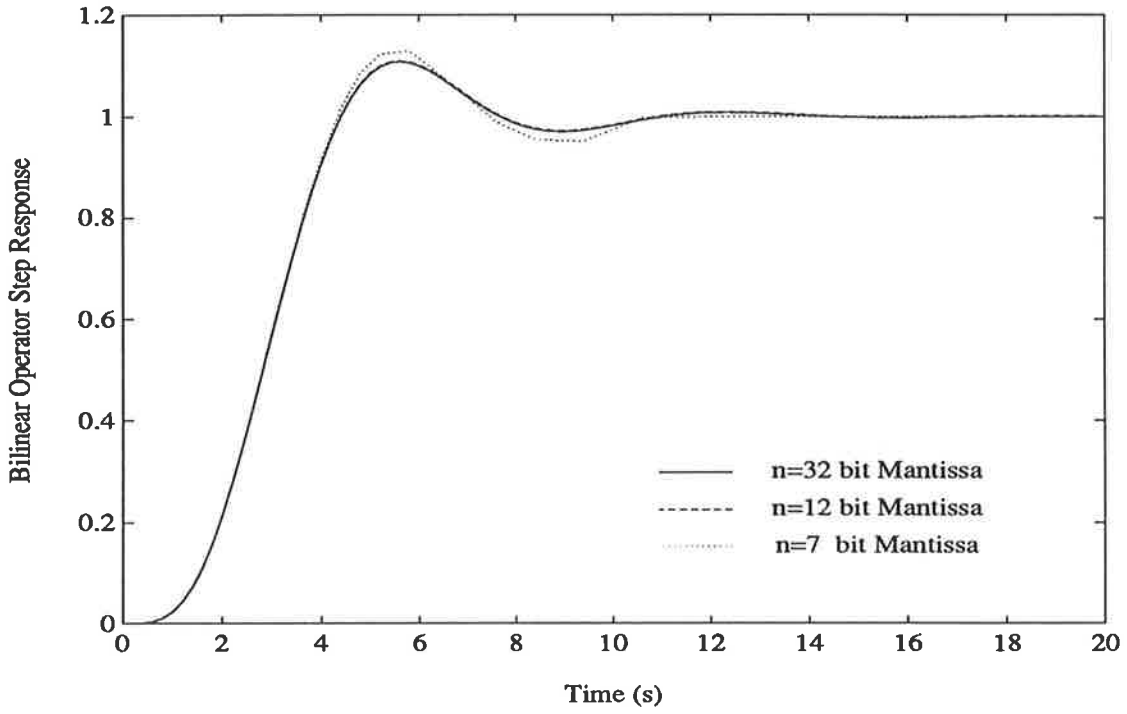

Figure 2.4: The step response for the state-space w-operator implementation, eqn. 2.20.

Laplace Transform

The Laplace transform of a continuous-time signal $u(t)$, where $u(t) = 0$ for $t < 0$, is defined by [6]

$$U(s) \triangleq \mathcal{L}\{u(t)\} \triangleq \int_0^\infty u(t)e^{-st}dt \tag{2.21}$$

The Laplace-transform maps the time domain signal $u(t)$ to a function $U(s)$ in the complex variable s.

Taking the Laplace transform of the continuous-time differential equation (eqn. 2.1), assuming zero initial conditions ($y(0) = \rho y(0) = \ldots = \rho^{n-1}y(0) = u(0) = \ldots = \rho^{m-1}u(0) = 0$), yields the Laplace-transform model

$$\begin{aligned} &a_n s^n Y(s) + a_{n-1}s^{n-1}Y(s) + \cdots + a_0 Y(s) \\ &\quad = b_m s^m U(s) + b_{m-1}s^{m-1}U(s) + \cdots + b_0 U(s), \end{aligned} \tag{2.22}$$

which can be expressed conveniently as

$$a(s)Y(s) = b(s)U(s),$$

where $a(s)$ and $b(s)$ are polynomials in the complex variable s. This algebraic equation can be rearranged to give the Laplace transform of the output signal $Y(s)$ as a function of the input transform $U(s)$,

$$Y(s) = H(s)U(s)$$

where

$$H(s) = \frac{Y(s)}{U(s)} = \frac{b(s)}{a(s)} = \frac{b_m s^m + b_{m-1}s^{m-1} + \cdots + b_0}{a_n s^n + a_{n-1}s^{n-1} + \cdots + a_0} \tag{2.23}$$

The function $H(s)$ completely characterises the input-output behaviour of the system and is termed the transfer function of the continuous-time system.

Note, comparing eqns. 2.1, 2.22 and 2.23, it is clear that the coefficients of the time-domain differential equation, and the coefficients of the Laplace-transform model and transfer function, are equal. Thus, given one form of the continuous-time model, it is a trivial exercise to deduce the other forms of the model.

For brevity, the abbreviation TF will generally be used within the text to represent

the term Transfer Function.

z Transform

As the Laplace transform is used in the continuous-time domain, so the z transform is employed in the discrete-time domain. Given a discrete-time sequence $\{u_k : k = 0, 1, \ldots \infty\}$, the z transform is defined as [6]

$$U(z) \triangleq \mathcal{Z}\{u_k\} \triangleq \sum_{k=0}^{\infty} u_k z^{-k} \tag{2.24}$$

where z is a complex variable. Taking the z transform of the discrete-time difference equation (eqn. 2.3) assuming zero initial conditions, yields the z-transform model

$$\begin{aligned} &A_n z^n Y(z) + A_{n-1} z^{n-1} Y(z) + \cdots + A_0 Y(z) \\ &\quad = B_m z^m U(z) + B_{m-1} z^{m-1} U(z) + \cdots + B_0 U(z) \end{aligned} \tag{2.25}$$

As is the case for the Laplace transform, the z-transform model can be rearranged to yield the transfer function of the discrete-time system.

$$H(z) = \frac{Y(z)}{U(z)} = \frac{B(z)}{A(z)} = \frac{B_m z^m + B_{m-1} z^{m-1} + \cdots + B_0}{A_n z^n + A_{n-1} z^{n-1} + \cdots + A_0} \tag{2.26}$$

Comparing eqns. 2.25, 2.26 and 2.3, it is clear that the coefficients of the discrete-time q-operator model and the corresponding z-transform models are equal. Consequently, it is common to use the symbols q and z interchangeably when describing these discrete-time models [6].

Because of the exact correspondence between the coefficients of the operator and transform models, the term q-domain model is often used throughout this thesis to refer to either the q-operator model, or the z-transform model or TF.

δ and w Transforms

For both the Laplace- and z-transform models discussed so far, the transform version of the system equations may be formed simply by replacing the operator in the time-domain system equation with the corresponding transform variable. The relationship

between the operator and transform models can be extended to both the δ- and w-operator models by defining the δ and w transforms, respectively, as

$$\begin{aligned} U(\gamma) &\triangleq \mathcal{Z}\{u_k\}\,|_{z=1+\Delta\gamma} \\ U(\beta) &\triangleq \mathcal{Z}\{u_k\}\,|_{z=\frac{2+\Delta\beta}{2-\Delta\beta}} \end{aligned}$$

where $\mathcal{Z}\{.\}$ is the z transform, and γ and β are the transform complex variables for the δ- and w-operator models respectively. Both γ and β are related to the complex variable z by

$$\begin{aligned} \gamma &= \frac{(z-1)}{\Delta} && \text{for the } \delta\text{-operator transform variable} \\ \beta &= \frac{2}{\Delta}\left(\frac{z-1}{z+1}\right) && \text{for the } w\text{-operator transform variable} \end{aligned}$$

Taking the δ and w transforms of the discrete-time difference equation (eqn. 2.3), assuming zero initial conditions, yields the transform models

$$\begin{aligned} &A'_n\gamma^n Y(\gamma) + A'_{n-1}\gamma^{n-1}Y(\gamma) + \cdots + A'_0 Y(\gamma) \\ &\quad = B'_m\gamma^m U(\gamma) + B'_{m-1}\gamma^{m-1}U(\gamma) + \cdots + B'_0 U(\gamma) \end{aligned} \tag{2.27}$$

and

$$\begin{aligned} &A''_n\beta^n Y(\beta) + A''_{n-1}\beta^{n-1}Y(\beta) + \cdots + A''_0 Y(\beta) \\ &\quad = B''_n\beta^n U(\beta) + B''_{n-1}\beta^{n-1}U(\beta) + \cdots + B''_0 U(\beta) \end{aligned} \tag{2.28}$$

These equations are rearranged to form the TFs of the δ- and w-operator models:

$$H'(\gamma) = \frac{Y(\gamma)}{U(\gamma)} = \frac{B'(\gamma)}{A'(\gamma)} = \frac{B'_m\gamma^m + B'_{m-1}\gamma^{m-1} + \cdots + B'_0}{A'_n\gamma^n + A'_{n-1}\gamma^{n-1} + \cdots + A'_0} \tag{2.29}$$

$$H''(\beta) = \frac{Y(\beta)}{U(\beta)} = \frac{B''(\beta)}{A''(\beta)} = \frac{B''_n\beta^n + B''_{n-1}\beta^{n-1} + \cdots + B''_0}{A''_n\beta^n + A''_{n-1}\beta^{n-1} + \cdots + A''_0} \tag{2.30}$$

Comparing the various forms of the discrete-time δ- and w-parameterised models, i.e. eqns. 2.6, 2.27 and 2.29 for the δ parameterisation, and eqns. 2.9, 2.28 and 2.30 for

the w parameterisation, it is clear that the coefficients of the operator and transform models are equal. Thus, given one form of the system model (i.e. either the operator or transform model), it is a simple exercise to deduce the other form.

Because of the exact correspondence between the coefficients of the operator and transform models for both the δ and w models, the terms δ-domain model and w-domain model are often used throughout this thesis to refer to either the operator, transform or TF model forms.

2.3 A Discrete-Time Model Which Approximates the Continuous-Time Model of a System

The main focus of this thesis is the estimation of the coefficients of continuous-time models (either ρ operator or Laplace transform) from the sampled input-output signals of a continuous-time system. Both the δ- and w-domain models provide discrete-time model representations that may be suitable for this task. They both provide discrete-time model parameterisations, the coefficients of which approximate those of the continuous-time model.

To accurately assess the merits of using the coefficients of either the δ- or w-domain models as direct approximations to those of the continuous-time model, some method of deriving analytically an equivalent discrete-time model from the continuous-time model is required. In section 2.3.1, the hold-equivalents technique [57] is used to derive equivalent discrete-time models of a continuous-time system. Specifically, discrete-time models which accurately represents the relationship between the sampled input and output signals of a continuous-time system are derived. In section 2.3.2, by way of an example, the suitability of using the δ- or w-domain coefficients directly as approximations to those of a continuous-time model is investigated.

It is worth stating that the work in this section (section 2.3) is included only to demonstrate how closely the coefficients of both the δ- and w-domain models approximate those of the corresponding continuous-time model. This work is not required for formulating the recursive estimation algorithms, discussed in chapter 3.

Later, in chapter 4, a simulation study is used to show that the triangle-hold-

equivalent discrete-time w-domain model derived in this section, in fact matches closely the model to which the estimation algorithms converge, thus confirming the comparisons made in this section are valid.

2.3.1 Which Discrete-Time Model ?

The question which arises when attempting to model the input-output behaviour of a continuous-time system in the discrete-time domain is, 'What discrete-time model will accurately represent the input-output relationship of the specified continuous-time system ?'

To state the problem clearly:

Given the continuous-time input-output signals $u(t)$ and $y(t)$, related by the continuous-time TF $H(s)$, find the discrete-time TF model $H(z)$ that *exactly* represents the relationship between the input-output signals $u(t)$ and $y(t)$ at the sample points $t = k\Delta : k = 0, 1, \ldots \infty$.

To find this discrete-time model, the idea of hold equivalents, as discussed in Franklin, Powell and Workman, will be used [57].

q-Domain Model

Consider a continuous-time system with TF $H(s)$. The impulse response of this system is given by the inverse Laplace transform [60]

$$h(t) = \mathcal{L}^{-1}\{H(s)\}$$

The z transform of the samples of this response are given by [61]

$$\begin{aligned} H(z) &= \mathcal{Z}\{h(k\Delta)\} \\ &= \mathcal{Z}\{\mathcal{L}^{-1}\{H(s)\} \mid_{t=k\Delta}\} \\ &\triangleq \mathcal{Z}\{H(s)\} \end{aligned}$$

The discrete-time model $H(z)$ provides a model of the continuous-time TF $H(s)$, which accurately represents the relationship between the sampled continuous-time

input and output signals of $H(s)$, only when the continuous-time input signal is a series of impulses [15,61]. Figure 2.5 shows this scenario. Of course in a practical

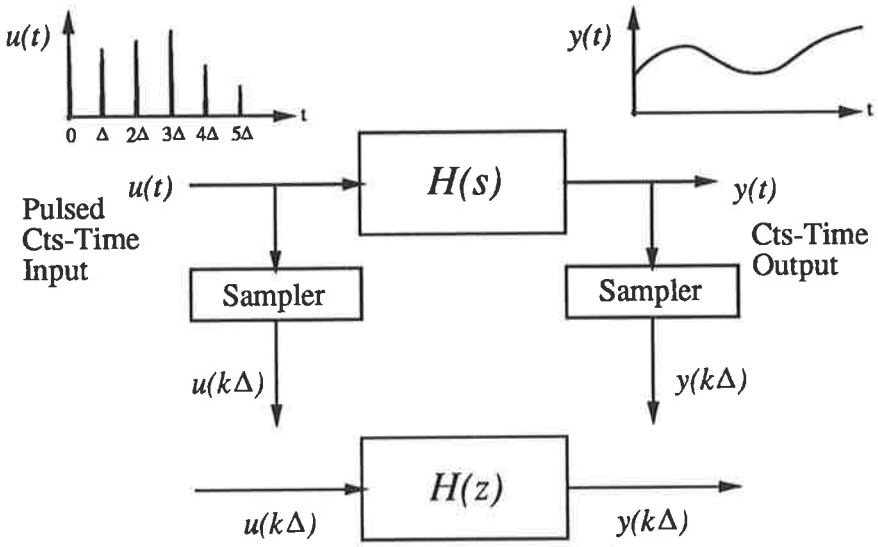

Figure 2.5: Discrete-time q-domain model of a continuous-time TF.

situation the continuous-time input signal is rarely a train of impulses. However, based on this z-transform relationship $H(z)$ for an impulsive input, the exact discrete-time model representation for a continuous-time TF $H(s)$ with a general input $u(t)$ can be deduced.

In order to explain the hold-equivalents technique, the system given in Figure 2.6 is constructed [57]. The basis of the hold-equivalent discrete-time model $H_{equiv}(z)$ is that, given the samples $u(k\Delta)$ of a continuous-time input signal $u(t)$, an output $\hat{y}(t)$ is generated which approximates the output $y(t)$ of a continuous-time TF with input $u(t)$. The hold-equivalent discrete-time model $H_{equiv}(z)$ is obtained by firstly reconstructing the approximate continuous-time input signal $\hat{u}(t)$ from the samples $u(k\Delta)$, and then passing this through the known TF $H(s)$. The accuracy of the reconstruction $\hat{u}(t)$ determines how closely the output $\hat{y}(t)$ will approximate $y(t)$. The hold-equivalent discrete-time model is thus given by the z-transform of the continuous-time TF with reconstruction included, i.e.

$$H_{equiv}(z) = \mathcal{Z}\{R(s)H(s)\} \tag{2.31}$$

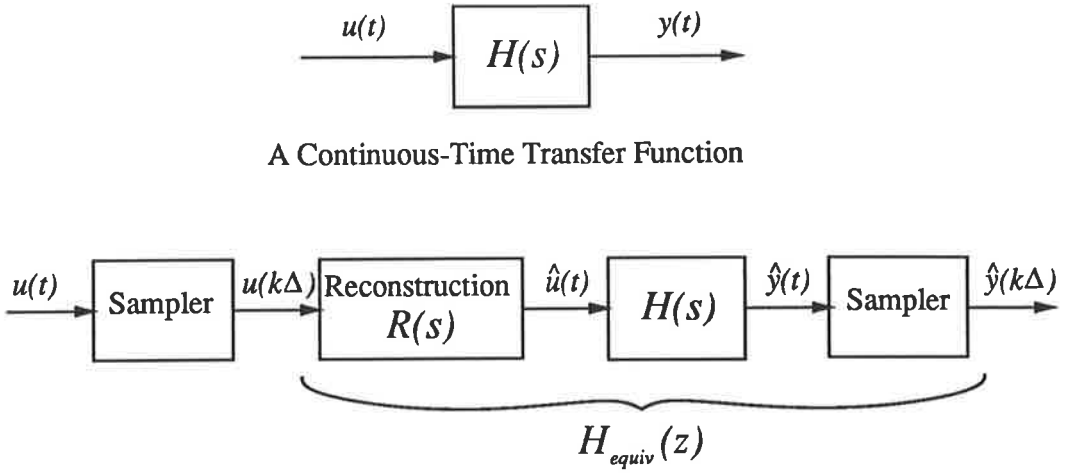

Figure 2.6: The discrete-time hold-equivalent model.

This highlights the fact that the discrete-time model which accurately describes the sampled input-output behaviour of a continuous-time system, is dependent on both the continuous-time system as well as the behaviour of the continuous-time input signal between sample points [62].

Whilst it is not feasible to define a general reconstruction TF $R(s)$ for all possible input signals, it is possible for certain classes of input.

ZOH Model

In applications of computer control of continuous-time systems it is common to use a digital-to-analogue (D/A) converter with Zero-Order Hold (ZOH) to convert the digital control signal to a piecewise-continuous, continuous-time signal. The D/A converter converts the digital signal to an analogue voltage which the ZOH maintains constant for the duration of the sampling period Δ. The action of a ZOH is shown in Figure 2.7

In terms of the reconstruction TF $R(s)$, the ZOH is given by [57]

$$R_{ZOH}(s) = \frac{1 - e^{-\Delta s}}{s} \tag{2.32}$$

Thus for a continuous-time TF $H(s)$ with a piecewise-continuous (i.e. ZOH) in-

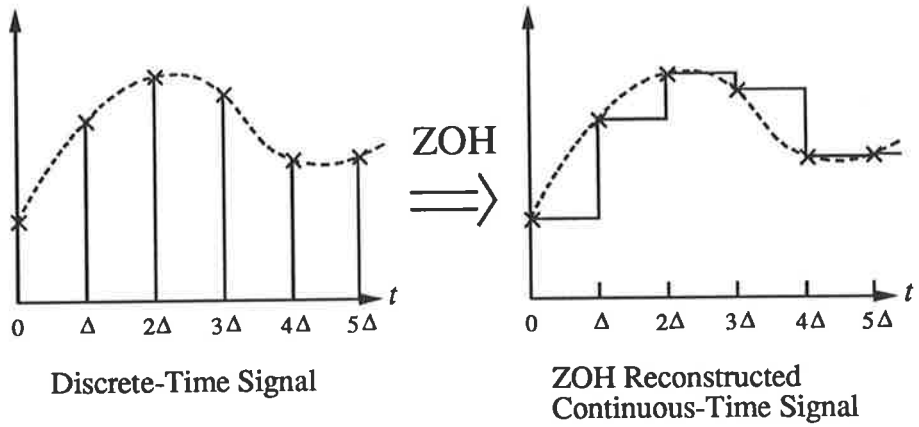

Figure 2.7: Reconstruction action of a ZOH.

put signal, the ZOH-equivalent discrete-time model representation is given by (using eqn. 2.31)

$$\begin{aligned} H_{ZOH}(z) &= H_{equiv}(z)\,|_{R_{ZOH}(s)} = \mathcal{Z}\{R_{ZOH}(s)H(s)\} \\ &= \left(\frac{z-1}{z}\right)\mathcal{Z}\left\{\frac{H(s)}{s}\right\} \end{aligned} \tag{2.33}$$

This discrete-time model is suitable, as mentioned, for cases involving computer control of continuous-time systems. However, this ZOH-equivalent discrete-time model is unlikely to accurately represent the relationship between the input and output signals sampled from a continuous-time system for the purpose of estimation. To explain this, consider the general test configuration of a continuous-time system, from which the input and output signals are sampled for use in discrete-time estimation (Figure 2.8). Firstly, the identification signal $u'(t)$ [1] is filtered by a low-pass filter $F(s)$ to remove any unwanted high-frequency signal components, and then applied to the continuous-time system under test through a power amplifier. This excitation signal is anti-alias filtered prior to sampling. Thus the continuous-time signal $u_f(t)$ is a filtered version of the (possibly) piecewise-continuous signal $u'(t)$. Thus the waveform of the continuous-time signal $u_f(t)$ is *not* likely to be similar to the signal reconstructed from $u_f(k\Delta)$ assuming a ZOH reconstruction. Due to the low-

[1] This signal is likely to be a piecewise-continuous signal, such as a Pseudo Random Binary Sequence (PRBS) which is the output from a digital computer with a ZOH reconstruction circuit.

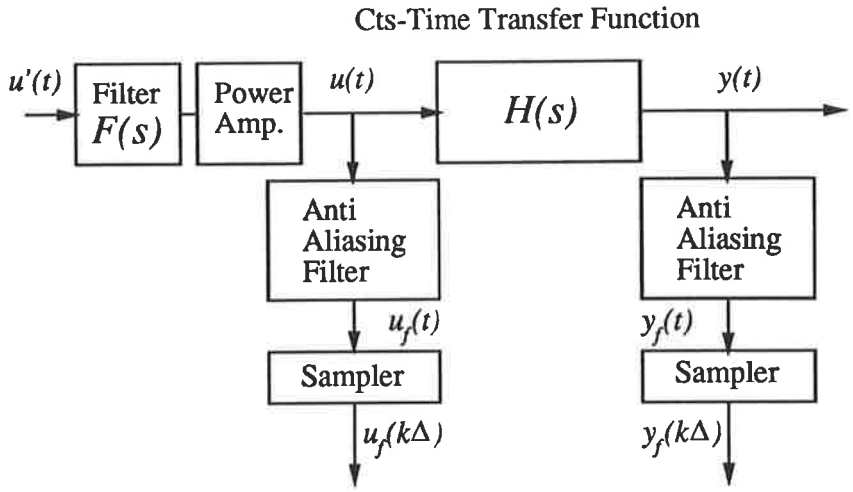

Figure 2.8: General system configuration for sampling input-output signals from a continuous-time system.

pass filtering of the signal, a far better reconstruction circuit would be the noncausal Triangle Hold (TH).

TH Model

The Triangle Hold (TH) circuit is a first-order reconstruction. Its effect is to perform a linear interpolation between the input signal samples. Figure 2.9 displays the reconstruction action of the TH. Note the triangle told is different to the conventional

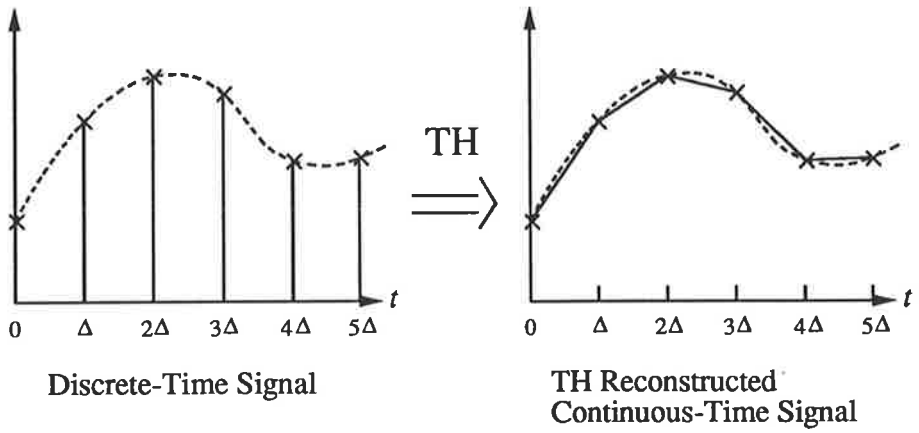

Figure 2.9: Reconstruction action of a Triangle Hold.

First-Order Hold (FOH) reconstruction. The TH performs a linear interpolation

between signal samples, whilst the FOH uses the previous two signal samples to produce a linear extrapolation of the signal. A comparison of Figures 2.7 and 2.9 (ZOH compared to TH) intuitively suggests that for a 'relatively smooth' continuous-time signal, the TH reconstruction from the sampled signal more closely matches the original continuous-time signal than does the ZOH reconstruction. In terms of the reconstruction TF $R(s)$, the TH is given by [57]

$$R_{TH}(s) = \frac{e^{\Delta s} - 2 + e^{-\Delta s}}{\Delta s^2} \tag{2.34}$$

Thus for a continuous-time TF $H(s)$ with an input signal corresponding to a TH-type signal, the TH-equivalent discrete-time model representation is given by (using eqn. 2.31)

$$\begin{aligned} H_{TH}(z) &= H_{equiv}(z) \mid_{R_{TH}(s)} = \mathcal{Z}\{R_{TH}(s)H(s)\} \\ &= \frac{(z-1)^2}{\Delta z}\mathcal{Z}\left\{\frac{H(s)}{s^2}\right\} \end{aligned} \tag{2.35}$$

From the preceding discussion, it is thus likely that the TH-equivalent discrete-time model will provide a reasonably accurate discrete-time model of the relationship between the sampled input and output signals acquired from the test configuration given in Figure 2.8. It is possible of course to use higher-order hold-circuit approximations for deriving the equivalent discrete-time model, however, this requires more detailed knowledge of the form of the continuous-time input signal between samples.

It should be emphasised that the purpose of deriving the TH-equivalent discrete-time model is only to postulate a discrete-time model representative of the relationship between the sampled input and output signals; the signals being sampled for the purpose of estimation. The TH-equivalent discrete-time model will be used in the next section to show how closely the coefficients of the discrete-time δ- and w-domain models approximate those of the underlying continuous-time model. For deriving the recursive estimation algorithms discussed later in chapter 3, no use is made of this TH-equivalent discrete-time model, nor its derivation.

2.3.2 q-, δ-, and w-Domain Models

In section 2.2, three different discrete-time models are introduced, namely the q-, δ-, and w-operator models (eqns. 2.3, 2.6 and 2.9). These are basically three different ways of expressing exactly the same discrete-time relationship between sampled input and output signals. To reiterate, the benefit of using either the δ- or w-operator parameterisations is that the coefficients of these discrete-time models approximate those of the underlying continuous-time model.

By way of an example, the coefficients of the TH-equivalent discrete-time q-, δ- and w-domain models will be examined for various sampling periods to establish how closely they approximate the coefficients of the corresponding continuous-time model.

Consider the continuous-time TF

$$\begin{aligned} H(s) &= \frac{s-1}{(s+1)(s^2+0.1s+2)} \\ &= \frac{s-1}{s^3+1.1s^2+2.1s+2} \end{aligned} \tag{2.36}$$

This is a non-minimum phase TF with poles and zero given by

$$\begin{aligned} \text{Poles} &: -1.0 \\ &\quad -0.05 \pm j1.4133 \\ \text{Zero} &: +1.0 \end{aligned}$$

The TH-equivalent discrete-time q-, δ- and w-domain models, calculated from the continuous-time TF using the z transform with TH, are given by

$$H_{TH}(z) = \frac{(z-1)^2}{\Delta z}\mathcal{Z}\left\{\frac{H(s)}{s^2}\right\} \tag{2.37}$$

$$H_{TH}(\gamma) = H_{TH}(z)\,|_{z=1+\Delta\gamma} \tag{2.38}$$

$$H_{TH}(\beta) = H_{TH}(z)\,|_{z=\frac{2+\Delta\beta}{2-\Delta\beta}} \tag{2.39}$$

All three discrete-time parameterisations result in third-order TFs of the form

$$H_{TH}(X) = \frac{B_3X^3+B_2X^2+B_1X+B_0}{X^3+A_2X^2+A_1X+A_0} \tag{2.40}$$

where X is either z, γ or β.

The coefficients of the discrete-time models are evaluated for sampling periods ranging from $\Delta = 1$ second (slow sampling, relative to the bandwidth of the continuous-time TF) to $\Delta = 0.1$ second (fast sampling, relative to the bandwidth of the continuous-time TF). The resulting discrete-time coefficients, and the TF poles and zeros are given in Tables 2.1 and 2.2 respectively.

	$\Delta = 1.0$s		$\Delta = 0.5$s		$\Delta = 0.2$s		$\Delta = 0.1$s		Cts-Time Coeffs
q-Domain Model Coefficients									
B_3	0.0841		0.0309		0.0060		0.0016		0.0
B_2	-0.0449		0.0416		0.0141		0.0042		0.0
B_1	-0.4626		-0.1343		-0.0213		-0.0052		1.0
B_0	-0.0843		-0.0304		-0.0059		-0.0016		-1.0
A_2	-0.6662		-2.0900		-2.7203		-2.8750		1.1
A_1	1.0146		1.8510		2.5370		2.7727		2.1
A_0	-0.3329		-0.5769		-0.8025		-0.8958		2.0
δ-Domain Model Coefficients									
B_3	0.0841	(-)	0.0309	(-)	0.0060	(-)	0.0016	(-)	0.0
B_2	0.2073	(-)	0.2688	(-)	0.1601	(-)	0.0898	(-)	0.0
B_1	-0.3002	(130)	0.1672	(83)	0.6207	(38)	0.8026	(20)	1.0
B_0	-0.5078	(49)	-0.7361	(26)	-0.8914	(11)	-0.9453	(6)	-1.0
A_2	2.3338	(112)	1.8199	(65)	1.3987	(27)	1.2498	(14)	1.1
A_1	2.6822	(28)	2.6838	(28)	2.4133	(15)	2.2705	(8)	2.1
A_0	1.0155	(49)	1.4723	(26)	1.7828	(11)	1.8906	(6)	2.0
w-Domain Model Coefficients									
B_3	-0.0827	(-)	-0.0207	(-)	-0.0033	(-)	-0.0008	(-)	0.0
B_2	0.3363	(-)	0.0684	(-)	0.0104	(-)	0.0026	(-)	0.0
B_1	1.2249	(22)	1.0428	(4)	1.0064	(0.6)	1.0016	(0.2)	1.0
B_0	-1.3479	(35)	-1.0672	(7)	-1.0101	(1)	-1.0025	(0.3)	-1.0
A_2	1.0970	(0.3)	1.0933	(0.6)	1.0987	(0.1)	1.0997	(0.03)	1.1
A_1	3.0764	(46)	2.2901	(9)	2.1286	(1)	2.1071	(0.3)	2.1
A_0	2.6957	(35)	2.1345	(7)	2.0202	(1)	2.0050	(0.3)	2.0

Table 2.1: Discrete-time q-, δ-, and w-domain coefficients calculated from the continuous-time TF $H(s)$ (eqn. 2.36), assuming a Triangle Hold. The bracketed numbers are the magnitude of the difference between the discrete-time and continuous-time coefficients as a percentage of the continuous-time coefficients.

Consider each model in turn.

	$\Delta = 1.0$s	$\Delta = 0.5$s	$\Delta = 0.2$s	$\Delta = 0.1$s	Cts-Time Poles/Zeros
q-Domain Model Poles/Zeros					
Zeros	2.7053	1.6483	1.2214	1.1052	+1.0
	–1.9846	–2.7781	–3.3411	–3.5261	–
	–0.1868	–0.2143	–0.2427	–0.2546	–
Poles	0.3679	0.6065	0.8187	0.9048	–1.0
	$0.15 \pm j0.94$	$0.74 \pm j0.63$	$0.95 \pm j0.28$	$0.99 \pm j0.14$	$-0.05 \pm j1.41$
δ-Domain Model Poles/Zeros					
Zeros	1.7053	1.2967	1.1070	1.0517	+1.0
	–2.9846	–7.5562	–21.7055	–45.3606	–
	–1.1868	–2.4286	–6.2135	–12.5462	–
Poles	–0.6321	–0.7869	–0.9063	–0.9516	–1.0
	$-0.85 \pm j0.94$	$-0.52 \pm j1.27$	$-0.25 \pm j1.38$	$-0.15 \pm j1.40$	$-0.05 \pm j1.41$
w-Domain Model Poles/Zeros					
Zeros	0.9205	0.9792	0.9967	0.9992	+1.0
	–2.9191	–6.1823	–16.4099	–33.6642	–
	6.0624	8.4992	18.5430	35.7725	–
Poles	–0.9242	–0.9797	–0.9967	–0.9992	–1.0
	$-0.09 \pm j1.71$	$-0.06 \pm j1.48$	$-0.05 \pm j1.42$	$-0.05 \pm j1.42$	$-0.05 \pm j1.41$

Table 2.2: Discrete-time q-, δ-, and w-domain model poles and zeros. The discrete-time models are calculated from the continuous-time TF $H(s)$ (eqn. 2.36), assuming a Triangle Hold.

q-Domain Model

From Table 2.1 it is clear that the coefficients of the q-domain model show no resemblance to those of the continuous-time TF for the sampling periods considered. This is not surprising as the q operator is not an approximation to the continuous-time differential operator ρ.

The discrete-time poles, z_{di}, are related to the continuous-time poles, s_{di}, by [6]

$$z_{di} = e^{s_{di}\Delta}$$

Thus, as the sampling period approaches zero, all the discrete-time q-domain poles approach unity, independent of the poles, s_{di}, of the continuous-time TF. This can be seen in Table 2.2. A consequence of this is that for *any* q-domain model, the expected denominator polynomial as the sampling period approaches zero is

$$\lim_{\Delta \to 0} \text{den}(z) = (z-1)^n$$

Thus for a third-order denominator

$$\lim_{\Delta \to 0} \text{den}(z) = z^3 - 3z^2 + 3z - 1$$

From Table 2.1 the q-domain denominator coefficients A_2, A_1 and A_0 confirm this, with $A_2 \to -3$, $A_1 \to 3$, and $A_0 \to -1$.

The behaviour of the model zeros as the sampling period approaches zero is more complicated. In this example, the continuous-time TF numerator is a first-order polynomial, whilst the discrete-time q-domain model numerator is third-order. The extra discrete-time zeros, introduced by the sampling process, are called 'sampling zeros'. The location of these sampling zeros is dependent on both the sampling period and the pole-zero excess of the original continuous-time TF [63]. The non-sampling zeros, z_{ni}, are approximately related to the continuous-time TF zeros, s_{ni}, by

$$z_{ni} \approx e^{s_{ni}\Delta}$$

This approximate relationship can be seen for the non-sampling zero of the q-domain model in Table 2.2. As the sampling period approaches zero, the non-sampling zeros approach unity, independent of the continuous-time zeros s_{ni}.

δ-Domain Model

From Table 2.1 it is clear that as the sampling period approaches zero, the coefficients of the δ-domain model approach those of the continuous-time TF. In fact it has been shown in [6] that as the sampling period approaches zero, the coefficients of the δ-domain model, calculated assuming a ZOH, approach those of the continuous-time TF. It is a simple exercise to extend this result to the case of a TH reconstruction (see Appendix A).

From Table 2.2 it is also clear that the poles and non-sampling zero of the δ-domain model approach those of the continuous-time TF. The poles, γ_{di}, are related to the poles, s_{di}, of the continuous-time TF by

$$\gamma_{di} = \frac{e^{s_{di}\Delta} - 1}{\Delta}$$

and the non-sampling zero by the approximate relation

$$\gamma_{ni} \approx \frac{e^{s_{ni}\Delta} - 1}{\Delta}$$

From these equations, and the expansion of $e^{s\Delta}$,

$$e^{s\Delta} = 1 + s\Delta + \frac{(s\Delta)^2}{2!} + \frac{(s\Delta)^3}{3!} + \cdots,$$

it can easily be shown that as the sampling period approaches zero, the poles and non-sampling zero approach those of the continuous-time TF, i.e. $(\gamma_{di} \rightarrow s_{di})$ and $(\gamma_{ni} \rightarrow s_{ni})$ as $(\Delta \rightarrow 0)$.

The sampling zeros of the δ-domain model approach $-\infty$ as the sampling period approaches zero [6].

w-Domain Model

From Table 2.1 it is clear that the coefficients of the w-domain model approach those of the continuous-time TF as the sampling period approaches zero. In Appendix A it is proved that the TH-equivalent w-domain model approaches the equivalent continuous-time model as the sampling frequency approaches zero.

From Table 2.2 it is also clear that the poles and non-sampling zero approach those of the continuous-time TF. The w-domain model poles, β_{di}, are related to the continuous-time TF poles, s_{di}, by

$$\beta_{di} = \frac{2}{\Delta}\left(\frac{e^{s_{di}\Delta} - 1}{e^{s_{di}\Delta} + 1}\right)$$

and the non-sampling zero, β_{ni}, by the approximate relation

$$\beta_{ni} \approx \frac{2}{\Delta}\left(\frac{e^{s_{ni}\Delta} - 1}{e^{s_{ni}\Delta} + 1}\right)$$

Using the expansion for the exponential term $e^{s\Delta}$, it can be easily shown that the discrete-time poles and non-sampling zero approach the continuous-time values as the sampling period approaches zero.

The sampling zeros of the w-domain model approach $\pm\infty$ as the sampling period approaches zero. Note that the sampling zeros may be non-minimum phase.

From Table 2.1 it should be noted that, for a given sampling period, the coefficients of the w-domain model are significantly closer to those of the continuous-time TF than those of the δ-domain model. For example, at a sampling frequency of $f_s = 5$ Hz (sample period $\Delta = 0.2$ s), the maximum difference between the w-domain and continuous-time coefficients is approximately 1%, whereas the maximum difference for the δ-domain coefficients is 38%. This sampling frequency (5 Hz) is approximately 14 times the –3dB bandwidth of the continuous-time TF. At a sampling frequency of $f_s = 10$ Hz, the maximum coefficient difference decreases to approximately 0.3% for the w-domain model.

Figure 2.10 graphically displays the maximum and minimum difference (in percent) of the the δ- and w-domain coefficients as a function of the sampling frequency. These figures clearly show that, for a given sampling frequency, the coefficients of

the w-domain model provide a closer approximation to those of the continuous-time TF, than do the δ-domain coefficients. Thus if the intended use of the discrete-time δ- or w-domain coefficients is to approximate the coefficients of the continuous-time system model, then the w-domain model is clearly superior.

This type of graph (figure 2.10) can be particularly useful in selecting the sampling frequency for the discrete-time model. For example, the sampling frequency $f_s = 5$ Hz yields a w-domain model with coefficients within approximately 1% of those of the continuous-time TF. For $f_s = 20$ Hz, the coefficients are within approximately 0.1%. This comparison also highlights the rate of convergence of the w-domain coefficients to those of the continuous-time TF with increasing sampling frequency.

A general rule of thumb to ensure the coefficients of the w-domain model are within a few percent of the continuous-time TF coefficients is to select the sampling frequency to be greater than approximately ten times the –3 dB bandwidth of the continuous-time TF. If the TF contains poles or zeros of interest outside of this bandwidth, the sampling frequency should be selected to be at least ten times the highest corner frequency of these poles or zeros. See for example the sampling frequency validation tests performed in chapter 5 with the estimated TFs of the synchronous machine at standstill.

2.4 Summary and Conclusions

In this chapter, the common continuous-time differential-operator and discrete-time shift-operator models, as well as their corresponding transform TFs, are introduced. In addition, two alternative discrete-time model parameterisations, namely the δ- and w-operator models (and their transform models), are introduced. The major advantage of both of these discrete-time parameterisations is that, because the discrete-time operators approximate the continuous-time differential operator, the coefficients of the discrete-time models approximate those of the equivalent continuous-time model.

Another advantage of the δ- and w-operator parameterisations is that, with respect to finite word-length calculations, they are numerically superior to the conventional q-operator discrete-time parameterisation. This is demonstrated in a state-space filter

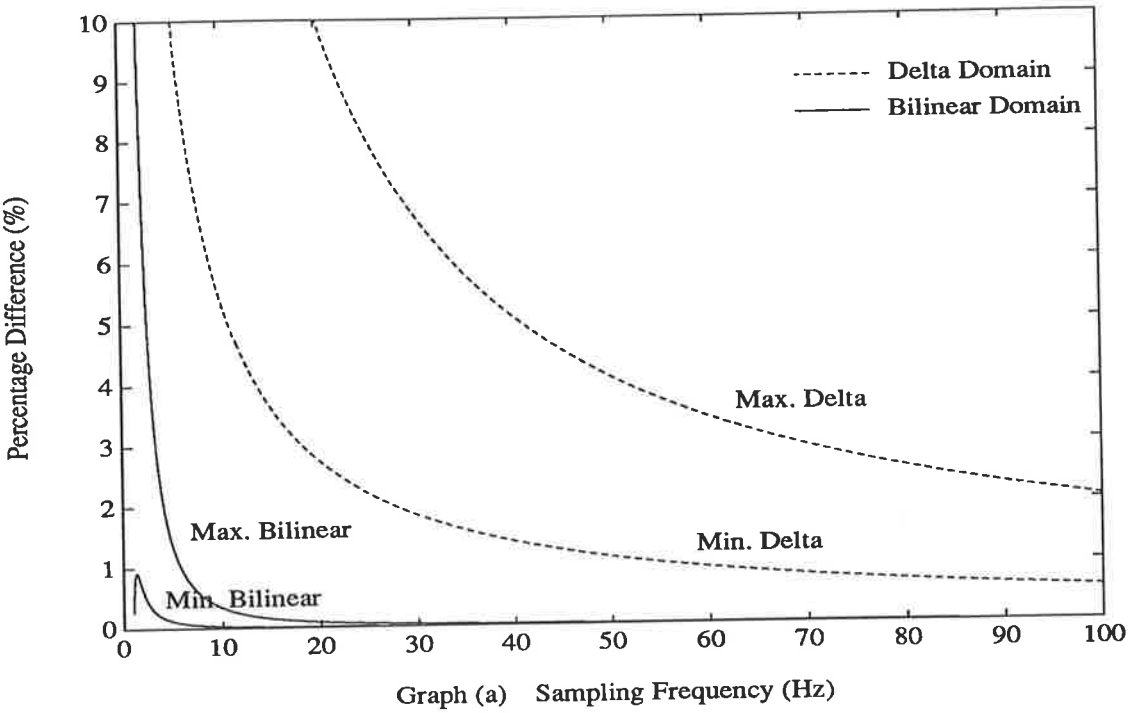

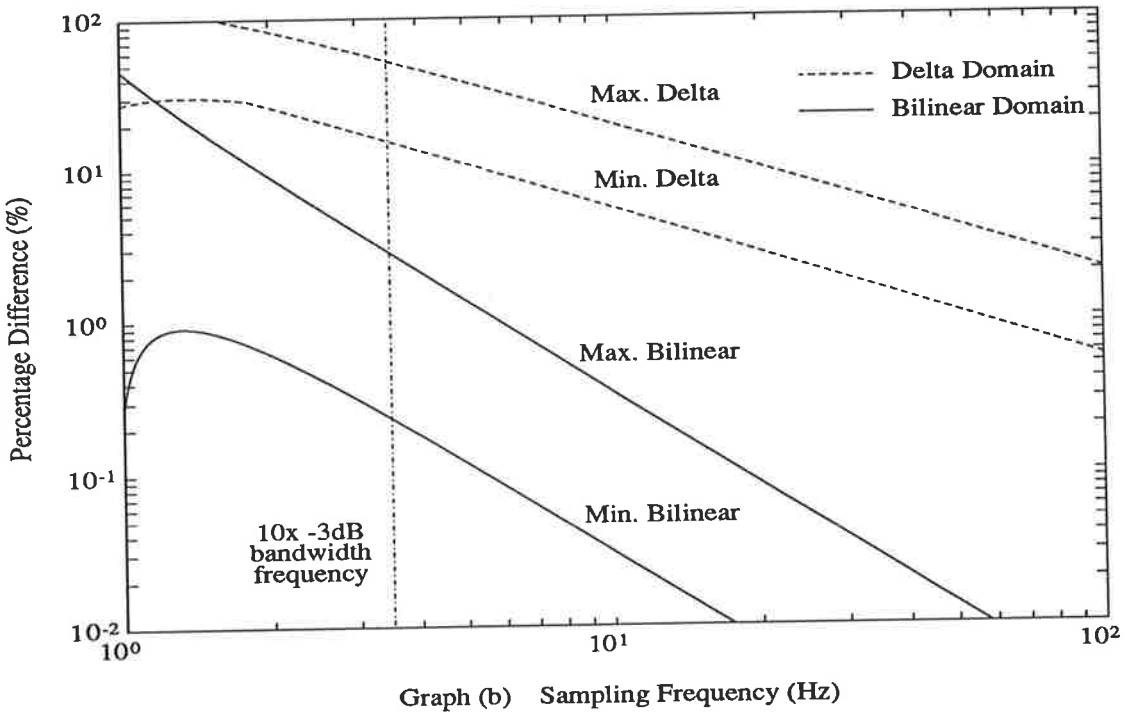

Figure 2.10: The maximum and minimum percentage difference between the coefficients of the δ- and w-domain models and those of the continuous-time TF, as a function of the sampling frequency. Graphs (a) and (b) display the same results, the axes being plotted on linear and logarithmic scales, respectively.

example.

Using the hold-equivalents technique [57], the discrete-time equivalent models of a continuous-time model are derived. The hold-equivalent discrete-time model is dependent on the continuous-time system, as well as the behaviour of the continuous-time input signal between sample points. It is postulated that the input and output signals sampled from a continuous-time system for the purpose of estimation would best be represented by a discrete-time hold-equivalent model derived from the continuous-time model assuming a triangle-hold reconstruction.

A numerical example is used to demonstrate how closely the coefficients of both the discrete-time δ- and w-domain models, calculated from the continuous-time TF assuming a triangle hold, approximate the coefficients of the continuous-time TF. For a given sampling period, the w-domain coefficients provide a clearly superior approximation to those of the continuous-time TF, than do the coefficients of the δ-domain model. A general rule of thumb for the coefficients of the discrete-time w-domain model to approximate within a few percent those of the continuous-time model, is to select the sampling frequency to be at least ten times greater than the –3 dB bandwidth of, or highest corner frequency of interest in, the continuous-time model.

Due to the superiority of the discrete-time w-domain coefficients in approximating those of the equivalent continuous-time model, recursive estimation algorithms employing the w-operator model are introduced in the next chapter for the purpose of estimating, from sampled input and output signals, the coefficients of a continuous-time model.

The following contributions of this chapter are original:

- An investigation, by numerical simulation, of the effects of finite word-length computation on a state-space implementation of a discrete-time w-operator model, in comparison with the corresponding state-space q- and δ-operator model implementations (section 2.2.3).

- A comparison of the TH-equivalent discrete-time q-, δ- and w-domain coefficients for varying sampling periods (section 2.3.2).

- The proof of the convergence of the TH-equivalent discrete-time w-domain TF to the corresponding continuous-time TF as the sampling period converges to zero (Appendix A).

Chapter 3

Bilinear-Operator Model in Recursive Estimation

3.1 Introduction

In the previous chapter the discrete-time w-operator model and its associated TF are introduced. In this chapter, discrete-time recursive estimation algorithms are developed which incorporate the w-operator model. The primary benefit of the w-operator model in this application is that it allows, from sampled input-output signals, a discrete-time model to be estimated, the coefficients of which accurately approximate those of the underlying continuous-time system model.

In section 3.2, the recursive least-squares estimation algorithm using the w operator is introduced. The selection of prefiltering and estimation filters are also discussed, as well as the effects of noise on estimation.

In section 3.3, the estimation algorithm is extended to a recursive instrumental-variable algorithm, which is suitable for estimation when the sampled output signal contains high-level or coloured additive output noise.

Both the recursive least-squares and recursive instrumental-variable estimation algorithms introduced in this chapter are demonstrated in simulation studies in chapter 4. Chapters 5 and 6 contain practical estimation examples, dealing with the estimation of the coefficients of various TFs of a synchronous machine.

The work on developing the w-operator model for use in recursive estimation

(sections 3.2 and 3.3) is original work. Section 3.4 discusses briefly some recent parallel work on this topic in relation to the original work in this thesis.

Section 3.5 contains a brief conclusion on the main results of this chapter.

3.2 Recursive Least-Squares Estimation using the Bilinear Operator

Consider a discrete-time w-operator model of the form

$$A(w)y_k = B(w)u_k \tag{3.1}$$

where u_k, y_k are the sampled input-output signals, and $A(w)$, $B(w)$ are w-operator polynomials given by

$$A(w) = w^n + a_{n-1}w^{n-1} + \cdots + a_1 w + a_0 \tag{3.2}$$

$$B(w) = b_m w^m + b_{m-1}w^{m-1} + \cdots + b_1 w + b_0 \tag{3.3}$$

Note that for the development of the estimation algorithm it is assumed that $m = n - 1$.

In order to remove the differentiation effect of the w operator on the sampled input-output signals, a monic, stable, filter polynomial $J(w)$, also of degree n, is defined

$$J(w) = w^n + j_{n-1}w^{n-1} + \cdots + j_1 w + j_0 \tag{3.4}$$

This polynomial is incorporated into eqn. 3.1 to derive a linear regression form of eqn. 3.1 suitable for estimation [6,54,64]. A rearrangement of eqn. 3.1 into the form, $-A(w)y_k + B(w)u_k = 0$, and adding $J(w)y_k$ to both sides results in

$$J(w)y_k = J(w)y_k - A(w)y_k + B(w)u_k \tag{3.5}$$

Dividing through by $J(w)$, yields

$$y_k = \frac{[J(w) - A(w)]}{J(w)} y_k + \frac{B(w)}{J(w)} u_k \tag{3.6}$$

or

$$y_k = \left[\frac{(j_{n-1} - a_{n-1})}{J(w)} w^{n-1} + \cdots + \frac{(j_0 - a_0)}{J(w)}\right] y_k + \left[\frac{b_{n-1}}{J(w)} w^{n-1} + \cdots + \frac{b_0}{J(w)}\right] u_k \tag{3.7}$$

Note that in both eqns. 3.6 and 3.7 the initial condition terms have been ignored. This is because they decay to zero exponentially fast due to the stability of the filter polynomial $J(w)$ [65].

Eqn. 3.7 may be presented in a more suitable form for estimation by the regression equation,

$$y_k = \phi_k^T \theta \tag{3.8}$$

where the regression and parameter vectors, respectively, are given by,

$$\phi_k^T = [\frac{w^{n-1}}{J(w)} y_k, \cdots \frac{1}{J(w)} y_k, \frac{w^{n-1}}{J(w)} u_k, \cdots \frac{1}{J(w)} u_k] \tag{3.9}$$

$$\theta^T = [j_{n-1} - a_{n-1}, j_{n-2} - a_{n-2}, \ldots j_0 - a_0, b_{n-1}, b_{n-2}, \ldots b_0] \tag{3.10}$$

(From eqn. 3.9, it is seen that the effect of the polynomial $J(w)$ is to filter both the input and output signals used in the regression vector, thus reducing the effect of differentiation by the w operator of the sampled signals.)

Based on the linear regression model given in eqn. 3.8, a weighted, least-squares estimate $\hat{\theta}_t$ of the coefficient vector θ (eqn. 3.10) can be formulated [10]

$$\hat{\theta}_t = \arg\min \theta' \sum_{k=1}^{t} \beta(t,k) \left(y_k - \phi_k^T \theta'\right)^2, \tag{3.11}$$

where $\beta(t,k)$ is the weighting sequence, which is discussed later (see eqn. 3.13). This least-squares minimisation can be performed recursively with the following weighted Recursive Least-Squares estimation algorithm employing the Bilinear Operator (RLS-BO), for evaluating at time $t = k\Delta$, the parameter estimate vector $\hat{\theta}_k$ [10].

RLS-BO Estimation Algorithm

$$
\begin{aligned}
e_k &= y_k - \phi_k^T \hat{\theta}_{k-1} && \text{(3.12a)} \\
\hat{\theta}_k &= \hat{\theta}_{k-1} + \frac{P_{k-1}\phi_k e_k}{\lambda_k + \phi_k^T P_{k-1}\phi_k} && \text{(3.12b)} \\
P_k &= \frac{1}{\lambda_k}\Big[P_{k-1} - \frac{P_{k-1}\phi_k\phi_k^T P_{k-1}}{\lambda_k + \phi_k^T P_{k-1}\phi_k}\Big] && \text{(3.12c)}
\end{aligned}
$$

where

$$
\begin{aligned}
e_k &= \text{prediction error} \\
P_k &= \text{estimation covariance matrix} \\
\lambda_k &= \text{forgetting factor} \\
\phi_k &= \text{regression vector (eqn. 3.9)} \\
\hat{\theta}_k &= \text{parameter estimate vector}
\end{aligned}
$$

The weighting sequence $\beta(t,k)$ (in eqn. 3.11) is related to the forgetting factor in the RLS-BO estimation algorithm by the following equations [10]

$$
\begin{aligned}
\beta(t,k) &= \lambda_t \beta(t-1,k), \qquad 1 \le k \le t-1 \\
\beta(t,t) &= 1 \\
& 0 < \lambda_t \le 1 && \text{(3.13)}
\end{aligned}
$$

The weighting sequence is used to selectively weight, in time, the measured input-output signals. The above weighting sequence choice exponentially weights the measured signals, with higher weight (more importance) given to the most recently measured signals. For a constant forgetting factor λ, the estimator has an approximate 'time constant' $T = 1/(1-\lambda)$, which means that the current parameter estimate is dependent only on approximately the last $1/(1-\lambda)$ samples of input-output signal. The main benefit of using an exponential-type weighting function is that it allows the RLS-BO estimation algorithm to track possible variations in the system parameters with time. It also allows the effects of initial conditions to decay with time. The selection of the forgetting factor is a trade-off between the tracking ability of the

estimator, and its sensitivity due to noise.

Initial Conditions

To use the RLS-BO estimation algorithm, initial values for the covariance matrix and parameter estimate vector are required. A common choice is to initialise

$$P_0 = cI$$

where I is the identity matrix and c is a suitably large constant. The vector of parameter estimates can be initialised to

$$\hat{\theta}_0 = [j_{n-1}, j_{n-2}, \ldots, j_0, 0, 0, \ldots, 0]$$

(i.e. the a_i, b_i terms in the parameter vector, eqn. 3.10, are set to zero).

The covariance matrix P_k can be interpreted as a measure of the covariance of the parameter estimates $\hat{\theta}_k$ [6, page 369]. Thus this initial choice of $P_0 = cI$ (with c large) reflects the little confidence that the initial estimate of the parameter vector $\hat{\theta}_0$ is correct.

From the weighted RLS-BO estimation algorithm (eqn. 3.12) it can be shown that the effects of this initial selection of both $\hat{\theta}_I$ and P_0 decay with time [10] (see also section 3.2.1); their selection is thus not critical to the results of estimation.

Recursive Updating of the Regression Vector

Using the w-operator parameterisation, the regression vector (eqn. 3.9) can be recursively updated easily using a state-space form of the $J(w)$ filter polynomial. From section 2.2.3, the elements

$$[\frac{w^{n-1}}{J(w)}y_k, \ldots, \frac{1}{J(w)}y_k]$$

of the regression vector can be updated by the matrix multiplication (i.e. for a third-order system)

$$\begin{bmatrix} \frac{w^3}{J(w)}y_k \\ \frac{w^2}{J(w)}y_k \\ \frac{w}{J(w)}y_k \\ \frac{1}{J(w)}y_k \end{bmatrix} = \begin{bmatrix} 1 & j_2 & j_1 & j_0 \\ -\Delta/2 & 1 & 0 & 0 \\ 0 & -\Delta/2 & 1 & 0 \\ 0 & 0 & -\Delta/2 & 1 \end{bmatrix}^{-1} \begin{bmatrix} 1 & 0 & 0 & 0 & 0 \\ 0 & \Delta/2 & 1 & 0 & 0 \\ 0 & 0 & \Delta/2 & 1 & 0 \\ 0 & 0 & 0 & \Delta/2 & 1 \end{bmatrix} \begin{bmatrix} y_k \\ \frac{w^3}{J(w)}y_{k-1} \\ \frac{w^2}{J(w)}y_{k-1} \\ \frac{w}{J(w)}y_{k-1} \\ \frac{1}{J(w)}y_{k-1} \end{bmatrix} \tag{3.14}$$

An identical relationship holds for the $w^i u_k/J(w)$ elements of the regression vector. Note that because the elements of these two matrices are constant for selected values of the sampling period and $J(w)$ polynomial coefficients; the matrix product may be evaluated before recursion commences.

3.2.1 Properties of the RLS-BO Estimate

When undertaking identification tests on a practical system, it is inevitable that there will be some form of noise present in the measured output signal. It is therefore important to ascertain the effect of noise on the RLS-BO estimation algorithm.

Consider a system that is described by the equation

$$y_k = \frac{B(w)}{A(w)}u_k + \eta_k \tag{3.15}$$

where $\{\eta_k\}$ is some noise sequence. Eqn. 3.15 is shown diagramatically in Figure 3.1, as a noise-free, linear, time-invariant system with additive output noise $\{\eta_k\}$.

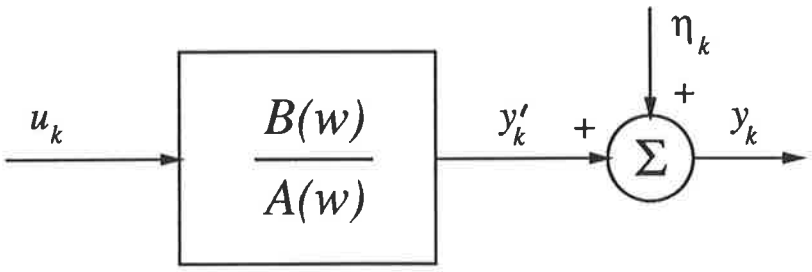

Figure 3.1: Assumed model of the system with additive output noise

Eqn. 3.15 can be rearranged into a linear regression form, (following the same procedure used for deriving eqn. 3.8 from eqn. 3.1), given by

$$y_k = \phi_k^T \theta + \frac{A(w)}{J(w)} \eta_k \tag{3.16}$$

where θ and ϕ_k are given by eqns. 3.10 and 3.9 respectively; θ is considered to be the *true* value of the parameter vector.

When RLS-BO estimation is performed on data generated from this model (eqn. 3.16), it is highly desirable that the estimated parameters, $\hat{\theta}_t$, converge towards the true parameters, θ, as $t \rightarrow \infty$.

It can be shown that the parameter estimates at time t, using the weighted RLS-BO estimation algorithm (eqn. 3.12), are given by [10, page 308]

$$\begin{aligned} \hat{\theta}_t = & \left[\beta(t,0) P_0^{-1} + \sum_{k=1}^{t} \beta(t,k) \phi_k \phi_k^T \right]^{-1} \times \\ & \left[\beta(t,0) P_0^{-1} \hat{\theta}_0 + \sum_{k=1}^{t} \beta(t,k) \phi_k y_k \right] \end{aligned} \tag{3.17}$$

Given that $\beta(t,0) = \prod_{j=1}^{t} \lambda_j$ (from eqn. 3.13), and assuming $\lambda_j < 1$, then for large t, the term $\beta(t,0) \approx 0$. Thus the estimated parameters are given by (as $t \rightarrow \infty$)

$$\hat{\theta}_t = \left[\sum_{k=1}^{t} \beta(t,k) \phi_k \phi_k^T \right]^{-1} \left[\sum_{k=1}^{t} \beta(t,k) \phi_k y_k \right] \tag{3.18}$$

Assuming the true system model is given by eqn. 3.16, y_k can be replaced in eqn. 3.18 to obtain

$$\begin{aligned} \hat{\theta}_t &= \left[\sum_{k=1}^{t} \beta(t,k) \phi_k \phi_k^T \right]^{-1} \left[\sum_{k=1}^{t} \beta(t,k) \phi_k \phi_k^T \theta + \sum_{k=1}^{t} \beta(t,k) \phi_k \frac{A(w)}{J(w)} \eta_k \right] \\ &= \left[\sum_{k=1}^{t} \beta(t,k) \phi_k \phi_k^T \right]^{-1} \left[\sum_{k=1}^{t} \beta(t,k) \phi_k \phi_k^T \right] \theta \\ &\qquad + \left[\sum_{k=1}^{t} \beta(t,k) \phi_k \phi_k^T \right]^{-1} \left[\sum_{k=1}^{t} \beta(t,k) \phi_k \frac{A(w)}{J(w)} \eta_k \right] \\ &= \theta + \left[\sum_{k=1}^{t} \beta(t,k) \phi_k \phi_k^T \right]^{-1} \left[\sum_{k=1}^{t} \beta(t,k) \phi_k \frac{A(w)}{J(w)} \eta_k \right] \end{aligned} \tag{3.19}$$

Thus the estimated parameter vector equals the true system parameter vector, θ, *plus* a bias term due to the additive output noise.

In order to determine the effects of noise on the estimates, it is necessary to consider various forms of the noise signal $\{\eta_k\}$.

No Additive Noise

If the true system has no additive output noise $\{\eta_k\}$, eqn. 3.19 clearly shows that the estimated parameters converge to the true system parameters.

Additive White Noise

Consider the case in which the additive noise sequence $\{\eta_k\}$ is white, with zero mean and variance σ_η^2.

From eqn. 3.16 for the regression form of the system model, it is noted that the additive white noise appears as coloured noise, coloured by the filter $A(w)/J(w)$.

The coefficients of the polynomial $A(w)$ are fixed, defined by the system under test. However, the coefficients of the filter polynomial $J(w)$ are selectable, and thus it is possible by appropriate choice of these coefficients, to modify the characteristics of the additive system noise in the regression equation (eqn. 3.16).

Selection of $J(w) \neq A(w)$ produces coloured noise which is discussed later.

Selection of $J(w) = A(w)$, according to eqn. 3.16, results in the additive noise remaining white. Note that in practice it is impossible to select $J(w) = A(w)$, because the polynomial $A(w)$ is unknown. It is possible however to select $J(w)$ equal to an estimate of $A(w)$, which may be derived after several exploratory runs of the RLS-BO estimation algorithm on the measured system input-output signals. An alternative approach is to set $J(w)$ equal to the estimate of $A(w)$ *during* estimation, an approach adopted in [30]. Assuming $J(w) = A(w)$ in eqn. 3.19, the estimated parameter vector is given by

$$\hat{\theta}_t = \theta + \left[\sum_{k=1}^{t} \beta(t,k)\phi_k\phi_k^T\right]^{-1}\left[\sum_{k=1}^{t} \beta(t,k)\phi_k\eta_k\right] \tag{3.20}$$

For the bias term to be zero, the regression vector ϕ_k and noise signal $\{\eta_k\}$ must be uncorrelated. From the expression for recursively updating several elements of

the regression vector ϕ_k (eqn. 3.14), it is clear the regression vector at time $t = k\Delta$ is dependent on the signal y_k. From eqn. 3.16, the output signal at time $t = k\Delta$ contains the measurement noise η_k, and thus the regression vector ϕ_k at time $t = k\Delta$ also contains the measurement noise η_k. Hence there is some correlation between ϕ_k and η_k. Note for a conventional shift-operator RLS estimation algorithm, the regression vector ϕ_k contains only past output noise terms η_{k-1}, η_{k-2}, etc, and hence is uncorrelated with the noise if η_k is white.

Thus for white additive noise, with $J(w) = A(w)$, the RLS-BO estimation algorithm is biased. However, for many practical situations in which the white additive noise is relatively small, the choice of $J(w) \approx A(w)$ results in only a small bias term. This is confirmed in the results of simulation studies given in the next chapter. For situations where the noise level is high, the RLS-BO estimation algorithm may require modification to help reduce the bias, for example, with the aid of the RIV-BO estimation algorithm (section 3.3).

Additive Coloured Noise

Generally when the additive noise is coloured, significant bias may result in the parameter estimates. This bias is dependent on the magnitude of the noise, as well as its 'colouration', because the bias is dependent on the correlation between the regression vector ϕ_k and the noise term $\frac{A(w)}{J(w)}\eta_k$ (eqn. 3.19).

There are several methods to help reduce the bias due to coloured noise.

When the spectral properties of the coloured noise are known, it is possible to use prefiltering to approximately 'whiten' the noise [6]. In much the same way, the $J(w)$ filter polynomial can be used to help shape the spectrum of the noise term $\frac{A(w)}{J(w)}\eta_k$ to approximate that of white noise.

For cases in which the spectral properties of the noise are not known, or it is impractical to 'whiten' the noise with filtering, it is suggested that the RLS-BO estimation algorithm should be modified to explicitly deal with the noise problem. In section 3.3, the RLS-BO estimation algorithm is modified by the inclusion of Instrumental Variables to remove the bias due to noise.

Persistent Excitation

In the preceding discussion it has been implicitly assumed that the matrix inverse $[\sum_{k=1}^{t} \beta(t,k)\phi_k\phi_k^T]^{-1}$ exists. It can be shown that this is the case, providing the system input signal $\{u_k\}$ is *persistently exciting* of order $n+m+1$, where n,m are respectively the orders of the estimated polynomials of the w-operator model (eqns. 3.2 and 3.3) [2].

The persistent excitation requirement relates to the ability of the input signal to excite adequately the dynamics of the system under test. Persistent excitation requires the input signal to have a power spectrum which is non-zero for at least $n+m+1$ frequencies across the two-sided frequency spectrum. For example, an input signal consisting of $(n+m+1)/2$ sinusoids is persistently exciting of order $n+m+1$.

Note that with the weighted RLS-BO estimation algorithm, the regression vector ϕ_k, and hence the matrix inverse $[\sum_{k=1}^{t} \beta(t,k)\phi_k\phi_k^T]^{-1}$, are dependent only on approximately the last $1/(1-\lambda)$ samples of input-output signal (due to the exponential weighting effect of $\beta(t,k)$). Thus for the inverse to always exist, the input signal must continuously satisfy the persistent excitation requirement.

For all estimation tests performed in later chapters, a pseudo random binary sequence is used as the excitation signal, which is persistently exciting of an order much greater than $n+m+1$ (see section 4.2).

3.2.2 The Effects of Prefiltering and of the $J(w)$ Filter Polynomial on RLS-BO Estimation

In section 3.2.1, the effects of the $J(w)$ filter polynomial and prefiltering of the measured input-output signals are briefly discussed in connection with reducing the bias of the RLS-BO parameter estimates. Whilst giving some insight into the effects and possible selection of these filters, further insight can be gained by considering their effects in the context of estimation of a practical system.

When attempting to identify a model of a system, an accurate representation of the systems behaviour is generally only required over a limited bandwidth. For example,

in the modeling of subsynchronous resonance in synchronous machines, modeling accuracy is generally only required over the frequency range of approximately 10 Hz to 50 Hz [66]. Any system response outside of this range is unimportant (as far as the effects on subsynchronous resonance are concerned), unless these high- or low-frequency dynamics are modulated to within the frequency range of interest. Thus from this point of view, some form of filtering is required in estimation to minimise the effect of the unmodeled system dynamics which lie outside the frequency range of interest. As will be shown, this filtering can be accomplished by prefiltering the measured input and output signals prior to use in the recursive estimation algorithm. Another concern in estimation is that system disturbances outside of the frequency range of interest, be it dc offsets or high- and low-frequency noise, may effect the accuracy of estimation. The prefiltering has the added benefit of attenuating these disturbances.

Over the limited frequency range of interest, it is logical to assume that the true system, which is being identified, is of higher order than the model assumed for the estimation algorithm. This is often referred to as undermodeling, or considering the true system as containing unmodeled dynamics. This means that within the frequency range of interest, some modeling errors will be present. It would be useful to be able to control the distribution of the modeling errors across the frequency spectrum. This can be particularly important, for example, for the purpose of control in which an accurate model of the system, particularly around the gain-crossover frequency, may be required. As will be shown, the $J(w)$ filter polynomial can be used to help control the distribution of modeling errors.

To analyse the effects of both the prefilter and $J(w)$ filter polynomial on estimation, the general least-squares error criterion is investigated. The least-squares error criterion is given by

$$V(\hat{\theta}) = \frac{1}{N}\sum_{k=1}^{N}(y_k - \hat{y}_k)^2 \tag{3.21}$$

Taking the limit as $N \to \infty$, this error function can be expressed in the frequency domain by (see Appendix B) [10]

$$\bar{V}(\hat{\theta}) = \Delta \int_{-\frac{1}{2\Delta}}^{\frac{1}{2\Delta}} \Phi_e(f, \hat{\theta}) df \tag{3.22}$$

where

$$\Phi_e(f,\hat{\theta}) = |\mathrm{Pre}(\beta)|^2 \left|\frac{\hat{A}(\beta)}{J(\beta)}\right|^2 \left\{\left|\frac{B(\beta)}{A(\beta)} - \frac{\hat{B}(\beta)}{\hat{A}(\beta)}\right|^2 \Phi_u(f) + \Phi_\eta(f)\right\} \tag{3.23}$$

$$\begin{aligned}
f &= \text{frequency (Hz)} \\
\Phi_e(f,\hat{\theta}) &= \text{power spectral density of the error signal } (y_k - \hat{y}_k) \\
\Phi_u(f) &= \text{power spectral density of the input signal} \\
\Phi_\eta(f) &= \text{power spectral density of the additive system noise} \\
\mathrm{Pre}(\beta) &= w\text{-domain TF of the prefilter} \\
\frac{B(\beta)}{A(\beta)} &= w\text{-domain TF of the true system} \\
\frac{\hat{B}(\beta)}{\hat{A}(\beta)} &= \text{estimate of the true } w\text{-domain TF} \\
J(\beta) &= w\text{-transform of the filter polynomial } J(w) \\
\beta &= w\text{-domain transform variable} \\
&= \frac{2}{\Delta}\left(\frac{z-1}{z+1}\right) \\
&= \frac{2}{\Delta}\left(\frac{e^{j2\pi f\Delta}-1}{e^{j2\pi f\Delta}+1}\right) \\
\Delta &= \text{sampling frequency}
\end{aligned}$$

From eqns. 3.21 and 3.22, it is clear that minimising the least-squares error criterion in the time domain is equivalent to minimising the integral of the power spectral density of the error signal across the frequency range $-f_s/2$ Hz to $f_s/2$ Hz, where f_s is the sampling frequency.

An examination of eqn. 3.23 reveals that, for zero additive output noise, the least-squares estimator attempts to minimise the mean square error between the true TF ($B(\beta)/A(\beta)$) and the estimated model TF ($\hat{B}(\beta)/\hat{A}(\beta)$), weighted across the frequency spectrum by the factor $|\mathrm{Pre}(\beta)|^2|\frac{\hat{A}(\beta)}{J(\beta)}|^2\Phi_u(f)$. Thus the selection of the prefilter, filter polynomial $J(w)$, and the power spectral density of the input excitation signal, can be used to influence the distribution of the error between the true and the estimated models across the frequency spectrum. Selecting the filters

and input excitation such that the magnitude of the weighting factor is large in certain frequency ranges, results in more importance being assigned to minimising the error between the true and the estimated system models in these ranges. In frequency regions where the magnitude of the weighting factor is small, the modeling error is assigned relatively less importance.

Consider the elements of the weighting factor seriatim:

$|\mathbf{Pre}(\beta)|^2$ The prefilter, commonly a bandpass filter, can be designed to 'select' the frequency range over which the estimated model is matched to that of the true system. The prefilter focuses the parameter estimator on the relevant frequency range of interest by attenuating the effects of noise and unmodeled dynamics outside the frequency range of interest, reducing their influence on estimation [65].

Strictly speaking, prefiltering refers to any filtering performed on both the input and output signals of the continuous-time system, and thus includes the analogue anti-aliasing filters as well as any digital filtering performed. However, throughout this thesis, the term prefilter is generally used to refer only to the digital filtering performed on the input and output signals after sampling.

$|\frac{\hat{A}(\beta)}{\hat{J}(\beta)}|^2$ The $J(w)$ filter polynomial [1] affects the distribution of the error between the true and estimated models across the frequency range of interest. We have found that a guide for choosing $J(w)$ is to match it approximately to the denominator of the continuous-time TF under test. The 'best' choice of $J(w)$ is dependent on several factors, including the proposed practical application of the estimated model, the characteristics of the system under test, and the spectrum of the input signal. The choice of the $J(w)$ filter polynomial is generally made during the analysis of the data (i.e. after the sampled input-output signal measurements have been completed), when a few estimation runs can be performed and the resulting error weighting effect of $|\frac{\hat{A}(\beta)}{J(\beta)}|^2$ checked.

It should be noted that, in frequency regions in which the magnitude of the

[1] As discussed in chapter 2, the coefficients of the transform and operator representations are numerically equal, and thus it is common to refer to the polynomial $J(\beta)$ simply as $J(w)$.

true system TF ($|B(\beta)/A(\beta)|$) is small, the modeling error will be given relatively less weight than in regions where the true system TF magnitude is large. Selecting the filter polynomial $J(w)$ to boost the weighting factor $|\frac{\hat{A}(\beta)}{J(\beta)}|^2$ in these frequency regions may be used to minimise this problem (see Simulation Study 6, section 4.6.1).

$\Phi_u(f)$ The power spectral density of the input signal also has an effect on the estimated model. For both the simulation studies of chapter 4, and practical estimation examples of chapters 5 and 6, an input signal with an approximately uniform power spectral density is employed (see section 4.2). However, in situations in which it is possible to tailor the input signal spectrum, it could be used in much the same way as $J(w)$ to weight selectively desired frequency regions by choosing an excitation signal with the desired power spectral density.

From eqn. 3.23 it can be seen that the additive system noise is also effected by the choice of both the prefilter and $J(w)$ filter polynomial. For example, choosing a combination of the prefilter and $J(w)$ to give a large weighting to the high-frequency TF error will also boost the high-frequency noise content, as well as altering the colouration of the additive output noise.

It should be noted that the element $|\frac{\hat{A}(\beta)}{J(\beta)}|^2$ of the weighting factor is a function of the complex variable β, where β is given by

$$\begin{aligned} \beta &= \frac{2}{\Delta}\left(\frac{e^{j2\pi f\Delta}-1}{e^{j2\pi f\Delta}+1}\right) \\ &= j\frac{2}{\Delta}\tan\left(\frac{2\pi f\Delta}{2}\right) \end{aligned}$$

When evaluating the frequency response of this weighting element $|\frac{\hat{A}(\beta)}{J(\beta)}|^2$ (when assessing the selection of the $J(w)$ filter polynomial), the above expression for β should be employed. However, for frequencies less than approximately 1/10th of the sampling frequency, β is approximately related to frequency by

$$\beta \approx j2\pi f$$

Thus, generally when evaluating the frequence response of $|\frac{\hat{A}(\beta)}{J(\beta)}|^2$, this approximate

value of β may be employed.

Similarly, the result of the RLS-BO estimation algorithm is an estimated discrete-time w-operator model, given by the polynomials $\hat{A}(w)$ and $\hat{B}(w)$. To calculate the frequency response of this model, the TF $\hat{B}(\beta)/\hat{A}(\beta)$ should be used. However, as the coefficients of both the $\hat{A}(w)$ and $\hat{B}(w)$ polynomials are used directly as estimates of the continuous-time system coefficients, the frequency response is evaluated as if these polynomials are continuous-time polynomials, i.e. $\hat{B}(s)/\hat{A}(s)$. This is equivalent to assuming $\beta = j2\pi f$.

3.3 Recursive Instrumental-Variable Estimation using the Bilinear Operator

The RLS-BO estimation algorithm discussed in the previous section will in general give biased estimates when the system under test contains additive output noise. For cases in which the signal-to-noise ratio is high, the bias is likely to be small. However, if there is a low signal-to-noise ratio, or the additive output noise is coloured, the bias of the estimates may be significant.

There are many different variations on the standard RLS algorithm to explicitly remove the bias in estimates due to noise. One such variation is the Recursive Instrumental Variable (RIV) estimation algorithm. The RIV algorithm ideally eliminates the bias by replacing the noise-correlated regression vector (eqn. 3.9), with an Instrumental Variable (IV) vector. The IV vector has the properties that it is uncorrelated with the system noise, but highly correlated with the noise-free system input-output data [2].

A weighted, Recursive, Instrumental-Variable estimation algorithm, using the Bilinear Operator (RIV-BO) is given by [2]

RIV-BO Estimation Algorithm

$$e_k = y_k - \phi_k^T \hat{\theta}_{k-1} \tag{3.24a}$$

$$\hat{\theta}_k = \hat{\theta}_{k-1} + \frac{P_{k-1} z_k e_k}{\lambda_k + \phi_k^T P_{k-1} z_k} \tag{3.24b}$$

$$P_k = \frac{1}{\lambda_k}\left[P_{k-1} - \frac{P_{k-1}z_k\phi_k^T P_{k-1}}{\lambda_k + \phi_k^T P_{k-1} z_k}\right] \tag{3.24c}$$

where

$$\begin{aligned} e_k &= \text{prediction error} \\ P_k &= \text{estimation 'covariance' matrix} \\ \lambda_k &= \text{forgetting factor} \\ \phi_k &= \text{regression vector (eqn. 3.9)} \\ z_k &= \text{instrumental variable vector} \\ \hat{\theta}_k &= \text{parameter estimate vector} \end{aligned}$$

The IV vector is given by

$$z_k^T = [\frac{w^{n-1}}{J(w)}x_k, \ldots \frac{1}{J(w)}x_k, \frac{w^{n-1}}{J(w)}u_k, \ldots \frac{1}{J(w)}u_k] \tag{3.25}$$

A comparison of the IV vector with the regression vector used for the RLS-BO estimation algorithm (eqn. 3.9), reveals the noise-contaminated output signal, y_k, has been replaced by the instrumental variable, x_k.

One possible choice of the IV, x_k, is $\hat{y}_k^c$, given by [2]

$$\hat{y}_k^c = \frac{\hat{B}(w)}{\hat{A}(w)}u_k \tag{3.26}$$

This IV satisfies the requirements of being uncorrelated with the system output noise, yet (depending on the accuracy of the estimates $\hat{A}(w)$ and $\hat{B}(w)$) is highly correlated with the measured output signal y_k. Thus the IV vector becomes

$$z_k^T = [\frac{w^{n-1}}{J(w)}\hat{y}_k^c, \ldots \frac{1}{J(w)}\hat{y}_k^c, \frac{w^{n-1}}{J(w)}u_k, \ldots \frac{1}{J(w)}u_k] \tag{3.27}$$

The estimation algorithm using this IV vector is often referred to as a bootstrap IV estimation algorithm [67].

Initial Conditions

In contrast to the RLS-BO estimation algorithm, more care must be taken in selecting the initial conditions for the RIV-BO estimation algorithm. This is because the initial values of the RIV-BO parameter estimates are used to calculate the initial values of the IV $\hat{y}_k^c$ (eqn. 3.26). If reasonable initial values for the coefficients $(\hat{a}_i^0, \hat{b}_i^0)$ of $\hat{A}(w)$ and $\hat{B}(w)$ are known prior to estimation, the initial selection of

$$\begin{aligned} P_0 &= cI \\ \hat{\theta}_0 &= [j_{n-1} - \hat{a}_{n-1}^0, j_{n-2} - \hat{a}_{n-2}^0, \ldots, j_0 - \hat{a}_0^0, \hat{b}_{n-1}^0, \ldots, \hat{b}_0^0] \end{aligned}$$

may be sufficient for successful estimation. However, as is often the case, approximate initial values for the coefficient estimates are not known. The problem of initialising the parameter estimates vector can be avoided by initially running the estimator as the RLS-BO estimation algorithm (eqn. 3.12) [68]. Once the RLS-BO estimated parameters have approximately converged (to biased values), the estimator is then switched to RIV-BO operation. This is the method adopted in later chapters when using the RIV-BO estimation algorithm.

3.3.1 Properties of the RIV-BO Estimate

As discussed previously, the RIV-BO estimation algorithm is introduced because it overcomes the problem of biased estimates in the presence of additive output noise. This is a problem encountered with the RLS-BO estimation algorithm.

The full analysis of the asymptotic properties of the RIV-BO estimation algorithm is a complex task. This is due to the nature of the IV vector, which, as well as being dependent on the measured input signal, depends on the time-varying coefficient estimates. The asymptotic behaviour of the RIV estimation algorithm is analysed in [67].

To give an insight into how the IV method overcomes the noise-induced estimator bias, an 'idealized' version [67] of the RIV-BO estimation algorithm is analysed. The 'idealized' algorithm assumes that the true system coefficients are known, and uses these known coefficients instead of the estimated coefficients to calculate the

instrumental variable (eqn. 3.26). The 'idealized' IV vector is denoted by

$$\zeta_k^T = [\frac{w^{n-1}}{J(w)}y_k^c, \ldots \frac{1}{J(w)}y_k^c, \frac{w^{n-1}}{J(w)}u_k, \ldots \frac{1}{J(w)}u_k] \tag{3.28}$$

where the IV y_k^c is calculated from the true system coefficients by

$$y_k^c = \frac{B(w)}{A(w)}u_k \tag{3.29}$$

It can be shown that the parameter estimates at time t, using the RIV-BO estimation algorithm (eqn. 3.24) with the 'idealized' IV vector (eqn. 3.28), are given by [10]

$$\hat{\theta}_t = \left[\beta(t,0)P_0^{-1} + \sum_{k=1}^{t}\beta(t,k)\zeta_k\phi_k^T\right]^{-1} \times \left[\beta(t,0)P_0^{-1}\hat{\theta}_0 + \sum_{k=1}^{t}\beta(t,k)\zeta_k y_k\right] \tag{3.30}$$

(compare to eqn. 3.17 for the RLS-BO estimation algorithm). Assuming the true system is described by eqn. 3.16 (repeated here)

$$y_k = \phi_k^T\theta + \frac{A(w)}{B(w)}\eta_k$$

and assuming t is large such that $\beta(t,0) \approx 0$, eqn. 3.30 becomes (as $t \to \infty$)

$$\hat{\theta}_t = \theta + \left[\sum_{k=1}^{t}\beta(t,k)\zeta_k\phi_k^T\right]^{-1}\left[\sum_{k=1}^{t}\beta(t,k)\zeta_k\frac{A(w)}{J(w)}\eta_k\right], \tag{3.31}$$

(following the same steps used in deriving eqn. 3.19).

Thus, as for the RLS-BO estimation algorithm, the RIV-BO estimate is given by the true parameter vector, θ, plus a bias term due to the additive noise. For the bias term to be zero, there must be no correlation between the IV vector ζ_k and the 'filtered' additive output noise $\frac{A(w)}{B(w)}\eta_k$. The IV vector ζ_k is given by eqn. 3.28, which is generated using only the measured input signal u_k (and $J(w)$, $A(w)$ and $B(w)$). Thus, unless the 'filtered' noise and input signals are correlated — which is very unlikely — the bias term will be zero for both coloured and white additive output noise.

3.3.2 The Effects of Prefiltering and of the $J(w)$ Filter Polynomial on RIV-BO Estimation

The same general comments for the RLS-BO estimation algorithm (section 3.2.2), concerning the requirement for some from of prefiltering of the measured input-output signals, and a method of distributing the modeling errors across the frequency range of interest, apply to the RIV-BO estimation algorithm. An expression in the form of eqn. 3.23 however cannot easily be derived to demonstrate simply the effects of the prefilter and $J(w)$ filter polynomial on RIV-BO estimation. This can be understood by examining the least-squares and instrumental-variables error criterions.

The least-squares error criterion, given by eqn. 3.21, can be solved analytically to yield the least-squares estimate, given by

$$\hat{\theta}_N^{LS} = \text{sol}\left\{\frac{1}{N}\sum_{k=1}^{N}\phi_k(y_k - \phi_k^T\theta) = 0\right\} \tag{3.32}$$

where $\hat{\theta}_N^{LS}$ is the sol(ution) of the equation in brackets { } [10]. The IV estimate can be characterised by a similar equation,

$$\hat{\theta}_N^{IV} = \text{sol}\left\{\frac{1}{N}\sum_{k=1}^{N}z_k(y_k - \phi_k^T\theta) = 0\right\}. \tag{3.33}$$

The IV estimate however is not derived from the minimisation of a least-squares error criterion (eqn. 3.21), but from an error criterion of the form [69]

$$V(\hat{\theta}) = \| \frac{1}{N}\sum_{k=1}^{N}z_k(y_k - \hat{y}_k) \|^p \tag{3.34}$$

in which the norm $\| \, . \, \|$ can be freely chosen, and $p > 0$. This error criterion, when expressed in the frequency domain, does not provide significant insight into the effect of both the prefilter and $J(w)$ filter polynomial selections on estimation, as is the case for the least-squares criterion (eqns. 3.21, 3.22 and 3.23).

It is reasonable to expect that the prefilter will have similar effects as for the RLS-BO estimation algorithm, reducing the influence of unmodeled dynamics and system noise outside the frequency range of interest. The exact effect of $J(w)$ is a little less

clear. From a practical point of view however, it has been found from simulation studies (chapter 4) and practical examples (chapter 6), that selecting $J(w)$ based on the criterion used for the RLS-BO estimation algorithm produces good results.

3.4 Concurrent Work

The work described in this chapter on formulating the recursive estimation algorithms using the discrete-time w-operator is original work, developed from the work of Middleton and Goodwin [6,64] on the application of the delta operator to discrete-time control and estimation theory.

Recently however, a similar recursive estimation approach, using a discrete-time q-operator model, derived from the continuous-time model using the bilinear transformation, has appeared in the literature [30,31]. These two papers appeared in the literature in February 1991 and July 1991 respectively. The work of this thesis on the use of the w-operator model in estimation was first documented in personal communications with Dr. M.J. Gibbard, dated 29 August 1989. The initial results of the application of the method to performing standstill tests on a synchronous machine were first reported in January 1991 in personal communications with Dr. M.J. Gibbard. This work on standstill testing was submitted for publication in April 1991 [54].

The publications [30,31] are two in a recent series of articles by Sagara *et al.* who have been investigating general methods for estimating the coefficients of continuous-time models from sampled input-output signals [28,29,70,71]. The recursive least-squares estimation algorithm given in [31] will be studied in detail next, in relation to the original work in this thesis. Firstly however, a brief overview of the work in [30,31] will be given.

In [30], which appeared in the literature in February 1991, a discrete-time q-operator model, derived from the continuous-time model using the bilinear transformation, is formulated for use in recursive estimation. As the $J(w)$ filter polynomial is employed in this thesis, so a similar filter containing the estimated polynomial $\hat{A}(q^{-1})$ is used in [30]; i.e. the filter is used to convert the discrete-time q-operator model into a linear regression form suitable for use in recursive estimation. This

discrete-time model is used in formulating several conventional recursive estimation algorithms such as the least-squares algorithm, and instrumental-variable and generalised instrumental-variable algorithms.

In [31], which appeared in July 1991, the ideas of [30] are extended to use a simple low-pass digital filter $Q(q^{-1})$, instead of the time-varying filter constructed from the estimated polynomial $\hat{A}(q^{-1})$. Several simulation examples, on a relatively simple continuous-time model, are used to compare the recursive least-squares and recursive instrumental-variable estimation algorithms, as well as to show the effects on estimation of the choice of bandwidth for the low-pass digital filter.

The recursive least-squares (RLS) estimation algorithm in [31] is formulated in terms of the discrete-time q-operator. From [31], the algorithm can be written as

$$\epsilon(k) = \xi_{ny}(k) - \psi^T(k)\hat{h}(k-1) \tag{3.35a}$$

$$\hat{h}(k) = \hat{h}(k-1) + \frac{P(k-1)\psi(k)\epsilon(k)}{\lambda(k) + \psi^T(k)P(k-1)\psi(k)} \tag{3.35b}$$

$$P(k) = \frac{1}{\lambda(k)}\Big[P(k-1) - \frac{P(k-1)\psi(k)\psi^T(k)P(k-1)}{\lambda(k) + \psi^T(k)P(k-1)\psi(k)}\Big] \tag{3.35c}$$

where the parameter and regression vectors are defined respectively as

$$\hat{h}^T(k) = [-\hat{a}_{n-1}, \ldots, -\hat{a}_0, \hat{b}_{n-1}, \ldots, -\hat{b}_0] \tag{3.36}$$

$$\psi^T(k) = [\xi_{n-1y}(k), \ldots, \xi_{0y}(k), \xi_{n-1u}(k), \ldots, \xi_{0u}(k)] \tag{3.37}$$

The signals $\xi_{iy}(k)$ and $\xi_{iu}(k)$ in eqn. 3.37 are filtered versions of the sampled input-output signals, given by

$$\xi_{iy}(k) = Q(q^{-1})\left(\frac{\Delta}{2}\right)^{n-i}(1+q^{-1})^{n-i}(1-q^{-1})^i y(k), (i = 0, 1, \ldots, n) \tag{3.38}$$

$$\xi_{iu}(k) = Q(q^{-1})\left(\frac{\Delta}{2}\right)^{n-i}(1+q^{-1})^{n-i}(1-q^{-1})^i u(k), (i = 0, 1, \ldots, n-1) \tag{3.39}$$

where $Q(q^{-1})$ is either a Finite Impulse Response (FIR), or Infinite Impulse Response (IIR) digital filter. Reference [31] recommends using standard low-pass filters, say with a Butterworth or Chebyshev response. The bandwidth of the filter is selected to approximately match the bandwidth of the continuous-time system. A FIR filter

for example of length M_F may be employed,

$$Q(q^{-1}) = \sum_{m=0}^{M_F} Q_m q^{-m}$$

or say an k-th order Butterworth IIR filter with cut-off frequency ω_c

$$Q(q^{-1}) = \frac{\left(\frac{\Delta}{2}\right)^{k-n}(1+q^{-1})^{k-n}}{\left(\frac{1-q^{-1}}{\omega_c}\right)^{k} + \sum_{i=1}^{k} c_i \left(\frac{1-q^{-1}}{\omega_c}\right)^{k-i}\left(\frac{\Delta}{2}\right)^{i}(1+q^{-1})^{i}}$$

It is worth noting that the calculation of the elements (eqns. 3.38 and 3.39) of the regression vector requires $n+1$ separate digital filters. Each of the $2n$ elements (eqns. 3.38 and 3.39) of the regression vector are calculated independently of the other elements, using the corresponding digital filter. In [31] there is no expression given for recursively updating the regression vector.

Similarities

To allow an easier comparison of the estimation algorithm in [31] with the RLS-BO estimation algorithm of this thesis, the definitions of the filtered signals $\xi_{iy}(k)$ and $\xi_{iu}(k)$ (eqns. 3.38 and 3.39) are reparameterised in terms of the w operator.

From eqn. 3.38,

$$\begin{aligned}
\xi_{iy}(k) &= Q(q^{-1})\left(\frac{\Delta}{2}\right)^{n-i}(1+q^{-1})^{n-i}(1-q^{-1})^{i}y(k) \\
&= Q(q^{-1})\left(\frac{\Delta}{2}\right)^{n}(1+q^{-1})^{n}\left(\frac{2}{\Delta}\left[\frac{1-q^{-1}}{1+q^{-1}}\right]\right)^{i}y(k) \\
&= Q(q^{-1})\left(\frac{\Delta}{2}\right)^{n}\left(\frac{q+1}{q}\right)^{n}\left(\frac{2}{\Delta}\left[\frac{q-1}{q+1}\right]\right)^{i}y(k) \qquad (3.40)
\end{aligned}$$

Based on the definitions for the w operator (eqns. 2.7 and 2.8), eqn. 3.40 can be reparameterised as

$$\begin{aligned}
\xi_{iy}(k) &= Q(w)\left(\frac{2}{w+2/\Delta}\right)^{n} w^{i}y(k) \\
&= w^{i}H(w)y(k) \qquad (3.41)
\end{aligned}$$

where

$$H(w) = Q(w)\left(\frac{2}{w + 2/\Delta}\right)^n \tag{3.42}$$

Similarly, eqn. 3.39 for $\xi_{iu}(k)$ can be reparameterised in the w-operator notation. Furthermore, the RLS estimation algorithm in [31] (eqn. 3.35), reparameterised in terms of the w operator, becomes (the notation $u(k)$ has been replaced by u_k for a sampled signal):

SAGARA-RLS

$$\epsilon_k = w^n H(w) y_k - \psi_k^T \hat{h}_{k-1} \tag{3.43a}$$

$$\hat{h}_k = \hat{h}_{k-1} + \frac{P_{k-1}\psi_k \epsilon_k}{\lambda_k + \psi_k^T P_{k-1}\psi_k} \tag{3.43b}$$

$$P_k = \frac{1}{\lambda_k}\left[P_{k-1} - \frac{P_{k-1}\psi_k\psi_k^T P_{k-1}}{\lambda_k + \psi_k^T P_{k-1}\psi_k}\right] \tag{3.43c}$$

where the parameter and regression vectors are respectively

$$\hat{h}_k^T = [-\hat{a}_{n-1}, \ldots, -\hat{a}_0, \hat{b}_{n-1}, \ldots, -\hat{b}_0] \tag{3.44}$$

$$\psi_k^T = [w^{n-1}H(w)y_k, \ldots, H(w)y_k, w^{n-1}H(w)u_k, \ldots, H(w)u_k] \tag{3.45}$$

This RLS estimation algorithm in the w-operator notation is referred to as the SAGARA-RLS estimation algorithm. The RLS-BO estimation algorithm introduced in this thesis is given by eqn. 3.12, with the parameter and regression vectors given by eqns. 3.10 and 3.9 respectively. Comparing these equations (eqns. 3.9, 3.10 and 3.12) with those of the SAGARA-RLS estimation algorithm (eqns. 3.43 to 3.45), it appears as if the algorithms are different, primarily due to the difference in the prediction error equations (eqns. 3.12a and 3.43a). In 3.12a, the prediction error uses the unfiltered output signal, y_k, but eqn. 3.43a uses a filtered version of the output signal. It will be shown however, that providing the $J(w)$ filter polynomial and $H(w)$ filter (eqn. 3.42) are related by

$$H(w) = 1/J(w), \tag{3.46}$$

both estimation algorithms are mathematically equivalent.

Consider the quadratic error functions minimised by each estimation algorithm. A weighted least-squares estimation algorithm minimises a quadratic error function of the form (see eqn. 3.11)

$$E(\hat{\theta}) = \sum_{k=1}^{t} \beta(t,k)\,(error_k)^2 \tag{3.47}$$

where $error_k$ is given by either eqn. 3.12a or 3.43a. Expanding the error term e_k of the RLS-BO estimation algorithm of this thesis (using eqns. 3.9 and 3.10) yields

$$\begin{aligned}
e_k &= y_k - \phi_k^T \hat{\theta} \qquad (3.48)\\
&= y_k - (j_{n-1} - \hat{a}_{n-1})\frac{w^{n-1}}{J(w)}y_k - \cdots - (j_0 - \hat{a}_0)\frac{y_k}{J(w)} \\
&\qquad - \hat{b}_{n-1}\frac{w^{n-1}}{J(w)}u_k - \cdots - \hat{b}_0\frac{u_k}{J(w)} \\
&= y_k - (j_{n-1}w^{n-1} + \cdots + j_0)\frac{y_k}{J(w)} \\
&\quad +(\hat{a}_{n-1}w^{n-1} + \cdots + \hat{a}_0)\frac{y_k}{J(w)} - (\hat{b}_{n-1}w^{n-1} + \cdots + \hat{b}_0)\frac{u_k}{J(w)} \\
&= (w^n + j_{n-1}w^{n-1} + \cdots + j_0)\frac{y_k}{J(w)} - (j_{n-1}w^{n-1} + \cdots + j_0)\frac{y_k}{J(w)} \\
&\quad +(\hat{a}_{n-1}w^{n-1} + \cdots + \hat{a}_0)\frac{y_k}{J(w)} - (\hat{b}_{n-1}w^{n-1} + \cdots + \hat{b}_0)\frac{u_k}{J(w)} \\
&= w^n\frac{y_k}{J(w)} \\
&\quad +(\hat{a}_{n-1}w^{n-1} + \cdots + \hat{a}_0)\frac{y_k}{J(w)} - (\hat{b}_{n-1}w^{n-1} + \cdots + \hat{b}_0)\frac{u_k}{J(w)} \\
&= w^n\frac{y_k}{J(w)} - \phi_k^T[-\hat{a}_{n-1}, \ldots, -\hat{a}_0, \hat{b}_{n-1}, \ldots, \hat{b}_0]^T
\end{aligned}$$

If the $J(w)$ filter polynomial is selected such that $H(w) = 1/J(w)$, then, from eqns. 3.9 and 3.45, it is clear that $\phi_k^T = \psi_k^T$. Thus the prediction error becomes

$$e_k = w^n H(w) y_k - \psi_k^T[-\hat{a}_{n-1}, \ldots, -\hat{a}_0, \hat{b}_{n-1}, \ldots, \hat{b}_0]^T \tag{3.49}$$

Comparing this prediction error with eqn. 3.43a, it is clear that both the least-squares estimation algorithms derived in this thesis and in [31] minimise the same quadratic error function, and thus their coefficient estimates are equal.

Hence, providing the $H(w)$ filter and $J(w)$ filter polynomial are related by eqn. 3.46,

the RLS-BO estimation algorithm of this thesis and the RLS estimation algorithm of [31] are equivalent.

Differences

Whilst it has just been shown that, providing the $H(w)$ filter and $J(w)$ filter polynomial are related by eqn. 3.46, the RLS estimation algorithms are mathematically equivalent, the implementation of each algorithm is significantly different.

The RLS-BO estimation algorithm introduced in this thesis is implemented directly using the discrete-time w operator. The RLS estimation algorithm of [31] is implemented using the q operator. The benefits of the direct w-operator formulation include:

- The regression vector is easily updated by a simple matrix multiplication of the previous time-sample regression vector (see section 3.2). This is in comparison to the RLS estimation algorithm of [31], which has separate, relatively complicated, discrete-time q-operator filters (eqns. 3.38 and 3.39) for updating each element of the regression vector. These regression vector elements are not updated in a recursive formulation.

- For high sampling frequencies, the discrete-time w-operator parameterisation is numerically superior to the q-operator parameterisation (see section 2.2.3). In [6], the discrete-time δ operator is introduced partly due to the numerical difficulties associated with the q operator for relatively high sampling frequencies. From the finite word-length simulation example of section 2.2.3, the numerical properties of the w operator are similar to those of the δ operator, which are vastly superior to those of the q operator. The numerical properties are particularly important in this application, due to the requirement for a high sampling frequency such that the coefficients of the discrete-time w-operator model closely approximate those of the corresponding continuous-time model.

- The w-operator parameterisation allows the filter polynomial $J(w)$ to be designed from background knowledge based on the frequency response of the continuous-time system. The filter polynomial $J(w)$ is then directly employed

in this form for estimation. In [31], the filter $H(w)$ is generally designed firstly in the continuous-time domain and then converted, using the bilinear transformation, to the corresponding discrete-time q operator parameterisation required for implementation.

Another difference between the estimation algorithms is in the selection of the $J(w)$ polynomial or $H(w)$ filter. In [31] it is recommended that the filter $H(w)$ be selected as a standard low-pass filter, with a bandwidth approximately matching that of the continuous-time system. The design process for this filter is conducted for both an 'ideal' low-pass FIR filter, and a Butterworth low-pass IIR filter.

As is evident from sections 3.2.1 and 3.2.2 of this thesis, the recommended selection of the $J(w)$ filter polynomial is dependent on many factors. These include, the characteristics of the continuous-time model, the spectral characteristics of the input signal, and even the nature of the practical application of the estimated model.

Summary

In summary, the similarity between the recursive estimation algorithms introduced in [30,31] and those in this thesis are:

- Both estimation algorithms use the w operator (or bilinear transformation) to derive a discrete-time model, the coefficients of which approximate those of the continuous-time model.
- Some form of filtering is introduced to restructure the discrete-time model into a linear regression form suitable for recursive estimation.
- Providing these filters in each estimation method are related by $H(w) = 1/J(w)$, both estimation algorithms are mathematically equivalent.

The differences can be summarised as:

- The estimation algorithms are implemented differently. In [30,31], the discrete-time q operator is used. In this thesis, the algorithms are implemented directly using the w operator. The w-operator formulation offers several benefits, including simplified updating of the estimation regression vector, and numerical

superiority. Also, the coefficients of filters designed in the continuous-time domain can be applied directly for implementation with the w operator, as opposed to being converted to the q operator (via the bilinear transformation) for implementation in [30,31].

- The filter polynomial $J(w)$ and filter $H(w)$ are selected differently. In [30], the filter $H(w)$ is related to the coefficients of the estimated polynomial $\hat{A}(q^{-1})$. This filter is updated during estimation, and thus $H(w)$ is time varying. In [31], the filter $H(w)$ is selected as a standard low-pass filter, with a bandwidth matching that of the continuous-time system. In this thesis, the selection of the filter polynomial $J(w)$ is based on many considerations, including the characteristics of the continuous-time system under test and the spectral content of the excitation signal used. The filter polynomial $J(w)$ controls the distribution of the modeling errors between the true and the estimated models in frequency.

3.5 Summary and Conclusions

This chapter introduces the use of the discrete-time w-operator model in recursive estimation. The primary benefit of using this discrete-time w-operator parameterisation is that it allows, from sampled input-output signals, a direct estimate of the coefficients of the underlying continuous-time model to be calculated.

In section 3.2, a RLS-BO estimation algorithm is developed (eqn. 3.12). This algorithm is suitable for estimation when the signal-to-noise ratio of the sampled output signal is high. The parameter estimates will in general be biased in the presence of output noise, however, if the signal-to-noise ratio is high, and the estimation filter polynomial $J(w)$ and prefilter are chosen correctly, this bias will be small. The effects of the prefilter and $J(w)$ polynomial, as well as the excitation signal spectral characteristics on estimation, are examined in the frequency domain. This provides insight to help with the proper selection of these various parameters.

In section 3.3, a RIV-BO estimation algorithm is developed (eqn. 3.24). This algorithm is suitable for estimation when the sampled output signal is contaminated with either high-level white, or coloured additive output noise. The parameter estimates

are asymptotically unbiased in the presents of both white and coloured output noise.

In section 3.4, the estimation algorithms developed in this thesis are compared to some recent parallel work. Whilst the estimation algorithms may be shown to be equivalent, the implementation of the method proposed in this thesis shows significant advantages.

In the next chapter, simulation studies are used to show the effectiveness of the proposed estimation algorithms. The effects of noise, prefilter selection, and the filter polynomial $J(w)$ selection are examined.

The following contributions in this chapter are original contributions:

- The application of the discrete-time w-operator model to recursive least-squares estimation (RLS-BO estimation algorithm, eqn. 3.12).

- The analysis in the frequency domain of the effects of prefiltering and of the $J(w)$ filter polynomial on RLS-BO estimation (section 3.2.2).

- The application of the discrete-time w-operator model to recursive instrumental-variable estimation (RIV-BO estimation algorithm, eqn. 3.24).

Chapter 4

Simulation Studies

4.1 Introduction

In this chapter, simulation studies are undertaken to demonstrate the effectiveness of both the RLS-BO and RIV-BO estimation algorithms introduced in the previous chapter. The studies include the effects of unmodeled dynamics, and both white and coloured additive output noise. The effects of prefiltering of the sampled input and output signals on estimation, as well as the selection of the filter polynomial $J(w)$, are investigated.

In section 4.2, the Pseudo Random Binary Sequence (PRBS) is introduced. This class of signal is used as the input for all simulation studies in this chapter, as well as in the practical estimation examples in later chapters. Guidance is given on selecting the various parameters of the PRBS to tailor it to the specific estimation task.

In section 4.3, two continuous-time models, with no additive output noise or unmodeled dynamics, are identified using the RLS-BO estimation algorithm. The first is a relatively simple model, which is initially introduced in section 2.3.2. The purpose of this study (Simulation Study 1) is to allow a comparison of the estimated model coefficients with those of the derived triangle-hold-equivalent w-domain model (section 2.3.2). The second model considered (Simulation Study 2) is a relatively complicated system for estimation, with pairs of complex poles and zeros which are both lightly damped, and are in close proximity of each other. This model is used for the simulation studies in the following sections.

In section 4.4 (Simulation Study 3), unmodeled dynamics are included in the simulated output signal. The effects of both the $J(w)$ filter polynomial and prefilter on RLS-BO estimation are investigated.

In section 4.5, two simulation studies are conducted. In Simulation Study 4, additive white noise with a signal-to-noise ratio (SNR) of 10 is included in the simulated output signal. The effect of this on estimation, and the choice of the $J(w)$ filter polynomial and the prefilter, are investigated. In the second simulation, Simulation Study 5, a high level of white additive output noise (SNR=2) is included in the simulated output signal. The use of both the RLS-BO and RIV-BO estimation algorithms is investigated.

In section 4.6, coloured, additive noise is included in the simulated output signal. In Simulation Study 6, one form of coloured noise, generated by filtering white noise is included, whilst in Simulation Study 7 the effects of dc offset are investigated.

Section 4.7 contains some concluding remarks concerning the proposed recursive estimation algorithms, and offers some limited guidance on the methodology for selecting the various options for a practical estimation study.

4.2 PRBS Excitation Signal

As discussed in the previous chapter, the input excitation signal must be persistently exciting of order $n+m+1$ in order to estimate the $n+m+1$ unknown coefficients of a TF having an n-th order denominator and m-th order numerator. This is a theoretical requirement on the input signal for asymptotic convergence of the estimates. From a practical point of view, however, when the input-output signal sample is finite in length, the parameter convergence may still be poor, even with a persistently exciting input signal [2]. Thus, in practice, it is common to use an excitation signal that is persistently exciting of an order much greater than $n+m+1$.

In the frequency domain, the requirement of persistent excitation is equivalent to the power spectral density of the exciting signal being non-zero for at least $n+m+1$ frequencies. Theoretically there is no requirement on the distribution of these frequency components in the excitation signal for convergence of the parameter es-

timates. However, to improve the rate of convergence, the frequency components should span the approximate bandwidth of the system to be identified [2].

A deterministic signal which satisfies these requirements is the Pseudo Random Binary Sequence (PRBS), providing its parameters are correctly chosen. A PRBS is a periodic sequence of binary values (amplitude $\pm a$), of length N 'bits'. The sequence can easily be generated by an n-stage shift register in combination with and Exclusive-OR operation [2]. The length of the PRBS is $N = 2^n - 1$ 'bits'. Figure 4.1 displays a PRBS sequence of length 7, and the shift register used for its generation.

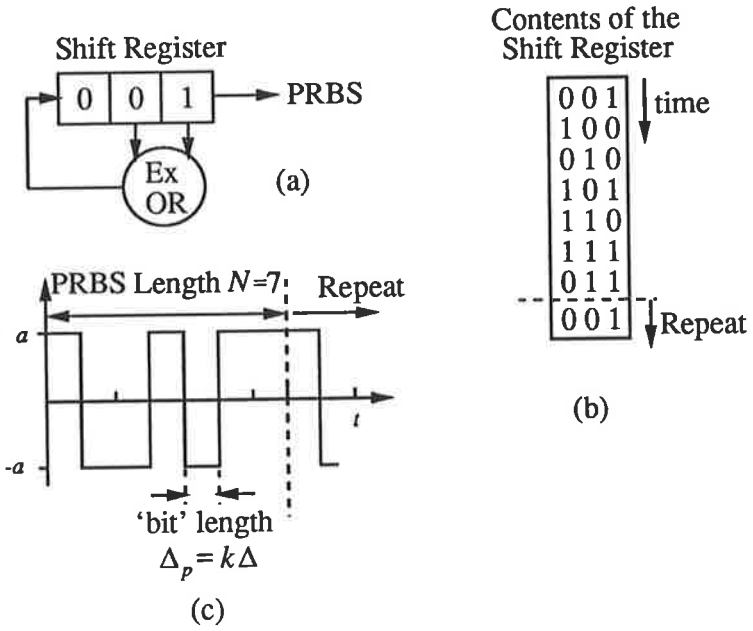

Figure 4.1: A PRBS of length 7, generated using a 3-stage shift register.

Often the 'bit' length, Δ_p, of a PRBS is taken as the sampling period, Δ, of the discrete-time system. However, it can be useful to allow the PRBS 'bit' length to be some integral number of sample periods, i.e. $\Delta_p = k\Delta$.

As stated before, the requirement of persistent excitation is equivalent to the power spectral density of the excitation signal being non-zero for at least $n + m + 1$ frequencies. The power spectral density of a PRBS signal is given by [72]

$$\Phi(f) = \frac{a^2}{N}\delta(f) + a^2\left(\frac{1+N}{N}\right)\sum_{i=-\infty,\neq 0}^{\infty} \mathrm{sinc}^2\frac{i}{N}\delta(f - \frac{i}{N\Delta_p}) \qquad (4.1)$$

This spectrum is a line spectrum, with frequency components at discrete frequencies $i/(N\Delta_p)$ Hz. These discrete frequency components are windowed by a sinc^2 function which limits the –3 dB bandwidth of the signal to approximately $0.44N/(N\Delta_p)$ Hz (see Figure 4.2).

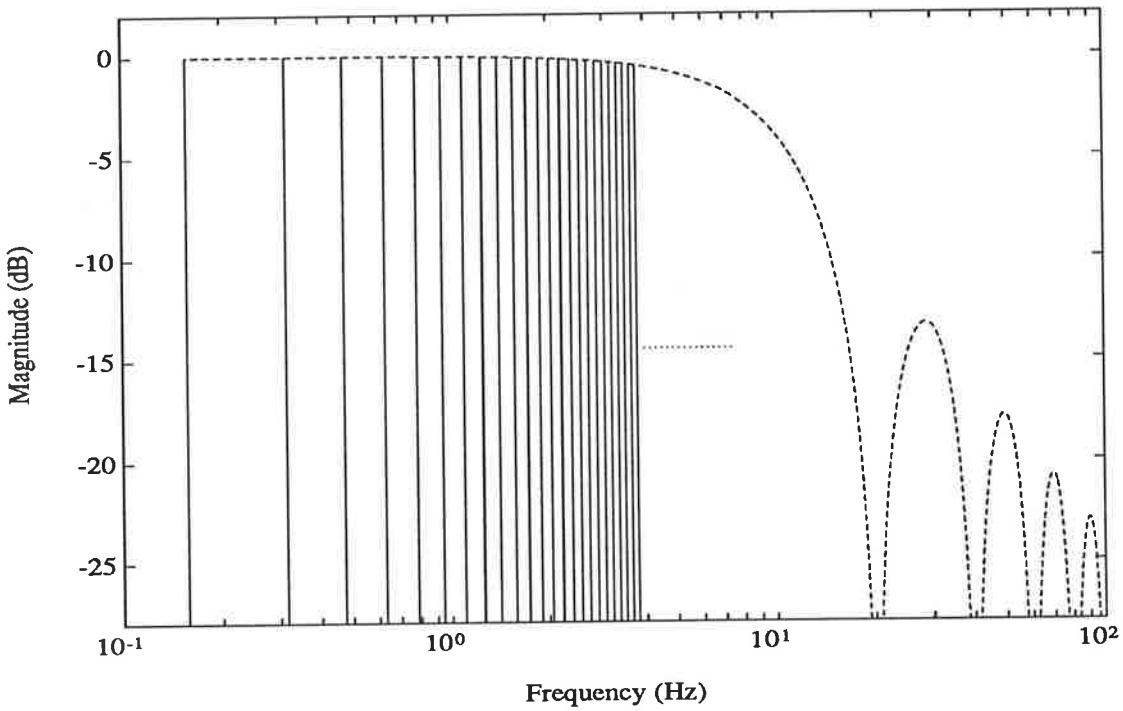

Figure 4.2: The power spectral density of a pseudo random binary sequence, $N = 127$, $k = 5$, and $\Delta = 0.01$.

Some benefits of using a PRBS excitation signal in estimation include:

- The PRBS is persistently exciting of order approximately $0.88N$, where N is the length of the PRBS in 'bits'. For estimation of a practical system, N will typically be large, say $N = 127$ $(= 2^7 - 1)$, and thus the PRBS will be persistently exciting of order approximately $0.88N \approx 112$. For estimating the coefficients of say a seventh-order model, $n + m + 1 = 7 + 6 + 1 = 14$, and thus the PRBS more than satisfies the persistent excitation requirement, with $112 >> 14$.

- The frequency content of the PRBS is spread approximately evenly across the frequency range, from $1/(N\Delta_p)$ Hz to approximately $0.44N/(N\Delta_p)$ Hz.

- The PRBS is easily generated digitally by an n-stage shift register. This digital signal can be converted to a continuous-time analogue signal by a D/A converter with ZOH.

With reference to Figure 4.1(c), there are three parameters of the PRBS that require selection.

a : The amplitude of the PRBS: The selection of this parameter is based on the allowable or desired amplitude of perturbation for the system under test. For example, for the online identification of a synchronous generator discussed in chapter 6, the level a is selected to give a terminal voltage perturbation of less than 2% peak-to-peak.

N **and** Δ_p : The length of the PRBS N, and its 'bit' length Δ_p: Given that the sampling period Δ has already been selected (on the basis that the sampling frequency $f_s = 1/\Delta$ is at least ten times the –3 dB bandwidth, or highest frequency pole or zero of the continuous-time system (see chapter 2)), the parameters N and $\Delta_p = k\Delta$ are chosen to yield the desired frequency spectrum of the PRBS. N and Δ_p control both the bandwidth of the PRBS (from $1/(N\Delta_p)$ Hz to approximately $0.44N/(N\Delta_p)$ Hz), and the spacing of the frequency components (every $1/(N\Delta_p)$ Hz). For example, a PRBS with parameters $N = 127$, $k = 5$ and $\Delta = 0.01$ s excites frequencies across the range of approximately 0.16 Hz to 8 Hz, at frequency points 0.16 Hz apart (see Figure 4.2).

A PRBS excitation signal is used for all estimation studies in this thesis.

4.3 Recursive Estimation: No Additive Noise

In section 2.3.2, the continuous-time TF (eqn. 2.36)

$$\begin{aligned} H(s) &= \frac{s-1}{s^3+1.1s^2+2.1s+2} \\ &= \frac{(s-1)}{(s+1)(s+0.05+j1.41)(s+0.05-j1.41)} \end{aligned}$$

is used to compare how closely the coefficients of the discrete-time q-, δ-, and w-domain models approximate those of the continuous-time TF for the purposes of estimation. The z transform with triangle hold (TH) is used to calculate these equivalent discrete-time models. It will now be shown that the coefficients of the TH-equivalent w-domain model, derived using the z transform with TH, closely match those calculated from RLS-BO estimation.

4.3.1 Simulation Study 1

To allow a comparison of the estimated model coefficients with the TH-equivalent coefficients calculated in Table 2.1 (section 2.3.2), the sampling period $\Delta = 0.2$ s is selected for the simulation study. This corresponds to a sampling frequency $f_s = 5$ Hz, which is approximately 14 times the –3 dB bandwidth of the continuous-time TF.

For successful estimation of the coefficients of the continuous-time TF (eqn. 2.36), the various parameters of the PRBS excitation signal must be selected. The corner frequencies of the poles and zeros of the continuous-time TF (eqn. 2.36) range in frequency from 1 rad/s (0.16 Hz), to approximately 1.4 rad/s (0.22 Hz). Thus to improve the convergence of estimation, the spectrum of the PRBS input excitation signal should cover at least this frequency range. With the sampling period $\Delta = 0.2$ s, the PRBS parameters N and k are selected as $N = 127$ and $k = 5$, resulting in the frequency spectrum of the PRBS spanning the frequency range of approximately 0.08 Hz to 0.44 Hz, at discrete frequency points 0.08 Hz apart. It should be noted that the poles and zeros of the simulated continuous-time system are distributed over a very narrow frequency range (0.16 Hz to 0.22 Hz). The continuous-time system considered in the next study covers a greater frequency range.

In Figure 2.8, the general test configuration for sampling the input and output signals of a continuous-time system for use in discrete-time estimation is given. For the simulated input-output signals to accurately reflect signals sampled from this configuration, they must be anti-alias filtered. Two identical fifth-order, Butterworth, low-pass filters, each with a cut-off frequency of $f_c = 0.8$ Hz are used. This would ensure, in a practical estimation study, that signals which are aliased to frequencies below approximately 0.5 Hz are attenuated by at least 75 dB. The level of –75 dB rep-

resents the resolution available with 12 bit analogue-to-digital converters. The input filter $F(s)$ of Figure 2.8, which may be used to attenuate high-frequency components of the input excitation signal, is chosen as an all-pass filter.

To implement the RLS-BO estimation algorithm, the $J(w)$ filter polynomial must be selected. From section 3.2.2 it is shown that the error between the true and the estimated models is weighted in frequency by the factor,

$$\mid \mathrm{Pre}(\beta) \mid^2 \mid \frac{\hat{A}(\beta)}{J(\beta)} \mid^2 \Phi_u(f).$$

For this simulation study, the power spectral density of the PRBS excitation signal ($\Phi_u(f)$) is approximately flat across the frequency range from 0.08 Hz to 0.44 Hz. The input and output signals are anti-alias filtered but not prefiltered prior to estimation, and thus $\mid \mathrm{Pre}(\beta) \mid^2$ should have little effect on the weighting. Thus the frequency weighting factor $\mid \frac{\hat{A}(\beta)}{J(\beta)} \mid^2$ provides an indication of how the model error is weighted in frequency. Assuming the denominator of the estimated w-domain model will accurately approximate the true TF denominator, the selection of $J(w) \approx A(w)$ should thus result in an approximately even weighting being given to the error between the true and estimated models. The selection of the roots of $J(w)$ to approximately match the magnitude of the roots of $A(w)$ is a possible selection for $J(w)$, i.e.

$$J(w) = (w + 1)(w + 1.4)^2,$$

and is used for this study.

A constant forgetting factor is used for this simulation study.

The conditions for the study are thus summarised:

Simulation Study 1

Simulated Input-Output Signals

Continuous-Time TF:	$H(s) = \frac{s-1}{s^3+1.1s^2+2.1s+2}$
Anti-Aliasing Filters:	Fifth-order Butterworth, low-pass, $f_c = 0.8$ Hz
Sampling Period:	$\Delta = 0.2$ s ($f_s = 1/\Delta = 5$ Hz)
Input Signal:	PRBS; N=127, k=5

Recursive Estimation

Estimation Algorithm:	RLS-BO, 500 iterations
Estimated TF Form:	$\hat{H}(\beta) = \frac{\hat{b}_3\beta^3+\hat{b}_2\beta^2+\hat{b}_1\beta+\hat{b}_0}{\beta^3+\hat{a}_2\beta^2+\hat{a}_1\beta+\hat{a}_0}$
$J(w)$ Filter Polynomial:	$J(w) = (w+1)(w+1.4)^2$
Prefilter:	none
Forgetting Factor:	$\lambda = 0.99$
Initialisation:	$P_0 = 10^5 I$
	$\hat{\theta}_0 = [j_{n-1}, j_{n-2}, \ldots, j_0, 0, \ldots, 0]$

Figure 4.3 displays the variation of the coefficient estimates during estimation. The coefficient estimates converge very rapidly; after less than 50 iterations the estimates are approximately constant. The values of the coefficient estimates after 500

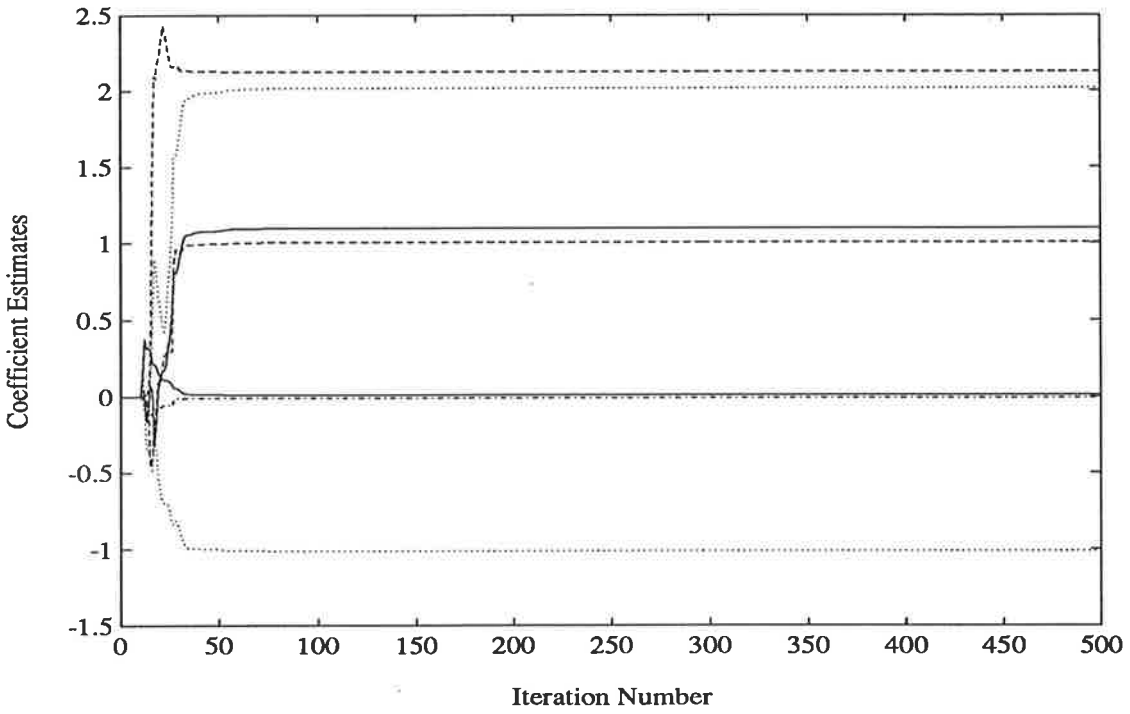

Figure 4.3: RLS-BO coefficient estimates, Simulation Study 1.

iterations are given in Table 4.1, together with the TH-equivalent w-domain coeffi-

cients calculated in section 2.3.2. The coefficients of the ZOH-equivalent w-domain model are also given for comparison.

	Cts-Time Coeffs.	RLS-BO Estimated Coeffs.	TH-equivalent w-domain Coeffs. *	ZOH-equivalent w-domain Coeffs. *
a_2	1.10	1.0986	1.0987	1.0987
a_1	2.10	2.1286	2.1286	2.1286
a_0	2.00	2.0200	2.0202	2.0202
b_3	0.00	–0.0066	–0.0033	–0.0007
b_2	0.00	0.0139	0.0104	–0.0936
b_1	1.00	1.0064	1.0064	1.1074
b_0	–1.00	–1.0100	–1.0101	–1.0101

Table 4.1: Comparison of the RLS-BO estimated and hold-equivalent w-domain coefficients for the continuous-time TF, eqn. 2.36, Simulation Study 1. (* – These coefficients are listed in Table 2.1.

It is clear that the estimated coefficients closely approximate those of the TH-equivalent w-domain model. Several of the numerator coefficients of the ZOH-equivalent w-domain model clearly differ from the estimated coefficients. The results in Table 4.1 suggest that the comparisons made in section 2.3.2, using the TH-equivalent w-domain model, are a valid comparison for showing how well, for the purposes of estimation, the w-domain coefficients approximate those of the corresponding continuous-time model.

These results also suggest that, if an 'approximate' continuous-time model of the system is known before estimation, then the calculated TH-equivalent w-domain coefficients can be used to help select a sampling period for estimation. For example, given the coefficients of an 'approximate' continuous-time model, the TH-equivalent w-domain coefficients can be calculated and used as a prediction of the estimated w-domain coefficients for a given sampling period. If the error between the predicted coefficients and those of the 'approximate' continuous-time model are unacceptable, then the sampling period may be decreased, and the predicted coefficients recalculated.

A related post-estimation check that can be performed is based on considering the estimated w-domain model to be the 'approximate' continuous-time model. By

calculating the TH-equivalent coefficients from this 'approximate' continuous-time model, they can be used as before to assess the suitability of the selected sampling period.

4.3.2 Simulation Study 2

The continuous-time TF used in the previous simulation is a relatively simple TF, with only one lightly damped complex pole. In this simulation, the following continuous-time TF is used [43]

$$\begin{aligned} H(s) &= \frac{0.1812(s^3 + 1.036s^2 + 107.74s + 107.7)}{s^4 + 0.9s^3 + 56.4s^2 + 27.6s + 19.8} \\ &= \frac{0.1812s^3 + 0.1877s^2 + 19.5225s + 19.5152}{s^4 + 0.9s^3 + 56.4s^2 + 27.6s + 19.8}. \end{aligned} \tag{4.2}$$

The poles and zeros of this TF are

$$\begin{aligned} \text{Poles}: \quad & -0.2042 \quad \pm j7.4701 \\ & -0.2458 \quad \pm j0.5423 \\ \text{Zeros}: \quad & -0.0180 \quad \pm j10.3780 \\ & -1.0 \end{aligned}$$

The TF has both lightly-damped and well-damped complex poles, as well as a very lightly-damped complex zero. The Bode plot of this TF is given in Figure 4.4. The corner frequencies of the systems poles and zeros span a reasonable frequency range, from approximately 0.086 Hz to 1.65 Hz, which is a ratio of approximately 20:1.

For this TF, a sampling frequency of $f_s = 100$ Hz is chosen. This is significantly higher than the highest corner frequency of any of the poles or zeros of the TF, and should ensure the coefficients of the discrete-time w-domain model provide a close approximation to those of the continuous-time TF. As shown in Simulation Study 1, the coefficients of the TH-equivalent w-domain model, calculated from the continuous-time TF, approximate the values which result from estimation. These calculated TH-equivalent coefficients are given in Table 4.2. For comparison, the TH-equivalent δ-domain coefficients are also given.

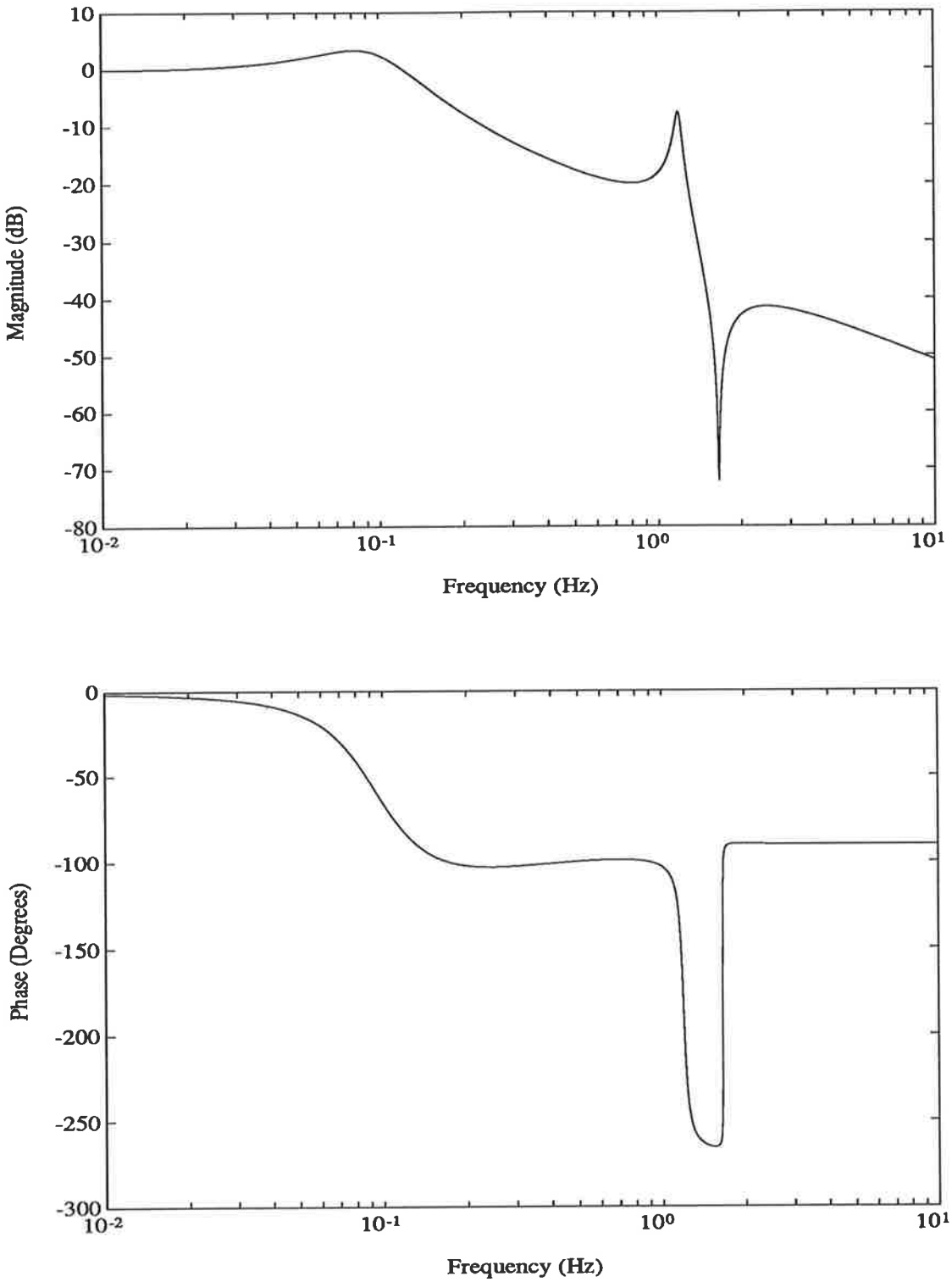

Figure 4.4: Bode plot of the continuous-time TF, eqn. 4.2.

	Cts-Time TF Coeffs.	Predicted TH-equivalent w-domain Coeffs.		Predicted TH-equivalent δ-domain Coeffs.	
a_3	0.9	0.9006	(0.1)	1.4585	(62)
a_2	56.4	56.4522	(0.1)	56.5350	(0.2)
a_1	27.6	27.6259	(0.1)	27.8574	(0.9)
a_0	19.8	19.8185	(0.1)	19.7019	(0.5)
b_4	0.0	-2.05×10^{-7}	(–)	0.0009	(–)
b_3	0.1812	0.1810	(0.1)	0.1833	(1)
b_2	0.1877	0.1876	(0.1)	0.4808	(156)
b_1	19.5225	19.5409	(0.1)	19.8143	(1.5)
b_0	19.5152	19.5335	(0.1)	19.4186	(0.5)

Table 4.2: Comparison of the TH-equivalent w- and δ-domain coefficients with those of the continuous-time TF, eqn. 4.2. The bracketed numbers indicate the percentage difference between the continuous- and discrete-time coefficients. (The sampling frequency is $f_s = 100$ Hz).

From Table 4.2 it is clear that the TH-equivalent w-domain coefficients closely approximate the corresponding continuous-time coefficients. Note also that the majority of the δ-domain coefficients are close to those of the continuous-time TF. The coefficients a_3 and b_2 however are significantly larger than those of the continuous-time TF. These coefficients primarily determine the damping of the complex poles and zeros of the TF, and highlight the fact that the δ-domain model greatly overestimates the magnitude of the damping constants [1] of these complex poles and zeros.

From Table 4.2, the leading numerator coefficient, b_4, of the w-domain model is almost zero. This is the case for the discrete-time w-domain model for high sampling frequencies, providing the continuous-time TF is strictly proper. Appendix A proves that as the sampling period approaches zero, the TH-equivalent w-domain TF approaches the continuous-time TF, and thus b_n approaches zero for strictly proper TFs. For the rest of the simulation studies, and for the majority of the practical estimation studies in this thesis, this leading numerator coefficient will be assumed to be zero. This is because all the continuous-time systems considered (except for the field-to-stator TF in chapter 5) are strictly proper.

For successful estimation of the coefficients of the continuous-time TF (eqn. 4.2),

[1] The damping constant is defined as the real part, $-\alpha$, of the complex roots, $-\alpha \pm j\beta$.

the PRBS excitation signal should excite frequencies across the range of at least 0.08 Hz to 1.65 Hz, which covers the range of corner frequencies of the poles and zeros of the continuous-time TF. Let the PRBS parameters be selected as $N = 511$ $(= 2^9 - 1)$ and k=20. The sampling period is $\Delta = 0.01$ s. The PRBS thus excites frequencies over the range from approximately 0.01 Hz to 2.2 Hz. The discrete frequency components of the PRBS are spaced approximately 0.01 Hz $(1/(512 \times 20 \times 0.01) \approx 0.01)$ apart. It is worth noting that this PRBS length of 511 'bits' is reasonably long; at 20 samples per 'bit', the length of the PRBS is 10220 samples. For some of the simulation studies with lower noise levels, the coefficient estimates will converge well before this length. However, for the simulation studies with high-level or coloured noise, it may take longer than one cycle of the PRBS for convergence.

As in the previous simulation study, in order to simulate the estimation of a practical system, the input and output signals must be anti-alias filtered. Two identical fourth-order, Butterworth, low-pass filters, with a cut-off frequency of $f_c = 10$ Hz ensure that any signals aliased below 10 Hz are attenuated by at least 75 dB. It is again assumed that the filter $F(s)$ (Figure 2.8) is all-pass. The signals are not prefiltered prior to estimation, except for the anti-aliasing filtering.

As in the previous simulation study, the $J(w)$ filter polynomial is again selected to approximately match the denominator of the continuous-time TF. The roots of the denominator polynomial $A(s)$ are given approximately by $s : -0.2 \pm j7.47$, $-0.25 \pm j0.54$; and thus a possible filter selection is

$$J(w) = (w + 0.5)^2(w + 7.5)^2.$$

The effect of this $J(w)$ filter polynomial on the relative weighting applied to the error between the true and the estimated models across the frequency range will be discussed once the estimated coefficients have been calculated.

A constant forgetting factor is selected for this simulation study.

In Appendix C, a listing of a version of the Matlab code used for implementing the RLS-BO estimation algorithm is provided.

Thus the conditions for this simulation study are:

Simulation Study 2

Simulated Input-Output Signals

Continuous-Time TF:	$H(s) = \frac{0.1812s^3+0.1877s^2+19.5225s+19.5152}{s^4+0.9s^3+56.4s^2+27.6s+19.8}$
Anti-Aliasing Filters:	Fourth-order Butterworth, low-pass, $f_c = 10$ Hz
Sampling Period:	$\Delta = 0.01$ s ($f_s = 1/\Delta = 100$ Hz)
Input Signal:	PRBS; N=511, k=20

Recursive Estimation

Estimation Algorithm:	RLS-BO, 3000 iterations
Estimated TF Form:	$\hat{H}(\beta) = \frac{\hat{b}_3\beta^3+\hat{b}_2\beta^2+\hat{b}_1\beta+\hat{b}_0}{\beta^4+\hat{a}_3\beta^3+\hat{a}_2\beta^2+\hat{a}_1\beta+\hat{a}_0}$
$J(w)$ Filter Polynomial:	$J(w) = (w+0.5)^2(w+7.5)^2$
Prefilter:	none
Forgetting Factor:	$\lambda = 0.99$
Initialisation:	$P_0 = 10^5 I$
	$\hat{\theta}_0 = [j_{n-1}, j_{n-2}, \ldots, j_0, 0, \ldots, 0]$

In Figure 4.5 the variation in coefficient estimates during estimation are displayed. It is seen from this figure that the coefficient estimates converge after approximately 700 iterations. The coefficient estimates after 3000 iterations are given in Table 4.3. It

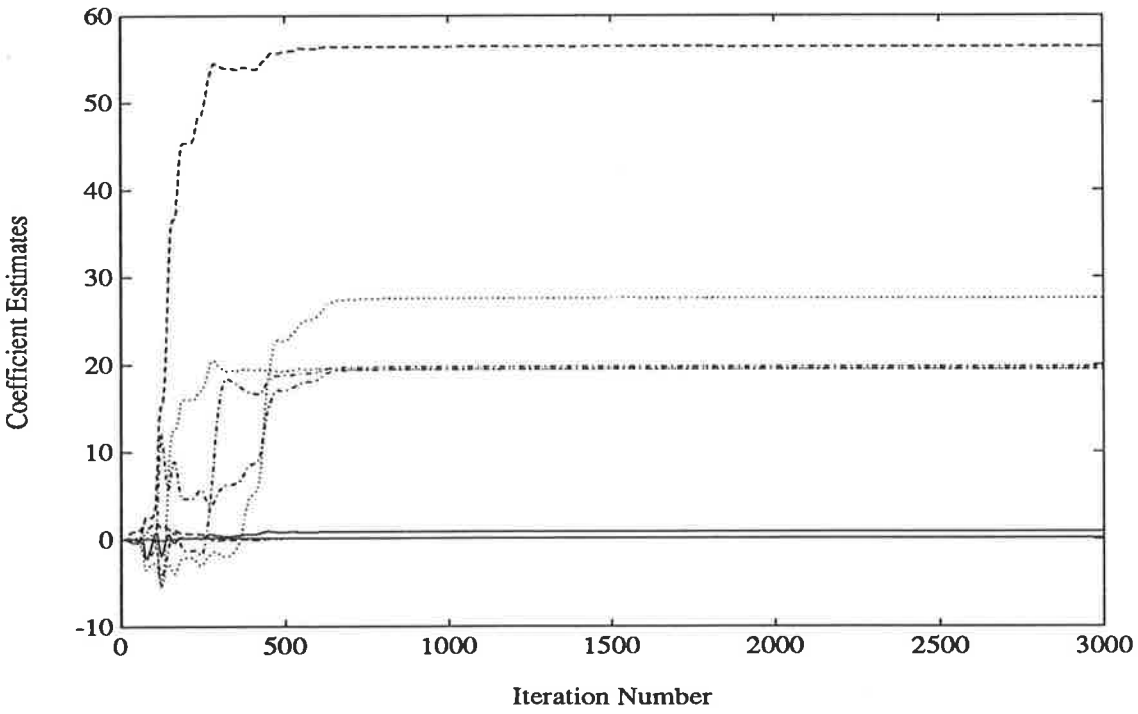

Figure 4.5: RLS-BO coefficient estimates, Simulation Study 2.

	Cts-Time TF Coeffs.	w-domain Coeff. Estimates	
a_3	0.9	0.9006	(0.1)
a_2	56.4	56.4429	(0.1)
a_1	27.6	27.6218	(0.1)
a_0	19.8	19.8153	(0.1)
b_3	0.1812	0.1812	(0.0)
b_2	0.1877	0.1877	(0.0)
b_1	19.5225	19.5395	(0.1)
b_0	19.5152	19.5308	(0.1)

Table 4.3: RLS-BO estimated coefficients, Simulation Study 2. The bracketed numbers indicate the percentage difference between the continuous-time and estimated coefficients.

is clear that the estimated w-domain coefficients approximate accurately both those of the TH-equivalent w-domain model in Table 4.2, as well as those of the actual continuous-time TF.

The $J(w)$ Filter Polynomial

For this simulation study, the $J(w)$ filter polynomial is chosen as

$$J(w) = (w + 0.5)^2(w + 7.5)^2$$

In chapter 3, it is shown that the RLS-BO estimation algorithm minimises the error between the true and estimated models, weighted in frequency by

$$| \text{Pre}(\beta) |^2 | \frac{\hat{A}(\beta)}{J(\beta)} |^2 \Phi_u(f).$$

In this simulation, the input and output signals are not prefiltered (except for the anti-alias filtering), and the power spectral density of the PRBS input signal is approximately flat over the frequency range from 0.01 Hz to 2.2 Hz. Thus the frequency weighting factor $| \frac{\hat{A}(\beta)}{J(\beta)} |^2$ provides an indication of how the error between the true and estimated models is weighted in frequency. Figure 4.6 displays this frequency weighting factor (calculated assuming $\beta = j2\pi f$, see section 3.2.2). It shows that, except in the vicinity of the high-frequency complex poles, the error is weighted 'approximately'

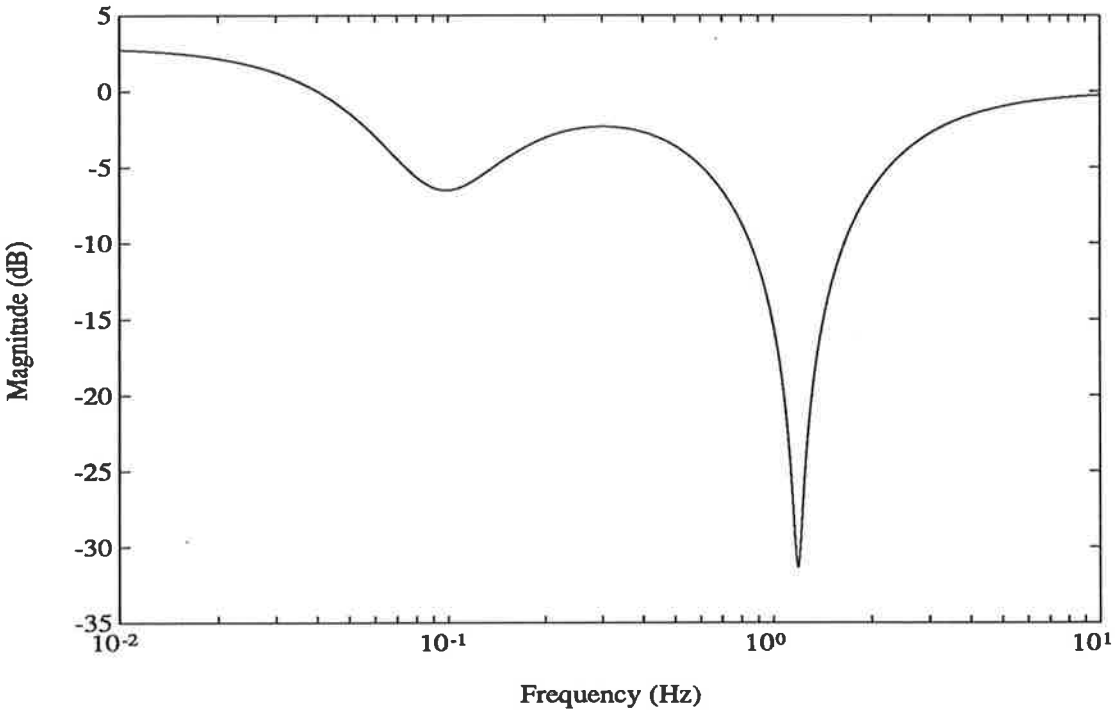

Figure 4.6: The frequency weighting factor $\mid \frac{\hat{A}(\beta)}{J(\beta)} \mid^2$, Simulation Study 2.

evenly across the frequency range. In this example, with no additive output noise and no unmodeled dynamics, a wide choice of $J(w)$ polynomials is available without significantly affecting the results of estimation.

4.4 Recursive Estimation: Unmodeled Dynamics

In the previous section, the RLS-BO estimation algorithm is used successfully in estimating the coefficients of both a simple and a relatively complicated continuous-time TF. In these studies, output noise and unmodeled dynamics are not considered.

In practical estimation studies however, both noise and unmodeled dynamics may be present. The simulation examples in this section include unmodeled dynamics. In these studies, the effects of both prefiltering and the $J(w)$ filter polynomial on estimation are examined.

As mentioned in section 3.2.2, unmodeled dynamics or undermodeling occurs when the chosen model cannot completely describe the response of the true system. This can include the case in which the order of the estimated model is less than that of the true system, or for example, the case in which a linear model is selected to represent a nonlinear system.

For the simulation studies of this section, unmodeled dynamics are considered by selecting the order of the estimated model to be less than that of the true system model used to simulate the system output signal. The relatively complicated fourth-order TF of eqn. 4.2 is used to generate the output signal for estimation, whilst only a third-order w-domain model is assumed for estimation.

4.4.1 Simulation Study 3

Effect of the $J(w)$ Filter Polynomial on Estimation

As discussed in section 3.2.2, the $J(w)$ filter polynomial can be used to control the distribution of the errors between the true and the estimated models across the frequency range of interest. Two simulations, Cases 3(a) and 3(b), are performed with different $J(w)$ filter polynomials to demonstrate this effect.

The $J(w)$ filter polynomials are selected essentially on a trial-and-error basis. The

reason for this is that $J(w)$ weights the error between the true and the estimated models through the factor $|\ \mathrm{Pre}(\beta)\ |^2 |\ \frac{\hat{A}(\beta)}{J(\beta)}\ |^2\ \Phi_u(f)$. Prior to estimation, the polynomial $\hat{A}(w)$ (or $\hat{A}(\beta)$) is unknown, and thus the exact weighting factor is unknown. Whilst the exact factor is unknown, a general 'rule of thumb' can be used to select the initial $J(w)$ filter polynomial. Selecting a $J(w)$ filter polynomial with high-frequency roots (i.e. Case 3(b)) generally weights relatively heavily the high-frequency modeling error, and similarly, a $J(w)$ filter polynomial with low-frequency roots weights relatively heavily the low-frequency modeling error. This is due to the relative positioning of the roots of the polynomials $\hat{A}(w)$ and $J(w)$.

A variable forgetting factor, which exponentially converges towards unity is used for this study. This forgetting factor initially enhances convergence of the estimates, whilst later minimising their variation.

The conditions for the simulation study are:

Simulation Study 3, Case 3(a) and 3(b)

Simulated Input-Output Signals

Fourth-Order Continuous-Time TF:	$H(s) = \frac{0.1812s^3+0.1877s^2+19.5225s+19.5152}{s^4+0.9s^3+56.4s^2+27.6s+19.8}$
Anti-Aliasing Filters:	Fourth-order Butterworth, low-pass, $f_c = 10$ Hz
Sampling Period:	$\Delta = 0.01$ s ($f_s = 1/\Delta = 100$ Hz)
Input Signal:	PRBS; N=511, k=20

Recursive Estimation

Estimation Algorithm:	RLS-BO, 5000 iterations
Third-Order Estimated TF Form:	$\hat{H}(\beta) = \frac{\hat{b}_2\beta^2+\hat{b}_1\beta+\hat{b}_0}{\beta^3+\hat{a}_2\beta^2+\hat{a}_1\beta+\hat{a}_0}$
$J(w)$ Filter Polynomial:	Case 3(a) Even Frequency Weighting $J(w) = (w+0.5)^2(w+0.1)$ Case 3(b) High Frequency Weighting $J(w) = (w+10)^3$
Prefilter:	none
Forgetting Factor:	$\lambda_k = 0.995\lambda_{k-1} + 0.005$; $\lambda_0 = 0.97$
Initialisation:	$P_0 = 10^5 I$
	$\hat{\theta}_0 = [j_{n-1}, j_{n-2}, \ldots, j_0, 0, \ldots, 0]$

Figure 4.7 displays the magnitude of the frequency response of the estimated w-domain models after 5000 iterations. The magnitude response of the true fourth-order continuous-time TF is also displayed for comparison. Note that the coefficient

estimates are not given in this study because they offer limited insight into the success, or lack of, in estimation. This is because there is no clear relationship between the estimated coefficients and those of the fourth-order continuous-time TF. The results are best interpreted by comparing the magnitude plots of the estimated models.

From Figure 4.7, the magnitude response of the estimated model for Case 3(a), closely matches that of the continuous-time TF for frequencies up to approximately 0.3 Hz. This can be explained by observing the magnitude of the frequency weighting factor $\mid \frac{\hat{A}(\beta)}{J(\beta)} \mid^2$, shown in Figure 4.8 (Case 3(a)). With $J(w) = (w+0.5)^2(w+0.1)$, the weighting of the error between the true and the estimated models is approximately flat across the frequency range of interest. The close low-frequency match between the continuous-time and estimated models is due to the fact that the magnitude of $H(s)$ (eqn. 4.2) is larger at lower frequencies.

For Case 3(b), the filter polynomial $J(w) = (w + 10)^3$ is used. In Figure 4.8 it is seen that the frequency weighting factor $\mid \frac{\hat{A}(\beta)}{J(\beta)} \mid^2$ weights more heavily the high-frequency modeling error, relative to the low-frequency error. This weighting is reflected in the results of estimation shown in Figure 4.7, in which it is observed that the magnitude response of the estimated model approximately matches that of the continuous-time TF for frequencies greater than 0.3 Hz.

Thus, by varying the selection of the $J(w)$ filter polynomial, a w-domain model can be estimated which approximates the continuous-time TF over either the high- or low-frequency range.

Effects of the Prefilter on Estimation

The main effect of the prefilter is to attenuate both noise and unmodeled system dynamics outside the frequency range of interest. In a practical estimation task, prefiltering is an advisable step [12,65].

The first two simulation studies of this section demonstrate how the $J(w)$ filter polynomial can be employed, in the presence of unmodeled dynamics, to vary the distribution of the modeling errors across the frequency spectrum. In this simulation study, prefiltering is included to focus the RLS-BO estimation algorithm on a specific frequency range of interest, and thus improve the model match between the true and

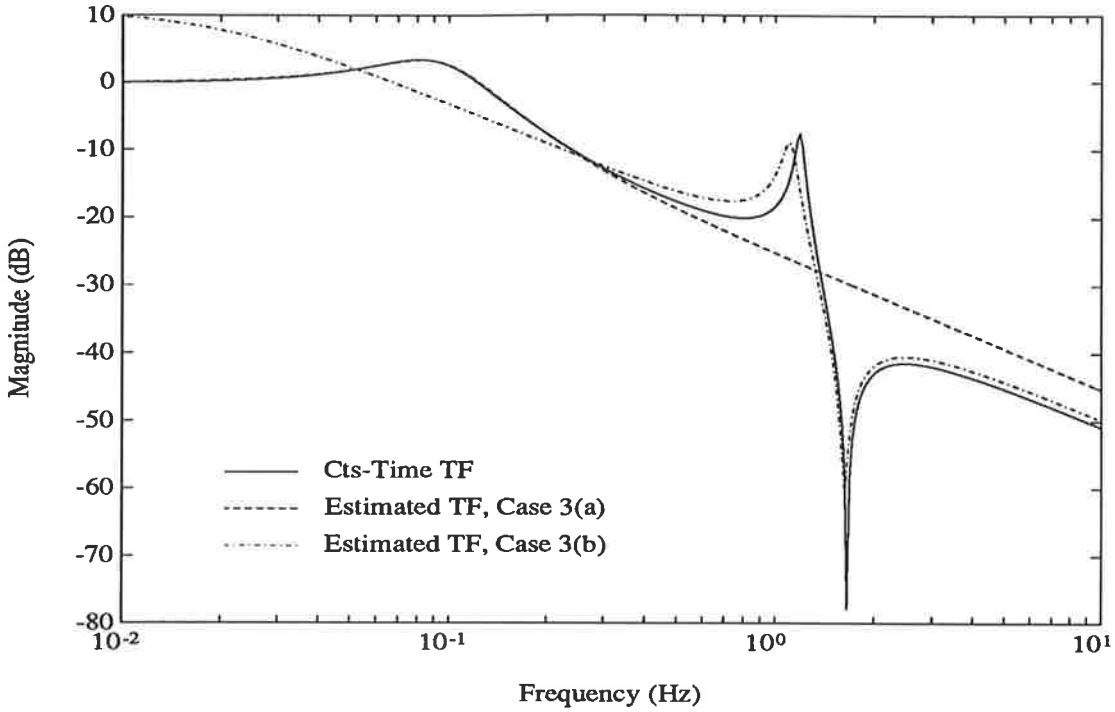

Figure 4.7: Magnitude response of the RLS-BO estimated w-domain models, Simulation Study 3, Cases 3(a) and 3(b).

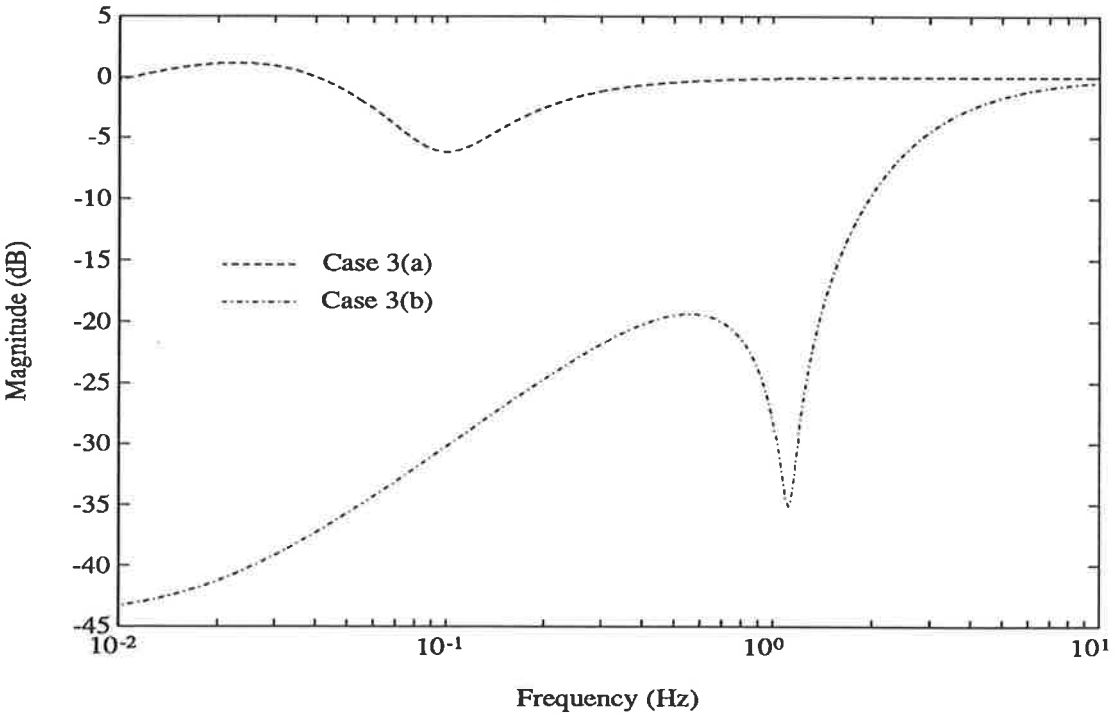

Figure 4.8: The frequency weighting factor $\mid \frac{\hat{A}(\beta)}{J(\beta)} \mid^2$, Simulation Study 3, Cases 3(a) and 3(b).

the estimated models over this frequency range.

The $J(w)$ filter polynomial used for Case 3(b), namely $J(w) = (w + 10)^3$, which weights the error between the true and the estimated models heavily in the high-frequency region (relative to the low-frequency region), is used for this simulation study. The prefilter is used to help improve the match between the true and the estimated models in the region of the high-frequency complex poles and zeros. Thus a bandpass filter, with a pass-band from 0.3 Hz to 4 Hz is used to prefilter both the input and output signals prior to estimation.

The simulation conditions are:

Simulation Study 3, Case 3(c)

Simulated Input-Output Signals

Same as for Simulation Study 3

Recursive Estimation

Same as for Simulation Study 3

$J(w)$ Filter Polynomial:	Case 3(c) $J(w) = (w + 10)^3$
Prefilter:	Fourth-order Butterworth, low-pass, $f_c = 4$ Hz.
	Fourth-order Butterworth, high-pass, $f_c = 0.3$ Hz.

Figure 4.9 displays both the magnitude response of the prefilter $\mid \mathrm{Pre}(\beta) \mid^2$, to graphically display the frequency range of interest, and the magnitude response of the frequency weighting factor $\mid \frac{\hat{A}(\beta)}{J(\beta)} \mid^2$. These responses reinforce the fact that the RLS-BO estimation algorithm attempts to match the estimated model to the continuous-time model across the range of frequencies 0.3 Hz to 4 Hz, with more weight given to the high-frequency modeling error.

Figure 4.10 displays the magnitude response of the estimated w-domain model, along with that of the true continuous-time TF. It is clear that across the range of approximately 0.3 Hz to >4 Hz the two responses match closely. Comparing this plot with that of Figure 4.7, it is clear that the prefiltering enables the estimated model to more closely match the true continuous-time TF, over the range specified by the prefilter. Because of the high-pass section of the prefilter, very little weight is given to the error between the true and estimated models below approximately 0.3 Hz. It is thus difficult to predict how the modeling error below this frequency will be distributed.

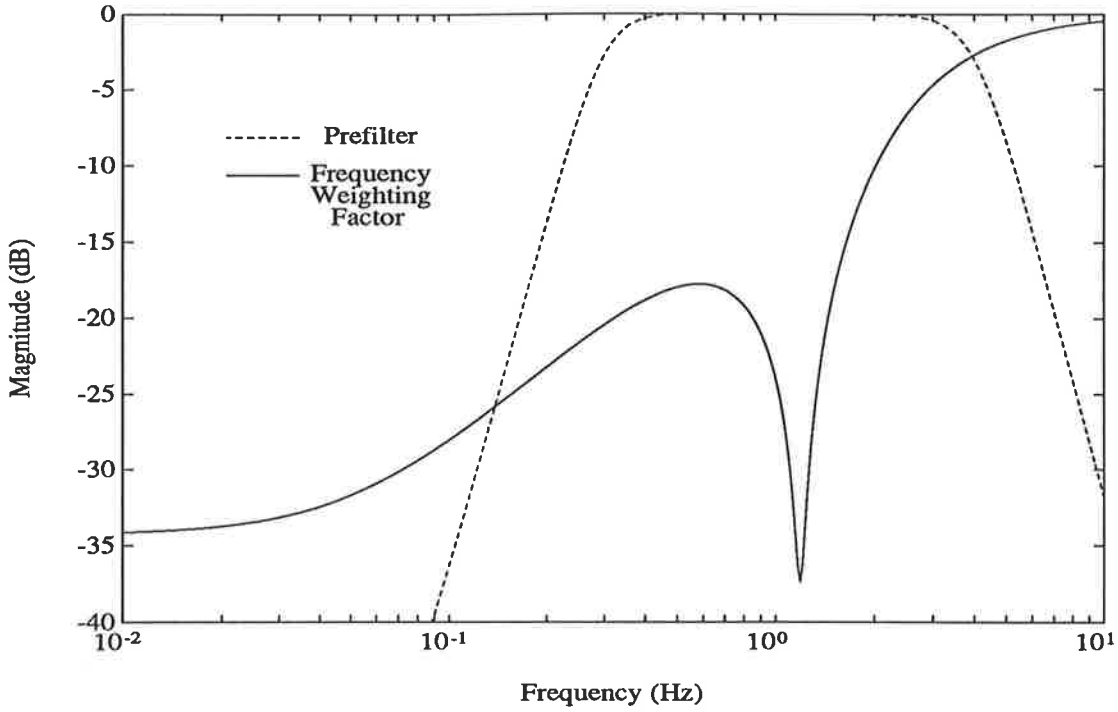

Figure 4.9: The frequency weighting factor $\mid \frac{\hat{A}(\beta)}{J(\beta)} \mid^2$ and prefilter factor $\mid \mathrm{Pre}(\beta) \mid^2$, Simulation Study 3, Case 3(c).

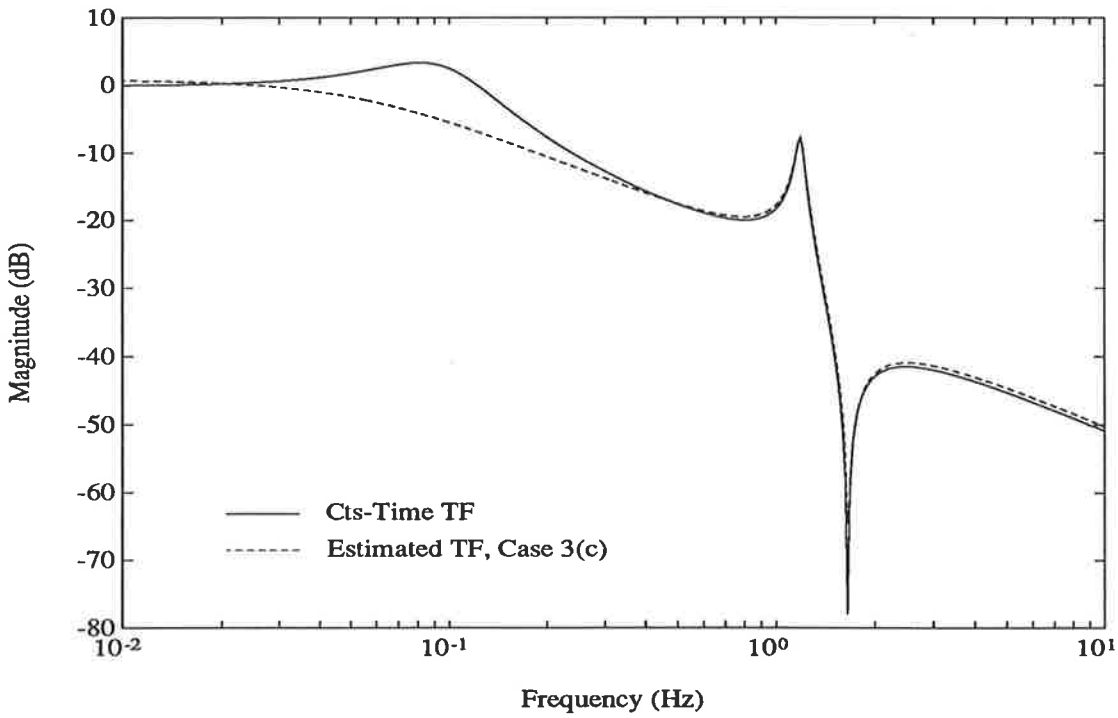

Figure 4.10: Magnitude response of the RLS-BO estimated w-domain model, Simulation Study 3, Case 3(c).

4.5 Recursive Estimation: White Additive Output Noise

In the previous section, the effects of both the prefilter and $J(w)$ filter polynomial on estimation are examined for the case in which unmodeled dynamics are present in the simulated system output. In this section, the effects of noise on estimation are considered. Specifically, relatively low-level, white additive noise is included in the simulated output signal for use in estimation.

Figure 4.11 shows the continuous-time TF $H(s)$ with additive white output noise $\eta(t)$. From this figure it is clear that the noise present in the measured output signal

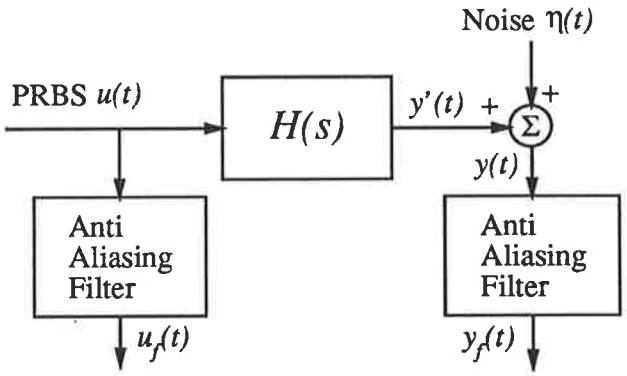

Figure 4.11: Simulated continuous-time TF with additive output noise $\eta(t)$.

$y_f(t)$ appears as band-limited white noise, due to the filtering performed by the anti-aliasing filters.

4.5.1 Simulation Study 4

Using the configuration of Figure 4.11, white noise is added to the simulated output signal prior to anti-alias filtering. The level of noise is such that the signal-to-noise ratio [2] (SNR) of the filtered output signal $y_f(t)$ is 10. Using this noise-contaminated output, three different $J(w)$ filter polynomials are tested in RLS-BO estimation.

[2]The signal-to-noise ratio is defined as SNR=$\sum_{k=1}^{N} s_k^2 / \sum_{j=1}^{N} n_j^2$ where $\{s_k\}, \{n_j\}$ are the sampled signal and noise sequences respectively.

The polynomials selected are, for Case 4(a), $J(w) = (w^4 + 15.7w^3 + 122.9w^2 + 564.4w + 1296)$, which is the denominator of a fourth-order, Butterworth, low-pass filter with w_c=6 rad/s. This selection is based on the recommendations in [31], which states the filter should be chosen as a standard low-pass filter, with a bandwidth approximately matching that of the continuous-time TF. It is difficult to use the –3 dB point of this continuous-time TF (eqn. 4.2) to define the system bandwidth, because the higher-frequency complex poles and zeros lie outside this frequency range. As a compromise between using the –3 dB bandwidth and including the higher-frequency TF dynamics, the cut-off frequency of $\omega_c = 6$ rad/s (≈ 1 Hz) is selected for the filter.

For Case 4(b), the $J(w)$ filter polynomial is selected as $J(w) = (w + 0.5)^2(w + 7.5)^2$, which approximately matches the denominator of the continuous-time TF (see Simulation Study 2).

For Case 4(c), the $J(w)$ filter polynomial is selected to equal the denominator of the continuous-time TF, namely $J(w) = A(w)$.

A forgetting factor that is switched between values is used for these studies. The initial value is low ($\lambda = 0.98$), to allow rapid initial convergence of the estimates, and is eventually switched to the value $\lambda = 0.9999$ after 2000 iterations.

The conditions for this simulation study are:

Simulation Study 4

Simulated Input-Output Signals

Continuous-Time TF:	$H(s) = \frac{0.1812s^3+0.1877s^2+19.5225s+19.5152}{s^4+0.9s^3+56.4s^2+27.6s+19.8}$
Anti-Aliasing Filters:	Fourth-order Butterworth, low-pass, $f_c = 10$ Hz
Sampling Period:	$\Delta = 0.01$ s ($f_s = 1/\Delta = 100$ Hz)
Input Signal:	PRBS; N=511, k=20
Output Noise:	White; SNR of $y_f(t) = 10$

Recursive Estimation

Estimation Algorithm:	RLS-BO, 15000 iterations
Estimated TF Form:	$\hat{H}(\beta) = \frac{\hat{b}_3\beta^3+\hat{b}_2\beta^2+\hat{b}_1\beta+\hat{b}_0}{\beta^4+\hat{a}_3\beta^3+\hat{a}_2\beta^2+\hat{a}_1\beta+\hat{a}_0}$
$J(w)$ Filter Polynomial:	Case 4(a) $J(w) = (w^4 + 15.7w^3 + 122.9w^2 + 564.4w + 1296)$
	Case 4(b) $J(w) = (w + 0.5)^2(w + 7.5)^2$
	Case 4(c) $J(w) = A(w)$
Prefilter:	none
Forgetting Factor:	Switched, $\lambda_0 = 0.98, \lambda_1 = 0.998, \lambda_2 = 0.9999$, switched at iterations 500 and 2000
Initialisation:	$P_0 = 10^5 I$
	$\hat{\theta}_0 = [j_{n-1}, j_{n-2}, \ldots, j_0, 0, \ldots, 0]$

The coefficient estimates during estimation are displayed in Figures 4.12 to 4.14. From these figures it is clear that the selection $J(w) = A(w)$ (Case 4(c)) provides the most rapid convergence for the coefficient estimates, as well as significantly reducing the estimate variation. Selecting $J(w)$ to equal the denominator of a Butterworth filter produces the noisiest estimates with the slowest convergence.

Table 4.4 gives the coefficient estimates after 15000 iterations for the three $J(w)$ filter polynomials considered. From this table it is clear the coefficient estimates for Case 4(a) are in error by a significant amount. For both Cases 4(b) and 4(c), the majority of the coefficient estimates closely approximate those of the continuous-time TF; in Case 4(b), the coefficient a_3 shows significant error, whilst in Case 4(c), the coefficients b_3 and b_2 are in error. The coefficients a_3 and b_2 primarily determine the damping of the complex poles and zeros of the TF; the coefficient b_3 effects the corner frequency of the complex zeros. Whilst the error in these coefficient estimates (a_3, b_3, b_2) may be significant, the effect on the estimated model frequency response is only small. This is clearly observed in the Bode plots of these estimated models, given in Figure 4.15. For Cases 4(b) and 4(c) the true and estimated model Bode plots agree almost exactly, up to approximately 1 Hz. Above this frequency, the error

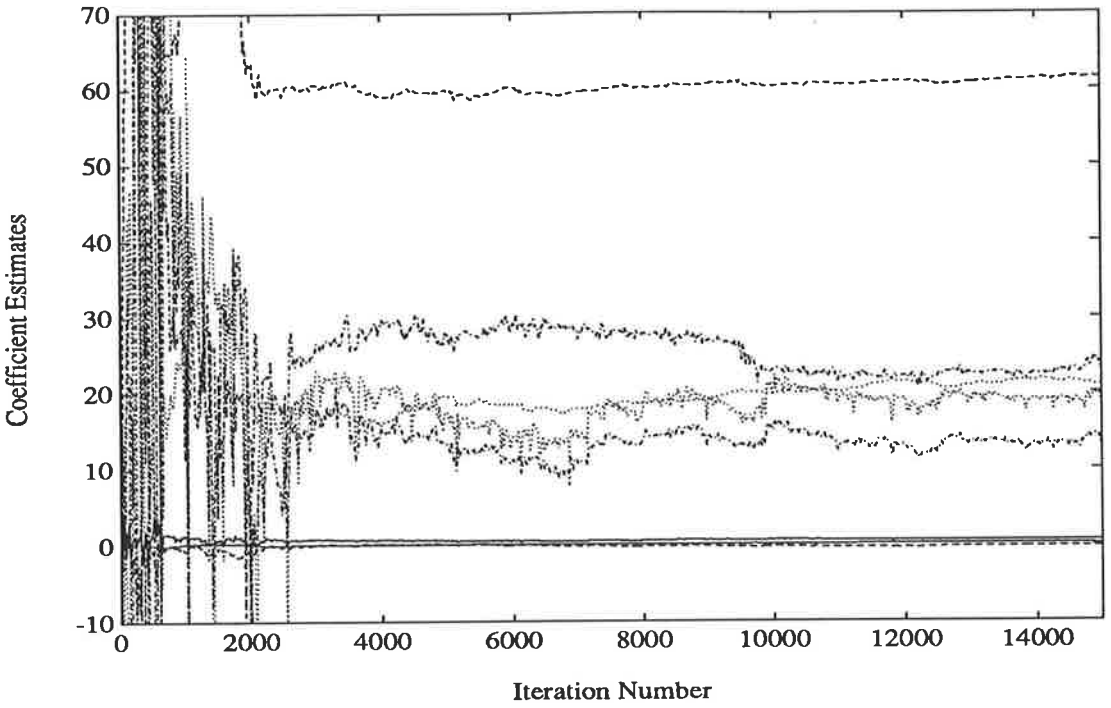

Figure 4.12: RLS-BO coefficient estimates, Simulation Study 4, Case 4(a), $J(w) =$ Butterworth.

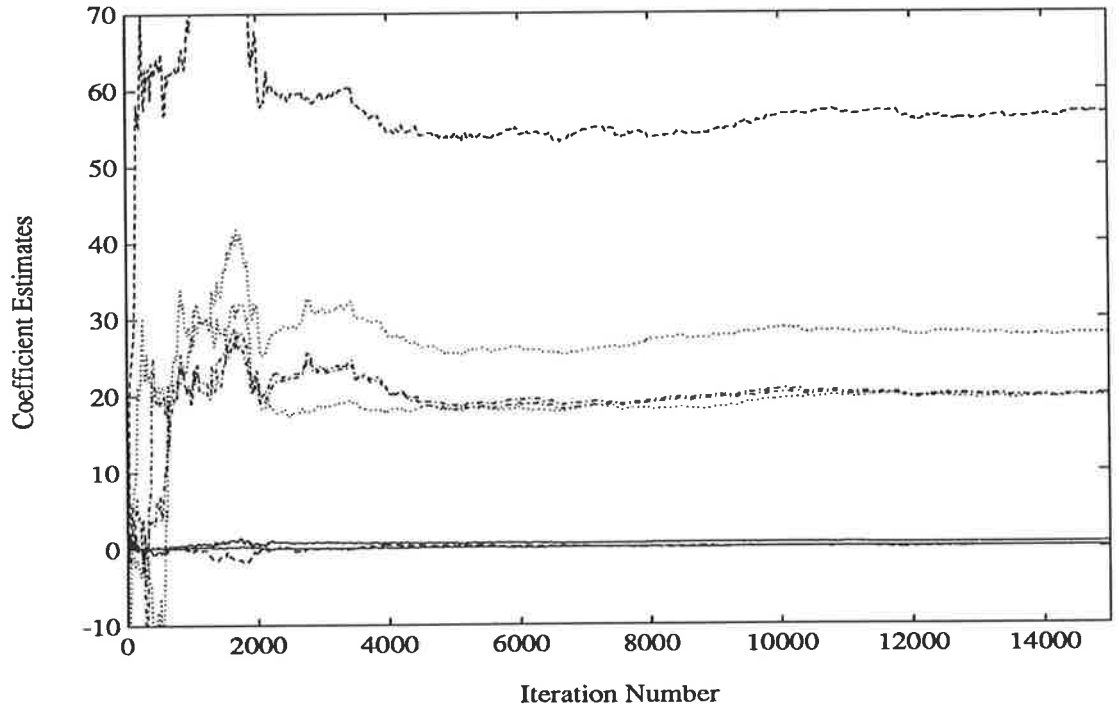

Figure 4.13: RLS-BO coefficient estimates, Simulation Study 4, Case 4(b), $J(w) \approx A(w)$.

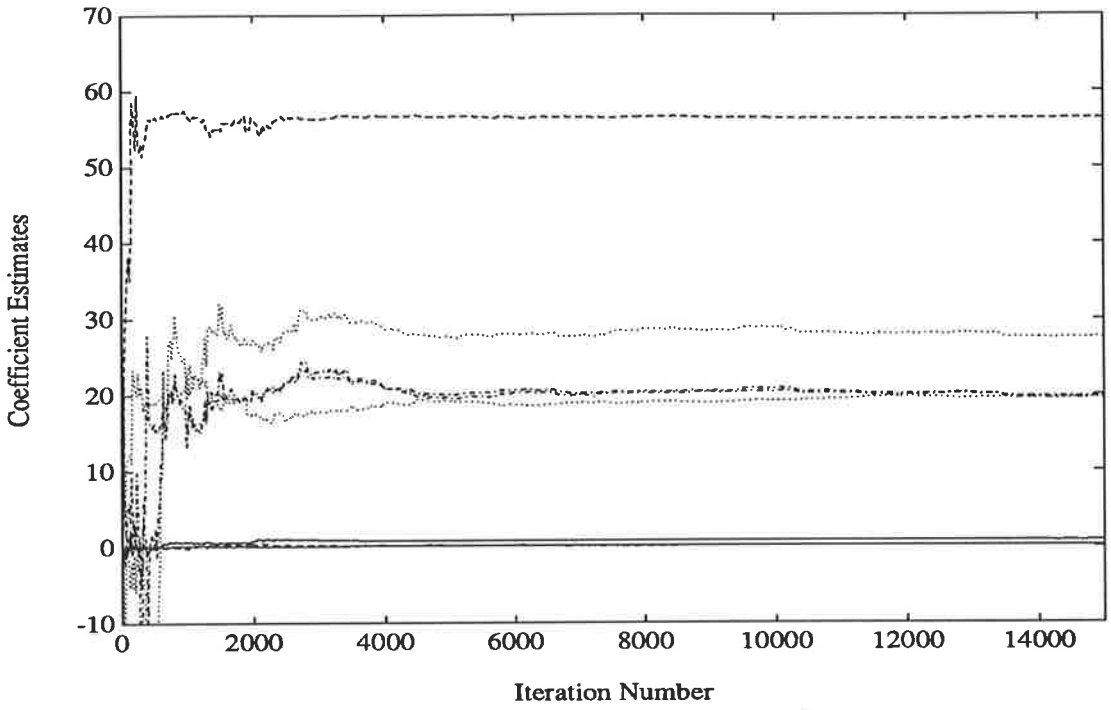

Figure 4.14: RLS-BO coefficient estimates, Simulation Study 4, Case 4(c), $J(w) = A(w)$.

	Cts-Time TF Coeffs.	Case 4(a) Estimates		Case 4(b) Estimates		Case 4(c) Estimates	
a_3	0.9	0.6514	(28)	0.7503	(17)	0.8473	(6)
a_2	56.4	61.5503	(9)	56.9670	(1)	56.4252	($\approx$0)
a_1	27.6	19.5099	(29)	27.9232	(1)	27.6321	(0.1)
a_0	19.8	23.9328	(21)	19.9348	(1)	19.8446	(0.2)
b_3	0.1812	0.1601	(12)	0.1697	(6)	0.1952	(8)
b_2	0.1877	-0.2230	(218)	0.1810	(4)	0.2163	(15)
b_1	19.5225	20.8916	(7)	19.8066	(1)	19.5182	($\approx$0)
b_0	19.5152	13.8064	(29)	19.9064	(2)	19.7099	(1)
$J(w)$ Polynomial		Butterworth		$\approx A(w)$		$= A(w)$	
Prefilter		None		None		None	
Estimation Alg.		RLS-BO		RLS-BO		RLS-BO	

Table 4.4: RLS-BO estimated coefficients, white additive output noise, Simulation Study 4. The bracketed numbers indicate the percentage difference between the continuous-time and estimated coefficients.

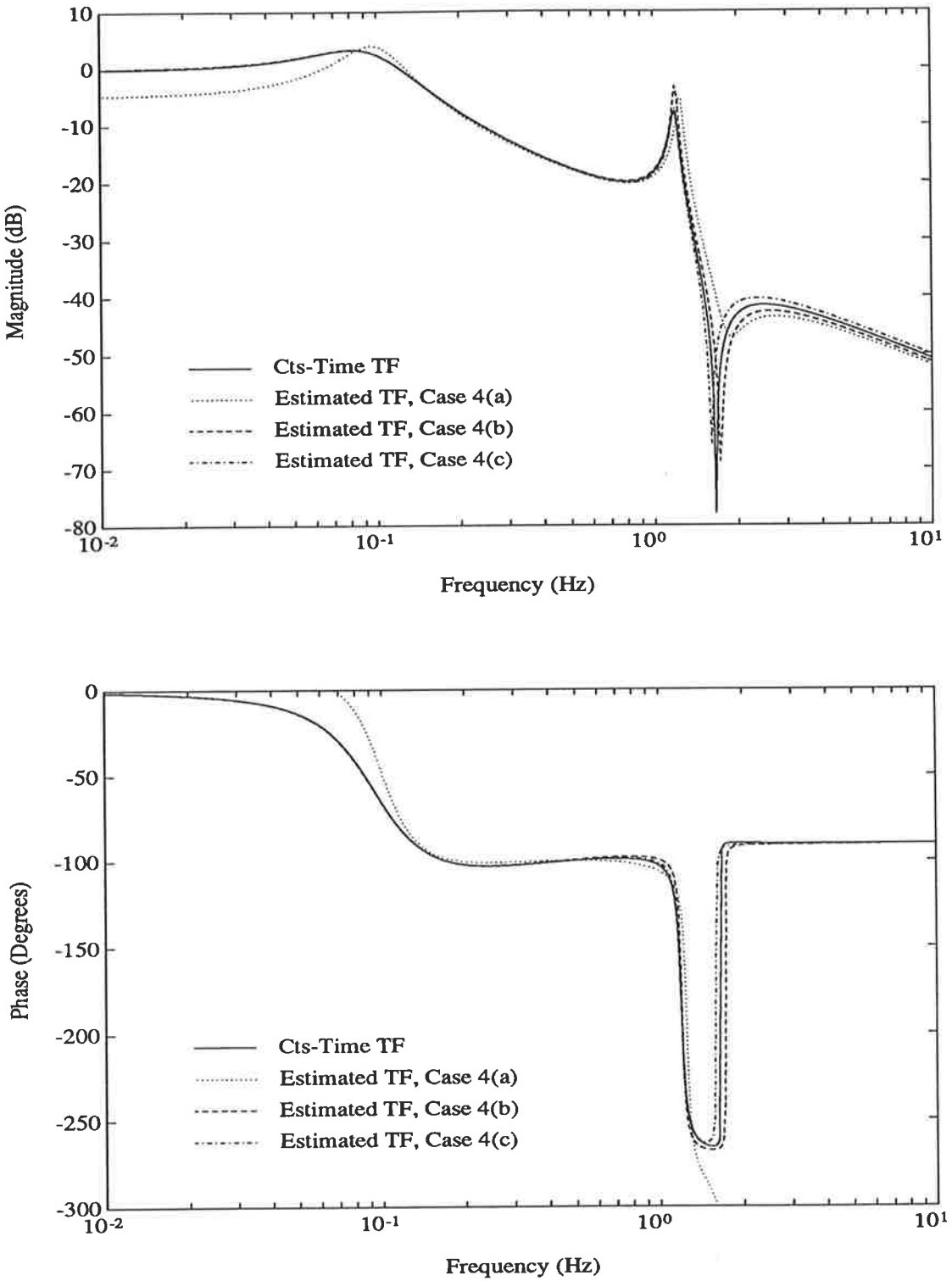

Figure 4.15: Bode plots of the RLS-BO estimated w-domain models, Simulation Study 4, Cases 4(a), 4(b) and 4(c).

appears mostly in the damping of the complex poles and the location of the corner frequency of the complex zeros of the estimated models. The Bode plot of the model estimate for Case 4(a) is significantly in error for both low and high frequencies.

These estimation results are consistent with the selected $J(w)$ filter polynomials for the following reasons:

- For Case 4(c), the $J(w)$ filter polynomial is set equal to the denominator of the continuous-time TF, namely $J(w) = A(w)$. As discussed in section 3.2.1, the filter $A(w)/J(w)$ thus does not colour the additive white output noise, and ensures the bias in the coefficient estimates is minimised.

- For Case 4(b), the filter polynomial $J(w)$ is selected to approximately match the denominator of the continuous-time TF. Thus the colouration effect of the filter $A(w)/J(w)$ on the additive white noise is small, and hence again the estimate bias is small.

- For Case 4(a), the filter polynomial $J(w)$ is selected as the denominator of a low-pass Butterworth filter. As such, $J(w)$ and $A(w)$ are significantly different, and the filter $A(w)/J(w)$ colours the additive noise. This results in relatively poor (biased) coefficient estimates.

Prefiltering

So far in this simulation study, prefiltering (apart from the anti-alias filtering) of the input and output signals has not been considered. For the case of RLS-BO estimation with white additive output noise, the prefiltering of the signals may have a detrimental effect on estimation. To explain this, consider RLS-BO estimation applied to a continuous-time TF with purely white, additive output noise. As discussed in section 3.2.1, providing the $J(w)$ filter polynomial is chosen equal to, or approximately equal to $A(w)$, the colouration effect of the filter $A(w)/J(w)$ is small, and hence the bias on the coefficient estimates is minimal. If, however, the measured signals are prefiltered prior to estimation, the additive white noise becomes coloured, and thus, even if $J(w)$ is chosen to equal $A(w)$, the additive coloured noise will produce some bias in the estimates.

On the other hand, prefiltering also reduces both unmodeled dynamics and system noise outside the frequency range of interest, thus 'focusing' the estimator and improving the SNR resulting in improved coefficient estimates. Thus the prefilter may have both a beneficial and adverse effect on RLS-BO estimation.

For completeness, Table 4.5 lists the coefficient estimates for Cases 4(a), 4(b) and 4(c) of Simulation Study 4, when the input and output signals are prefiltered by the band-pass filter

$$\begin{aligned} \text{Prefilter:} \quad & \text{Fourth-order Butterworth, low-pass, } f_c = 4 \text{ Hz} \\ & \text{Second-order Butterworth, high-pass, } f_c = 0.02 \text{ Hz} \end{aligned}$$

The pass-band of this filter is selected to allow signals across the frequency range from at least 0.08 Hz to 1.65 Hz (the range of corner frequencies of the poles and zeros of the continuous-time TF) to remain unattenuated, whilst attenuating any noise or signals significantly outside this range.

	Cts-Time TF Coeffs.	Case 4(a) Estimates		Case 4(b) Estimates		Case 4(c) Estimates	
a_3	0.9	0.6633	(26)	0.7652	(15)	0.8442	(6)
a_2	56.4	59.2942	(5)	52.3235	(7)	56.4010	(≈0)
a_1	27.6	19.4917	(29)	25.6469	(7)	27.5722	(0.1)
a_0	19.8	23.0089	(16)	18.4180	(7)	19.8305	(0.2)
b_3	0.1812	0.1582	(13)	0.1693	(7)	0.1951	(8)
b_2	0.1877	−0.1055	(156)	0.2929	(56)	0.2213	(18)
b_1	19.5225	19.8549	(2)	18.0232	(8)	19.4793	(0.2)
b_0	19.5152	13.6807	(30)	18.3841	(6)	19.6539	(0.7)
$J(w)$ Polynomial		Butterworth		$\approx A(w)$		$= A(w)$	
Prefilter		Band-pass		Band-pass		Band-pass	
Estimation Alg.		RLS-BO		RLS-BO		RLS-BO	

Table 4.5: RLS-BO estimated coefficients, white additive output noise, Simulation Study 4. The input and output signals are prefiltered. The bracketed numbers indicate the percentage difference between the continuous-time and estimated coefficients.

A comparison of Tables 4.4 and 4.5 reveals that for Case 4(a), the prefiltering of the input and output signals has very little effect on the coefficient estimates. This is because the additive noise is already coloured by the mis-match between the filter polynomial $J(w)$ and the equivalent continuous-time model denominator $A(w)$. For

Case 4(b), the prefiltering has a detrimental effect on the coefficient estimates. For this case, the $J(w)$ polynomial only approximately equals $A(w)$. The small colouration effect of $A(w)/J(w)$, in conjunction with the colouration due to prefiltering, degrades the coefficient estimates. For Case 4(c), the prefiltering appears to have no significant effect on the coefficient estimates, despite the colouration of the additive noise due to prefiltering.

Thus in general, for RLS-BO estimation with white additive output noise, unless the filter polynomial $J(w)$ is selected to very closely match the denominator of the continuous-time TF (Case 4(c)), prefiltering of the input and output signals may have a detrimental effect on estimation.

4.5.2 Simulation Study 5

The signal-to-noise ratio of the white additive output noise considered in Simulation Study 4 is relatively high, with the SNR=10. Under these conditions, the RLS-BO estimation algorithm provides a reasonably accurate estimate of the coefficients of the continuous-time TF (see Table 4.4 and Figure 4.15).

As will be shown, the RLS-BO estimation algorithm can also estimate reasonably accurately the coefficients of the continuous-time TF for lower signal-to-noise ratios. To demonstrate this, Simulation Study 4 is re-run with a SNR of 2. Only Case 4(b) is considered, with the $J(w)$ filter polynomial selection $J(w) = (w+0.5)^2(w+7.5)^2$. The input and output signals are not prefiltered prior to estimation. To allow comparison later in this study, the RIV-BO estimation algorithm is also used to estimate the TF coefficients using the simulated input-output signals.

Table 4.6 displays the estimated coefficients after 15000 iterations for both the RLS-BO and RIV-BO estimation algorithms. Considering the high-level of noise present in the simulated output signal, the majority of the estimated coefficients from both estimation algorithms approximate reasonably accurately those of the continuous-time TF.

Considering each algorithm in turn:

- There is a large variation in the errors of the RLS-BO coefficient estimates. Whilst some coefficients approximate closely those of the continuous-time TF

	Cts-Time TF Coeffs.	RLS-BO Estimates		RIV-BO Estimates	
a_3	0.9	0.5675	(37)	0.8725	(3)
a_2	56.4	58.1344	(3)	55.8218	(1)
a_1	27.6	27.6340	(0.1)	27.8157	(0.8)
a_0	19.8	19.4699	(2)	19.6400	(0.8)
b_3	0.1812	0.1602	(12)	0.1471	(19)
b_2	0.1877	0.0561	(70)	0.2921	(56)
b_1	19.5225	20.6595	(6)	19.4400	(0.4)
b_0	19.5152	19.5729	(0.3)	19.9685	(2)
$J(w)$ Polynomial		$\approx A(w)$		$\approx A(w)$	
Prefilter		None		None	
Estimation Alg.		RLS-BO		RIV-BO	

Table 4.6: RLS-BO and RIV-BO estimated coefficients, high-level white additive output noise. Simulation Study 5. The bracketed numbers indicate the percentage difference between the continuous-time and estimated coefficients.

(i.e. a_2, a_1, a_0, b_0), there are some coefficients that are significantly in error. In particular, the estimated coefficients a_3, b_3 and b_2 are less than those of the continuous-time TF. The coefficients a_3 and b_2 predominantly effect the damping of the high-frequency complex poles and zeros of the TF. Underestimating their value generally results in the magnitude of the damping constants [3] of the complex poles and zeros being underestimated. Figure 4.16 displays the Bode plot of the RLS-BO estimated model, together with the Bode plot of the true continuous-time TF and the RIV-BO estimated model. From this figure it is clear that the majority of the error between the true and RLS-BO estimated models occurs around the corners of the high-frequency complex poles/zeros. The underestimated magnitude of the damping constant of the complex poles is clear from the overestimated peak at approximately 1.2 Hz in the magnitude plot. From the phase plot, the estimated model is in error by 360° at frequencies above the complex zeros. This is due to the incorrect sign of the damping constant of the estimated model complex zeros.

- The majority of the RIV-BO coefficient estimates closely approximate those of the continuous-time TF. The main error in coefficients occurs for both b_3 and

[3] The damping constant is defined as the real part, $-\alpha$, of the complex roots, $-\alpha \pm j\beta$.

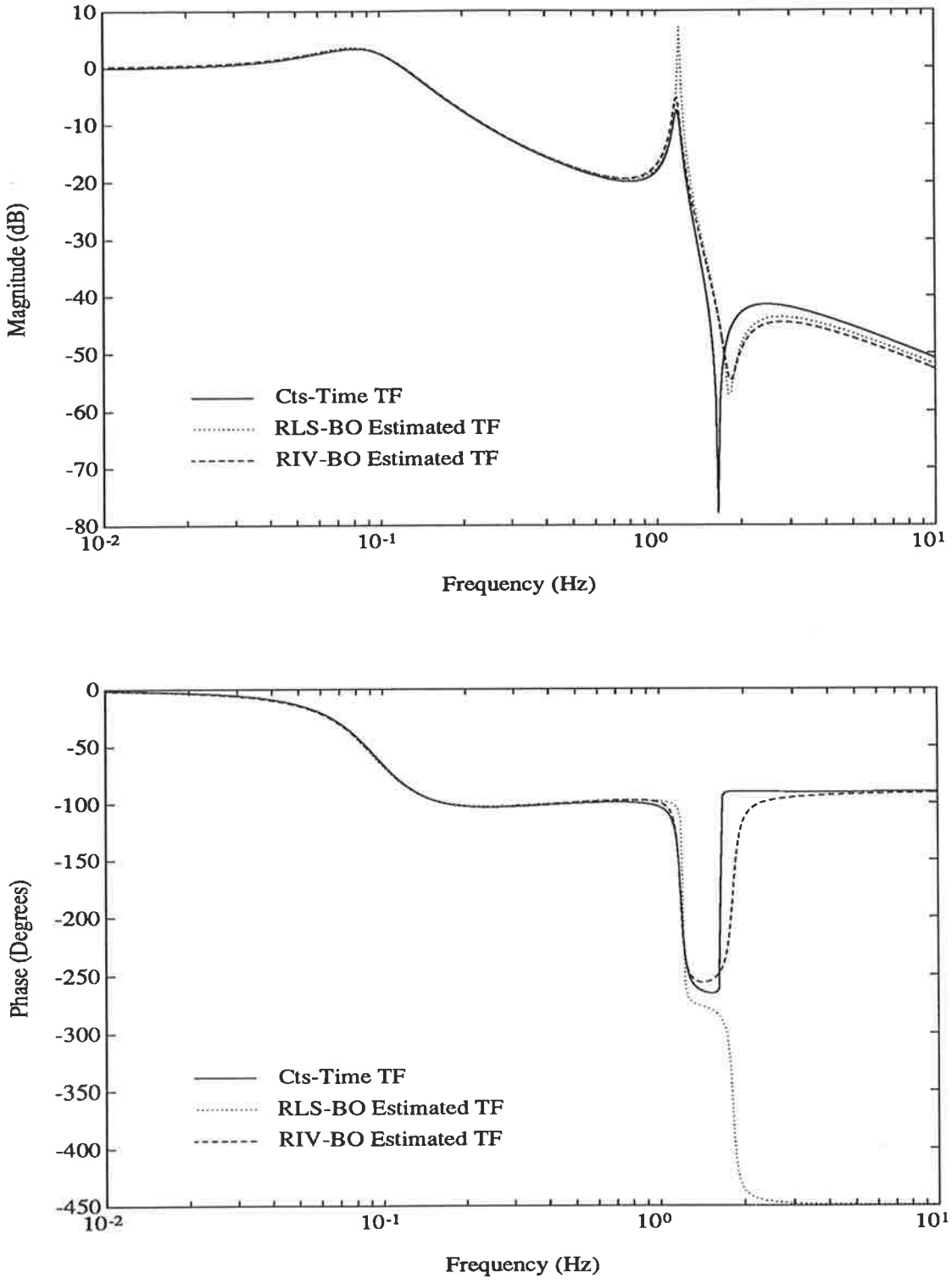

Figure 4.16: Bode plot of the RLS-BO and RIV-BO estimated w-domain models, high-level white additive output noise. Simulation Study 5.

b_2. Figure 4.16 displays the Bode plot of this estimated model, showing the majority of the error again occurs around the high-frequency poles/zeros. A better estimate of the damping of the complex poles is obtained, relative to RLS-BO estimation. The high-frequency phase is also correct. The sign of the damping constant of the estimated TF complex zeros is now correct, however the magnitude of the damping constant is overestimated.

Thus overall, both the RLS-BO and RIV-BO estimation algorithms provide reasonable estimates of the continuous-time TF coefficients in the presence of high-level white additive output noise. The RIV-BO coefficient estimates show an improvement over those of the RLS-BO estimation algorithm, as seen in the correctly estimated high-frequency phase, and the improved estimate of the damping of the high-frequency complex poles. For both algorithms, the majority of the modeling errors occur around the high-frequency poles/zeros, which is not surprising, considering that in this high-frequency range, the output signal of the continuous-time system is attenuated by up to 40 dB, compared to its magnitude at lower frequencies.

4.6 Recursive Estimation: Coloured Additive Output Noise

So far, the effects on estimation of unmodeled dynamics and white additive output noise have been examined. In this section, the effects of coloured noise on both RLS-BO and RIV-BO estimation are examined.

It is common to consider coloured noise as filtered white noise [10]. In these simulation studies the noise signal used is given by

$$\eta(t) = H_\eta(s)e(t) \tag{4.3}$$

where $e(t)$ is white noise, and the filter TF $H_\eta(s)$ is given by

$$H_\eta(s) = \frac{1}{s+1}$$

The noise is low-pass filtered white noise. This is representative of the noise encountered in the practical online estimation task considered later in chapter 6. The signal-to-noise ratio used for these simulations is the same as that used for the white noise simulations, namely SNR=10.

4.6.1 Simulation Study 6

Simulation Study 6 compares both the RLS-BO and RIV-BO estimation algorithms with coloured additive output noise, without prefiltering of the input and output signals.

Only two $J(w)$ filter polynomials are considered with the RLS-BO estimation algorithm, namely $J(w) = A(w)$ and $J(w) = (w + 0.5)^2(w + 7.5)^2$. These are the filter polynomials which perform best in all previous noise simulations.

For the RIV-BO estimation algorithm, four different $J(w)$ filter polynomials are examined. For Case 6(c), the $J(w)$ filter polynomial is selected as the denominator of a fourth-order, Butterworth, low-pass filter (ω_c=6 rad/s), as selected for Case 4(a) of Simulation Study 4. For Case 6(d), the $J(w)$ filter is selected to approximately match the continuous-time TF denominator, namely $J(w) = (w+0.5)^2(w+7.5)^2$. For Case 6(e), the filter polynomial is selected to equal the continuous-time TF denominator. Finally, for Case 6(f), the filter polynomial selected is similar to that employed for Case 6(d). As will be shown later in this study, this filter polynomial has the advantage that it boosts the relative weight given to the errors between the true and the estimated models in the frequency region of the model complex zeros.

A switched forgetting factor is used for estimation.

The simulation conditions are:

Simulation Study 6

Simulated Input-Output Signals

Continuous-Time TF:	$H(s) = \frac{0.1812s^3+0.1877s^2+19.5225s+19.5152}{s^4+0.9s^3+56.4s^2+27.6s+19.8}$
Anti-Aliasing Filters:	Fourth-order Butterworth, low-pass, $f_c = 10$ Hz
Sampling Period:	$\Delta = 0.01$ s ($f_s = 1/\Delta = 100$ Hz)
Input Signal:	PRBS; N=511, k=20
Output Noise:	Coloured; SNR of $y_f(t) = 10$
	$H_\eta(s) = \frac{1}{s+1}$

Recursive Estimation

Estimation Algorithm:	Case 6(a) and 6(b), RLS-BO, 30000 iterations
	Case 6(c),6(d),6(e) and 6(f), RIV-BO, 30000 iterations
Estimated TF Form:	$\hat{H}(\beta) = \frac{\hat{b}_3\beta^3+\hat{b}_2\beta^2+\hat{b}_1\beta+\hat{b}_0}{\beta^4+\hat{a}_3\beta^3+\hat{a}_2\beta^2+\hat{a}_1\beta+\hat{a}_0}$
$J(w)$ Filter Polynomial:	Case 6(a) $J(w) = A(w)$
	Case 6(b) $J(w) = (w+0.5)^2(w+7.5)^2$
	Case 6(c) $J(w) = (w^4 + 15.7w^3 + 122.9w^2 + 564.4w + 1296)$
	Case 6(d) $J(w) = (w+0.5)^2(w+7.5)^2$
	Case 6(e) $J(w) = A(w)$
	Case 6(f) $J(w) = (w+0.5)^2(w+1+j10.4)(w+1-j10.4)$
Prefilter:	none
Forgetting Factor:	Switched, $\lambda_0 = 0.98, \lambda_1 = 0.998, \lambda_2 = 0.9999$, switched at iterations 500 and 2000
Initialisation:	$P_0 = 10^5 I$
	$\hat{\theta}_0 = [j_{n-1}, j_{n-2}, \ldots, j_0, 0, \ldots, 0]$

Table 4.7 displays the RLS-BO coefficient estimates (Cases 6(a) and 6(b)) after 30000 iterations. Considering each simulation in turn:

- Case 6(a). Most of the estimated coefficients differ significantly from those of the continuous-time TF. From section 3.2.1, there is expected to be some bias present in the coefficient estimates, because the additive output noise is coloured.

  Whilst the coefficient estimates contain significant errors, the resulting Bode plot of the estimated model compares favourably with that of the continuous-time TF. The magnitude responses are displayed in Figure 4.17 (Case 6(a)). This highlights one difficulty with using the errors in coefficient estimates as the sole judge of the success of estimation. Depending on the application of the estimated model, the Bode plot may provide a more suitable measure of the success of estimation.

	Cts-Time TF Coeffs.	Case 6(a) Estimates		Case 6(b) Estimates	
a_3	0.9	0.7978	(11)	0.7957	(12)
a_2	56.4	55.4296	(2)	19.2359	(66)
a_1	27.6	21.1001	(24)	7.0597	(74)
a_0	19.8	16.8927	(15)	5.8350	(71)
b_3	0.1812	0.2103	(16)	0.1512	(17)
b_2	0.1877	0.3131	(67)	0.9164	(388)
b_1	19.5225	21.1604	(8)	6.6171	(66)
b_0	19.5152	15.4488	(21)	5.5450	(72)
$J(w)$ Polynomial		$= A(w)$		$\approx A(w)$	
Prefilter		None		None	
Estimation Alg.		RLS-BO		RLS-BO	

Table 4.7: RLS-BO estimated coefficients, coloured additive output noise, Simulation Study 6. The bracketed numbers indicate the percentage difference between the continuous-time and estimated coefficients.

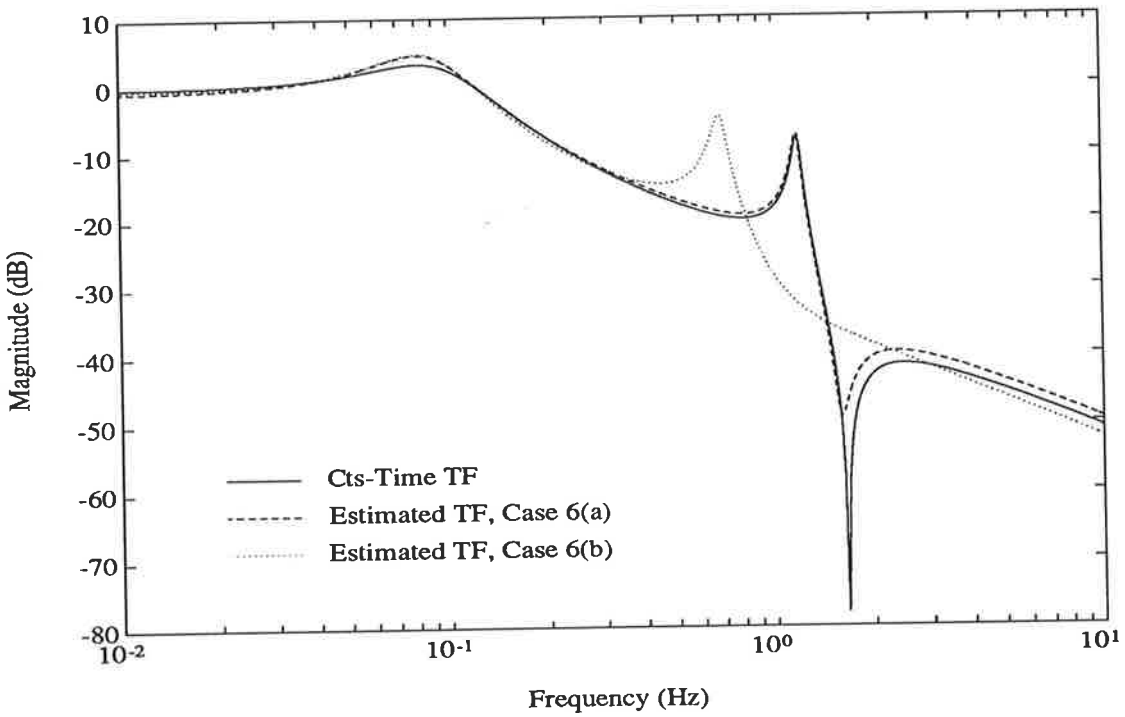

Figure 4.17: Bode plots of the RLS-BO estimated w-domain models, Simulation Study 6, Cases 6(a) and 6(b).

For all estimation studies conducted, it is found that the errors in coefficient estimates are correlated between coefficients, and thus the errors in the estimated model poles and zeros (or gain) may not be as large as implied by the separate coefficient errors [73]. For example, for Case 6(a), the errors in the estimated coefficients a_0 and b_0 are 15% and 21% respectively, however, the error in the dc gain (b_0/a_0) of the estimated TF model is only approximately 7%. Thus for Case 6(a), whilst the coefficient errors appear large, the estimated model Bode plot still provides a reasonable approximation to that of the continuous-time TF.

- Case 6(b). For this simulation, the estimated coefficients are significantly different to those of the continuous-time TF. All coefficients, except possibly a_3 and b_3 are in error. The magnitude response of this estimated model is also displayed in Figure 4.17. The response is clearly in error in the region of the high-frequency complex poles and zeros of the continuous-time TF.

Thus from these results it appears that for coloured additive output noise, the RLS-BO coefficient estimates may be in error by a significant amount. If the $J(w)$ filter polynomial is selected to *very* closely match the denominator of the continuous-time TF, the Bode plot of the estimated model may satisfactorily approximate that of the continuous-time TF, even though the estimated coefficient error may be large. Note that in estimation of a practical system it is impossible to select $J(w) = A(w)$, because the polynomial $A(w)$ is unknown, and thus in general for identification in the presence of coloured noise, the RLS-BO estimation algorithm is unsuitable.

Considering the RIV-BO estimation algorithm. Table 4.8 displays the estimated coefficients for Cases 6(c), 6(e) and 6(f) of this simulation study, which employs the RIV-BO estimation algorithm. Let each simulation case be considered in turn:

- Case 6(c). From Table 4.8, the estimated coefficients do not appear to provide a reasonable approximation to those of the continuous-time TF. Some of the estimated coefficients are in error by a significant amount (i.e. a_3, a_1, a_0, b_2, b_0), whilst some are reasonably close (i.e. a_2, b_3, b_1).

- Case 6(d). The coefficient estimates are not displayed for this simulation be-

	Cts-Time TF Coeffs.	Case 6(c) Estimates		Case 6(e) Estimates		Case 6(f) Estimates	
a_3	0.9	1.0773	(20)	0.8875	(1)	1.0110	(12)
a_2	56.4	56.7079	(0.5)	56.4674	(0.1)	56.5193	(0.2)
a_1	27.6	33.9487	(23)	25.5911	(7)	25.0201	(9)
a_0	19.8	23.6000	(19)	18.5335	(6)	18.3738	(7)
b_3	0.1812	0.1882	(4)	0.2164	(19)	0.1954	(8)
b_2	0.1877	0.2190	(17)	0.1529	(18)	0.2043	(9)
b_1	19.5225	20.6809	(6)	21.6119	(11)	21.4105	(10)
b_0	19.5152	23.9448	(23)	18.4959	(5)	17.8493	(9)
$J(w)$ Polynomial		Butterworth		$= A(w)$		$(w+0.5)^2(w+1\pm j10.4)^2$	
Prefilter		None		None		None	
Estimation Alg.		RIV-BO		RIV-BO		RIV-BO	

Table 4.8: RIV-BO estimated coefficients, coloured additive output noise, Simulation Study 6. The bracketed numbers indicate the percentage difference between the continuous-time and estimated coefficients.

cause the RIV-BO estimation algorithm fails during estimation, with the estimated model $\hat{B}(w)/\hat{A}(w)$, used to generate the instrumental variables, becoming unstable. This is easily detected during estimation, because the coefficient estimates 'burst' (rapidly climb to large positive and negative values), and then recover.

- Case 6(e). From Table 4.8, the estimates on the whole provide a closer approximation to those of the continuous-time TF than those of Case 6(c). The exception to this is for the coefficients b_3 , b_2 and b_1. The error in these coefficients causes the phase of the estimated model to be in error by 360° at frequencies above the corner frequency of the TF complex zeros.

- Case 6(f). The estimated coefficients are similar to those of Case 6(e), however, the error in coefficient estimates is spread more evenly across the estimates. The estimated model phase response accurately represents the phase of the continuous-time TF for high frequencies.

In Figure 4.18 are displayed the Bode plots of the estimated models for Cases 6(c), 6(e) and 6(f), together with the Bode plot of the continuous-time TF. Despite the relatively large errors in some of the estimated coefficients (Table 4.8), these plots reveal how

closely the frequency responses of the estimated models approximate that of the continuous-time TF. From these plots it is clear that Case 6(e) contains relatively large high-frequency errors, in both magnitude and phase. Note the 360° phase error for Case 6(e) is not fully displayed on the phase response. For both Cases 6(c) and 6(f) it is difficult to judge from these plots the superiority of either estimate. Case 6(c) results in a slightly more accurate phase response around the high-frequency complex poles and zeros, whilst Case 6(f) displays a slightly superior low- to mid-frequency phase response.

From the estimated models phase responses (Figure 4.18), it is observed that Cases 6(c) and 6(f) correctly identify the high-frequency phase of the continuous-time TF. Case 6(e) does not. This can be explained by observing the frequency weighting factor $|\ \frac{\hat{A}(\beta)}{J(\beta)}\ |^2$ for these three estimation cases. Figure 4.19 displays these weighting factors. For both Cases 6(c) and 6(f), the high-frequency error between the true and the estimated models is weighted heavily, relative to the low-frequency modeling error, resulting in the accurate high-frequency phase response. Case 6(e) weights the modeling error evenly across the frequency range, and thus, because the continuous-time TF is attenuated by up to 40 dB at higher frequencies, the high-frequency phase error occurs.

It is worth noting that the difference between failure and success in estimation is as little as a slight modification of the $J(w)$ filter polynomial. Case 6(d), in which $J(w)$ is selected to approximately match the continuous-time TF denominator, should provide an 'approximately' flat frequency weighting factor, similar to Figure 4.6. This case fails to estimate the coefficients of the continuous-time TF. By changing the high-frequency roots of the $J(w)$ polynomial from -7.5 to $-1 \pm j10.4$, to boost the relative weighting given to the error between the true and estimated models around the TF complex zeros (corner frequency $f_c \approx 1.7$ Hz, see Figure 4.19, Case 6(f)), the RIV-BO estimation algorithm in Case 6(f) is able to successfully identify the coefficients of the continuous-time TF.

In a brief summary of these results, the coefficient estimates of Table 4.8 reveal Case 6(f) to provide the best overall coefficient estimates, in terms of percentage error from the true continuous-time TF coefficients. The Bode plots of the estimated

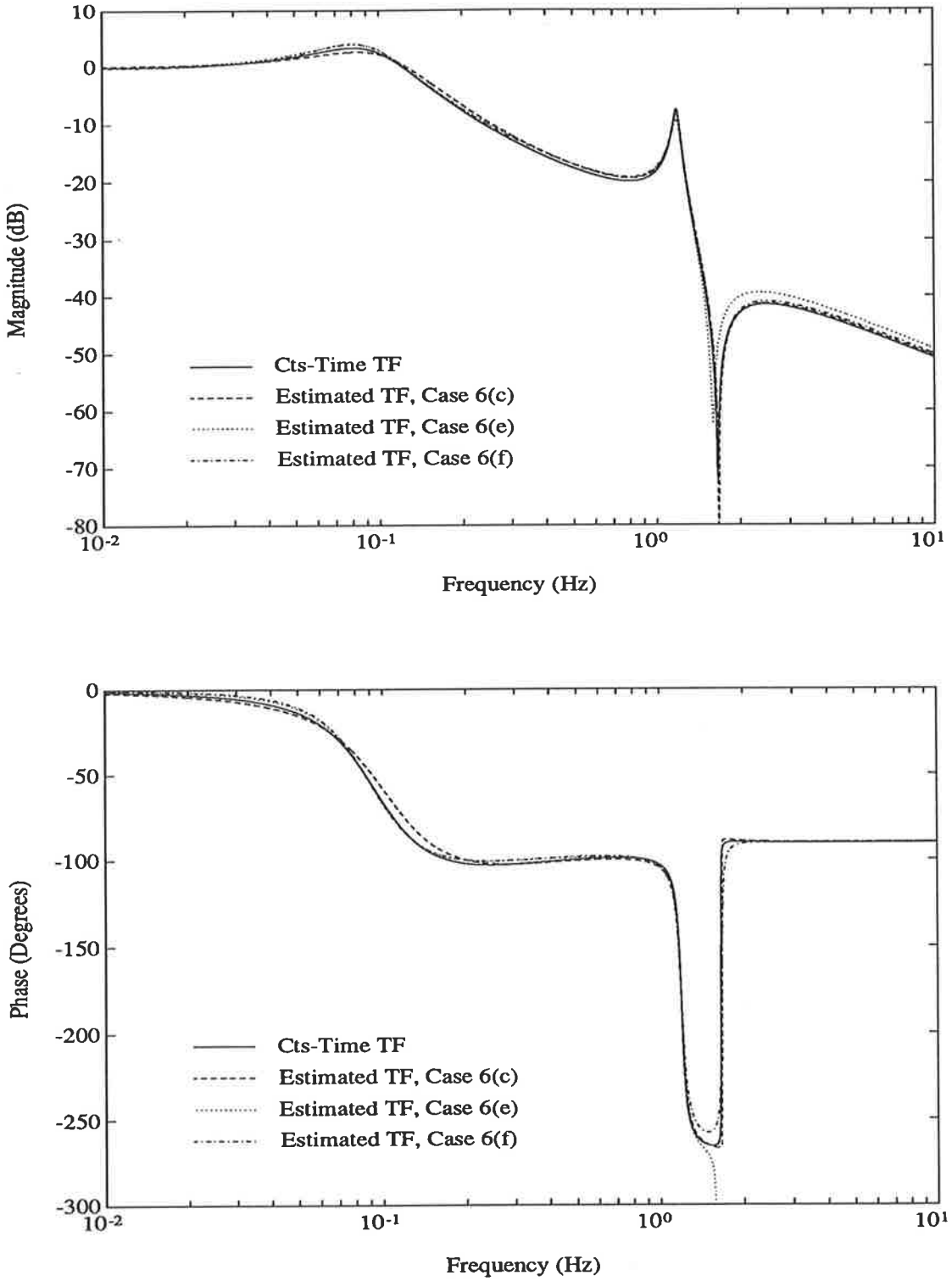

Figure 4.18: Bode plots of the estimated w-domain models, Simulation Study 6, Cases 6(c), 6(e) and 6(f).

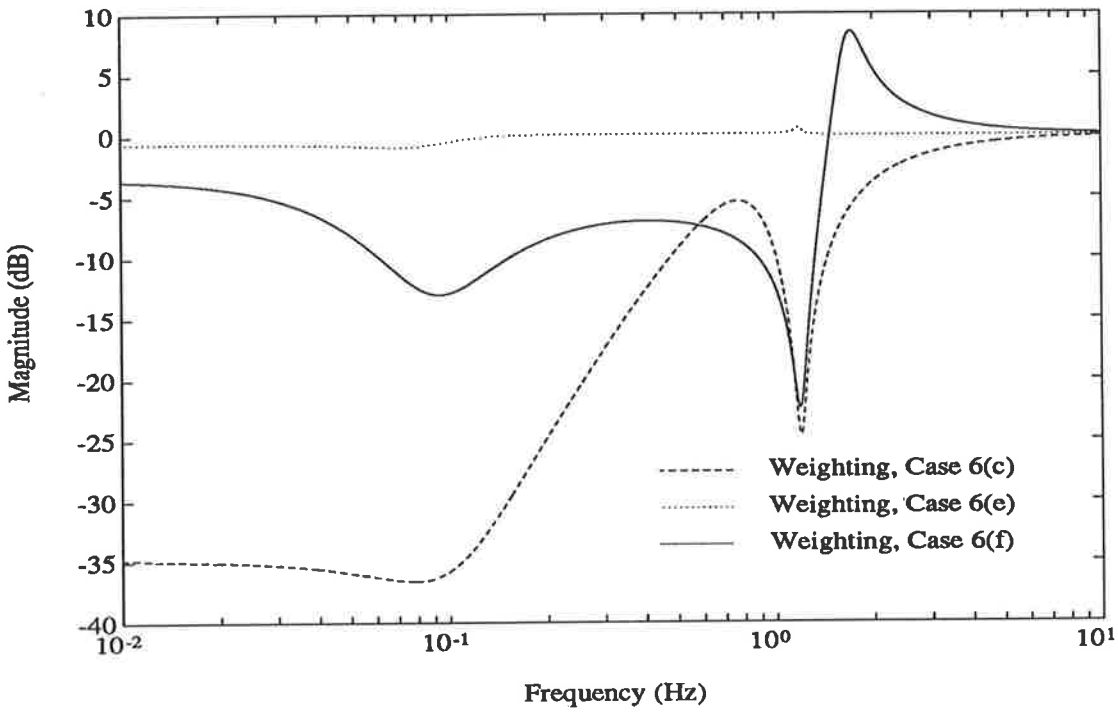

Figure 4.19: The frequency weighting factors $|\frac{\hat{A}(\beta)}{J(\beta)}|^2$, Simulation Study 6, Case 6(c), 6(e) and 6(f).

models (Figure 4.18) show both Cases 6(c) and 6(f) provide the better approximation to the Bode plot of the continuous-time TF. Thus for successful estimation of the coefficients of the continuous-time TF (eqn. 4.2) with the given coloured additive output noise, the $J(w)$ filter polynomial must be selected to weight heavily the high-frequency modeling error relative to the low-frequency error.

Prefiltering

For the simulation cases just considered, the input and output signals are not pre-filtered (except for anti-alias filtering) prior to estimation. Simulation studies are performed with prefiltered signals, and for most cases, the effect on the coefficient estimates is minimal. The one exception to this is for simulation study Case 6(d). Without prefiltering, the RIV-BO estimation algorithm fails, with the estimated model $\hat{B}(w)/\hat{A}(w)$ becoming unstable. Prefiltering enables the estimation algorithm to remain stable. The coefficient estimates however are reasonably noisy, and only roughly approximate those of the continuous-time TF.

Due to the similarity with the majority of the results of Simulation Study 6, the coefficient estimates with prefiltering are not given.

4.6.2 Simulation Study 7

For the simulation studies conducted so far, prefiltering of the input and output signals has only a significant effect on estimation in the presence of unmodeled dynamics (Simulation Study 3). For both white and coloured (low-pass filtered white noise) additive output noise, the effects of prefiltering are minimal.

In this simulation, the effects on estimation of dc offset in the output signal are studied. The dc offset considered is only small, resulting in a SNR of 50 in the anti-alias filtered output signal $y_f(t)$. The simulations are performed using the RLS-BO estimation algorithm. The studies using the RIV-BO estimation algorithm are not given, because the results display the same characteristics as those for the RLS-BO estimation algorithm.

Two $J(w)$ filter polynomials, namely $J(w) = A(w)$ and $J(w) = (w+0.5)^2(w+7.5)^2$ are considered in estimation. Each simulation study is conducted twice, firstly without

prefiltering of the input and output signals, and then with prefiltering. The prefilter used for these studies is

Prefilter: Second-order Butterworth, high-pass, $f_c = 0.02$ Hz.

The cut-off frequency of this high-pass prefilter is selected to be significantly lower than the corner frequency of any pole or zero of the continuous-time TF.

A switched forgetting factor is used for this simulation study.

The simulation conditions are:

Simulation Study 7

Simulated Input-Output Signals

Continuous-Time TF:	$H(s) = \frac{0.1812s^3+0.1877s^2+19.5225s+19.5152}{s^4+0.9s^3+56.4s^2+27.6s+19.8}$
Anti-Aliasing Filters:	Fourth-order Butterworth, low-pass, $f_c = 10$ Hz
Sampling Period:	$\Delta = 0.01$ s ($f_s = 1/\Delta = 100$ Hz)
Input Signal:	PRBS; N=511, k=20
Output Noise:	dc Offset; SNR of $y_f(t) = 50$

Recursive Estimation

Estimation Algorithm:	RLS-BO, 10000 iterations
Estimated TF Form:	$\hat{H}(\beta) = \frac{\hat{b}_3\beta^3+\hat{b}_2\beta^2+\hat{b}_1\beta+\hat{b}_0}{\beta^4+\hat{a}_3\beta^3+\hat{a}_2\beta^2+\hat{a}_1\beta+\hat{a}_0}$
$J(w)$ Filter Polynomial:	Case 7(a) and 7(b), $J(w) = A(w)$ Case 7(c) and 7(d), $J(w) = (w+0.5)^2(w+7.5)^2$
Prefilter:	Case 7(a) and 7(c), none Case 7(b) and 7(d): Second-order Butterworth, high-pass, $f_c = 0.02$ Hz
Forgetting Factor:	Switched, $\lambda_0 = 0.98, \lambda_1 = 0.998, \lambda_2 = 0.9998$, switched at iterations 500 and 2000
Initialisation:	$P_0 = 10^5 I$ $\hat{\theta}_0 = [j_{n-1}, j_{n-2}, \ldots, j_0, 0, \ldots, 0]$

Table 4.9 displays the estimated coefficients for all simulation studies. Considering each case in turn:

- Case 7(a). The estimated coefficients provide only a fair approximation to those of the continuous-time TF. Some coefficients are in error by a significant amount (i.e. a_0, b_3, b_2, b_0). The estimated model is non-minimum phase with a 360° phase error at frequencies above the complex zeros of the estimated model.

- Case 7(b). The conditions of this simulation are the same as Case 7(a), except that the input and output signals are prefiltered. The coefficient estimates

	Cts-Time TF Coeffs.	Case 7(a) Estimates		Case 7(b) Estimates		Case 7(c) Estimates		Case 7(d) Estimates	
a_3	0.9	0.8619	(4)	0.9006	(0.1)	0.8392	(7)	0.8998	(≈ 0)
a_2	56.4	56.3257	(0.1)	56.4517	(0.1)	23.1223	(59)	56.1150	(0.5)
a_1	27.6	25.0586	(9)	27.6273	(0.1)	8.4526	(69)	27.4317	(0.6)
a_0	19.8	17.4793	(12)	19.8093	($\approx$0)	4.7689	(76)	19.6592	(0.7)
b_3	0.1812	0.2054	(13)	0.1811	(0.1)	0.2233	(23)	0.1815	(0.2)
b_2	0.1877	0.1410	(25)	0.1875	(0.1)	0.5863	(212)	0.1911	(1.8)
b_1	19.5225	20.9666	(7)	19.5482	(0.1)	9.2711	(53)	19.4392	(0.4)
b_0	19.5152	16.3485	(16)	19.5325	(0.1)	4.2311	(78)	19.3815	(0.7)
$J(w)$ Polynomial		$= A(w)$		$= A(w)$		$\approx A(w)$		$\approx A(w)$	
Prefilter		None		High-pass		None		High-pass	
Estimation Alg.		RLS-BO		RLS-BO		RLS-BO		RLS-BO	

Table 4.9: RLS-BO estimated coefficients with an output dc offset, Simulation Study 7. The bracketed numbers indicate the percentage difference between the continuous-time and estimated coefficients.

accurately match those of the continuous-time TF. This is expected, because the high-pass prefilter should ideally completely remove the dc offset, resulting in coefficient estimates comparable to those of Simulation Study 2.

- Case 7(c). The coefficient estimates are significantly different to those of the continuous-time TF. The dc offset, with the $J(w)$ filter polynomial chosen to approximately match the denominator of the continuous-time TF $A(w)$, results in unacceptable coefficient estimates.

- Case 7(d). Prefiltering of the signals significantly improves the coefficient estimates from Case 7(c). The coefficient estimates closely approximate those of the continuous-time TF. Again, this is expected.

Thus in summary, dc offsets can have a severe effect on estimation. These effects can be minimised by prefiltering the sampled input and output signals with a high-pass filter. For both $J(w)$ filter polynomial selections, this results in very accurate coefficient estimates. For estimation of practical systems, this is an attractive method for reducing the effects of dc offsets.

Another possible method for reducing the effects of dc offset, which has not been considered, is to include the dc offset directly in the estimated model, and thus

estimate its value along with the TF coefficients [12].

The simulation studies described above, employ the RLS-BO estimation algorithm. It is found from further simulation studies that the conclusions reached apply equally well to the RIV-BO estimation algorithm.

4.7 Summary and Conclusions

Seven simulation studies are conducted in this chapter to demonstrate the application of the RLS-BO and RIV-BO algorithms to estimating the coefficients of continuous-time models from sampled input-output signals. The studies include the effects of unmodeled dynamics, as well as white and coloured additive output noise and dc offsets. The effects of the $J(w)$ filter polynomial and prefilter on estimation are also investigated.

Specifically the following conclusions can be reached from the simulation studies:

- Simulation Study 1. This study shows, in the absence of noise and unmodeled dynamics, the RLS-BO estimation algorithm can successfully estimate the coefficients of a relatively simple continuous-time TF. The coefficient estimates converge towards values that are closely predicted by the discrete-time TH-equivalent w-domain model.

- Simulation Study 2. This study extends Simulation Study 1 to consider a relatively complicated system with both lightly damped complex poles and zeros. The study demonstrates that, even for a relatively high sampling frequency (approximately 60 times the highest corner frequency of the continuous-time system poles/zeros), the RLS-BO estimation algorithm can accurately estimate the coefficients of the continuous-time TF model. The coefficient estimates again converge towards values closely predicted by the TH-equivalent discrete-time w-domain model. The continuous-time TF introduced in this study is employed for all the following simulation studies.

- Simulation Study 3. The effects of unmodeled dynamics on RLS-BO estimation are considered in this study. The study demonstrates the use of the $J(w)$ filter

polynomial in controlling the distribution of the errors between the true and the estimated models, across the frequency range of interest. The use of prefiltering to define the range of frequencies over which modeling accuracy is required, is also demonstrated. These simulation results confirm the frequency domain analysis of section 3.2.2.

- Simulation Study 4. This simulation includes white additive noise in the simulated output signal (SNR=10). The results of RLS-BO estimation demonstrate that reasonable coefficient estimates may be calculated, providing the filter polynomial $J(w)$ is chosen to (approximately) match the denominator of the continuous-time system TF. This confirms the discussion in section 3.2.1 on the bias of the estimated coefficients.

  It is shown that prefiltering of the input and output signals prior to estimation can have a detrimental effect on estimation, due to the colouration of the white additive output noise.

- Simulation Study 5. The level of white additive output noise is increased to a SNR of 2 for this study. With the high level of output noise, the RLS-BO coefficient estimates provide only a reasonable approximation to those of the continuous-time TF. The RIV-BO estimation algorithm is also used to estimate the continuous-time model coefficients, resulting in relatively accurate coefficient estimates, in comparison with those of the RLS-BO estimation algorithm.

- Simulation Study 6. This study includes coloured additive noise in the simulated output signal (SNR=10).

  The results show that the performance of the RLS-BO estimation algorithm is unsatisfactory, unless the $J(w)$ filter polynomial is set equal to the continuous-time TF denominator. Even with this selection, the coefficient estimates are significantly in error.

  The RIV-BO estimation algorithm performs satisfactorily. The algorithm performs best when the $J(w)$ filter polynomial is selected to weight relatively heavily the error between the true and the estimated models in the frequency region around the complex zeros of the continuous-time TF.

Prefiltering of the input and output signals has little effect on the estimated model coefficients.

- Simulation Study 7. In this study, a small dc offset is included in the simulated output signal. The results of estimation show clearly that dc offsets can severely effect the coefficient estimates. One method of reducing the effect of the dc offset is to prefilter the input and output signals with a high-pass filter.

The simulation studies considered in this thesis are not an exhaustive list of the studies conducted in the investigations. They do however provide some insight into the likely success, or lack of, of RLS-BO and RIV-BO estimation in the presence of noise and unmodeled dynamics. The studies demonstrate how the prefilter and $J(w)$ filter polynomial can be selected to enhance the accuracy of the coefficient estimates.

For the application of the estimation algorithms to practical estimation problems, it is difficult to provide strict guidelines for the selection of the prefilter and $J(w)$ filter polynomial, as well as the selection of either the RLS-BO or RIV-BO estimation algorithms. The choices are very dependent on the characteristics of the particular estimation problem. As well as the selection of these various options, quantities such as the order of the estimated model, the sampling frequency, and the excitation signal must also be selected.

The typical considerations and selections that may be involved in a practical estimation study include:

- The frequency range of interest over which modeling accuracy is required must be selected. This selection is based on the prior knowledge of the system under test, which may include knowledge of an approximate mathematical model of the system, or information obtained from some form of preliminary tests on the system.

The frequency range of interest loosely determines the bandwidth of the prefilter. The prefilter should pass frequencies within the range of interest, whilst attenuating system unmodeled dynamics, noise, and dc offsets outside of this range. Prefiltering is mandatory for estimation. The frequency range of interest also determines several of the parameters of the PRBS excitation signal (if a PRBS is employed), such that the spectral components of the excitation signal span sufficiently the frequency range of interest.

• Prior knowledge may be used to help select the sampling frequency for estimation. An approximate rule of thumb is to select the sampling frequency to be ten times greater than the system bandwidth or highest frequency pole or zero of interest. Depending on the form of the system prior knowledge, the TH-equivalent discrete-time w-domain model may also be calculated to help assess the sampling frequency selected. Once the sampling frequency is selected, anti-aliasing filters must be constructed. For estimation, these may be high-order low-pass filters, as the phase shift introduced by the filtering of the input and output signals is unimportant, providing the responses of the two anti-aliasing filters are closely matched. Prior knowledge of the system may also be useful in selecting the initial order of the system model for estimation.

• The selection of the estimation algorithm, either the RLS-BO or RIV-BO algorithm, is dependent on the system output noise. For either high-level white or coloured output noise, the RIV-BO algorithm should be employed; otherwise the RLS-BO algorithm may be satisfactory. For linear systems, it may be possible to increase the amplitude of the (PRBS) excitation signal, thus improving the SNR for estimation. For nonlinear systems, however, where a small-signal incremental model is estimated, this is not possible.

• The $J(w)$ filter polynomial is generally selected by trial and error. Based on prior knowledge of the continuous-time TF, a good initial selection of $J(w)$ is to approximately match it to the denominator of the continuous-time TF. If there is only very limited prior knowledge of the system characteristics, the $J(w)$ polynomial may be selected such that its roots approximately match the expected bandwidth of the continuous-time system. Following estimation, the accuracy of the estimated model is assessed (see section 5.3.1), and the frequency weighting effect of $|\ \mathrm{Pre}(\beta)\ |^2 |\ \frac{\hat{A}(\beta)}{J(\beta)}\ |^2\ \Phi_u(f)$ examined. Depending on these results, a different $J(w)$ filter polynomial may be selected and estimation repeated. The $J(w)$ filter polynomial may be selected to weight relatively heavily specific frequency regions of interest, which may be dependent on the dynamics of the true continuous-time system. If the RLS-BO estimation algorithm is employed, the colouration of any system output noise by the mis-match between $J(w)$ and $A(w)$, may need to be considered.

This discussion highlights several of the selections that must be made when applying the proposed estimation method to practical estimation tasks. In the following two chapters, the recursive estimation algorithms are applied to the practical tasks of estimating the coefficients of both the standstill and online TFs of a synchronous generator.

The following contributions in this chapter are original contributions:

- The simulation studies confirming that the coefficient estimates of the RLS-BO estimation algorithm converge towards approximately the coefficients of the TH-equivalent w-domain model (sections 4.3.1 and 4.3.2).

- Simulation studies demonstrating the proposed RLS-BO and RIV-BO estimation algorithms. The effects on estimation of the filter polynomial $J(w)$ and prefilter are examined, in the presence of unmodeled dynamics, dc offsets, and both white and coloured additive output noise (sections 4.4.1 to 4.6.2).

Chapter 5

Evaluation of Machine Parameters from Standstill Tests.

5.1 Introduction.

In order to analyse and simulate power system behaviour, accurate models of synchronous machines are required. Accurate models, combined with well designed controllers, can result in predictable and stable response of the power system. Inaccurate models can result in poor system response, and possibly even unstable system behaviour. Coupled with the need for accurate machine models, is the requirement for accurate values of parameters for these models.

Many methods exist for measuring or calculating the parameters of a synchronous machine. These range from conventional large-signal open-circuit and short-circuit tests, slip tests, etc. [43,74] to finite-element analysis of the synchronous machine flux distributions [41,42] to calculate the machine parameter values under the desired saturation conditions.

One method which appears to be gaining common acceptance is the Standstill Frequency Response (SSFR) method [39,44,75]. The purpose of the SSFR tests is to measure the frequency response of the relevant synchronous machine TFs with the machine at standstill. The frequency responses can be measured by exciting, over a range of discrete frequencies, the appropriate machine windings with sinusoidal excitation signals, from which the relevant magnitudes and phases of the system

response can be measured. The coefficients of suitable machine TF models are then calculated by iteratively fitting these TF models to the measured frequency responses. The synchronous machine parameters can then be directly evaluated from these TF coefficients. An alternative method of deriving the machine parameters at standstill is by measuring the step response of the relevant standstill machine configurations [45]. The response waveforms provide the data for a set of equations which can be solved by a least-squares algorithm to yield the machine parameters. The step excitation used by this method has a frequency spectrum which varies as 1/frequency. As such it is not possible to evenly excite the modes of response of the machine across a range of frequencies.

It is worth noting that these standstill tests are generally performed with low-level excitation signals, about a zero steady-state flux level. A consequence of the low-level excitation is that the effects of "incremental permeability" must be considered. For low-level excitation, the magnetisation of the rotor and stator [1] iron will not follow the conventional large-signal B-H curve. Instead, a minor hysteresis loop will be described, whose permeability (called the incremental permeability) is significantly less than that of the large-signal hysteresis curve [48]. Generally the machine parameters derived from these small-signal tests are adjusted upwards to compensate for the effects of incremental permeability [36].

Some advantages of the standstill tests are: (i) Very little stress is placed on the machine during the tests, as the voltage-current levels used for testing are relatively small [39]. In contrast, tests such as the sudden short-circuit test places unnecessary high stress on the machine [43]. (ii) Accurate direct- and quadrature-axis models of the machine can be derived as the excitation is applied directly to the required machine axis. (iii) If the sinusoidal SSFR method is employed, the frequency response can be measured over a wide range of frequencies, and hence the effects of damper windings can be accurately measured.

Despite the advantages of the standstill tests, there are several disadvantages. (i) Because the machine under test is stationary, rotational effects, such as contact

[1] Under standstill conditions the stator is also subjected to the same small perturbation signal as the rotor. This is not the case under operating conditions.

pressure on slot wedges, are excluded [36]. (ii) The use of low-level test signals means that the behaviour of the rotor and stator iron is described by the iron's incremental permeability [36]. (iii) The machine must be offline for testing, and (iv) some form of numerical curve fitting is required to calculate the coefficients of the machine TF models from the measured magnitude and phase responses. If the sinusoidal SSFR method is employed, additional disadvantages such as: (v) A high-powered, linear amplifier is required to excite the machine with the sinusoidal signal, and (vi) sinusoidal testing is time consuming (see section 5.3.5).

This chapter discusses the application of the RLS-BO estimation algorithm, introduced in chapter 3, to performing standstill tests on a synchronous machine. This recursive estimation algorithm is well-suited to standstill tests because: (i) One test excitation signal is used to excite frequencies evenly across the entire frequency range of interest, and thus the testing time is short relative to conventional sinusoidal SSFR methods. (ii) The coefficients of the machine TFs are estimated directly from the sampled input and output signals, removing the requirement for some iterative curve-fitting technique, which is required in sinusoidal SSFR tests. (iii) There is no strict requirement on the form of the excitation signal, thus relaxing the need for a high-powered linear amplifier which is required for sinusoidal SSFR testing.

The practicality of the RLS-BO estimation algorithm is demonstrated by estimating the coefficients of the TFs of a laboratory synchronous machine at standstill. From these estimated TF coefficients, the synchronous machine parameters are calculated.

In section 5.2, the model of the synchronous machine at standstill is defined. The method of testing, and the machine test configurations required are also described.

Section 5.3 employs the RLS-BO estimation algorithm for estimating directly the coefficients of the TFs of the laboratory synchronous machine. A comparison is made between the frequency responses calculated from the estimated machine TF models with those measured from conventional sinusoidal SSFR tests. Several model validation techniques are also introduced in this section.

In section 5.4, the machine parameters are calculated from the estimated TF coefficients. Consideration is given to obtaining a single set of consistent machine parameters from the three standstill tests. The calculated machine parameters are

compared to the conventional large-signal machine parameters.

Section 5.5 contains a summary and conclusions on the application of the RLS-BO estimation algorithm to standstill tests.

The work covered in this chapter is published in [54].

5.2 Standstill Test Method

5.2.1 Machine Equations

The conventional direct(d)- and quadrature(q)-axis model is used for representing the synchronous machine. This model formulation is particularly suited to standstill tests because the machine can be configured such that the d- and q-axis models can be identified independently of each other. A d-q-axis machine model, consisting of three direct-axis windings (two rotor, one stator) and two quadrature-axis windings (one rotor, one stator) is used. The d-q-axis flux and voltage equations in SI units are [1]

$$\begin{bmatrix} \psi_d \\ \psi_q \\ \psi_f \\ \psi_D \\ \psi_Q \end{bmatrix} = \begin{bmatrix} L_d & 0 & kM_f & kM_D & 0 \\ 0 & L_q & 0 & 0 & kM_Q \\ kM_f & 0 & L_f & M_R & 0 \\ kM_D & 0 & M_R & L_D & 0 \\ 0 & kM_Q & 0 & 0 & L_Q \end{bmatrix} \begin{bmatrix} i_d \\ i_q \\ i_f \\ i_D \\ i_Q \end{bmatrix} \tag{5.1}$$

$$\begin{bmatrix} v_d \\ v_q \\ v_f \\ 0 \\ 0 \end{bmatrix} = \begin{bmatrix} r_a & 0 & 0 & 0 & 0 \\ 0 & r_a & 0 & 0 & 0 \\ 0 & 0 & r_f & 0 & 0 \\ 0 & 0 & 0 & r_D & 0 \\ 0 & 0 & 0 & 0 & r_Q \end{bmatrix} \begin{bmatrix} i_d \\ i_q \\ i_f \\ i_D \\ i_Q \end{bmatrix} + \omega \begin{bmatrix} \psi_q \\ -\psi_d \\ 0 \\ 0 \\ 0 \end{bmatrix} + \frac{d}{dt} \begin{bmatrix} \psi_d \\ \psi_q \\ \psi_f \\ \psi_D \\ \psi_Q \end{bmatrix} \tag{5.2}$$

In these equations, the variables v, i and ψ are the machine voltages, currents and flux-linkages, respectively. The subscripts d, q, f, D and Q define the machine winding of the respective variable, i.e. the d- and q-axis stator windings, the field winding, and the d- and q-axis damper windings, respectively. The resistance terms r_a, r_f, r_D and r_Q are the d- and q-axis stator winding resistance, field winding resistance, and

the d- and q-axis damper winding resistances, respectively. The inductance terms L represent the self inductances of the machine windings, with the terms M or kM representing the mutual inductance between windings on the same axes.

Under standstill conditions, the speed voltage terms in eqn. 5.2 are zero because the rotor speed $\omega = 0$.

For the standstill tests it is more convenient to express the machine equations (eqns. 5.1 and 5.2) in operational impedance form, as they are directly represented as TFs. The operational impedance equations, in the Laplace domain become [45]

$$v_d(s) = (sL_d(s) + r_a)i_d(s) + sG(s)v_f(s), \tag{5.3}$$

$$v_q(s) = (sL_q(s) + r_a)i_q(s), \tag{5.4}$$

where $L_d(s)$ and $L_q(s)$ are the d- and q-axis machine operational inductances, and $sG(s)$ the machine field-to-stator TF. For a machine with a single damper winding on each of the d- and q-axes, this representation results in the following TFs [1,35]

$$L_d(s) = \frac{L_{d0}(1 + sT'_d)(1 + sT''_d)}{(1 + sT''_{d0})(1 + sT''_{d0})} \tag{5.5}$$

$$L_q(s) = \frac{L_{q0}(1 + sT''_q)}{(1 + sT''_{q0})} \tag{5.6}$$

$$sG(s) = \frac{sG_0(1 + sT_{kd})}{(1 + sT''_{d0})(1 + sT''_{d0})} \tag{5.7}$$

The aim of the standstill tests is to evaluate the parameters in the above machine TFs, as well as the unknown stator resistance r_a.

For completeness, the machine inductance terms and time constants in eqns. 5.5 to 5.7 are related to the d-q-axis machine parameters of eqns. 5.1 and 5.2 by the commonly used approximate relations [1,35]

$$L_{d0} = L_d \tag{5.8}$$

$$T'_d = L_f/r_f - (kM_f)^2/(r_f L_d) \tag{5.9}$$

$$T''_d = \frac{[2kM_f kM_D M_R + L_d L_f L_D - L_d(M_R)^2 - L_D(kM_f)^2 - L_f(kM_D)^2]}{[r_D(L_d L_f - (kM_f)^2)]} \tag{5.10}$$

$$T'_{d0} = L_f/r_f \tag{5.11}$$

$$T''_{d0} = [L_D - (M_R)^2/L_f]/r_D \tag{5.12}$$

$$L_{q0} = L_q \tag{5.13}$$

$$T''_q = L_Q/r_Q - (kM_Q)^2/(L_q r_Q) \tag{5.14}$$

$$T''_{q0} = L_Q/r_Q \tag{5.15}$$

$$G_0 = kM_f/r_f \tag{5.16}$$

$$T_{kd} = L_D/r_D - kM_D M_R/(r_D k M_f) \tag{5.17}$$

Given the values of the parameters on the left hand side of eqns. 5.8 to 5.15, it is a simple matter to calculate the transient and subtransient machine inductances

$$L'_d = L_{d0} T'_d/T'_{d0} \tag{5.18}$$

$$L''_d = L'_d T''_d/T''_{d0} \tag{5.19}$$

$$L''_q = L_{q0} T''_q/T''_{q0} \tag{5.20}$$

5.2.2 Standstill Test Configurations

Three tests are performed on the synchronous machine in order to evaluate all of the unknown machine parameters in eqns. 5.3 to 5.7 [45]. These tests are separated into two direct-axis tests, for determining the d-axis synchronous reactance and field-to-stator TFs, and one quadrature-axis test for determining the q-axis synchronous reactance TF.

For brevity the following notation generally will be used:

- 'direct-axis synchronous reactance TF' is written as 'd-axis TF'
- 'quadrature-axis synchronous reactance TF' is written as 'q-axis TF'

Direct-Axis Transfer Function

Setting the field voltage variable $v_f(s)$ in eqn. 5.3 to zero yields the d-axis TF

$$\frac{i_d(s)}{v_d(s)} = \frac{1}{r_a + sL_d(s)} \tag{5.21}$$

Using eqn. 5.5, eqn. 5.21 can be expanded into a third-order TF of the form

$$\frac{i_d(s)}{v_d(s)} = \frac{s^2 b_2 + s b_1 + b_0}{s^3 + s^2 a_2 + s a_1 + a_0} \tag{5.22}$$

where the coefficients b_i, a_i are related to the unknown d-axis machine parameters by

$$r_a = a_0/b_0 \tag{5.23}$$

$$L_{d0} = (a_1 b_0 - a_0 b_1)/b_0^2 \tag{5.24}$$

$$T'_{d0} = (b_1 + \sqrt{b_1^2 - 4 b_0 b_2})/(2 b_0) \tag{5.25}$$

$$T''_{d0} = (b_1 - \sqrt{b_1^2 - 4 b_0 b_2})/(2 b_0) \tag{5.26}$$

$$T'_d = \frac{(b_0 a_2 - a_0 b_2) - \sqrt{(b_0 a_2 - a_0 b_2)^2 - 4 b_0 (a_1 b_0 - a_0 b_1)}}{2(a_1 b_0 - a_0 b_1)} \tag{5.27}$$

$$T''_d = \frac{(b_0 a_2 - a_0 b_2) + \sqrt{(b_0 a_2 - a_0 b_2)^2 - 4 b_0 (a_1 b_0 - a_0 b_1)}}{2(a_1 b_0 - a_0 b_1)} \tag{5.28}$$

Figure 5.1 gives the test configuration for the measurement of this TF. The machine rotor is aligned such that the exciting signal applied to the machine stator results in excitation along the direct axis of the rotor [75]. The machine rotor is short circuited so that v_f in eqn. 5.3 is zero.

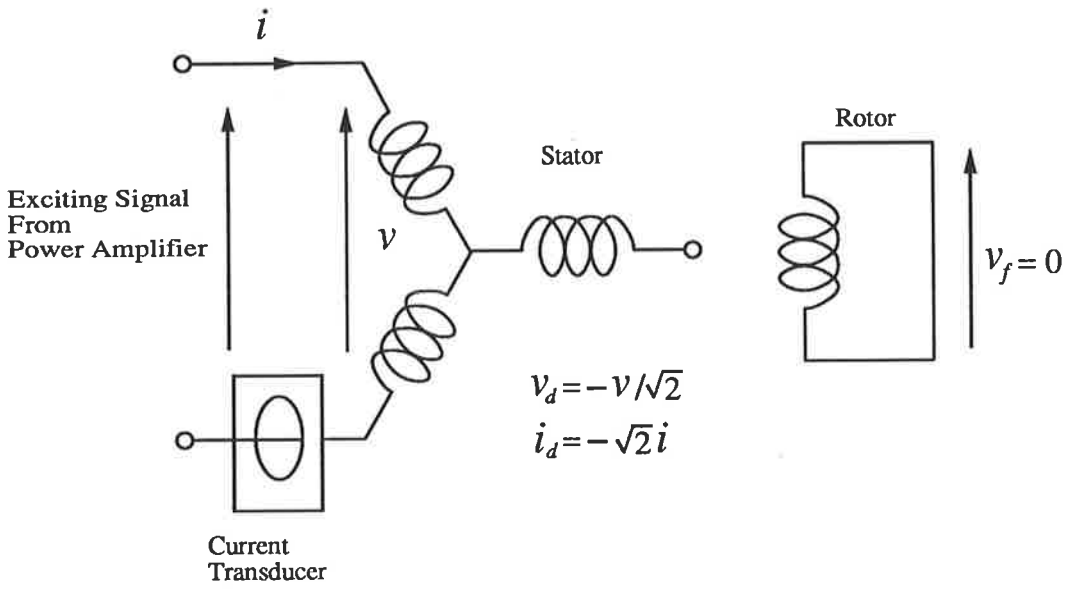

Figure 5.1: Test configuration for the measurement of the d-axis TF

The measured excitation voltage v, and the response i, must be scaled from their measured three-phase machine quantities to their corresponding d-q-axis values v_d and i_d. This is done using a modified Park's transform (see section 5.2.3). The resulting scaling is given by

$$i_d = -\sqrt{2}i \tag{5.29}$$

$$v_d = \frac{-v}{\sqrt{2}} \tag{5.30}$$

Quadrature-Axis Transfer Function

From eqn. 5.4, the q-axis TF is given by

$$\frac{i_q(s)}{v_q(s)} = \frac{1}{r_a + sL_q} \tag{5.31}$$

Using eqn. 5.6, eqn. 5.31 can be expanded into a second-order TF of the form

$$\frac{i_q(s)}{v_q(s)} = \frac{sb_1 + b_0}{s^2 + sa_1 + a_0} \tag{5.32}$$

where the coefficients b_i, a_i are related to the q-axis machine parameters by

$$r_a = a_0/b_0 \tag{5.33}$$

$$L_{q0} = (a_1b_0 - a_0b_1)/b_0^2 \tag{5.34}$$

$$T''_{q0} = b_1/b_0 \tag{5.35}$$

$$T''_q = b_0/(a_1b_0 - a_0b_1) \tag{5.36}$$

The configuration for this test is given in Figure 5.2. The configuration is similar to that for the d-axis test, except that the rotor is now aligned such that the applied stator excitation occurs along the q-axis of the rotor.

Measurements are made of the stator exciting voltage v and the resulting stator current i. These signals must be scaled to the required d-q-axis values for estimating the coefficients of the machine TF, eqn. 5.32. Using the modified Park's transform,

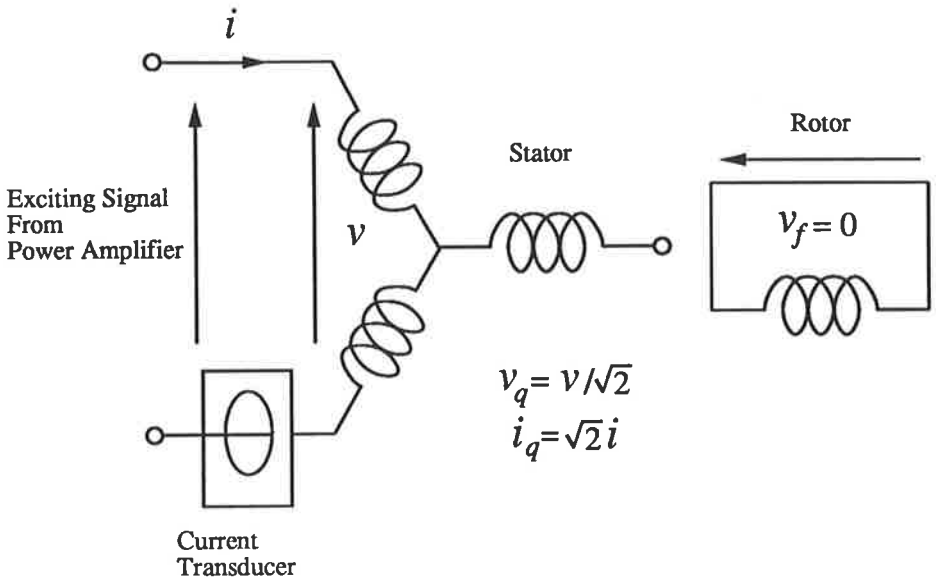

Figure 5.2: Test configuration for the measurement of the q-axis TF

the scaling required is given by

$$i_q = \sqrt{2}i \tag{5.37}$$

$$v_q = \frac{v}{\sqrt{2}} \tag{5.38}$$

Field-to-Stator Transfer Function

The field-to-stator TF is given by

$$\frac{v_d(s)}{v_f(s)} = sG(s) \tag{5.39}$$

This is obtained from eqn. 5.3 by setting the stator current to zero. Using eqn. 5.7, eqn. 5.39 can be expanded into a second-order TF of the form

$$\frac{v_d(s)}{v_f(s)} = \frac{s^2 b_2 + s b_1}{s^2 + s a_1 + a_0} \tag{5.40}$$

The coefficients b_i, a_i are related to the unknown machine parameters by

$$G_0 = b_1/a_0 \tag{5.41}$$

$$T_{kd} = b_2/b_1 \tag{5.42}$$

$$T'_{d0} = (a_1 + \sqrt{a_1^2 - 4a_0})/(2a_0) \tag{5.43}$$

$$T''_{d0} = (a_1 - \sqrt{a_1^2 - 4a_0})/(2a_0). \tag{5.44}$$

The configuration for this test is given in Figure 5.3. The machine rotor is aligned as for the d-axis test. The excitation signal is now applied to the field winding of the machine with the stator windings left on open circuit, thus ensuring i_d and i_q are zero. The signals measured are the exciting field voltage v_f and the stator voltage

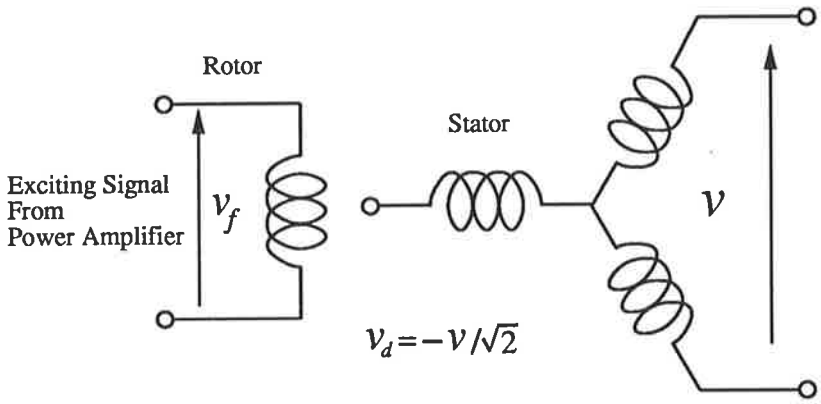

Figure 5.3: Test configuration for the measurement of the field-to-stator TF

response v. Only the measured stator voltage v requires scaling to provide the d-axis voltage v_d. The scaling required is given by eqn. 5.30.

5.2.3 Modified Park's Transform

To convert the three-phase synchronous machine quantities to the required d-q-axis values, a modified Park's transform is used [1]. This transform differs to that used in [39,45], and thus the voltage and current scaling equations (eqns. 5.29, 5.30, 5.37, 5.38) are different. The modified Park's transform employed is given by

$$P = \sqrt{\frac{2}{3}} \begin{bmatrix} 1/\sqrt{2} & 1/\sqrt{2} & 1/\sqrt{2} \\ \cos\theta & \cos(\theta - 2\pi/3) & \cos(\theta + 2\pi/3) \\ \sin\theta & \sin(\theta - 2\pi/3) & \sin(\theta + 2\pi/3) \end{bmatrix} \tag{5.45}$$

The benefits of using this this transform over the conventional Park's transform are that: (i) the transform is power invariant, and (ii) the transform converts the three-phase machine inductance matrix to a reciprocal (symmetric) d-q-axis inductance matrix [1].

The conventional Park's transform is given by [35]

$$Q = \frac{2}{3}\begin{bmatrix} 1/2 & 1/2 & 1/2 \\ \cos\theta & \cos(\theta - 2\pi/3) & \cos(\theta + 2\pi/3) \\ \sin\theta & \sin(\theta - 2\pi/3) & \sin(\theta + 2\pi/3) \end{bmatrix} \tag{5.46}$$

As far as standstill tests are concerned, the use of the modified Park's transform P, instead of Q, results in a small difference in the calculated machine parameter kM_f.

For both the d- and q-axis tests, in which the TFs i_d/v_d and i_q/v_q are estimated, the specific transform used has no effect on the estimated TF. This is because both the stator voltages and currents are transformed by the transform. However, for the field-to-stator TF, only the measured stator voltage is scaled by the transform; the field voltage is unscaled. Thus the modified Park's transform results in a field-to-stator gain G_0 that is $\sqrt{3/2}$ times larger than that obtained using the conventional Park's transform Q. From eqn. 5.16

$$G_0 = \frac{kM_f}{r_f}$$

and hence using the modified Park's transform results in a mutual inductance term kM_f that is $\sqrt{3/2}$ times larger than would be obtained with the conventional Park's transform.

5.2.4 Interface and Measurement Electronics

In section 5.2.2, the test configurations required for measurement of the input-output signals of the relevant TFs of the machine at standstill are discussed. For the purposes of estimation, each machine configuration must be excited with the desired PRBS voltage, and both the excitation waveform and the voltage or current response measured.

A block diagram showing the arrangement of the electronic equipment for conducting these tests is given in Figure 5.4.

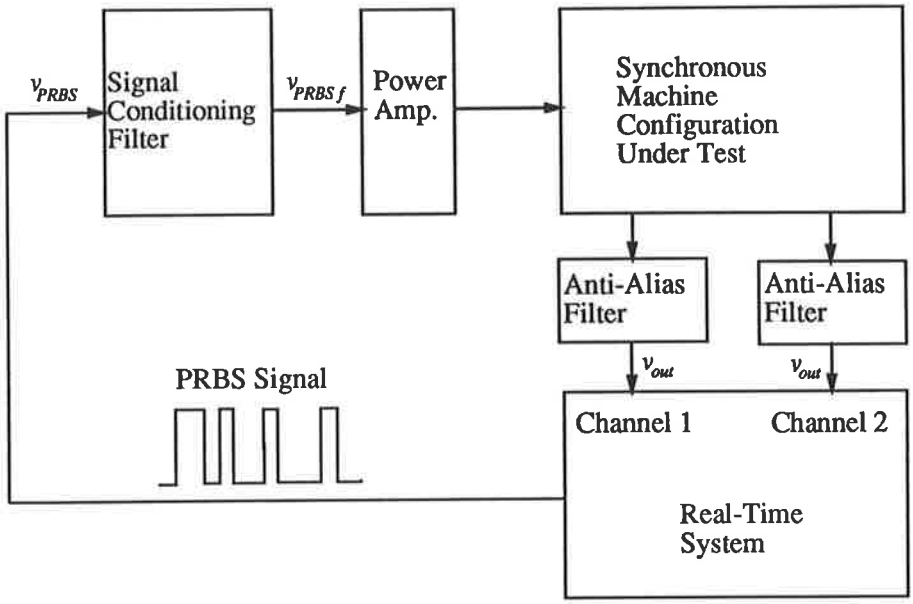

Figure 5.4: Block diagram of the arrangement for the measurement of the input-output signals for the standstill tests.

A real-time data acquisition and control system (RTS) is the heart of the test facility. The RTS is a VME based 68000 microprocessor system with both 12-bit analogue-to-digital (A/D) and digital-to-analogue (D/A) converters, as well as large memory storage capabilities. The RTS is interfaced with a PC for both permanent data storage and control of the RTS. For this application the RTS is configured and programmed to generate the required PRBS excitation signal, and to digitise and store the measured voltage and current waveforms.

The PRBS excitation signal is applied to the stator or rotor windings of the machine through a first-order low-pass signal conditioning filter (to reduce any excitation applied to the machine winding outside of the frequency range of interest) and a power amplifier. Depending on the test, the signals measured at standstill are the field voltage, the stator line-to-line voltage and the stator current. A Hall-effect current transducer is used to measure the current waveform. Both the measured voltage and current waveforms are filtered using variable gain, matched, fifth-order, Butterworth, anti-aliasing filters (cut-off frequency $f_c = 160$ Hz), prior to sampling

by the RTS. The circuit diagrams of these filters are given in Appendix D.

5.3 Estimation of Machine Transfer Functions

The laboratory machine on which the standstill tests are conducted is a 415 V, 5 kV.A, 50 Hz, three-phase, salient pole synchronous machine. Located in the pole faces are damper bars, the ends of which are connected with continuous conducting rings.

Only approximate values of the parameters of the laboratory machine are known prior to testing. For the three TFs of interest, it is anticipated that all the TF corner frequencies are to lie within the range of approximately 0.3 Hz to 100 Hz. Thus for the coefficients of the estimated w-domain model to provide a close approximation to those of the true continuous-time system TF, the sampling frequency is selected as $f_s = 1$ kHz. This is ten times the highest frequency pole or zero expected for the machine TFs under test. For the purposes of estimation, the PRBS excitation signal should excite frequencies covering at least the anticipated frequency range of interest. A PRBS of length $N = 2^{13} - 1$ (= 8191) 'bits', with a 'bit' length of 0.004s, results in a PRBS which evenly excites frequencies from 0.03 Hz to a –3 dB point at 125 Hz (see section 4.2).

Because of limitations of the available test equipment, the amplitude of the PRBS excitation signal is limited to ± 10 V for the d- and q-axis measurements, and between ± 3 V for the field-to-stator test. Despite this limitation on the PRBS excitation signal, measurements confirmed that the SNR for all standstill tests is greater than approximately 4×10^4. Thus the RLS-BO estimation algorithm is used for all standstill tests.

For each configuration under test, the PRBS excitation signal is applied to the relevant machine winding for 52 seconds. To allow any initial transients to decay, the first 20 seconds of the response is ignored. For the following 32 seconds the input-output signals are sampled at a sampling frequency of $f_s = 1$ kHz [2].

Prior to use in the RLS-BO estimation algorithm, the measured input and output

[2] 32000 samples per channel.

signals are bandpass filtered (prefiltered) [3] to reduce high-frequency noise, dc offsets, and low-frequency noise. The low-pass section of the prefilter is a fourth-order Butterworth filter with cut-off frequency $f_c = 200$ Hz, whilst the high-pass section is a first-order filter with cut-off frequency $f_c = 0.02$ Hz. The SNR of the measured output signal is very high, as mentioned previously. Thus the prefilter is only really required to reduce both unmodeled dynamics and dc offsets. This is why the low-pass section of the prefilter has such a high cut-off frequency; its effect on estimation is only small.

A time-varying forgetting factor of the form

$$\lambda_k = 0.998\lambda_{k-1} + 0.002, \ \lambda_0 = 0.95 \tag{5.47}$$

which exponentially converges towards unity, is used in all estimation calculations.

5.3.1 Estimated Model Validation Tests

For the simulation studies considered in chapter 4, the true continuous-time TF used for generating the simulated output signal is known. Thus it is a relatively simple task to judge the success of estimation by comparing the coefficients of the continuous-time TF and those of the estimated models, or by comparing the associated Bode plots. Another advantage with the simulation studies is that the true continuous-time TF can also be used to select the sampling frequency for estimation, to ensure the coefficients of the discrete-time w-domain model could closely approximate those of the continuous-time TF. For the standstill tests of this chapter, the true continuous-time TFs are unknown. Thus other methods must be used to both validate the accuracy of the estimated model, and to confirm the selected sampling frequency is sufficiently high for the coefficients of the w-domain model to closely approximate those of the corresponding continuous-time TF.

Several methods of model validation are briefly introduced in this subsection. Only a limited selection of techniques are discussed, in particular, the methods found useful

[3] The data prefiltering is performed digitally in software after the input-output signals are sampled.

for the practical examples of this thesis. There exists many more model validation techniques [2,10,12]. Two methods are considered for assessing the suitability of the sampling frequency, whilst three methods are used to assess the accuracy of the estimated model.

Sampling Frequency Test

As discussed in section 2.3.2, for the coefficients of the w-domain model to provide a reasonable approximation to those of the corresponding continuous-time model, the sampling frequency should be greater than approximately ten times the –3 dB bandwidth of the continuous-time system. If the continuous-time system contains poles or zeros of interest outside this bandwidth, then the sampling frequency should be approximately ten times the highest corner frequency of these poles or zeros. For a practical estimation task, the true continuous-time system model is unknown, and thus the selection of the sampling frequency is more complicated. Two related methods are found particularly useful for the studies conducted in this thesis.

(i) Prior to estimation, only the general knowledge about the characteristics of the system can be used to guide the selection of the sampling frequency. However, post estimation, the estimated w-domain model can be useful. Assuming estimation is successful, then the estimated w-domain model will accurately describe the relationship between the measured input and output signals of the continuous-time system. Providing the sampling frequency is greater than approximately ten times the highest corner frequency of the poles and zeros, or –3 dB bandwidth of the estimated w-domain model, then it is likely the estimated coefficients will provide a reasonable approximation to those of the continuous-time model. This can be checked easily by calculating both the –3 dB frequency, and the poles and zeros of the estimated w-domain model.

(ii) As mentioned in section 4.3.1, there is another post estimation check that can be used to asses the suitability of the selected sampling frequency. Again, assuming estimation is successful, the estimated w-domain model $\hat{H}(\beta)$ can be assumed to be the true continuous-time TF $H(s)$ (i.e. $H(s) = \hat{H}(\beta)\mid_{\beta=s}$). By calculating from $H(s)$ the TH-equivalent discrete-time w-domain model ($H_{TH}(\beta)$), a comparison of

the coefficients of $H(s)$ and $H_{TH}(\beta)$ can be performed. Providing the coefficients of these two models closely match, then it is likely the selected sampling frequency is sufficiently high.

Simulation-Mode Test

A common test of how accurately the estimated model represents the relationship between the measured input and output signals is to simulate the output signal using the estimated model coefficients and *only* the measured input signal. A comparison of the simulated and measured output signals, $y_m(k)$ and $y(k)$ respectively, "...provides a severe and informative test of a model...", showing up "...Deficiencies in model structure and poor parameter estimates..." [2].

The error between the measured and simulated output signals, $e(k) = y(k) - y_m(k)$, is due both to noise present in the measured output signal, as well as modeling errors. The cross correlation between the measured input signal, $u(k)$, and the error, $e(k)$, provides a measure of the error in the output due to modeling error. The cross correlation is given by

$$R_{eu}(\tau) = E\{e(k)u(k-\tau)\} \tag{5.48}$$

The cross-correlation function $R_{eu}(\tau)$ does not provide a particularly useful 'figure of merit' for assessing the accuracy of the estimated system model. This is because $R_{eu}(\tau)$ is dependent on both the magnitude of the input excitation signal as well as the actual system model. To provide a more 'portable' measure of the modeling error, the cross correlation must be normalised. A 'figure of merit' measure of the modeling error that is found to be particularly useful in the practical estimation studies is the cross-correlation measure, $k(\tau)$, defined by

$$k(\tau) = \frac{R_{eu}(\tau)}{\sqrt{\frac{1}{N}\sum_{j=1}^{N} R_{yu}^2(j)}} \tag{5.49}$$

The cross-correlation measure, $k(\tau)$, provides a graphical measure of the correlation between the input excitation signal and the error between the measured and simulated output signals.

Whilst not being rigorously correct, the cross-correlation measure, $k(\tau)$, may be

interpreted as a plot of the normalised error between the true and estimated system impulse responses. Because the input excitation signal is a PRBS, its auto-correlation function is approximately an impulse function at $\tau = 0$. [4] Thus, providing the input PRBS and system output noise are uncorrelated, $R_{eu}(\tau)$ is approximately the impulse response of the system relating the input signal to the error signal [2], which is the error between the impulse responses of the true and the estimated system models. The normalising factor in eqn. 5.49 can similarly be interpreted as the root-mean-square of the impulse response of the true system.

This cross-correlation measure, $k(\tau)$, is used as a 'figure of merit' measure of the error between the true and the estimated system models.

Spectral Estimation Test

The previous simulation-mode test only provides a 'figure of merit' measure of the modeling error between the estimated w-domain model and the true system model.

Using spectral estimation, the measured input-output signals can be used to calculate a non-parametric frequency response (Bode) plot of the true continuous-time system. This can be compared with that calculated from the estimated model to establish where (if any) the errors between the true and estimated models lie across the frequency range.

The frequency response of a continuous-time system is given by [2]

$$H(j\omega) = \frac{\Phi_{uy}(j\omega)}{\Phi_u(j\omega)}, \tag{5.50}$$

where $\Phi_u(j\omega)$ and $\Phi_{uy}(j\omega)$ are the power spectral density of the input signal, and cross spectral density of the input-output signals, respectively.

All estimation calculations in this thesis are conducted using a software package called Matlab [76]. One of the routines, 'spectrum', supplied in the signal processing toolbox of Matlab, calculates from finite-length data sequences, an estimate of these power and cross spectral density functions, as well as an estimate of the frequency response, $\hat{H}(j\omega)$. The routine uses the Welch method to estimate the spectral den-

[4] Because the 'bit' length of the PRBS is several sample periods long, the auto-correlation function is actually a triangle function centered on $\tau = 0$, rather than an impulse function.

sities [77]. Each input-output data sequence of length N samples, is sectioned into K overlapping shorter sequences of length m. These shorter sequences are Hanning windowed, Fast Fourier Transformed (FFT'd) and summed to calculate the spectral estimate [77].

This routine 'spectrum' is used to calculate the spectral estimate of the continuous-time system frequency response.

Note that the frequency response of the estimated w-domain model for all model validation steps is calculated by replacing the w-transform variable β with the continuous-time Laplace variable $s = j2\pi f$. This is equivalent to assuming the coefficients of the w-domain model are continuous-time coefficients. Because the main goal of performing estimation with the w-operator is to directly use the estimated coefficients as if they are the coefficients of a continuous-time system model, this is a logical method for calculating the frequency response.

Sinusoidal Frequency Response Measurement Test

An independent method of confirming the accuracy of the estimated models is to perform conventional sinusoidal SSFR measurements on the synchronous machine in the various standstill configurations. These test measurements yield the Bode plot of the test configuration for the synchronous machine, and can be directly compared with the Bode plot calculated from the RLS-BO estimated model.

The level of the injected sinusoidal test signal used for these tests is comparable to that used in the PRBS tests. This is done to possibly reduce any differences that may occur due to the effects of different levels of excitation on the machine iron. The sinusoidal SSFR measurements are performed with a Solartron Schlumberger 1253 gain-phase analyser.

5.3.2 Estimation of the d-axis Transfer Function

For the measurement of the d-axis TF, the test arrangement shown in Figure 5.1 is used. The PRBS excitation voltage is applied to the synchronous machine stator and measurements are made of the exciting voltage and response current. These signals are scaled (using eqns. 5.29 and 5.30) to yield i_d and v_d, and prefiltered for application

in the RLS-BO estimation algorithm. The filtered signals are used to estimate the coefficients of a third-order w-domain model, which approximate the coefficients of the continuous-time machine TF (eqn. 5.21/5.22).

The $J(w)$ filter polynomial is chosen, after several estimation runs, to match approximately the estimated model denominator, yielding a more-or-less even weighting in frequency to the error between the true and estimated models. The $J(w)$ filter polynomial chosen is

$$J(w) = (w + 1.7)(w + 110)(w + 320) \tag{5.51}$$

Figure 5.5 shows the evolution of the estimated coefficients during estimation. They appear to have converged by iteration 32000. The estimated w-domain model after 32000 iterations is (expressed in TF form)

$$\frac{i_d}{v_d} = \frac{\beta^2 100.53 + \beta 33496 + 69567}{\beta^3 + \beta^2 479.53 + \beta 42717 + 77907} \tag{5.52}$$

To check the accuracy of the estimated model in representing the d-axis response, the model validation tests as outlined in section 5.3.1 are performed.

Sampling Frequency Test

(i) The poles and zeros of the estimated w-domain model (eqn. 5.52) are

$$\begin{aligned} \text{Poles} \quad &: \quad -362.18 \ (\approx 58 \text{ Hz}) \\ &\quad\ \ -115.49 \ (\approx 19 \text{ Hz}) \\ &\quad\ \ -1.8626 \ (\approx 0.30 \text{ Hz}) \\ \text{Zeros} \quad &: \quad -331.10 \ (\approx 53 \text{ Hz}) \\ &\quad\ \ -2.09 \ (\approx 0.333 \text{ Hz}) \end{aligned}$$

The –3 dB bandwidth of the estimated model is approximately at $f = 20$ Hz. Thus, the –3 dB bandwidth and corner frequencies of the poles and zeros are all less than approximately 1/17th of the sampling frequency.

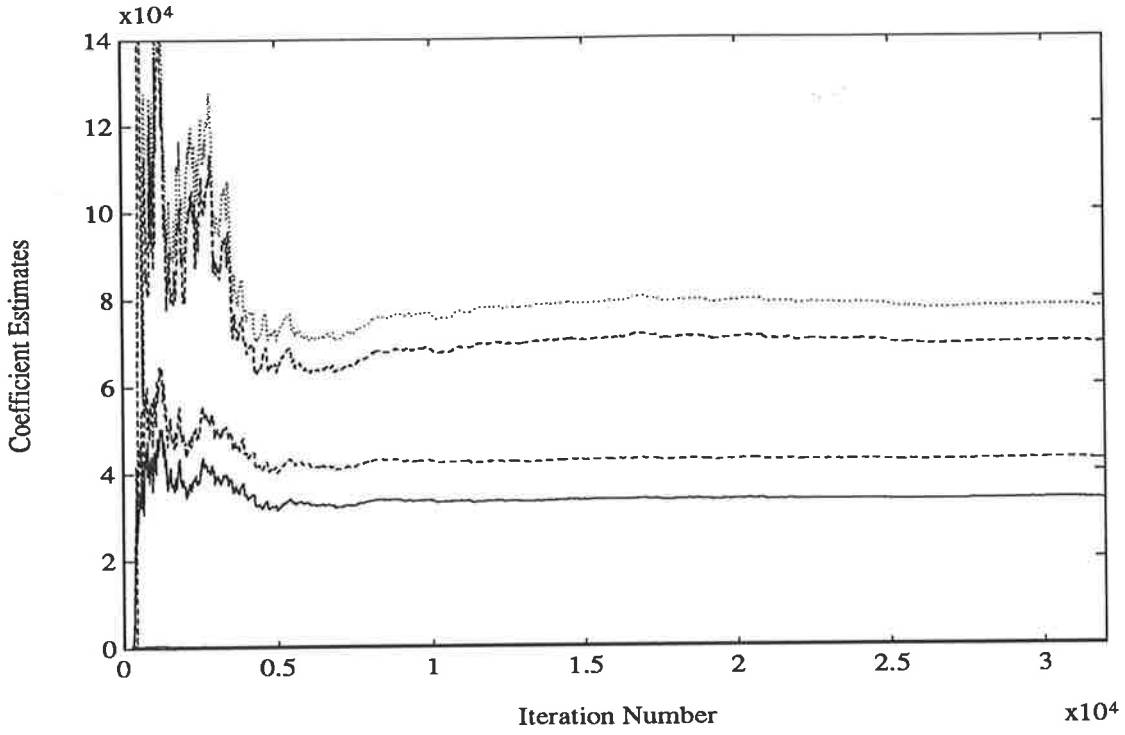

Figure 5.5: RLS-BO estimates of the d-axis TF coefficients

(ii) Table 5.1 displays the coefficients of the estimated w-domain model (eqn. 5.52), together with the coefficients of the predicted TH-equivalent w-domain model $H_{TH}(\beta)$. The percentage error between the coefficients of both models are less than 1.2%.

Thus it appears for this machine TF, providing estimation is successful, the estimated coefficients should provide a close approximation to those of the equivalent continuous-time TF. The success of estimation will be confirmed in the following tests.

Simulation-Mode Test

Figure 5.6 displays the cross correlation measure, $k(\tau)$, between the measured input signal, $v_d(k)$, and the error between the measured and simulated output signals, $e(k) = i_d(k) - i_{md}(k)$.

There are two relatively minor peaks in the cross correlation measure at $\tau \approx 40$ and 80 samples delay. After approximately 150 samples delay, the correlation between the input and error signals is virtually zero. In comparison to other cross-correlation

	Estimated Coeffs. (eqn. 5.52)	$H_{TH}(\beta)$ Coeffs.	Percentage Error
b_3	–	0.0012	–
b_2	100.53	100.64	0.1 %
b_1	33496	33101	1.2 %
b_0	69567	68740	1.2 %
a_2	479.53	475.49	0.8 %
a_1	42717	42212	1.2 %
a_0	77907	76981	1.2 %

Table 5.1: Comparison of the RLS-BO estimated coefficients with those of the predicted TH-equivalent w-domain model $H_{TH}(\beta)$.

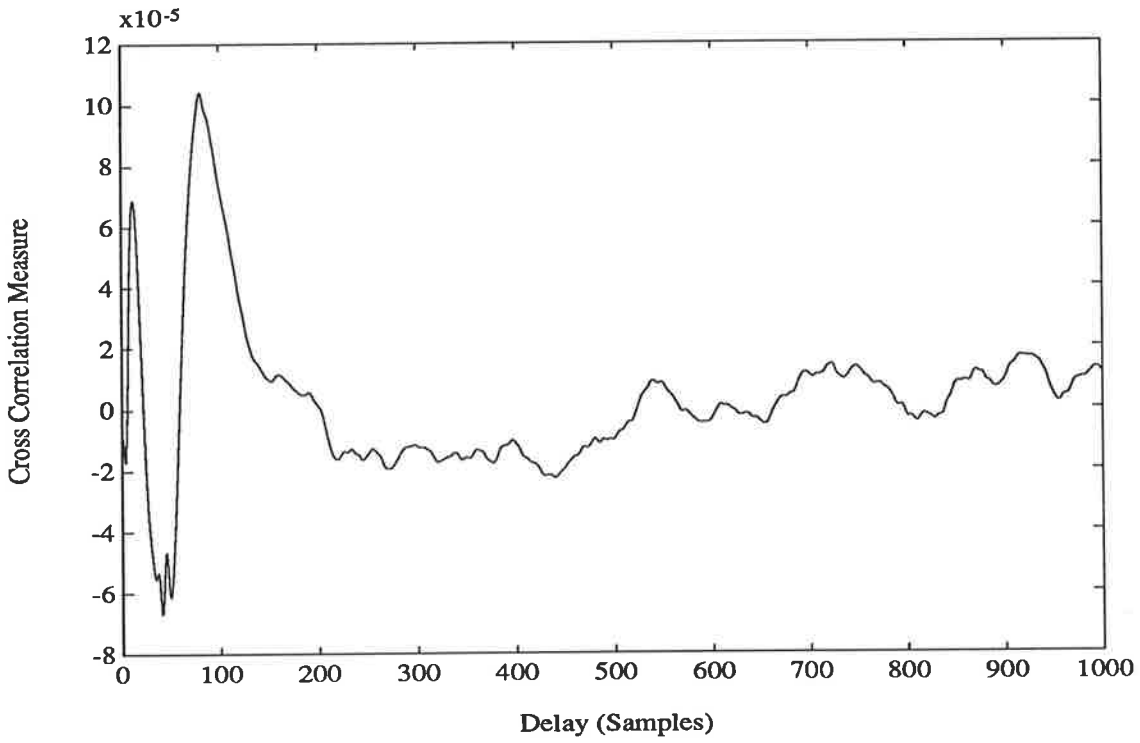

Figure 5.6: Cross correlation measure, $k(\tau)$, between the input and error signal, $e(k) = i_d(k) - i_{md}(k)$, for the estimated d-axis TF

measures displayed later, this measure represents only a very small modeling error, thus providing confidence that estimation is successful.

Spectral Estimation

Using the measured, scaled, prefiltered v_d and i_d signals, spectral estimation is employed to evaluate an estimate of the d-axis frequency response. Figure 5.7 displays the estimated response together with that calculated from the RLS-BO estimated model (eqn. 5.52).

The two sets of responses agree closely over the frequency range up to approximately 200 Hz. Above approximately 100 Hz, the spectral estimate of the phase becomes too noisy to interpret with confidence.

Sinusoidal Frequency Response Measurement Test

The third method used for verifying the accuracy of the RLS-BO estimated model is to compare its calculated frequency response with that measured using the conventional sinusoidal SSFR test. Figure 5.8 shows the measured sinusoidal SSFR magnitude and phase responses with the frequency response calculated from the RLS-BO estimated model (eqn. 5.52).

It should be noted that the SSFR tests were conducted once estimation had been completed. The SSFR results had no influence on any prefilter or $J(w)$ filter polynomial selection for the RLS-BO estimation algorithm.

The two sets of responses show excellent agreement over the frequency range of 0.05 Hz to at least 200 Hz.

5.3.3 Estimation of the q-axis Transfer Function

For the estimation of the q-axis TF, the test configuration shown in Figure 5.2 is employed. The PRBS excitation voltage is applied to the machine stator, and the exciting voltage and the stator current sampled. These sampled signals are scaled (eqns. 5.37 and 5.38) and prefiltered for application in the RLS-BO estimation algorithm to estimate the coefficients of a second-order w-domain model. The $J(w)$ filter polynomial chosen approximately matches the denominator of the estimated model,

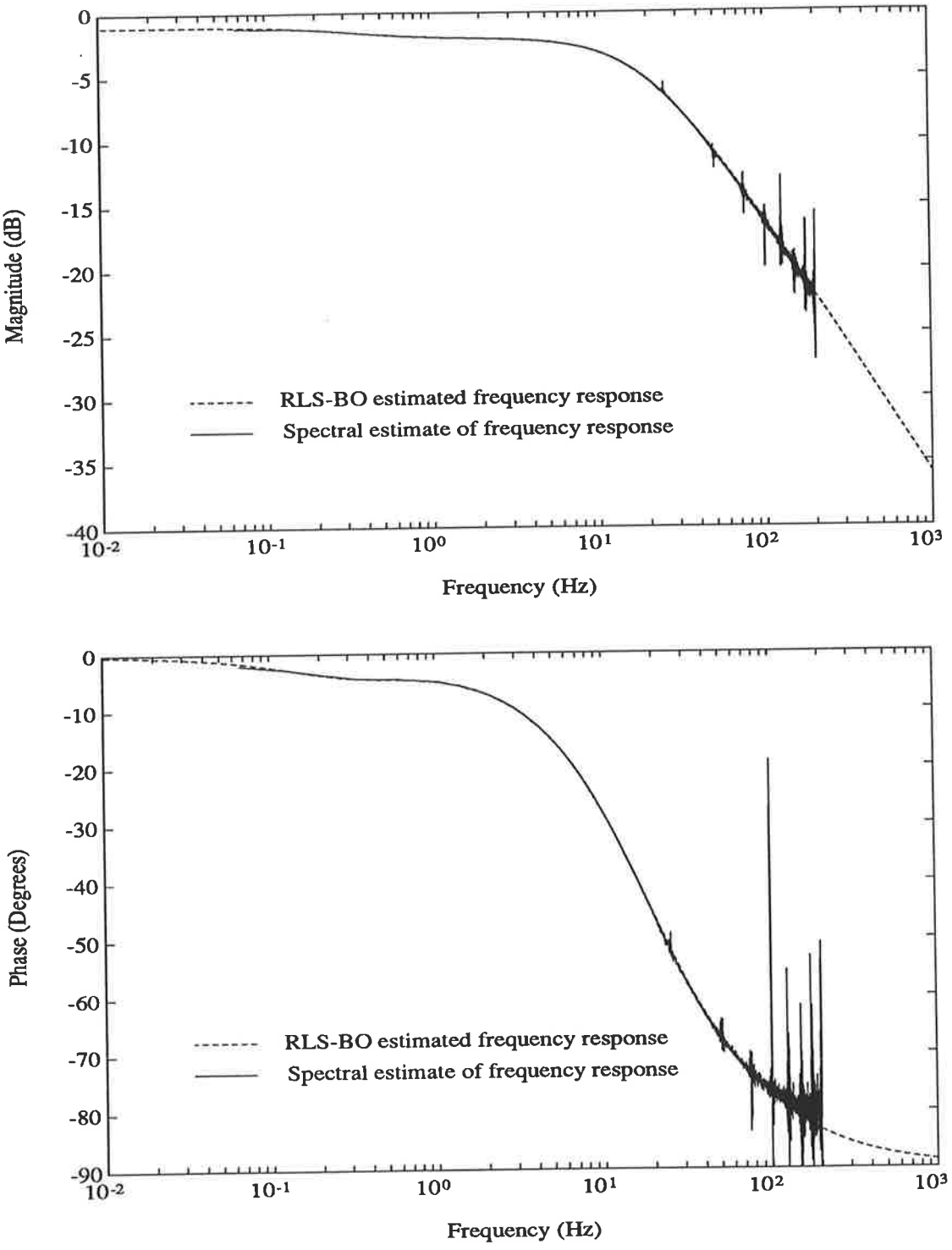

Figure 5.7: Spectral estimate of the d-axis frequency response, magnitude and phase.

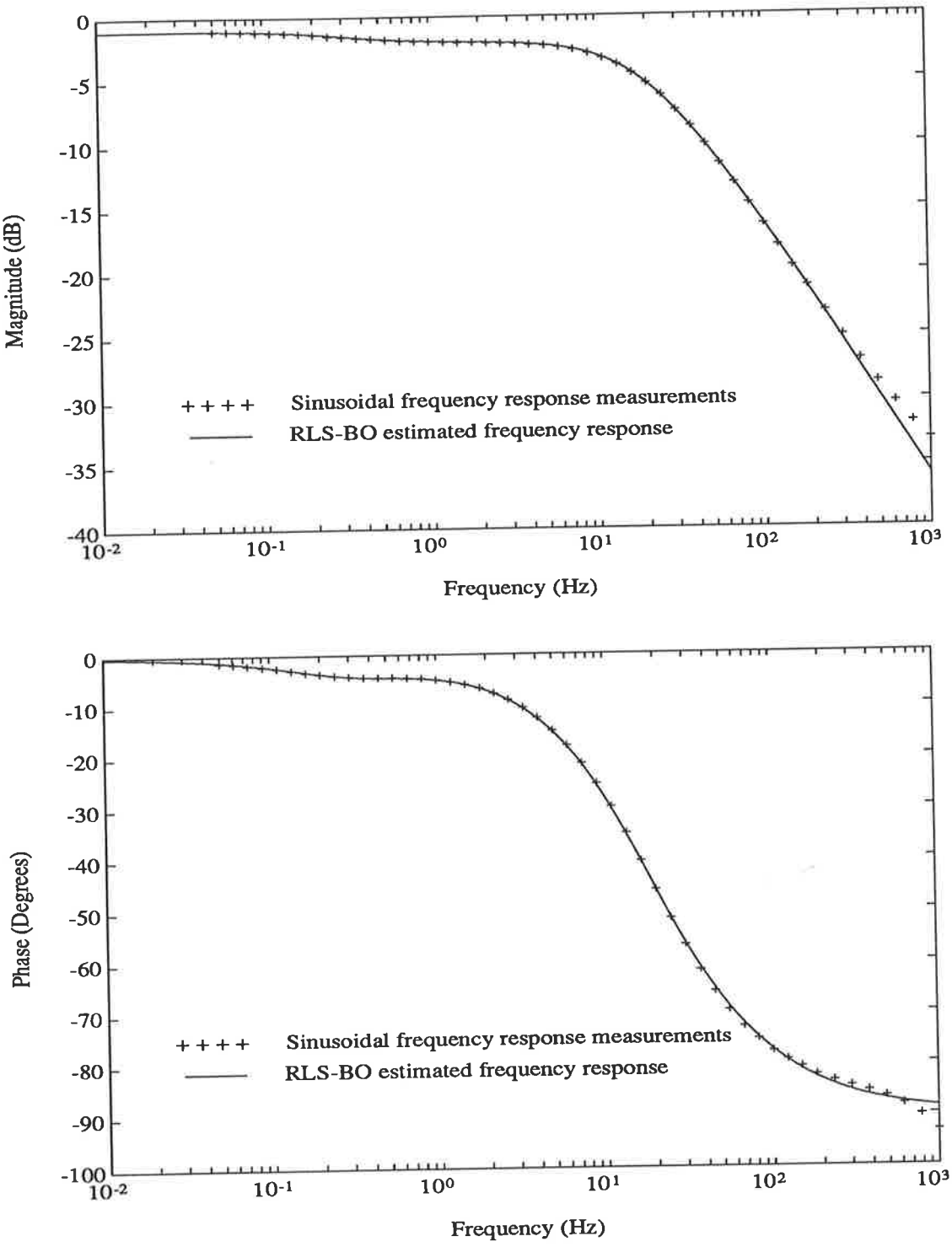

Figure 5.8: Sinusoidal SSFR measurement of the d-axis frequency response, magnitude and phase.

to provide an even weighting in frequency to the error between the true and estimated models. The $J(w)$ filter polynomial used is

$$J(w) = (w + 30)(w + 210) \tag{5.53}$$

The values of the coefficient estimates during estimation are shown in Figure 5.9. They appear to have converged well before the 32000 iterations. The estimated w-domain model after 32000 iterations is

$$\frac{i_q}{v_q} = \frac{\beta 34.490 + 5815.3}{\beta^2 + \beta 236.69 + 6515.0} \tag{5.54}$$

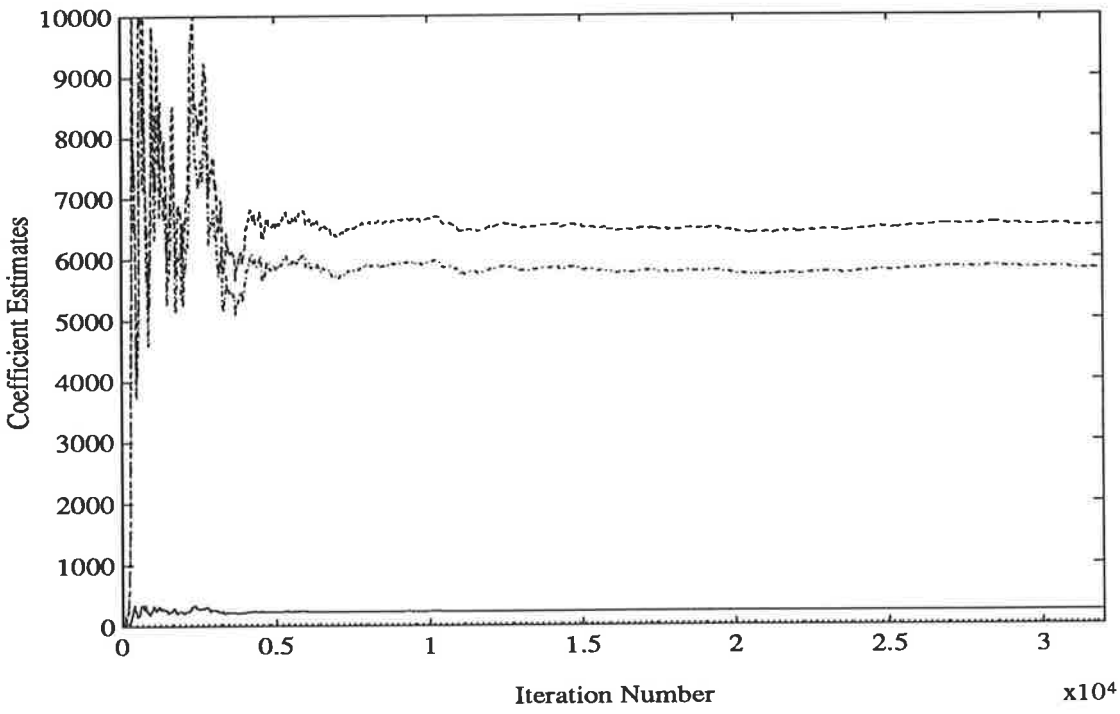

Figure 5.9: RLS-BO estimates of the q-axis TF coefficients

Employing the model validation procedures previously described:

Sampling Frequency Test

(i) The poles and zeros of the estimated w-domain model (eqn. 5.54) are

$$\begin{aligned} \text{Poles} &: -204.89\ (\approx 33\ \text{Hz}) \\ &\quad -31.80\ (\approx 5.0\ \text{Hz}) \\ \text{Zeros} &: -168.61\ (\approx 27\ \text{Hz}) \end{aligned}$$

The –3 dB bandwidth of the estimated model occurs at the frequency $f \approx 5$ Hz. Thus both the –3 dB bandwidth and corner frequencies of the estimated model poles and zeros are significantly lower than the sampling frequency, $f_s = 1$ kHz.

(ii) Assuming the estimated coefficients to be those of the true continuous-time TF, the predicted TH-equivalent w-domain coefficients are within at least approximately 0.4% of those of the estimated w-domain model.

From these two sampling frequency tests it appears the sampling frequency $f_s = 1$ kHz is sufficiently high for the estimated coefficients to closely approximate those of the equivalent continuous-time TF.

The results of the **Simulation-Mode Test** and the **Spectral Estimation Test** are similar to those obtained for the estimated d-axis TF, and therefore are not shown. They confirm that the estimated w-domain model describes the relationship between the measured q-axis voltage and current signals accurately.

Sinusoidal Frequency Response Measurement Test

Figure 5.10 displays the measured sinusoidal SSFR, together with that calculated from the RLS-BO estimated model (eqn. 5.54). A close agreement is obtained between the responses over the frequency range 0.01 Hz to approximately 100 Hz.

5.3.4 Estimation of the Field-to-Stator Transfer Function

The third test configuration (Figure 5.3) is employed in the measurement of the field-to-stator TF of the machine. The PRBS excitation signal is applied to the rotor of

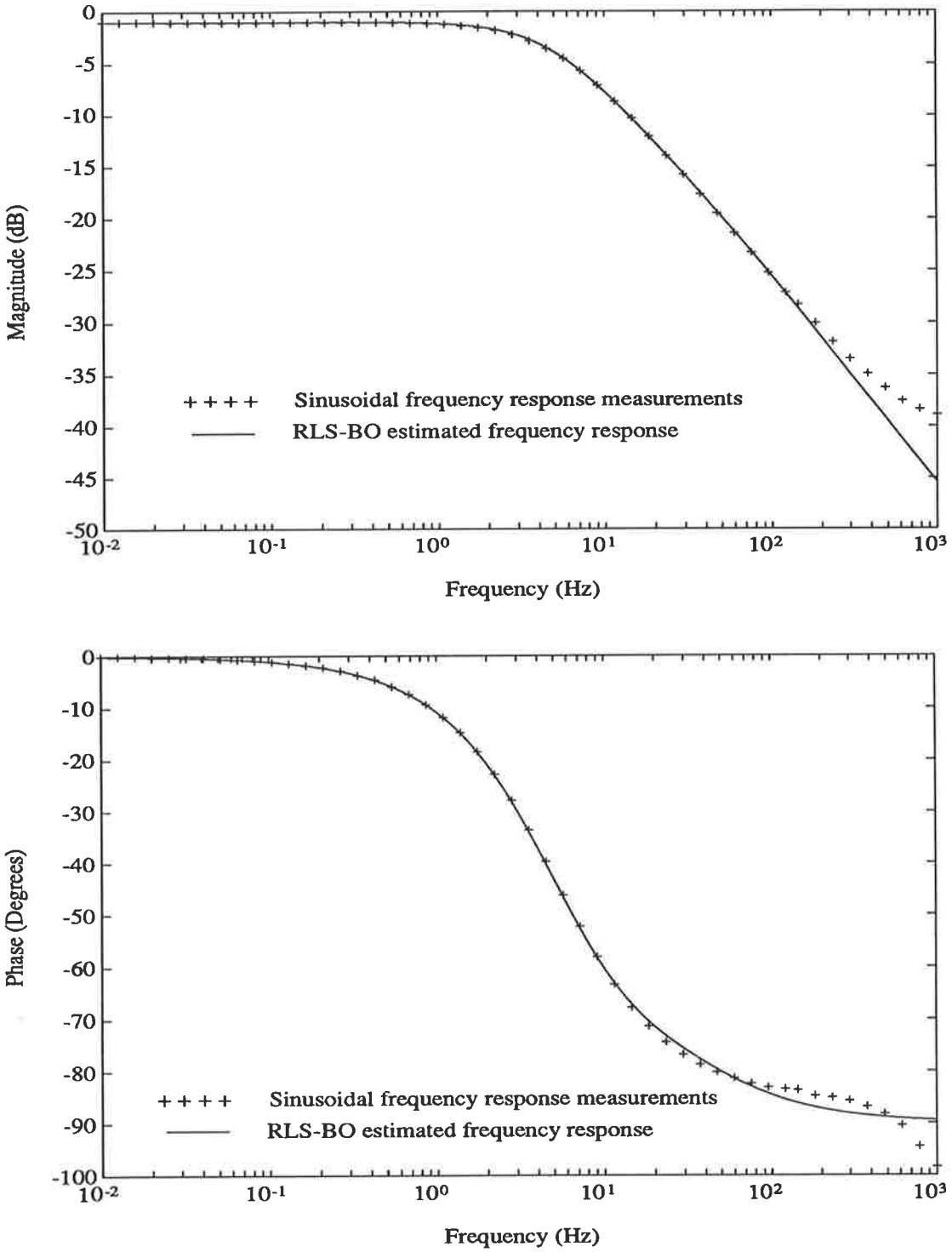

Figure 5.10: Sinusoidal SSFR measurement of the q-axis frequency response, magnitude and phase.

the machine, and measurements are taken of the field voltage and the stator voltage response. The measured stator voltage signal is scaled, using eqn. 5.30, then both voltage waveforms are prefiltered for use in the RLS-BO estimation algorithm. The evolution of the coefficient estimates during estimation is shown in Figure 5.11. They appear to have converged by iteration 32000. The $J(w)$ filter polynomial used for estimation is

$$J(w) = (w + 5)(w + 600) \tag{5.55}$$

This filter results in greater weight being given to the high-frequency error between

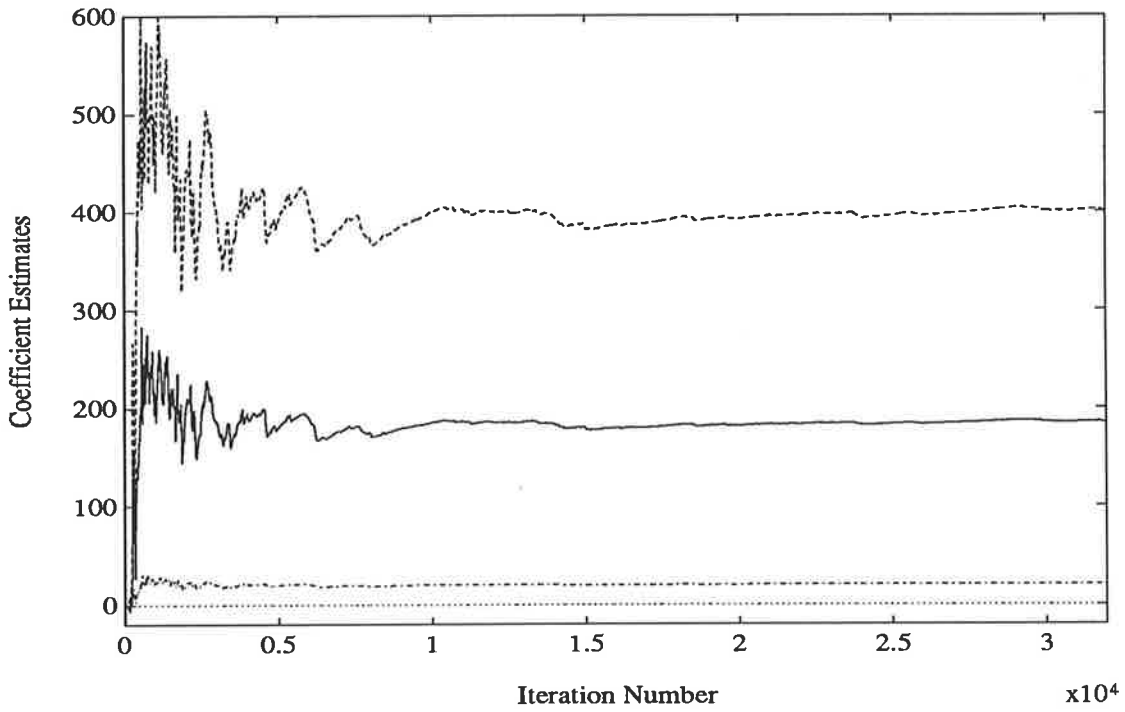

Figure 5.11: RLS-BO estimates of the field-to-stator TF coefficients

the true and the estimated machine models. The reasons for this filter selection are discussed in **Third-Order Field-to-Stator Model**, page 159, in which the accuracy of the estimated model is discussed.

After 32000 iterations, the estimated w-domain TF model is

$$\frac{v_d}{v_f} = \frac{\beta(\beta 0.10685 + 20.010)}{\beta^2 + \beta 184.89 + 400.96} \tag{5.56}$$

To confirm the accuracy of the estimated model, the model validation steps as outlined previously are performed.

Sampling Frequency Test

(i) The poles and zeros of the estimated w-domain model (eqn. 5.56) are

$$\begin{aligned} \text{Poles} \ : \ & -182.70 \ (\approx 29 \text{ Hz}) \\ & -2.19 \ (\approx 0.35 \text{ Hz}) \\ \text{Zeros} \ : \ & -187.27 \ (\approx 30 \text{ Hz}) \\ & 0 \qquad\qquad (0 \text{ Hz}) \end{aligned}$$

The corner frequencies of these poles and zeros are approximately 1/33rd of the sampling frequency. A –3 dB bandwidth for the estimated model cannot be defined.

(ii) The coefficients of a TH-equivalent w-domain model, calculated from the estimated w-domain model (eqn. 5.56) assuming it to be the true continuous-time TF, are all within approximately 0.3% of the coefficients of the estimated w-domain model.

These checks confirm, that for the field-to-stator TF, the sampling frequency of $f_s = 1$ kHz is sufficiently high for the estimated coefficients to closely approximate those of the equivalent continuous-time TF.

It is worth noting that the high-frequency pole and zero of the estimated field-to-stator model almost cancel, and thus their effect on the model is only small. This is discussed later in section 5.4 when evaluating the machine parameters from the estimated TF coefficients.

Simulation-Mode Test

Figure 5.12 displays the cross correlation measure, $k(\tau)$, between the measured input signal, $v_f(k)$, and the error between the measured and simulated output signals, $e(k) = v_d(t) - v_{md}(k)$. In comparison to the cross-correlation measure for the estimated d-axis model (Figure 5.6), there is significantly greater correlation between the input signal and output error for a range of delays τ. This implies that the estimated model may not accurately represent the true relationship between the measured field

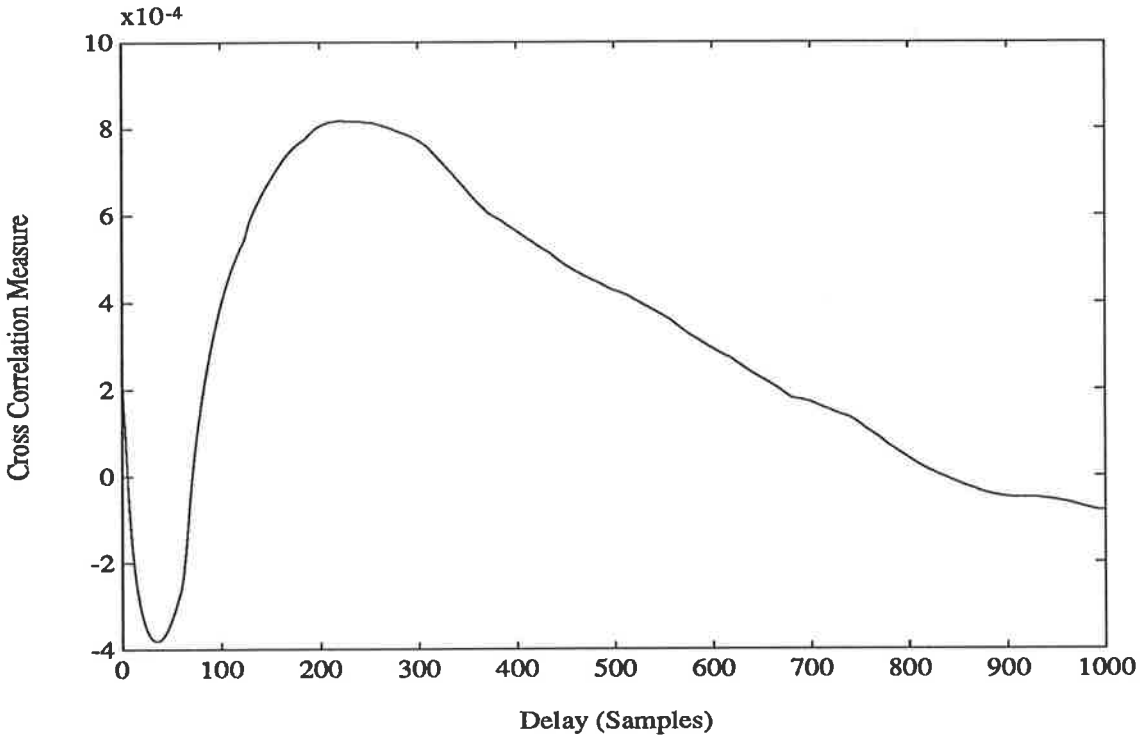

Figure 5.12: Cross correlation measure, $k(\tau)$, between the input and error signal, $e(k) = v_d(k) - v_{md}(k)$, for the estimated field-to-stator TF

and stator voltages.

Spectral Estimation Test

Using the measured, scaled and prefiltered field and terminal voltage signals, a spectral estimate of the field-to-stator frequency response is calculated. Figure 5.13 displays this frequency response, together with that calculated from the RLS-BO estimated model (eqn. 5.56). These two responses clearly match for the mid-to-high frequency region, but display some small modeling errors in the lower frequency region.

Sinusoidal Frequency Response Measurement Test

Figure 5.14 shows the sinusoidal SSFR measurements, together with the frequency response calculated from the RLS-BO estimated model. Again the results show good agreement for the mid-to-high frequency region, with some modeling errors at lower frequencies.

Third-Order Field-to-Stator Model

The model validation performed on the second-order RLS-BO estimated field-to-stator model (eqn. 5.56) shows that, whilst the sampling frequency is sufficient for the estimated w-domain coefficients to closely approximate those of the equivalent continuous-time TF, the estimated model does not exactly represent the field-to-stator response of the machine. The cross correlation measure, $k(\tau)$, (Figure 5.12) implies some modeling errors exist, and the spectral estimation test reveals that the errors lie in the low-frequency region. The low-frequency nature of the modeling error is confirmed in the sinusoidal SSFR test.

The low-frequency modeling error is consistent with the choice of the parameters of the $J(w)$ filter polynomial, which weights the error between the true and the estimated models more heavily in the high-frequency region, relative to the low frequency region. Note that the high-frequency match is close. The reason for selecting this $J(w)$ filter polynomial is that, the machine parameters calculated from the estimated field-to-stator TF coefficients (section 5.4.1) are thus comparable to those calculated from

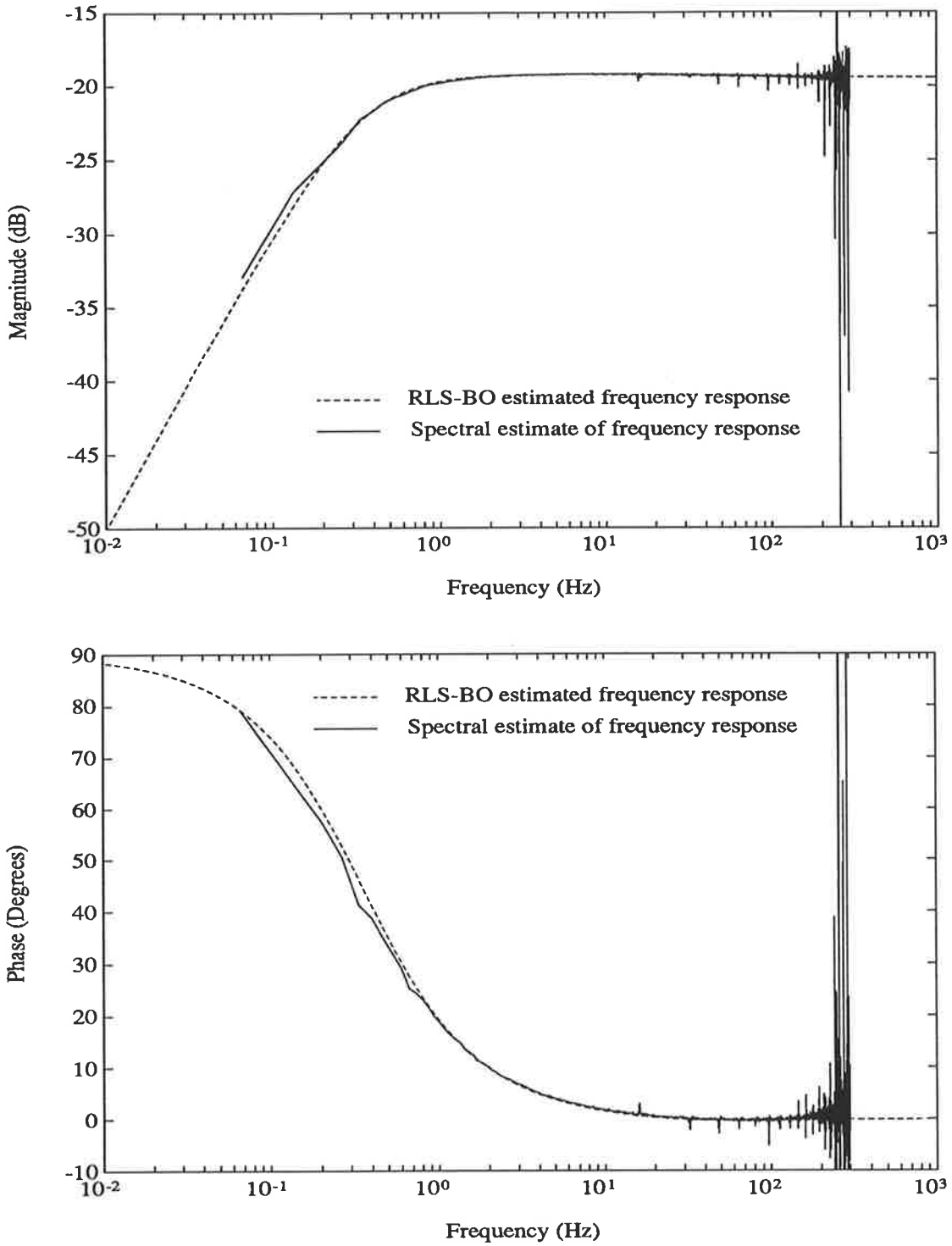

Figure 5.13: Spectral estimate of the field-to-stator frequency response, magnitude and phase.

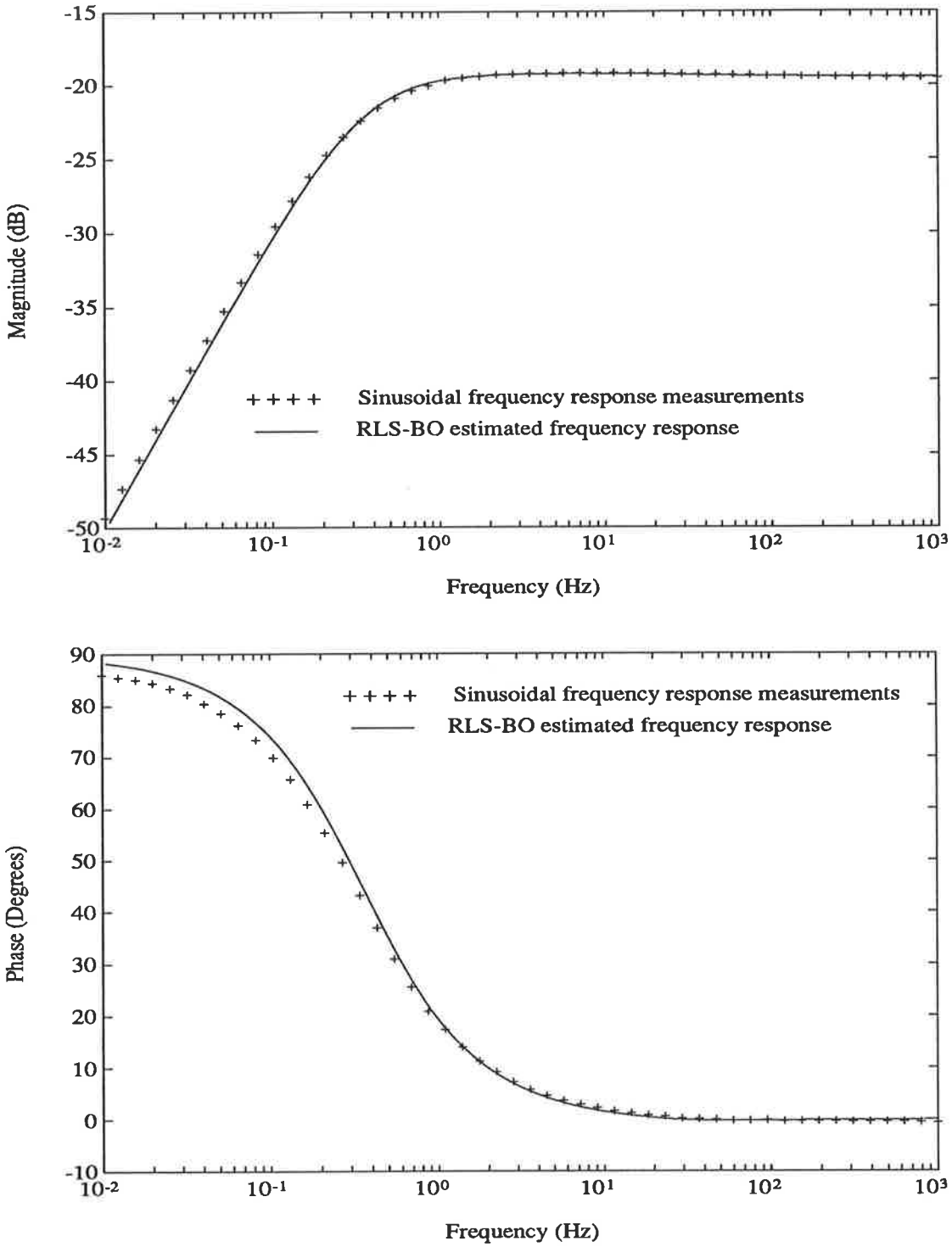

Figure 5.14: Sinusoidal SSFR measurement of the stator-to-field frequency response, magnitude and phase.

the estimated d-axis TF. The difficulty is that several of the machine parameters are calculated from more than one of the independently estimated machine TFs, and thus may yield two different values for the one machine parameter. This is discussed in section 5.4.2. If the $J(w)$ filter is selected to weight more heavily the low-frequency modeling error, a better low-frequency fit results —— but this is at the expense of increased error at higher frequencies.

This dilemma demonstrates that the second-order model for the field-to-stator TF may be inadequate for some applications of this model.

In an attempt to model more accurately the field-to-stator response, a third-order w-domain model is employed for estimation. Using the $J(w)$ filter polynomial

$$J(w) = (w+1)(w+4)(w+600) \tag{5.57}$$

the estimated w-domain model after 32000 iterations is

$$\frac{v_d}{v_f} = \frac{\beta(\beta^2 0.10682 + \beta 21.6790 + 63.5232)}{\beta^3 + \beta^2 200.0400 + \beta 1022.355 + 1173.783} \tag{5.58}$$

From both the cross-correlation measure, $k(\tau)$, (Figure 5.15) and the comparison of the Bode plot with the measured sinusoidal SSFR (Figure 5.16), this estimated third-order w-domain model provides a noticeable improvement over the previously estimated second-order model (Figure 5.14).

It is worth noting that the difference between this third-order field-to-stator model, and the originally estimated second-order model (eqn. 5.56), occurs around the low-frequency pole. The third-order model replaces the simple single pole at –2.19 in the second-order model with poles at –1.73, –3.49 and a zero at –2.97.

Although the third-order stator-to-field model provides a relatively accurate model of the stator-to-field response of the machine, it is not consistent with the overall machine model considered in section 5.2. Therefore the third-order model is not considered when deriving the machine parameters from the estimated machine TF coefficients.

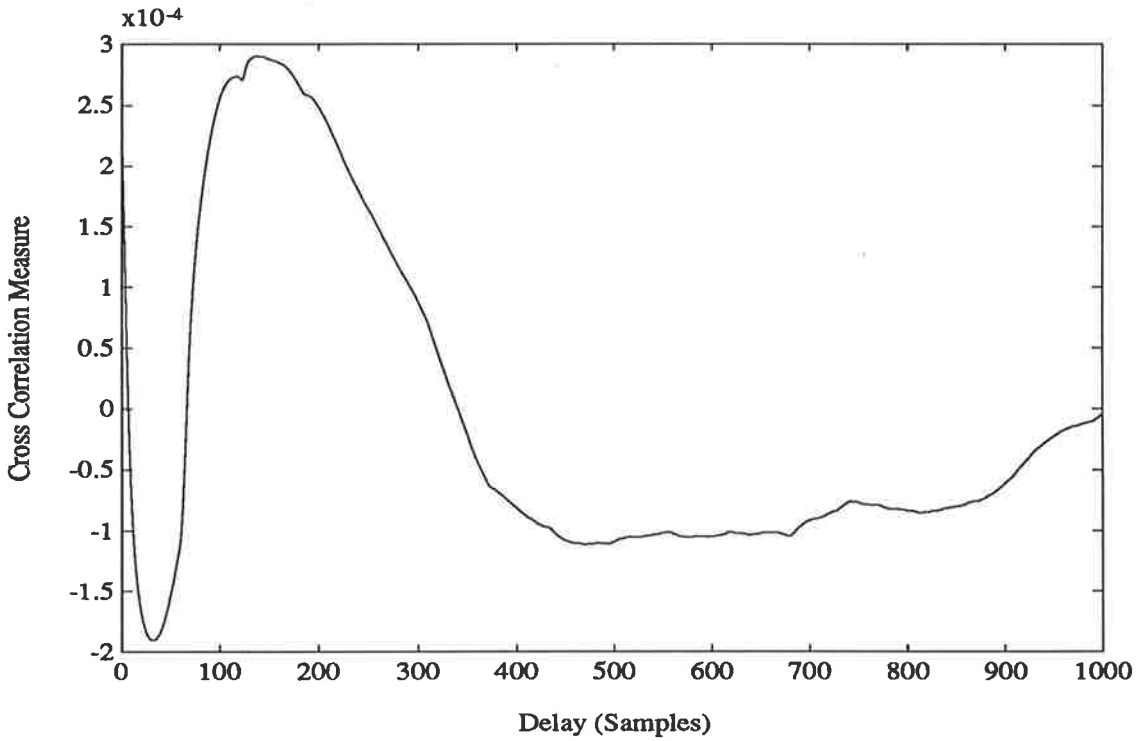

Figure 5.15: Cross correlation measure, $k(\tau)$, between the input and error signal, $e(t) = v_d(t) - \hat{v}_{md}(t)$, for the estimated third-order field-to-stator model.

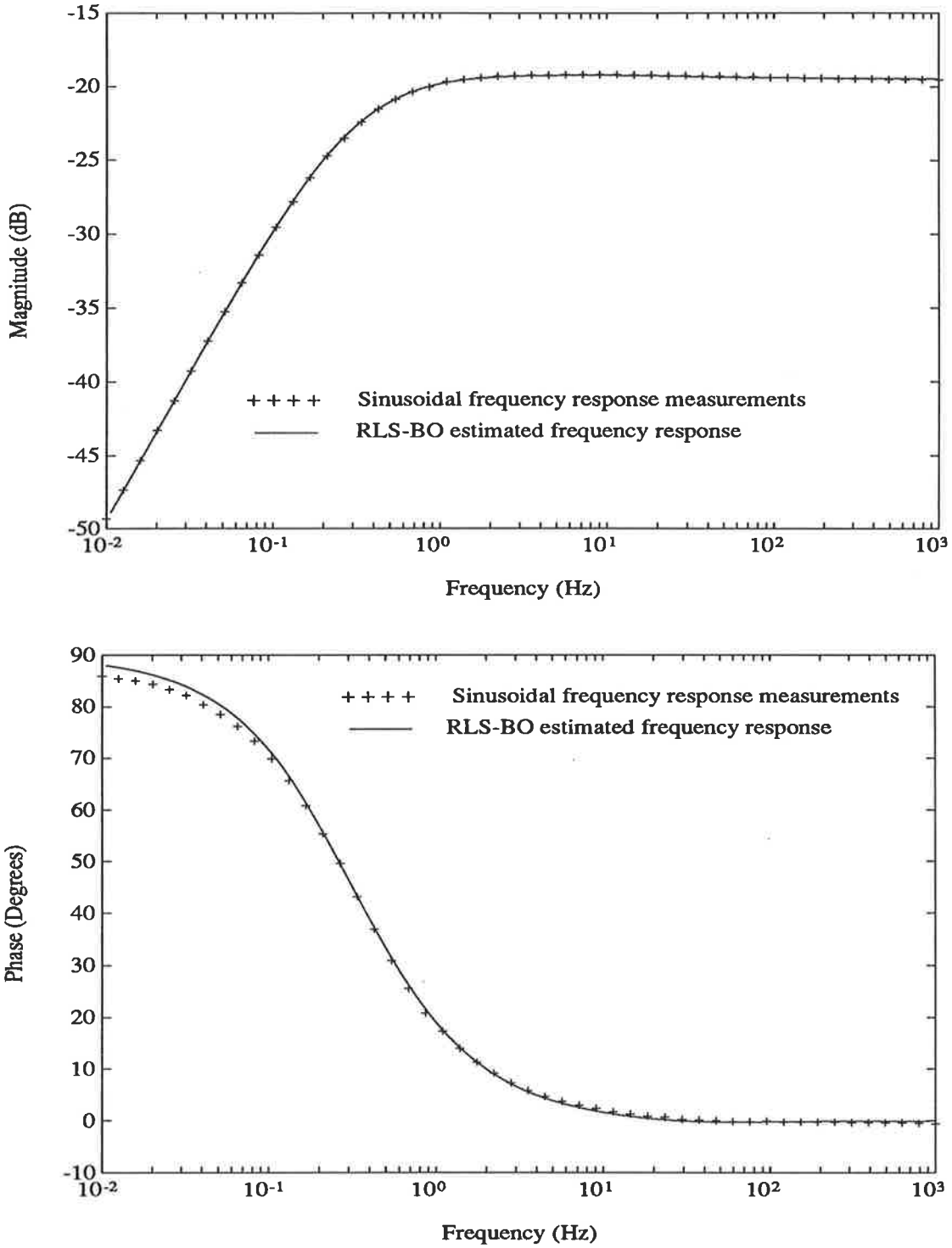

Figure 5.16: Sinusoidal SSFR measurement of the field-to-stator frequency response, magnitude and phase. Third-order field-to-stator model.

5.3.5 Discussion

In this section it is shown that the proposed RLS-BO estimation algorithm is well-suited to the practical task of estimating the coefficients of the continuous-time TFs of a synchronous machine at standstill. Accurate models are estimated for both the d- and q-axis synchronous reactance TFs of the machine, with the results agreeing closely with conventional SSFR measurements. For the field-to-stator TF of the synchronous machine, a second-order model provides a reasonable approximation to the TF. There are some modeling errors present with this second-order model, which can be reduced by using a third-order model for this machine TF.

The following are some general comments on the application of the proposed estimation algorithm to standstill tests.

In the proposed estimation algorithm, the exciting signal applied to the machine windings is not required to be a pure sinusoid, a square wave, or any special waveform. The only requirement on the exciting signal is that it be persistently exciting (see section 3.2.1). This non-stringent requirement on the form of the exciting signal would allow the power operational amplifier used in these tests (see Figure 5.4) to be replaced with a device similar to a pulse-width modulated (PWM) dc-ac converter, capable of providing a high current [78]. The exciting voltage would swing between $\pm$ V volts, the waveform being, say, a PRBS or Ternary Sequence [13]. The possible benefit of this approach would be that large voltage perturbation tests could be performed, reducing the effects of incremental permeability on the estimated machine TFs [48], as well as possibly providing some level of machine saturation.

The time required to perform these estimation tests is significantly less than that for the conventional SSFR test. In the SSFR test the magnitude and phase of the frequency response are measured at selected frequencies f_i by applying, for a period of at least 2 to 3 times $1/f_i$ seconds, a sinusoidal exciting signal of frequency f_i Hz. Thus the time required for testing is at least 2 to 3 times $\sum_{i=1}^{N} 1/f_i$ seconds, where N is the number of frequency points tested. For the proposed RLS-BO estimation algorithm, a PRBS excitation signal is employed, which excites frequencies evenly across the the frequency range of interest. The use of the one broad-bandwidth excitation signal reduces significantly the time for testing to the order of $1/f_1$ seconds, where f_1

is the lowest frequency of interest. For example, consider the tests conducted on the laboratory synchronous machine. For the proposed RLS-BO estimation algorithm, the duration of the PRBS excitation test is 52 seconds. To cover the same range of frequencies as the PRBS excitation, namely 0.03 Hz to 125 Hz, with say 50 logarithmically spaced measurement points, measurements using the sinusoidal SSFR method would take at least 10 minutes. [5] This is approximately 11 times longer than required for the PRBS testing.

Using the RLS-BO estimation algorithm, the coefficients of the continuous-time machine TFs are estimated directly from the measured excitation and response signals of the machine configuration under test. In contrast, the sinusoidal SSFR test method identifies only a frequency response model of each machine TF. To calculate the corresponding TF coefficients, iterative curve fitting techniques are required to match the TF models to the measured responses.

In the next section, the coefficients of the three estimated machine TFs are used to calculate the operational impedance parameters of the synchronous machine.

5.4 From Estimated Transfer Functions to Machine Parameters

Before evaluating the machine parameters from the estimated machine TF coefficients, it is worth noting that the machine tested is a 5kV.A, three-phase, salient pole, laboratory synchronous machine. Thus the resulting machine parameters are not necessarily representative of those of large generators used in industry. The purpose of the tests on the laboratory machine is to demonstrate the applicability of this identification technique to standstill tests.

5.4.1 Machine Parameters: Direct Evaluation

From the three estimated machine TF models, namely, the d-axis (eqn. 5.52), q-axis (eqn. 5.54) and field-to-stator (eqn. 5.56) models, it is a simple matter to evaluate the

[5] Assuming 3 sinusoidal averaging cycles per frequency point.

machine parameters using eqns. 5.23-5.28, 5.33-5.36 and 5.41-5.44. Table 5.2 displays the resulting machine parameters.

Estimated Coefficients		Derived Machine Parameters		
DIRECT-AXIS RESULTS				
a_2	479.53	r_a	1.12	Ω
a_1	4.2717×10^4	L_{d0}	7.48×10^{-2}	H
		$\omega_0 L_{d0}$	23.5	Ω
a_0	7.7907×10^4	T'_{d0}	0.479	s
b_2	100.53	T''_{d0}	3.02×10^{-3}	s
b_1	3.3496×10^4	T'_d	6.77×10^{-2}	s
b_0	6.9567×10^4	T''_d	2.84×10^{-3}	s
QUADRATURE-AXIS RESULTS				
a_1	236.69	r_a	1.12	Ω
a_0	6.5150×10^3	L_{q0}	3.42×10^{-2}	H
		$\omega_0 L_{q0}$	10.8	Ω
b_1	33.490	T''_{q0}	5.76×10^{-3}	s
b_0	5.8153×10^3	T''_q	5.02×10^{-3}	s
FIELD-TO-STATOR RESULTS				
a_1	184.89	T'_{d0}	0.456	s
a_0	400.96	T''_{d0}	5.47×10^{-3}	s
b_1	106.85×10^{-3}	G_0	4.99×10^{-2}	
b_0	20.010	T_{kd}	5.34×10^{-3}	s

Table 5.2: Estimated machine TF coefficients and the derived machine parameters

One difficulty in calculating directly the machine parameters from the coefficients of the three estimated TF models, is that some machine parameters are common to more that one TF. Thus there is a possibility that the parameter values calculated from one TF do not agree with those calculated from the second. This problem is discussed later.

Considering that machine parameters in Table 5.2 in turn:

r_a : The stator resistance is evaluated from both the estimated d- and q-axis models. These d- and q-axis tests are performed under virtually identical conditions and hence, not surprisingly, the resulting resistance values are identical. The value $r_a = 1.12\ \Omega$ agrees with that calculated independently from dc voltage-current measurements.

L_{d0} ($\omega_0 L_{d0}$) : From the conventional large-signal open-circuit and short-circuit tests

conducted in Appendix E, the unsaturated d-axis synchronous reactance is calculated as $X_{d_{unsat}} = 27.0\ \Omega$. The value calculated from the estimated machine TF coefficients, $\omega_0 L_{d0} = 23.5\ \Omega$, is significantly less than the unsaturated value. The lower value derived from the standstill test is to be expected, because under the small-signal standstill tests conditions, the magnetisation of the machine iron is described by its incremental permeability [48]. The usual practice is to increase the estimated small-signal value of $\omega_0 L_{d0}$ to correspond to the large-signal air-gap value [36]. In this case the difference between the large-signal unsaturated and the small-signal values is approximately 12%, which is within the expected range for such differences of 8% to 18% [36].

L_{q0} $(\omega_0 L_{q0})$: As for the d-axis synchronous reactance, the q-axis reactance calculated from the estimated q-axis model is less than the value calculated from the conventional slip test (Appendix E). From the standstill test $\omega_0 L_{q0} = 10.76\ \Omega$, whilst the slip test yields a value $X_{q_{unsat}} = 11.5\ \Omega$. This difference is again due to the incremental permeability of the machine iron.

G_0 : Using the value of G_0 calculated from the estimated field-to-stator model, along with the field resistance $r_f = 12.0\ \Omega$ (calculated from dc voltage-current measurements), eqn. 5.16 can be used to calculate the mutual reactance term $\omega_0 k M_f$, the value of which is approximately 188 Ω. From the open-circuit characteristic of the machine (Appendix E), the unsaturated mutual reactance $\omega_0 k M_{f_{unsat}}$ is approximately 210 Ω. Once again, due to the incremental permeability of the machine iron, the estimated standstill parameter is approximately 90% of the large-signal, unsaturated value.

T'_{d0} : The d-axis transient open-circuit time constant is calculated from both the estimated d-axis and stator-to-field TF models. From Table 5.2, there is approximately a 5 % difference between the two calculated values. These values are quite close considering it is not possible to estimate an accurate second-order model for the field-to-stator TF.

It should be noted that T'_{d0} is defined by the equation $T'_{d0} = L_f / r_f$ (eqn. 5.11), and hence its value is dependent on the incremental permeability of the machine

iron.

T'_d : The d-axis transient short-circuit time constant is given by eqn. 5.9. Using the values of $T'_{d0}(= L_f/r_f)$, kM_f and L_d evaluated from the standstill tests, and r_f evaluated from dc voltage-current measurements, it is possible to calculate a value for T'_d [6]

$$T'_d = L_f/r_f - (kM_f)^2/(r_f L_d) = \text{ 0.056s or 0.08s}$$

From the estimated d-axis model, the calculated value of T'_d (= 0.0677s) lies half-way between these values.

T''_{d0}, T''_d, T_{kd} : The d-axis subtransient open-circuit time constant T''_{d0} is evaluated from both the estimated d-axis and stator-to-field models. These two values are significantly different, i.e. 3.02×10^{-3}s and 5.47×10^{-3}s. The reason for this is partly the insensitivity of the field-to-stator TF model to variation in the values of T''_{d0} and T_{kd}. Comparing the values of T''_{d0} (= 5.47×10^{-3}s) and T_{kd} (= 5.34×10^{-3}s), and the associated TF pole and zero $-1/T''_{d0}$ (=–183) and $-1/T_{kd}$ (=–187), it is clear they are very similar in value. Hence, due to the almost pole-zero cancellation, their net effect on the overall field-to-stator TF model is small. It can be shown that reducing both T''_{d0} and T_{kd} by a factor of 0.522 [7] has minimal effect on the resulting field-to-stator frequency response.

The high-frequency time constants T''_{d0} and T''_d, calculated from the estimated d-axis model, are also close in value. Thus the effect of these time constants on the d-axis operational inductance TF, $L_d(s)$ (eqn. 5.5), is only small.

T''_{q0}, T''_q : As is the case for the d-axis, the subtransient time constants evaluated from the estimated q-axis model are close in value (i.e. $T''_{q0} = 5.76 \times 10^{-3}$s and $T''_q = 5.02 \times 10^{-3}$s). Thus, due to the near cancellation of their associated pole and zero, their effect on the q-axis operational inductance TF, $L_q(s)$ (eqn. 5.6), is also small.

[6] Note that two values of T'_{d0} are evaluated from the standstill tests, and thus two values of T'_d are calculated.

[7] So that T''_{d0} has the same value as calculated from the d-axis model.

Comparing the measured large-signal machine reactance values with those calculated from the estimated standstill machine TFs (namely $\omega_0 L_{d0}, \omega_0 L_{q0}$ and $\omega_0 k M_f$) highlights the fact that the standstill tests identify machine parameters that are representative of the incremental permeability of the machine iron. This is because the standstill tests are performed with only small-amplitude PRBS excitation signals. One possible benefit of using the RLS-BO estimation algorithm for performing standstill tests is the flexibility available in the choice of the excitation signal. As discussed briefly in section 5.3.5, a high-powered PWM signal could be used for exciting the windings of the machine for the standstill tests. This high-powered signal provides a means for performing large-signal tests, which may overcome the problem of the small-signal incremental permeability, as well as producing some level of saturation in the machine iron.

5.4.2 Machine Parameters: A Single Consistent Set

A problem with the standstill tests, as conducted, is that several of the machine parameters are derived from more than one test, resulting in two possibly differing values for some machine parameters. In order to obtain a single set of consistent machine parameters, the RLS-BO estimation algorithm can be modified to allow coefficients of either the numerator or denominator of the estimated w-domain model to be fixed during estimation. For the field-to-stator test, this is achieved by setting the denominator coefficients a_1 and a_0 of the estimated w-domain model (eqn. 5.40) to values consistent with the parameters T'_{d0} and T''_{d0} derived from the d-axis test, and estimating only the numerator coefficients b_1 and b_0. From these estimated numerator coefficients, the remaining unknown d-axis parameters G_0 and T_{kd} can be calculated.

After 32000 iterations, the modified RLS-BO estimation algorithm yields the second-order field-to-stator TF model

$$\frac{v_d}{v_f} = \frac{\beta(\beta 0.106656 + 36.121)}{\beta^2 + \beta 333.20 + 692.03} \tag{5.59}$$

Figure 5.17 shows the sinusoidal SSFR measurements together with the frequency response calculated from the estimated w-domain model (eqn. 5.59). The two sets of

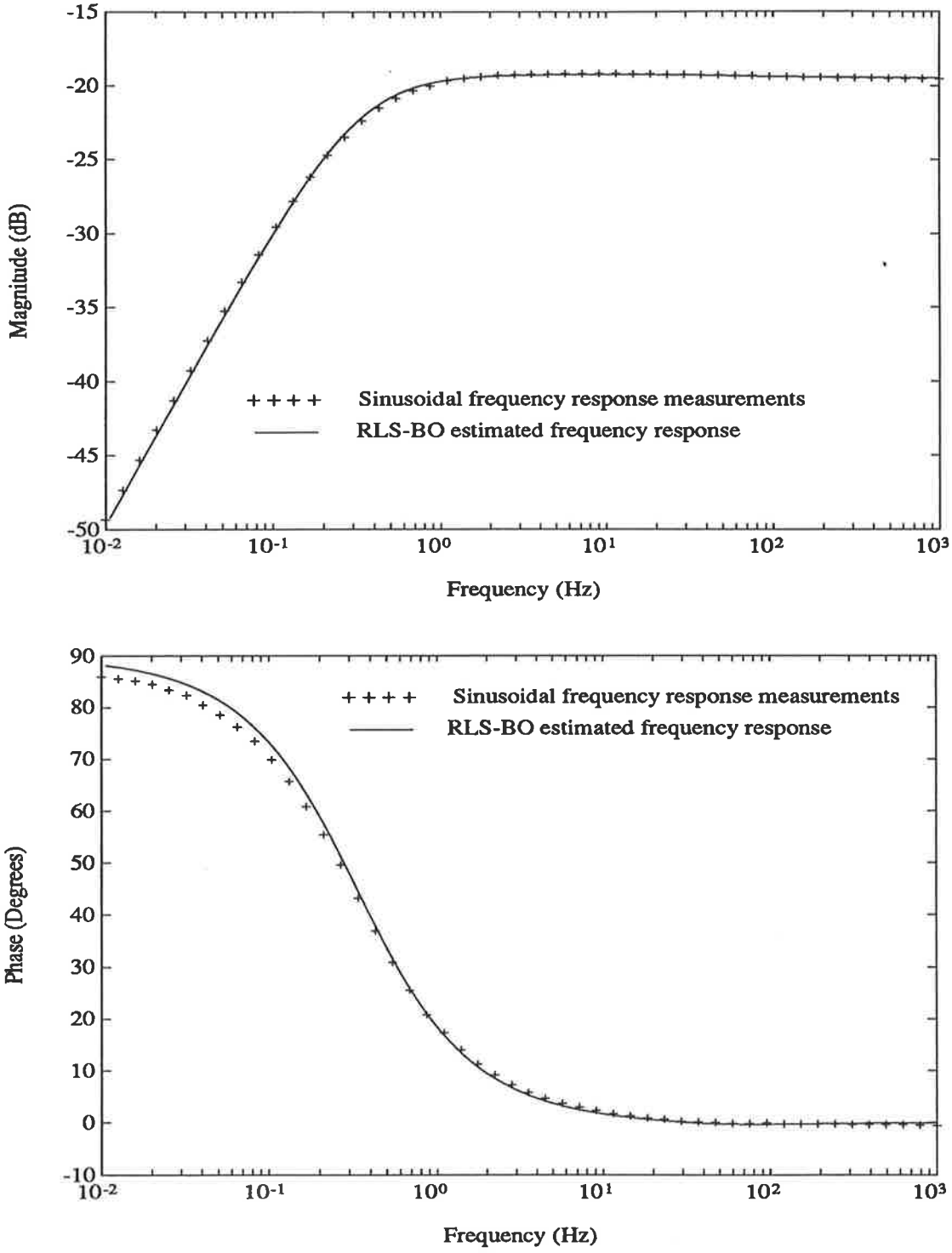

Figure 5.17: Sinusoidal SSFR measurement of the field-to-stator frequency response, magnitude and phase.

responses agree reasonably well over the entire measured frequency range. The phase errors become larger at low frequencies. Comparing these responses with those for the previously-estimated second-order field-to-stator model (Figure 5.14), the newly-estimated model provides a slight decrease in modeling error below 0.2 Hz, with a slight increase in error between 0.2 Hz to $\approx$ 20 Hz.

Using eqns. 5.41 and 5.42 and the estimated w-domain model (eqn. 5.59), the unknown machine parameters can be re-evaluated, and are given in Table 5.3. The

CONSTRAINED ESTIMATION FIELD-TO-STATOR RESULTS				
Fixed Coefficients		Fixed Parameters		
$\hat{a}_1$	333.20	T'_{d0}	0.479	s
$\hat{a}_0$	692.03	T''_{d0}	3.02×10^{-3}	s
Estimated Coefficients		Derived Machine Parameters		
$\hat{b}_1$	1.06656×10^{-3}	G_0	5.22×10^{-2}	
$\hat{b}_0$	36.121	T_{kd}	2.95×10^{-3}	s

Table 5.3: Estimated numerator coefficients of the field-to-stator machine TF and the derived machine parameters, with fixed denominator coefficients

calculated value of G_0 agrees well with that calculated previously in Table 5.2. The value of T_{kd} is reduced by a factor of 0.553.

5.5 Summary and Conclusions

In this chapter, the proposed RLS-BO estimation algorithm is successfully applied to the task of estimating the coefficients of the continuous-time TFs of a synchronous machine at standstill.

The algorithm is demonstrated by identifying three TFs of a 5 kV.A, 50 Hz, three-phase, salient-pole, laboratory synchronous machine at standstill. Accurate third- and second-order models are estimated for the d- and q-axis TFs respectively. A second-order model is estimated for the field-to-stator TF. This second-order model only approximately represents the field-to-stator response, with a small amount of low-frequency modeling error. It is found that a third-order model provides a more accurate modeling of this machine TF.

The unknown machine model parameters are easily calculated from the estimated TF coefficients. The effect of the incremental permeability [48] of the rotor and stator iron is observed in the evaluated machine TF gains (L_{d0}, L_{q0}, G_0).

One problem found with independently estimating the three machine TFs is obtaining a single consistent set of machine parameters. Several machine parameters are common to two of the estimated TF models. The RLS-BO estimation algorithm is modified to cope with this problem by setting some of the coefficients to be estimated to fixed values, evaluated from one of the previously estimated machine TFs.

The proposed RLS-BO estimation algorithm has several benefits over the conventional sinusoidal SSFR method of deriving the synchronous machine TFs at standstill. These benefits include: (i) The coefficients of the machine TFs are calculated directly from the measured input-output signals, as opposed to sinusoidal SSFR testing, which requires some form of iterative curve fitting technique to calculate the coefficients of the machine TFs from the measured magnitude and phase responses. (ii) The time required for the PRBS excitation test is significantly less than the time required for sinusoidal SSFR testing. A ratio of approximately 1:11 (RLS-BO : sinusoidal SSFR) is found for the practical machine tests. (iii) A general frequency-rich PRBS excitation signal is used to identify the TFs. This removes the requirement for a high-powered linear amplifier for sinusoidal testing, and leads to the possible use of high-powered PWM type excitation signals. The possible benefits of using high-powered signals are that large-signal standstill tests may be performed, and hence the small-signal incremental permeability effects of the machine iron are no longer relevant, whilst saturation effects can be included.

The original contribution of this chapter is:

- The application of the proposed RLS-BO estimation algorithm to performing standstill tests on an actual laboratory synchronous machine.

Chapter 6

Evaluation of Machine Parameters under Operating Conditions.

6.1 Introduction.

Conventionally, the parameters of synchronous machines are derived from such tests as the open-circuit and short-circuit tests, slip test, sudden short-circuit test, etc. As discussed in the previous chapter, the synchronous machine parameters can also be calculated from standstill tests performed on the synchronous machine. For all these tests, the synchronous machine must be offline for testing, restricting the times at which testing can be performed to planned shut-down periods of the machine. Another drawback of these test methods is that the conditions under which the machine parameters are evaluated are not necessarily representative of actual machine operating conditions.

For small-signal planning or design studies involving synchronous machines, parameters calculated from the above mentioned tests may not be suitable for accurately describing the small-signal behaviour of a synchronous machine. The synchronous machine model should employ small-signal incremental values of the machine parameters [79], relevant to the operating condition under which the study is conducted.

In this chapter, the RIV-BO estimation algorithm is used to estimate the coefficients of the small-signal field-to-terminal voltage TF of a synchronous generator operating both online in a single-machine infinite-bus (SMIB) configuration, and un-

der open-circuit conditions. A SMIB system is a relatively simple synchronous machine configuration, however, it can under certain conditions provide a reasonable representation of a machine on an interconnected power system [80]. From the estimated coefficients of the online TF, the small-signal linearised SMIB equations are employed to evaluate several of the unknown synchronous machine parameters. The parameters evaluated from the estimated TF coefficients are small-signal incremental machine parameters. These parameters are thus suitable for use in small-signal studies of synchronous machines, and have the advantage that they can be evaluated under the operating conditions for which the study will be performed. Another benefit of this online testing is that the machine can continue to operate under load during testing.

In section 6.2, the nonlinear equations describing a SMIB system are introduced. These equations are linearised about a steady-state operating condition, and rearranged to form a third-order, small-signal, field-to-terminal voltage TF of the SMIB system. Common simplifying assumptions are included in this third-order TF.

In section 6.3, the RIV-BO estimation algorithm is used to estimate the coefficients of a third-order small-signal field-to-terminal voltage TF of a laboratory SMIB system. Estimation is performed for three online operating conditions. To further demonstrate the practicality of the proposed RIV-BO estimation algorithm, estimation is performed for various other machine operating conditions, including both online and open-circuit conditions. These tests provide a practical evaluation of the proposed RIV-BO estimation algorithm.

In section 6.4, three of the estimated online TFs are used in conjunction with the linearised SMIB equations to evaluate several of the unknown parameters of the synchronous machine. Using the simplified linearised SMIB equations, several of the evaluated machine parameters appear inconsistent with known machine parameter values. In the following section (section 6.5), several of the assumptions made in deriving the simplified third-order field-to-terminal voltage TF are relaxed, with the aim of establishing consistent machine parameters from the estimated online TFs.

Section 6.6 contains a conclusion on the use of the RIV-BO estimation algorithm in estimating the coefficients of the field-to-terminal voltage TF of a synchronous gener-

ator operating online, and the subsequent evaluation of the small-signal synchronous machine parameters.

6.2 Model of the Single Machine Infinite Bus System

A third-order model is selected to represent the synchronous machine for these online tests. This model accounts for two stator windings and one field winding. Amortisseur or damper windings are not explicitly included in the model. Their effect can be included in a speed damping coefficient [32,43]. The reasons for not directly modeling discrete damper windings are, firstly, their effect is found to be small in the standstill frequency response tests performed in the previous chapter, and secondly, their effects are noticeable only at high frequencies (greater than approximately 30 Hz). For the online tests performed on this machine, a frequency range up to approximately 10 Hz is considered [14].

S.I. units are used for the system of equations representing the SMIB system. The reason S.I. units are selected over the per-unit system is that it avoids any possible confusion as to which base quantities have been selected for the system. The machine parameters evaluated in S.I. units can readily be converted to the desired per-unit values, based on the selected machine base quantities [1].

6.2.1 The Nonlinear SMIB Equations

Machine Equations

The conventional d- and q-axis model is selected for representing the SMIB system. Using generator convention, the flux-linkage equations of the synchronous machine with two d-axis and one q-axis windings are given by [1,43]

$$\begin{bmatrix} \psi_d \\ \psi_q \\ \psi_f \end{bmatrix} = \begin{bmatrix} -L_d & 0 & kM_f \\ 0 & -L_q & 0 \\ -kM_f & 0 & L_f \end{bmatrix} \begin{bmatrix} i_d \\ i_q \\ i_f \end{bmatrix} \tag{6.1}$$

The corresponding voltage equations are

$$\begin{bmatrix} v_d \\ v_q \\ v_f \end{bmatrix} = \begin{bmatrix} -r_a & 0 & 0 \\ 0 & -r_a & 0 \\ 0 & 0 & r_f \end{bmatrix} \begin{bmatrix} i_d \\ i_q \\ i_f \end{bmatrix} + \omega \begin{bmatrix} -\psi_q \\ \psi_d \\ 0 \end{bmatrix} + s \begin{bmatrix} \psi_d \\ \psi_q \\ \psi_f \end{bmatrix} \tag{6.2}$$

where s is the Laplace operator and ω the rotor speed in electrical radians per second. Combining eqns. 6.1 and 6.2 yields

$$\begin{bmatrix} v_d \\ v_q \\ v_f \end{bmatrix} = \begin{bmatrix} -r_a - L_d s & \omega L_q & kM_f s \\ -\omega L_d & -r_a - L_q s & \omega k M_f \\ -kM_f s & 0 & r_f + L_f s \end{bmatrix} \begin{bmatrix} i_d \\ i_q \\ i_f \end{bmatrix} \tag{6.3}$$

The synchronous machine parameters, and voltage, current and flux variables have been defined in chapter 5.

Machine Terminal Relations

The rms line-to-line machine terminal voltage, v_t, is related to the d- and q-axis terminal voltages by

$$v_t^2 = v_d^2 + v_q^2 \tag{6.4}$$

External Network Equations

The synchronous machine for this study is connected in a SMIB arrangement. In this configuration, the synchronous machine is connected to an infinite bus (three-phase mains supply) through an external reactance $r_e + j\omega L_e$ (Ω per phase). For a description of the laboratory SMIB system, see section 6.3.1. The resulting d-q-axis voltage equations of the external network are

$$\begin{aligned} v_d &= v_b \sin\delta + r_e i_d - \omega L_e i_q + L_e s i_d \\ v_q &= v_b \cos\delta + r_e i_q + \omega L_e i_d + L_e s i_q \end{aligned} \tag{6.5}$$

where v_b is the rms line-to-line voltage of the infinite bus, and δ the angle in radians between the infinite-bus voltage v_b and the q-axis of the synchronous machine.

Equation of Motion

The equation governing the shaft dynamics of the system is

$$[\omega(J/4)s + (B_1\omega + B_2(\omega - \omega_0))\omega] = P_{mech} - P_{elec} \tag{6.6}$$

where the total electrical power P_{elec} (W) is given by

$$P_{elec} = \omega(\psi_d i_q - \psi_q i_d) \tag{6.7}$$

The constants B_1 and B_2 represent viscous friction and windage damping effects, and damper winding effects, respectively (Nm/(rad/s)). The constant J is the polar moment of inertia of the rotor (kg m^2); the scaling by a factor of 4, i.e. $(J/4)$, is required because the machine is a 4 pole machine. The rotor speed ω is again in electrical radians per second.

The set of equations [eqns. 6.1, 6.3, 6.4, 6.5, 6.6 and 6.7] provide a nonlinear mathematical model for the SMIB system.

6.2.2 Linearised SMIB Equations.

The equations 6.1, 6.3, 6.4, 6.5, 6.6 and 6.7 are unsuitable for use directly for evaluating the unknown parameters of the synchronous machine from the estimated field-to-terminal voltage TFs. The recursive estimation algorithms are only used to estimate *linear* system models, and thus the set of nonlinear SMIB equations must be linearised about a steady-state operating condition.

The variables in the set of nonlinear equations of the SMIB system are flux, current, voltage, speed, rotor angle, and power. In linearising the equations, these variables are replaced by variables representing the perturbation of the corresponding signal about its steady-state value. When linearising the equations, the variation in the synchronous machine inductances with saturation must also be considered.

A common assumption when dealing with saturation of machine inductances is that the level of saturation is dependent on a resultant machine flux, which is a function of the d-q-axis currents of the machine [37]. For the derivation of the linearised

machine equations in this thesis, each machine inductance is assumed to be a function of the machine currents i_d, i_q and i_f. Hence

$$\begin{aligned} L_d &= L_d(i_d, i_q, i_f) \\ L_q &= L_q(i_d, i_q, i_f) \\ kM_f &= kM_f(i_d, i_q, i_f) \\ L_f &= L_f(i_d, i_q, i_f) \end{aligned} \tag{6.8}$$

To observe how this assumption effects the linearisation of the machine flux-linkage equations, consider the equation for the d-axis flux linkage from eqn. 6.1

$$\psi_d = -L_d(i_d, i_q, i_f)i_d + kM_f(i_d, i_q, i_f)i_f \tag{6.9a}$$

$$= \psi_d(i_d, i_q, i_f) \tag{6.9b}$$

The d-axis flux linkage is a function of all three d-q-axis machine currents. Linearising yields

$$\Delta\psi_d = \frac{\partial\psi_d}{\partial i_d}\Delta i_d + \frac{\partial\psi_d}{\partial i_q}\Delta i_q + \frac{\partial\psi_d}{\partial i_f}\Delta i_f$$

In this equation, the partial derivative terms $\partial\psi_d/\partial i_k$ $(k = d, q, f)$, give the variation in flux ψ_d with respect to i_k, with all other currents constant. With similar relationships holding for the ψ_q and ψ_f flux-linkage equations, the linearised form of eqn. 6.1 is

$$\begin{bmatrix} \Delta\psi_d \\ \Delta\psi_q \\ \Delta\psi_f \end{bmatrix} = \begin{bmatrix} -L_{dd} & A & kM_{df} \\ B & -L_{qq} & C \\ -kM_{fd} & D & L_{ff} \end{bmatrix} \begin{bmatrix} \Delta i_d \\ \Delta i_q \\ \Delta i_f \end{bmatrix} \tag{6.10}$$

where the small-signal incremental machine inductances are given by

$$L_{dd} = -\frac{\partial\psi_d}{\partial i_d} \tag{6.11a}$$

$$kM_{fd} = -\frac{\partial\psi_f}{\partial i_d} \tag{6.11b}$$

$$kM_{df} = \frac{\partial\psi_d}{\partial i_f} \tag{6.11c}$$

$$L_{ff} = \frac{\partial\psi_f}{\partial i_f} \tag{6.11d}$$

$$L_{qq} = -\frac{\partial \psi_q}{\partial i_q} \tag{6.11e}$$

$$A = \frac{\partial \psi_d}{\partial i_q} \tag{6.11f}$$

$$B = \frac{\partial \psi_q}{\partial i_d} \tag{6.11g}$$

$$C = \frac{\partial \psi_q}{\partial i_f} \tag{6.11h}$$

$$D = \frac{\partial \psi_f}{\partial i_q} \tag{6.11i}$$

The inductance terms A, B, C and D are due to intersaturation effects in the synchronous machine [81]. These intersaturation effects result from currents flowing on one axis of the d-q-axis machine model affecting saturation on the other.

The terms L_{dd}, L_{qq}, L_{ff}, kM_{fd} and kM_{df} are the small-signal incremental machine inductances. Their values vary with the steady-state operating conditions.

Equation 6.2 gives the machine voltages in terms of machine currents and flux linkages. Linearising eqn. 6.2 yields

$$\begin{bmatrix} \Delta v_d \\ \Delta v_q \\ \Delta v_f \end{bmatrix} = \begin{bmatrix} -r_a & 0 & 0 \\ 0 & -r_a & 0 \\ 0 & 0 & r_f \end{bmatrix} \begin{bmatrix} \Delta i_d \\ \Delta i_q \\ \Delta i_f \end{bmatrix} + \omega_0 \begin{bmatrix} -\Delta \psi_q \\ \Delta \psi_d \\ 0 \end{bmatrix} + \Delta\omega \begin{bmatrix} -\psi_{q0} \\ \psi_{d0} \\ 0 \end{bmatrix} + s \begin{bmatrix} \Delta \psi_d \\ \Delta \psi_q \\ \Delta \psi_f \end{bmatrix} \tag{6.12}$$

where the incremental variations in flux linkages are given by eqn. 6.10.

Linearising the terminal voltage relation (eqn. 6.4) yields

$$\Delta v_t = \left(\frac{v_{d0}}{v_{t0}}\right) \Delta v_d + \left(\frac{v_{q0}}{v_{t0}}\right) \Delta v_q \tag{6.13}$$

The linearised, external network equations are

$$\begin{aligned} \Delta v_d &= (v_{b0} \cos \delta_0 - L_e i_{q0} s)\Delta\delta + (r_e + L_e s)\Delta i_d - \omega_0 L_e \Delta i_q \\ \Delta v_q &= (-v_{b0} \sin \delta_0 + L_e i_{d0} s)\Delta\delta + (r_e + L_e s)\Delta i_q + \omega_0 L_e \Delta i_d \end{aligned} \tag{6.14}$$

In these equations, the external reactance ωL_e is assumed not to saturate. This is found to be the case with the iron-cored external reactances used in the laboratory

SMIB system (see section 6.3.1).

The linearised form of the equation of motion (eqn. 6.6) is

$$[\omega_0(J/4)s^2 + B'\omega_0 s]\Delta\delta = \omega_0(\psi_{d0}\Delta i_q - \psi_{q0}\Delta i_d + i_{q0}\Delta\psi_d - i_{d0}\Delta\psi_q) \tag{6.15}$$

where

$$B'\omega_0 = \omega_0(2B_1 + B_2) + \psi_{d0}i_{q0} - \psi_{q0}i_{d0} - K \tag{6.16}$$

and

$$\Delta\omega = s\Delta\delta \tag{6.17}$$

The damping coefficient K in eqn. 6.16 accounts for damping effects in the DC motor used as the prime mover in the laboratory SMIB system (see section 6.3.1).

Equations 6.10 to 6.15 represent the small-signal linearised equations of the SMIB system, which take account of the variation in the machine parameters due to saturation.

As these equations appear, they are still not very useful for the practical evaluation of the synchronous machine parameters from the estimated field-to-terminal voltage TF. However, with a few simplifying assumptions, the linearised system of equations can be reduced to a form which can be used later for evaluating the relevant synchronous machine parameters from the estimated field-to-terminal voltage TF.

6.2.3 Simplified Linearised SMIB Equations

Several simplifying assumptions are employed to reduce not only the order of the linearised SMIB equations, but also the number of unknown machine parameters.

Assumption A1 : Assume intersaturation effects are negligible.

Assumption A1 is equivalent to setting the incremental inductance terms A, B, C and D in eqn. 6.10 to zero. Whilst not necessarily a realistic assumption [81], it is made to reduce the number of unknown machine parameters.

Assumption A2 : Assume the incremental mutual inductance terms, kM_{fd} and kM_{df}, are equal.

The inductance terms kM_{fd} and kM_{df} represent the incremental mutual inductances between the two d-axis windings of the machine. For coupled lossless nonlinear inductances, the reciprocity property must hold for their mutual inductance terms [38] i.e.

$$kM_{fd} = \frac{\partial \psi_f}{\partial i_d} = kM_{df} = \frac{\partial \psi_d}{\partial i_f}$$

Thus, by assuming the small-signal mutual inductance terms to be equal in the synchronous machine model, the d-axis windings are implicitly assumed to be lossless. It is common practice to consider these inductances to be equal [42].

Assumption A3 : Assume the transformer-voltage and speed-variation terms are negligible in the stator voltage equations.

Assumption A3 is a common assumption in deriving the simplified SMIB system equations [1,37,43]. This assumption significantly reduces the complexity of the SMIB model, and reduces the system from fifth to third order.

Applying Assumptions A1, A2 and A3 to the linearised equations (6.10 to 6.15) yields the following set of simplified equations describing the small-signal dynamic behaviour of the SMIB system

$$\begin{bmatrix} \Delta\psi_d \\ \Delta\psi_q \\ \Delta\psi_f \end{bmatrix} = \begin{bmatrix} -L_{dd} & 0 & kM_{ff} \\ 0 & -L_{qq} & 0 \\ -kM_{ff} & 0 & L_{ff} \end{bmatrix} \begin{bmatrix} \Delta i_d \\ \Delta i_q \\ \Delta i_f \end{bmatrix} \tag{6.18}$$

$$\begin{bmatrix} \Delta v_d \\ \Delta v_q \\ \Delta v_f \end{bmatrix} = \begin{bmatrix} -r_a & \omega_0 L_{qq} & 0 \\ -\omega_0 L_{dd} & -r_a & \omega_0 kM_{ff} \\ -kM_{ff}s & 0 & r_f + L_{ff}s \end{bmatrix} \begin{bmatrix} \Delta i_d \\ \Delta i_q \\ \Delta i_f \end{bmatrix} \tag{6.19}$$

$$\Delta v_t = \left(\frac{v_{d0}}{v_{t0}}\right) \Delta v_d + \left(\frac{v_{q0}}{v_{t0}}\right) \Delta v_q \qquad \text{...(Eqn. 6.13)}$$

$$\begin{aligned} \Delta v_d &= v_{b0} \cos\delta_0 \Delta\delta + r_e \Delta i_d - \omega_0 L_e \Delta i_q \\ \Delta v_q &= -v_{b0} \sin\delta_0 \Delta\delta + r_e \Delta i_q + \omega_0 L_e \Delta i_d \end{aligned} \tag{6.20}$$

$$[\omega_0(J/4)s^2+B'\omega_0 s]\Delta\delta = -\omega_0(\psi_{d0}\Delta i_q-\psi_{q0}\Delta i_d+i_{q0}\Delta\psi_d-i_{d0}\Delta\psi_q) \quad ...(\text{Eqn. 6.15})$$

6.2.4 Deriving the Field-to-Terminal Voltage Transfer Function, $\Delta v_t/\Delta v_f$

Eqns. 6.13, 6.15, 6.18, 6.19 and 6.20 represent the simplified linearised model of the SMIB system; these equations are now rearranged to form the TF $\Delta v_t/\Delta v_f$.

A relatively simple method for rearranging these SMIB equations into the required TF form is firstly to express the linearised system of equations in matrix form [43]

$$\begin{bmatrix} 0 \\ \Delta v_f \\ 0 \\ 0 \\ 0 \\ 0 \\ 0 \\ 0 \\ 0 \\ 0 \end{bmatrix} = \begin{bmatrix} M1 & M2 \\ M3 & M4 \end{bmatrix} \begin{bmatrix} \Delta\delta \\ \Delta v_t \\ \Delta\psi_f \\ \Delta v_d \\ \Delta v_q \\ \Delta i_f \\ \Delta i_d \\ \Delta i_q \\ \Delta\psi_d \\ \Delta\psi_q \end{bmatrix} \tag{6.21}$$

where $M1$ to $M4$ are matrices defined by

$$M1 = \begin{bmatrix} \omega_0(J/4)s^2 + \omega_0 B' & 0 \\ 0 & 0 \end{bmatrix}$$

$$M2 = \begin{bmatrix} 0 & 0 & 0 & 0 & -\omega_0\psi_{q0} & \omega_0\psi_{d0} & \omega_0 i_{q0} & -\omega_0 i_{d0} \\ 0 & 0 & 0 & r_f + L_{ff}s & -kM_{ff}s & 0 & 0 & 0 \end{bmatrix}$$

$$M3 = \begin{bmatrix} 0 & 0 \\ 0 & 0 \\ 0 & 0 \\ 0 & 0 \\ 0 & 0 \\ v_{b0}\cos\delta_0 & 0 \\ -v_{b0}\sin\delta_0 & 0 \\ 0 & -1 \end{bmatrix}$$

and

$$M4 = \begin{bmatrix} 0 & -1 & 0 & 0 & -r_a & L_{qq}\omega_0 & 0 & 0 \\ 0 & 0 & -1 & kM_{ff}\omega_0 & -L_{dd}\omega_0 & -r_a & 0 & 0 \\ -1 & 0 & 0 & L_{ff} & -kM_{ff} & 0 & 0 & 0 \\ 0 & 0 & 0 & kM_{ff} & -L_{dd} & 0 & -1 & 0 \\ 0 & 0 & 0 & 0 & 0 & -L_{qq} & 0 & -1 \\ 0 & -1 & 0 & 0 & r_e & -X_e & 0 & 0 \\ 0 & 0 & -1 & 0 & X_e & r_e & 0 & 0 \\ 0 & v_{d0}/v_{t0} & v_{q0}/v_{t0} & 0 & 0 & 0 & 0 & 0 \end{bmatrix}$$

Equation 6.21 can be reduced to

$$\begin{bmatrix} 0 \\ \Delta v_f \end{bmatrix} = \left\{ M1 - M2(M4^{-1})M3 \right\} \begin{bmatrix} \Delta\delta \\ \Delta v_t \end{bmatrix} \tag{6.22}$$

and then reduced further by eliminating the variable $\Delta\delta$, to yield the third-order field-to-terminal voltage TF

$$\frac{\Delta v_t}{\Delta v_f} = \frac{b_2 s^2 + b_1 s + b_0}{s^3 + a_2 s^2 + a_1 s + a_0} \tag{6.23}$$

The six coefficients of this TF, namely a_2, a_1, a_0, b_2, b_1 and b_0 are nonlinear functions of the SMIB system parameters and the steady-state operating condition. Given any steady-state operating condition, and the corresponding machine and external network parameters, the coefficients of the field-to-terminal voltage TF can be cal-

culated. The process can also proceed in the opposite direction, namely, given the six TF coefficients and the steady-state operating conditions, six unknown machine parameters can be evaluated, providing the set of nonlinear equations can be solved.

The derivation of the machine parameters from the TF coefficients is described later in section 6.4.1. Firstly, however, the estimation of the field-to-terminal voltage TF of the laboratory SMIB system is investigated.

6.3 Estimation of $\Delta v_f/\Delta v_t$ Transfer Function

In the previous section, the simplified linearised SMIB equations are arranged to yield the third-order small-signal field-to-terminal voltage TF. In this section, the coefficients of this third-order TF are estimated for several different operating conditions of the laboratory SMIB system.

In sections 6.3.2, 6.3.3 and 6.3.4, the coefficients of the system TF are estimated for three closely spaced operating conditions listed in Table 6.1. The operating condi-

		OP2	OP1	OP3
P_{t0}	W	3350	3360	3330
Q_{t0}	var	−80	23	127
v_{t0}	V	374	384	390
v_{b0}	V	418	419	416

Table 6.1: SMIB Operating Conditions, OP1, OP2 and OP3.

tions all have a real output power level of approximately 3.3 kW (near the maximum attainable with the laboratory SMIB system, see section 6.3.1), and vary in reactive power from approximately –80 var to 130 var. The three closely spaced operating conditions are selected so that, when the machine parameters are derived later, any trends or common variation in parameters may be clearly seen. Largely spaced operating conditions, because of the nonlinear nature of the SMIB system, may reveal a seemingly random variation in parameters between operating conditions.

In section 6.3.6, the results of several online and open-circuit estimation studies are given to demonstrate further the application of the proposed estimation method.

6.3.1 Background to Estimation Tests

Laboratory SMIB System

Figure 6.1 provides a schematic diagram of the laboratory SMIB system. The syn-

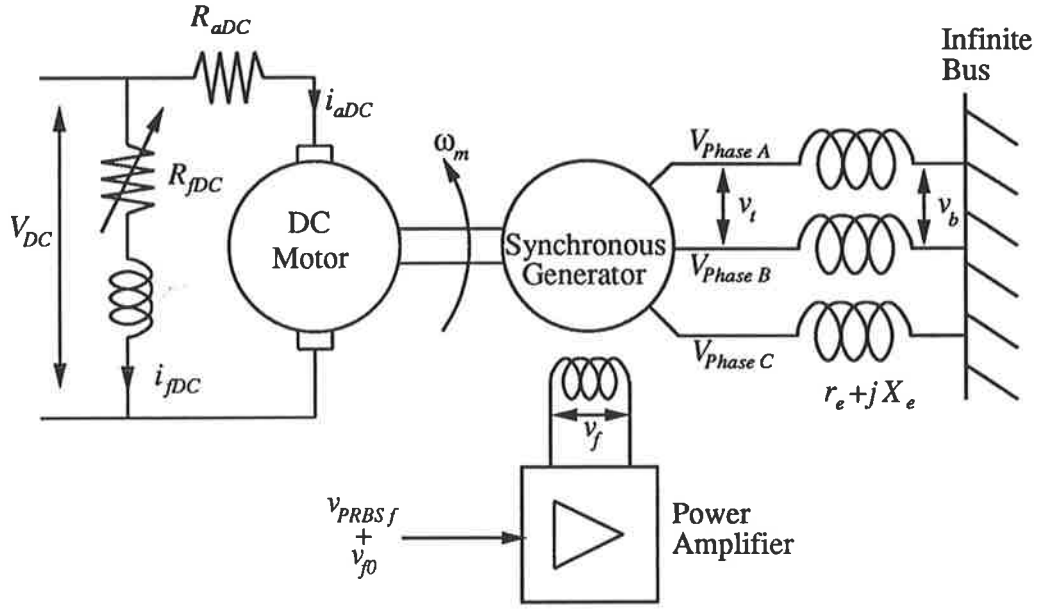

Figure 6.1: The laboratory SMIB system.

chronous machine is a 5 kV.A, three-phase, 415 V, four pole, salient-pole machine. This is the same machine used in the standstill tests described in the previous chapter. This is a small general-purpose synchronous machine, and its parameters are not representative of those of large industrial machines. The purpose of the laboratory system is to demonstrate the applicability of the proposed estimation method to estimation under actual operating conditions.

The laboratory synchronous machine is connected to the three-phase mains supply (infinite bus) through non-saturating iron-cored reactors simulating transmission lines. The external reactance values are measured at $r_e + jX_e = 1.7 + j22.4\ \Omega$ per phase.

The field voltage v_f of the synchronous machine is supplied by a power operational amplifier. The amplifier has the facility for superimposing on its steady-state output voltage any small-signal voltage perturbation applied to its input terminals. This facility is employed for exciting the SMIB system with the PRBS excitation signal

required for estimation. There is no automatic voltage regulator on the laboratory SMIB system.

The laboratory synchronous machine is driven by a separately-excited DC motor (prime mover) connected to the 220 V dc mains supply. The power output of the DC motor is adjusted by varying the external field circuit resistance R_{fDC}.

Due to the limitations in the configuration of the DC motor, the SMIB is limited to operating conditions in which the real output power is less than approximately 3.4 kW. Due to the limited voltage range of the power operational amplifier employed for the field voltage supply, the range of operating conditions with lagging power factors is also limited.

Interface and Measurement Electronics

In order to estimate the coefficients of the small-signal field-to-terminal voltage TF of the SMIB system, transducers, the associated filters and amplifiers are constructed for measuring both the field and terminal voltage small-signal perturbations, Δv_f and Δv_t. Figure 6.2 gives a block diagram of the arrangement of the electronic equipment for measuring these perturbation signals.

A three-phase precision rectifier is constructed for measuring the terminal voltage perturbation Δv_t [82]. The circuitry consists of a three-phase rectifier, followed by a first-order high-pass filter and a fifth-order low-pass Butterworth filter (cut-off frequencies $f_c = 0.023$ Hz, and $f_c = 40$ Hz, respectively). The low-pass filter, as well as reducing the rectification ripple, acts as the anti-aliasing filter.

To measure the field-voltage perturbation Δv_f, a low-pass and high-pass filter configuration, identical to those employed for the terminal voltage transducer, are used.

A second-order low-pass filter (Signal Conditioning Filter) is used to filter the PRBS generated by the real-time system (RTS) before connection to the power amplifier.

The details of these transducers and filters are given in Appendix D.

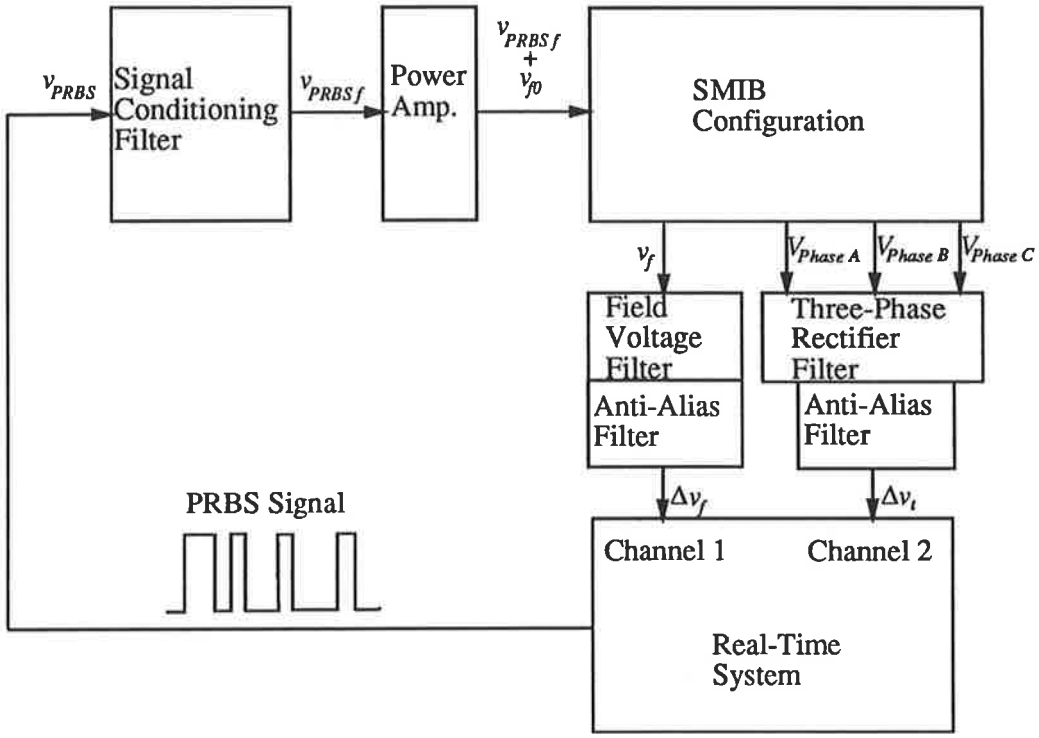

Figure 6.2: Block diagram of the arrangement for the measurement of the field- and terminal-voltage signals of the laboratory SMIB system.

PRBS Parameter Selection

From prior knowledge of the parameters of the SMIB system, obtained from both standstill and conventional large-signal tests, it is expected that the corner frequencies of the poles and zeros of the small-signal field-to-terminal voltage TF will lie within the range of approximately 0.5 Hz to 3 Hz. This frequency range was confirmed by preliminary online tests with the SMIB system.

The sampling frequency of the RTS is $f_s = 1$ kHz. This frequency is significantly higher that the expected frequency range of interest for this TF. This sampling frequency corresponds to a sampling period of $\Delta = 0.001$s, and should ensure that the coefficients of the discrete-time w-domain model closely approximate those of the continuous-time model. With $\Delta = 0.001$s, the PRBS parameters N and k are selected as $N = 2^9 - 1 = 511$, and $k = 50$. As explained in section 4.2, this yields a PRBS which excites frequencies evenly across the frequency range from 0.039 Hz to 8.8 Hz at 0.039 Hz intervals.

The other PRBS parameter of interest, particularly for this online estimation task, is the amplitude of the PRBS. Ideally, the disturbance to the SMIB system during measurement should be minimal, and thus a small amplitude PRBS selected. This also ensures the nonlinear SMIB system can be accurately represented by the small-signal linearised model, linearised about the steady-state operating condition. In contrast to these requirements, to improve the SNR for estimation, a large amplitude PRBS is desirable.

As a compromise, the PRBS amplitude is selected, after several exploratory online tests, such that the perturbation in the terminal voltage is approximately $\pm 1\%$ [43].

Prefilter Selection

As stated in the discussion on **PRBS Parameter Selection** above, the frequency range of interest is expected to extend from at least 0.5 Hz to 3 Hz. Thus the estimation prefilter should leave this frequency range unattenuated.

Significant coloured noise is present on the measured terminal voltage, the noise being predominantly low-frequency noise, plus high-frequency harmonics of 25 Hz and 50 Hz. The terminal voltage signal also contains 'bursts' of oscillatory noise, at

the modal frequency of the SMIB system, which is approximately 2.5 Hz [14]. The prefilter should attenuate the high-frequency harmonics, and reduce the low-frequency noise and any dc offset.

Another possible concern for estimation is high-frequency unmodeled dynamics. The third-order model to be estimated is only an approximation to the true field-to-terminal voltage TF of the system. To ensure the estimated model provides an accurate representation of the system over the frequency range of interest, the prefilter should attenuate any unmodeled dynamics outside of this frequency range.

A good compromise for the prefiltering is to filter both the measured input (Δv_f) and output (Δv_t) signals with a band-pass filter, consisting of a first-order high-pass filter (cut-off frequency $f_c = 0.05$ Hz), and a fourth-order Butterworth low-pass filter (cut-off frequency $f_c = 10$ Hz).

Recursive Estimation Algorithm

The noise present on the measured terminal voltage is mainly low frequency, with bursts of oscillatory noise. The previously described anti-aliasing filters (see Figure 6.2), with a cut-off frequency $f_c = 40$ Hz, and the low-pass section of the prefilter, reduce significantly the higher-frequency noise and harmonics. With the PRBS perturbation of the field voltage causing a terminal voltage variation of between $\pm 1\%$ of its steady-state value, a SNR of approximately 50 results. This noise level is reasonably low, however, due to the spectral characteristics of the terminal voltage noise, the RIV-BO estimation algorithm is selected for this online estimation task.

As employed in several of the simulation studies in chapter 4, a switched forgetting factor of the form

$$\lambda_0 = 0.995, \lambda_1 = 0.9995, \lambda_2 = 0.999;$$

switched at iterations 1000 and 10000, is employed for the online estimation task.

As discussed in chapter 3, the RIV-BO estimation algorithm is operated initially as a RLS-BO algorithm and is then switched to the RIV-BO algorithm after 5000 iterations.

6.3.2 Estimated Transfer Function: Operating Condition OP1

To measure the small-signal field-to-terminal voltage TF, the laboratory SMIB system is set up at the operating condition:

Operating Condition: OP1		
P_{t0}	3360	W
Q_{t0}	23	var
v_{t0}	384	V
v_{b0}	419	V

The machine is run for approximately one hour to allow components to reach normal operating temperatures. The steady-state operating conditions listed above are measured, and then the small-signal variation of Δv_f and Δv_t sampled with the PRBS perturbation present on the field voltage.

The measured field and terminal voltage signals $(\Delta v_f, \Delta v_t)$ are prefiltered and then used in the RIV-BO estimation algorithm to estimate the coefficients of a third-order, w-domain model. The $J(w)$ filter polynomial chosen for estimation is

$$\begin{aligned} J(w) &= (w+5.7)(w+1+j15.9)(w+1-j15.9) \\ &= w^3 + w^2 7.7 + w 265.21 + 1446.7 \end{aligned} \tag{6.24}$$

This is chosen after several estimation runs with the sampled signals, to match approximately the low frequency real pole of the estimated w-domain model and also to match the complex zeros of the model. As demonstrated in Simulation Study 6 (section 4.6.1), this form of $J(w)$ filter polynomial is beneficial in estimation when the continuous-time system contains lightly-damped complex zeros. After 32000 iterations, the estimated w-domain model is (expressed in TF form)

$$\hat{H}_{OP1}(\beta) = \frac{\beta^2 29.11 + \beta 12.51 + 7401}{\beta^3 + \beta^2 8.08 + \beta 247.2 + 1330} \tag{6.25}$$

The poles and zeros of this model are:

Zeros : $-0.215 \pm j15.94$

Poles : $-1.19 \pm j15.24$

-5.69

Figure 6.3 displays the coefficient estimates during estimation. Due to the wide vari-

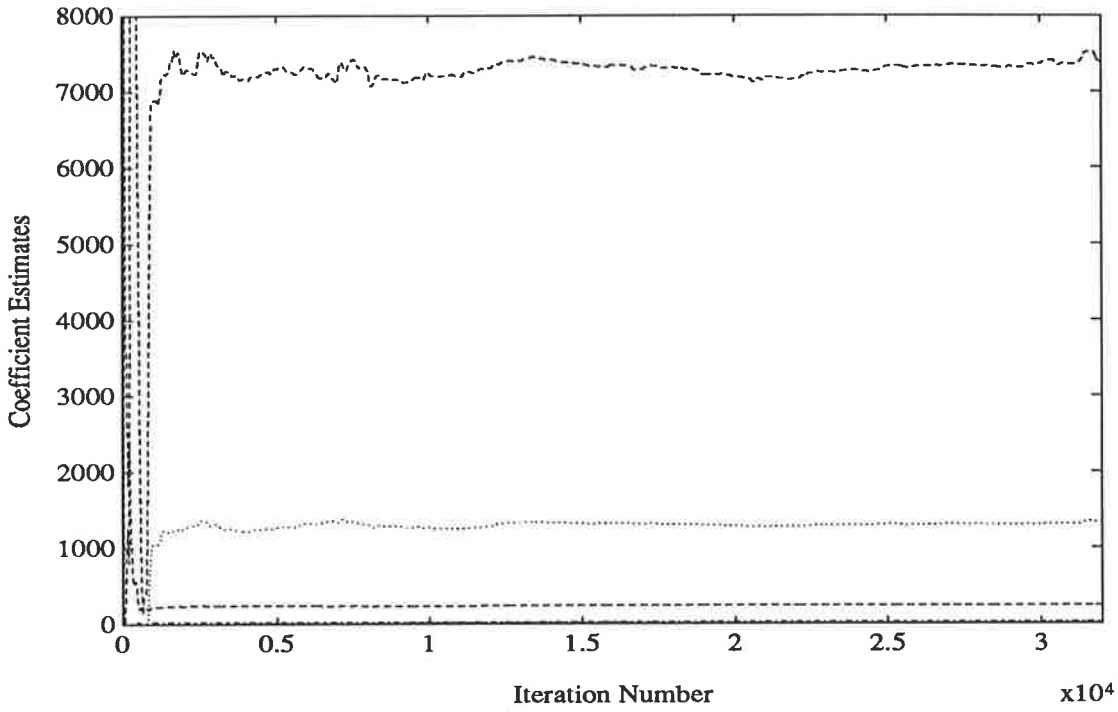

Figure 6.3: RIV-BO estimates of the field-to-terminal voltage TF coefficients, OP1.

ation in the magnitudes of the TF coefficients, it is difficult to conclude from this figure if all coefficient estimates have converged. Figure 6.4 displays the coefficient estimates again, this time normalised by the final value of each coefficient estimate. From this figure it is clear that after approximately 10000 iterations the coefficient estimates, except for $\hat{b}_1$, have converged. The coefficient estimate $\hat{b}_1$ displays significantly greater variation than all other coefficient estimates. Even after 32000 iterations, the estimate continues to vary. Because the numerator of the estimated model is second-order, and the zeros are complex, the coefficient $\hat{b}_1$ determines the damping constant of the zeros. [1] From the Bode plot of this estimated model (see Figure 6.5), the effect of the complex zeros at the frequency $f \approx 2.5$ Hz is clearly

[1]The damping constant is defined as the real part, $-\alpha$, of the complex roots, $-\alpha \pm j\beta$.

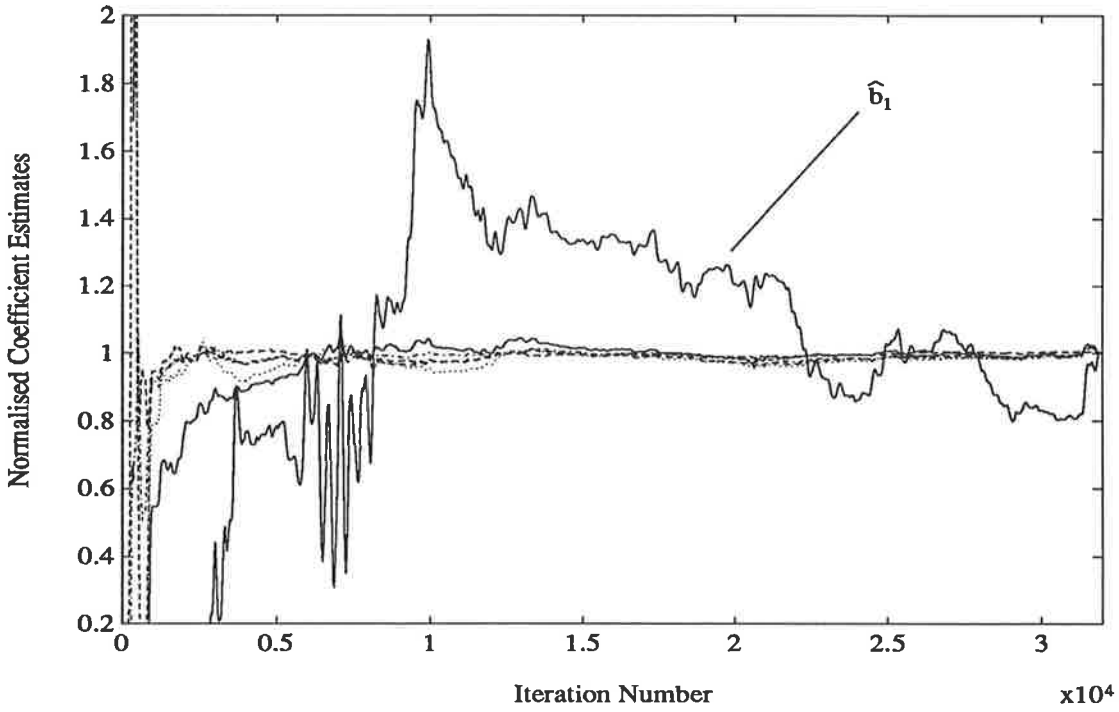

Figure 6.4: Normalised RIV-BO estimates of the field-to-terminal voltage TF coefficients, OP1.

seen by the 'notch' in the magnitude response. The damping constant of the zeros, and thus the coefficient $\hat{b}_1$, determines the magnitude of this 'notch'. Because of the significant attenuation of the magnitude plot at this 'notch' frequency relative to the low-frequency magnitude, it is not surprising that this coefficient $\hat{b}_1$ is difficult to estimate. A further difficulty associated with the accurate estimation of $\hat{b}_1$ is that the corner frequency of the complex zeros occurs close to the frequency of the oscillatory response mode of the system associated with rotor oscillations. Any external system disturbance, in either the infinite bus voltage or the DC motor prime mover, translates to an oscillatory disturbance at this modal frequency [14].

Although the variation in the coefficient estimate $\hat{b}_1$ is relatively large, the effect on the frequency response of the estimated model is relatively small. For example, Figure 6.5 displays the Bode plots calculated from the coefficient estimates taken at both 30000 and 32000 iterations. From Figure 6.4, the difference between the estimated $\hat{b}_1$ values at 30000 and 32000 iterations is approximately 20%. However, a comparison of the calculated Bode plots (Figure 6.5) reveals only a relatively small error between the responses.

To assess the accuracy of the estimated model in representing the field-to-terminal voltage response, the following model validation tests, previously outlined in section 5.3.1, are performed.

Sampling Frequency Test

(i) The highest corner frequency of the poles and zeros of the estimated w-domain model is $f_c \approx 2.5$ Hz. The –3 dB bandwidth occurs at a frequency of $f \approx 0.92$ Hz. The sampling frequency is significantly greater than ten times either of these frequencies.

(ii) Assuming the estimated w-domain model (eqn. 6.25) to be the true continuous-time TF, the coefficients predicted by the triangle-hold-equivalent w-domain model are within approximately 0.05% of those of the estimated w-domain model.

Thus the sampling frequency $f_s = 1$ kHz is sufficiently high for the coefficients of the estimated w-domain model to closely approximate those of the equivalent continuous-time TF.

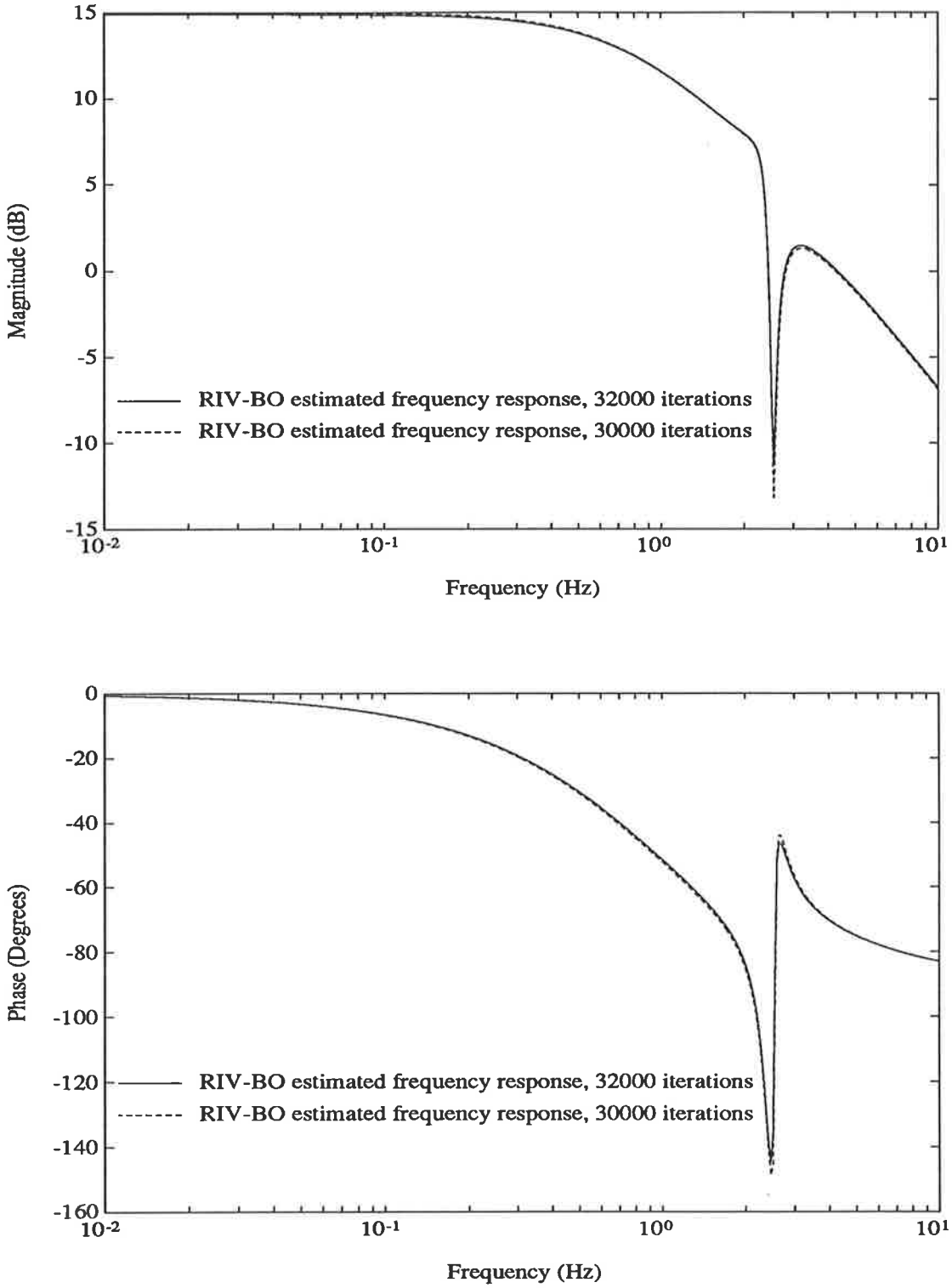

Figure 6.5: The effect of the coefficient $\hat{b}_1$ on the frequency response of the estimated w-domain model.

Simulation-Mode Test

Figure 6.6 displays the cross-correlation measure, $k(\tau)$, between the measured field-voltage perturbation, Δv_f, and the error between the measured and simulated terminal voltage signals, $e(k) = \Delta v_t(k) - \Delta v_{mt}(k)$. For the range of delays up to 1000

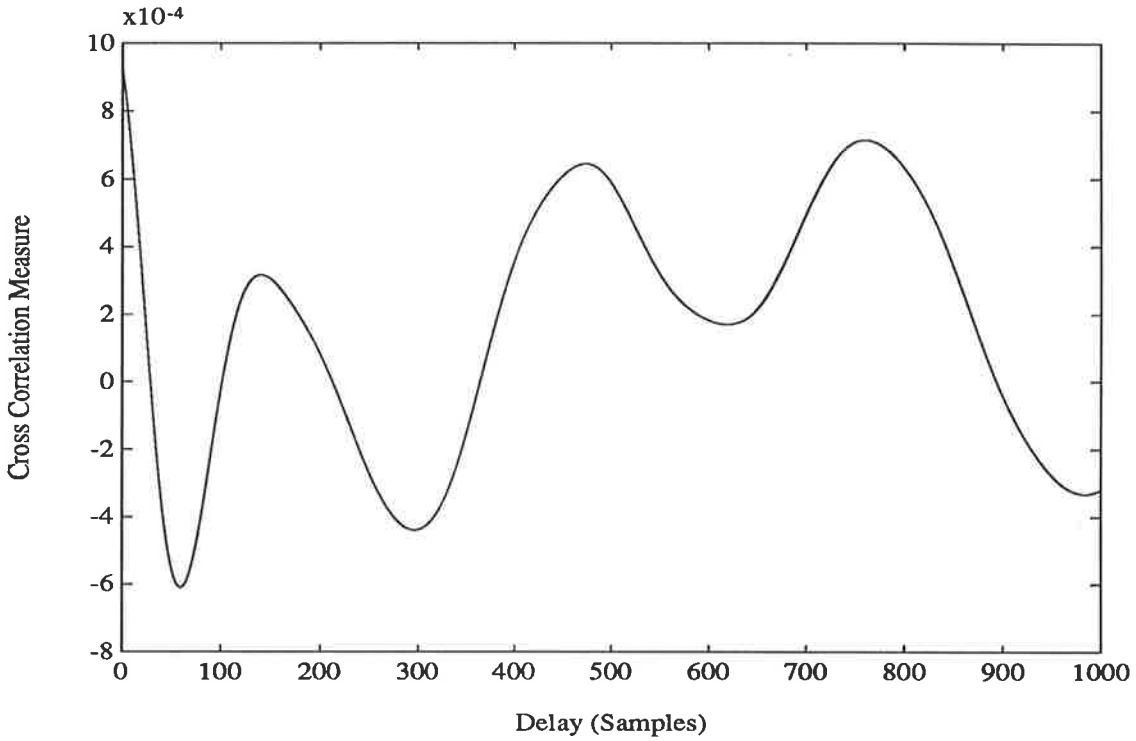

Figure 6.6: Cross correlation measure, $k(\tau)$, between the field voltage perturbation and the error signal, $e(k) = \Delta v_t(k) - \Delta v_{mt}(k)$, for the estimated field-to-terminal voltage TF, OP1.

samples there is no significant peak in the cross correlation measure. The magnitude of the cross-correlation measure, $k(\tau)$, is comparable to that calculated from the estimated field-to-stator model in chapter 5, section 5.3.4. This implies that there is some modeling error present, however, it is relatively small. Considering the significant level of coloured noise present for estimation, relative to that for the standstill tests, and the difficulty associated with estimating the coefficient $\hat{b}_1$, it is not surprising that there is some modeling error present. To investigate the estimated model accuracy further, the other model validation tests are performed.

Spectral Estimation Test

Using the measured Δv_f and Δv_t signals, spectral estimation is used to evaluate an estimate of the field-to-terminal voltage frequency response. Figure 6.7 displays the spectral estimate, together with the Bode plot calculated from the RIV-BO estimated model (eqn. 6.25). The two responses show close agreement over the displayed frequency range. The phase plot reveals approximately a 3 to 4 degree phase error at high frequencies.

Sinusoidal Frequency Response Measurement Test

For verification of the accuracy of the estimated model, small-signal sinusoidal frequency response (SSSFR) measurements are taken of the field-to-terminal voltage TF at OP1. The SSSFR tests employ the field and terminal voltage transducers previously described. The level of the sinusoidal excitation used for these tests is comparable to that used for the PRBS excitation test. The SSSFR measurements provide an independent assessment of how accurately the estimated model represents the actual $\Delta v_t/\Delta v_f$ TF. Figure 6.8 displays the SSSFR measurements [2] together with the Bode plot calculated from the estimated w-domain model (eqn. 6.25). The two responses show close agreement over the measured frequency range from 0.02 Hz to greater than 10 Hz.

It should be noted that the SSSFR measurements were taken after the RIV-BO estimation was performed. The SSSFR measurements had no bearing on the selection of the prefilter or $J(w)$ filter polynomial for RIV-BO estimation.

These model validation tests confirm that the estimated w-domain model provides an accurate model for the small-signal response of the field-to-terminal voltage TF of the SMIB system. The simulation-mode test indicates that there is a small amount of modeling error present, with both the spectral estimation test and SSSFR measurement test confirming the error is small.

[2] Using a Solartron Schlumberger 1253 gain-phase analyser.

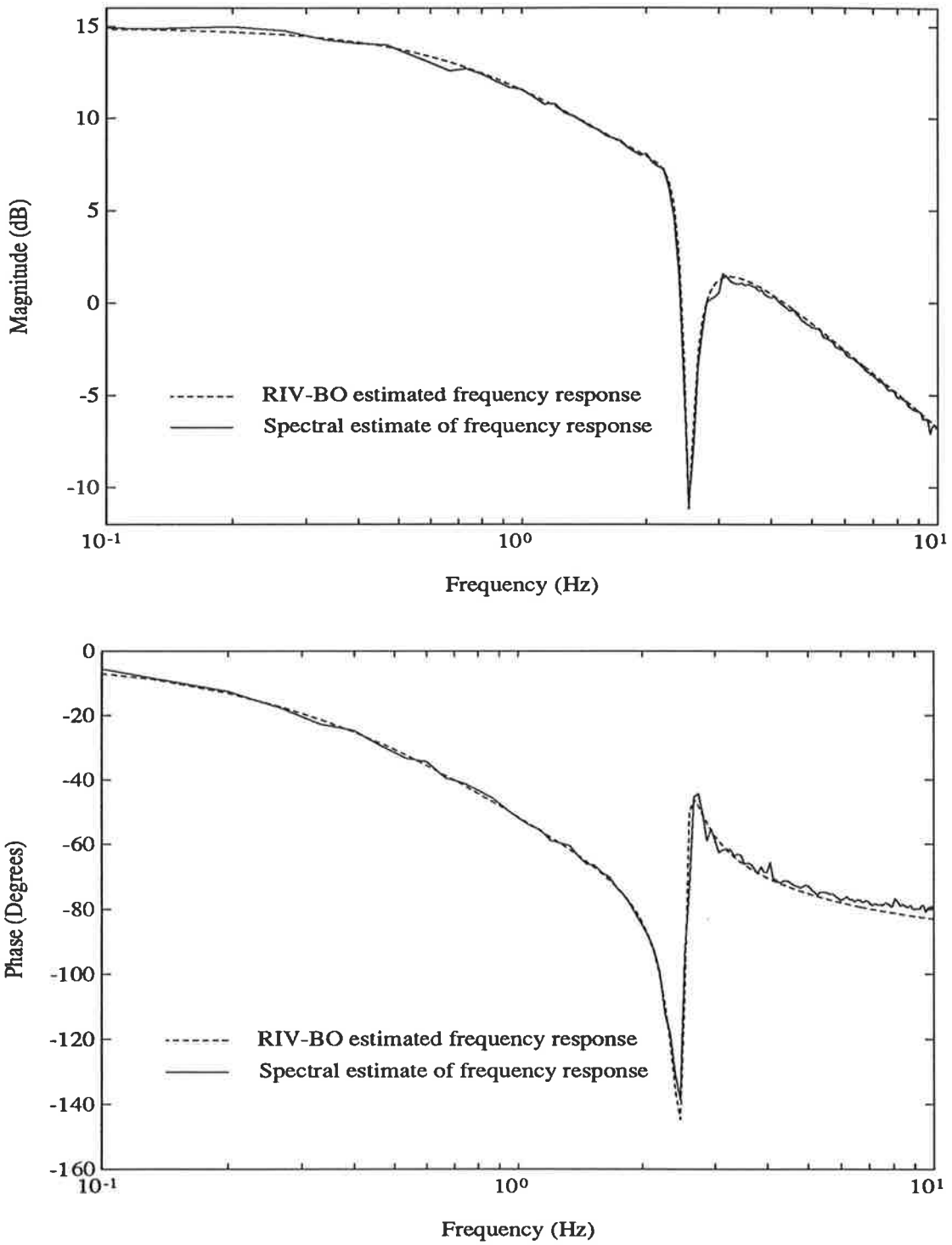

Figure 6.7: Spectral estimate of the field-to-terminal voltage frequency response, magnitude and phase, OP1.

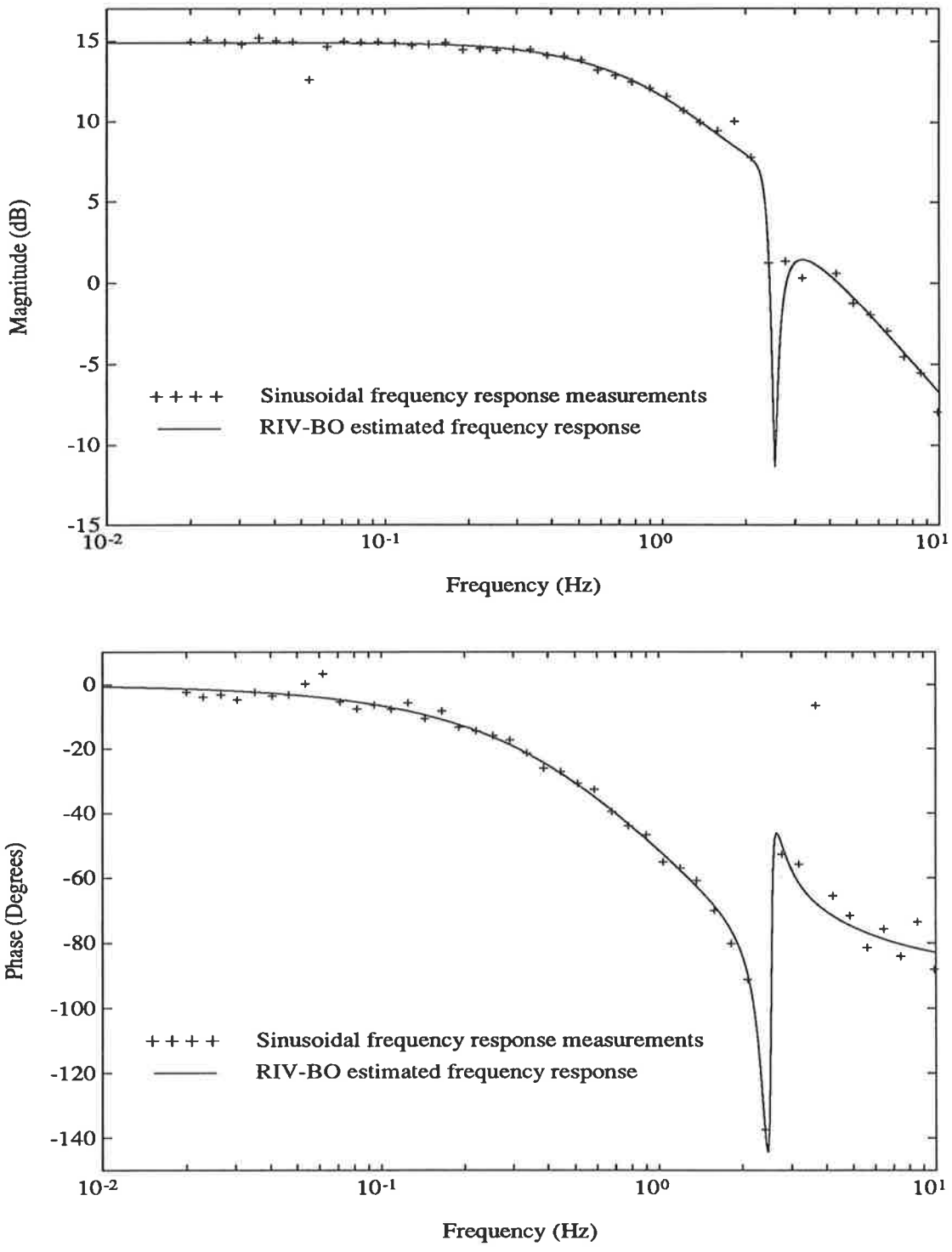

Figure 6.8: SSSFR measurement of the field-to-terminal voltage frequency response, magnitude and phase, OP1.

6.3.3 Estimated Transfer Function: Operating Condition OP2

The second steady-state operating condition investigated is

Operating Condition: OP2		
P_{t0}	3350	W
Q_{t0}	-80	var
v_{t0}	374	V
v_{b0}	418	V

At this operating condition, the PRBS perturbation is applied to the machine field voltage, and measurements made of the resulting Δv_f and Δv_t variations.

As for the previous test, the measured signals are prefiltered prior to use in the RIV-BO estimation algorithm. After several estimation runs the $J(w)$ filter polynomial

$$\begin{aligned} J(w) &= (w+5.1)(w+1+j15.6)(w+1-j15.6) \\ &= w^3 + w^2 7.1 + w254.56 + 1246.2 \end{aligned} \tag{6.26}$$

is selected. This $J(w)$ filter polynomial approximately matches the low-frequency pole and complex zeros of the estimated w-domain model.

The estimated w-domain model after 32000 iterations is

$$\hat{H}_{OP2}(\beta) = \frac{\beta^2 28.23 + \beta 13.07 + 6882}{\beta^3 + \beta^2 7.64 + \beta 234.5 + 1138} \tag{6.27}$$

Figure 6.9 displays the variation of the normalised coefficient estimates during estimation. Again, all of the coefficient estimates, except $\hat{b}_1$, converge after approximately 15000 iterations.

To assess the accuracy of the estimated model, the model validation tests are performed. The results of the first three tests, namely the **Sampling Frequency Test**, **Simulation-Mode Test** and **Spectral Estimation Test** are virtually identical to those obtained for operating condition OP1, and are therefore not shown. These tests confirm the estimated model provides an accurate representation of the small-signal

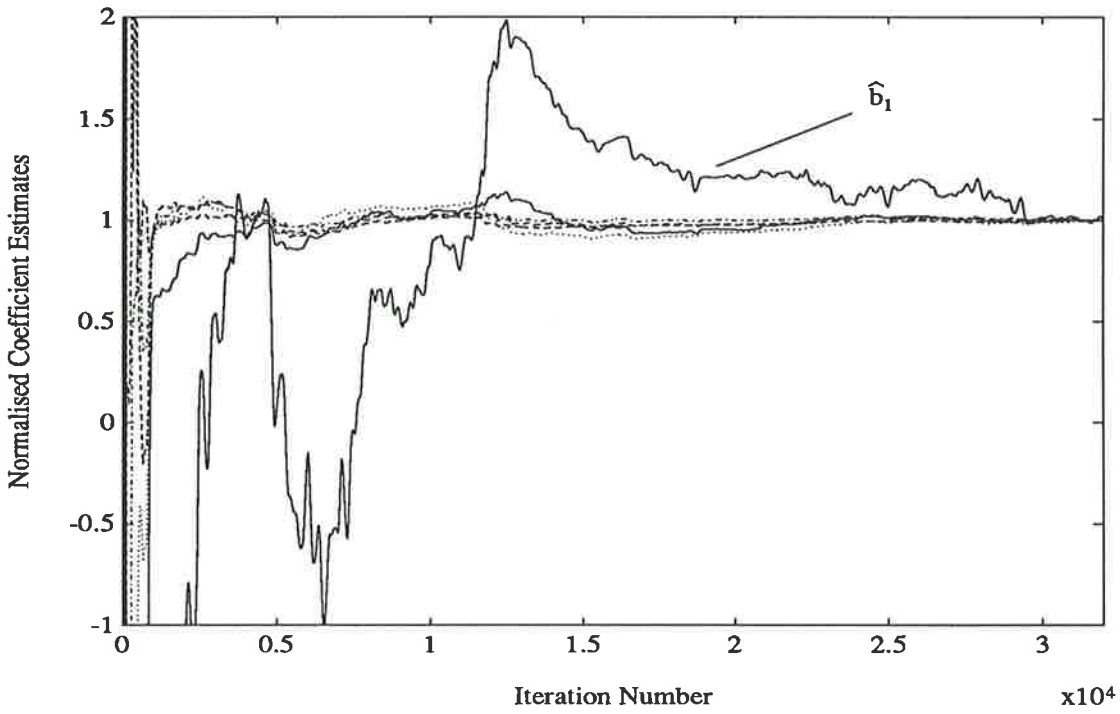

Figure 6.9: Normalised RIV-BO estimates of the field-to-terminal voltage TF coefficients, OP2.

response of the field-to-terminal voltage TF of the system, and that the sampling frequency is sufficient for the w-domain coefficients to accurately approximate those of the equivalent continuous-time TF.

Sinusoidal Frequency Response Measurement Test

Figure 6.10 displays the Bode plot calculated from the estimated w-domain model (eqn. 6.27), together with the SSSFR measurements performed on the system at the operating condition OP2. The two responses show close agreement across the frequency range from 0.02 Hz to approximately 10 Hz.

6.3.4 Estimated Transfer Function: Operating Condition OP3

The third steady-state operating condition considered is

Operating Condition: OP3		
P_{t0}	3330	W
Q_{t0}	127	var
v_{t0}	390	V
v_{b0}	416	V

At this third operating condition, the PRBS field voltage perturbation is applied and measurements taken of the Δv_f and Δv_t signals.

The measured Δv_f and Δv_t signals are prefiltered prior to use in the RIV-BO estimation algorithm. The $J(w)$ filter polynomial selected for estimation is

$$\begin{aligned} J(w) &= (w+6.1)(w+1+j16.1)(w+1-j16.1) \\ &= w^3 + w^2 8.1 + w 272.41 + 1587.3 \end{aligned} \tag{6.28}$$

After 32000 iterations, the estimated w-domain model is

$$\hat{H}_{OP3}(\beta) = \frac{\beta^2 28.86 + \beta 9.15 + 7471}{\beta^3 + \beta^2 8.22 + \beta 251.0 + 1453} \tag{6.29}$$

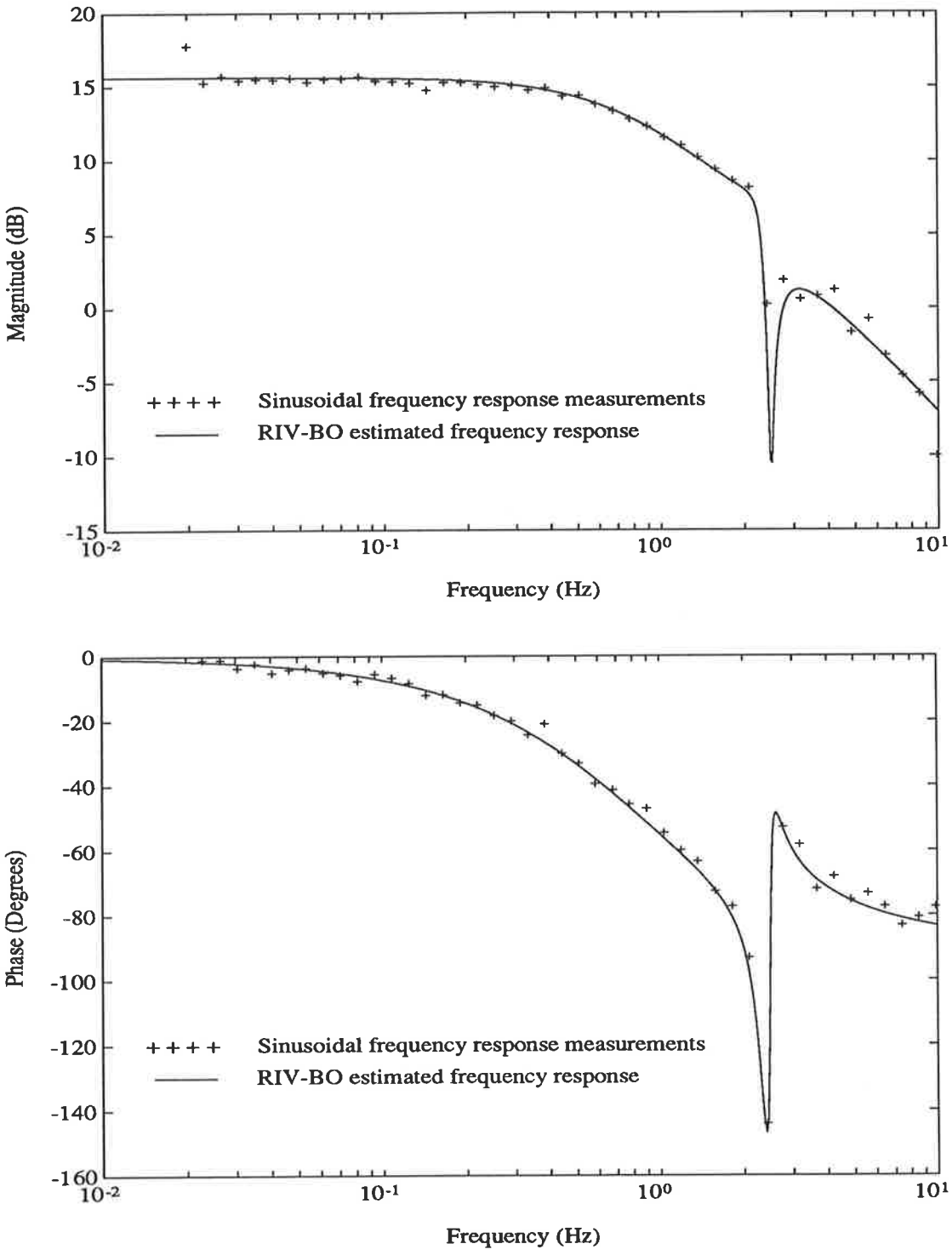

Figure 6.10: SSSFR measurement of the field-to-terminal voltage frequency response, magnitude and phase, OP2.

Figure 6.11 displays the variation in the normalised coefficient estimates during estimation. From this figure, it can be seen that five of the coefficient estimates have

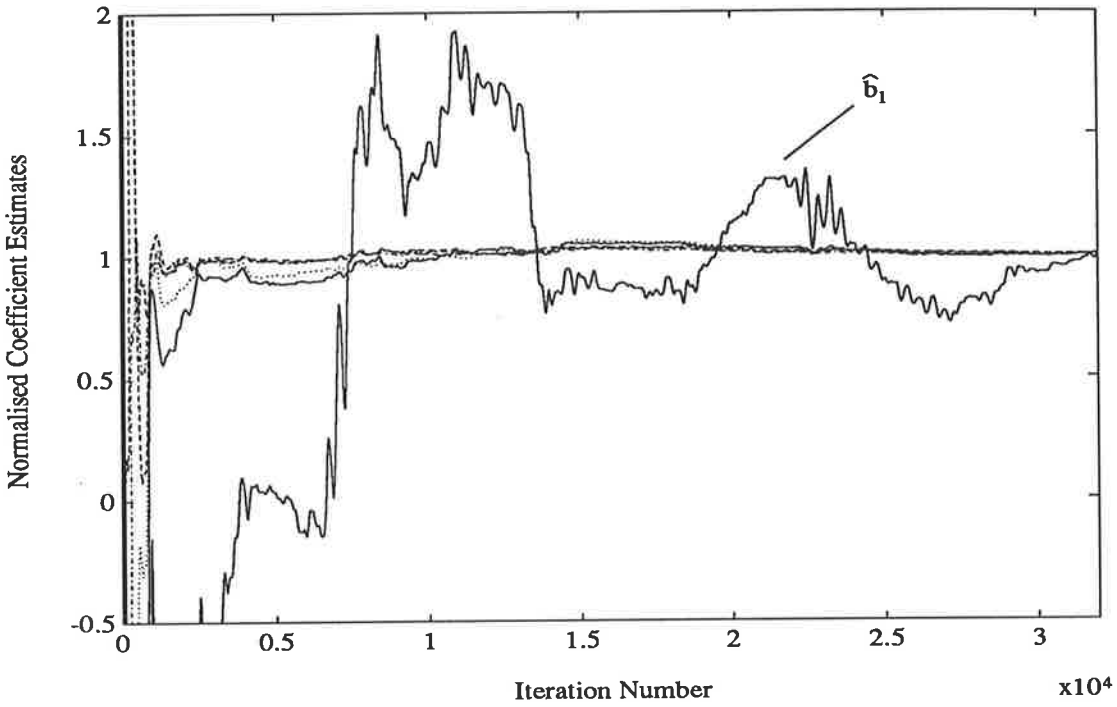

Figure 6.11: Normalised RIV-BO estimates of the field-to-terminal voltage TF coefficients, OP3.

converged after approximately 10000 iterations. As with the two previous estimation cases, the variation of the coefficient estimate $\hat{b}_1$ is significantly greater than all other coefficient estimates, as well as taking longer to converge.

The model validation tests outlined in chapter 5 are performed to assess the accuracy of the estimated w-domain model. The first three tests again confirm the estimated model accurately represents the response of the field-to-terminal voltage TF of the SMIB system, and that the sampling frequency is sufficiently high with respect to the frequency range of interest of the system TF. Due to the similarity with the results obtained for operating condition OP1, the results for operating condition OP3 are not displayed.

Sinusoidal Frequency Response Measurement Test

Figure 6.12 displays the measured SSSFR of the field-to-terminal voltage TF, together with the frequency response calculated from the estimated w-domain model (eqn. 6.29). Across the frequency range displayed, the two sets of responses show close agreement.

6.3.5 Discussion

For the three operating conditions considered (Table 6.1), the RIV-BO estimation algorithm is able to accurately estimate third-order w-domain models for the small-signal field-to-terminal voltage TF of the SMIB system. The accuracy of the estimated models is confirmed with the model validation tests described in chapter 5. The frequency responses calculated from the estimated models also agree closely with SSSFR measurements performed on the system.

For all three operating conditions, the coefficient estimate $\hat{b}_1$ is the most difficult to estimate. This is clear from the plots of the normalised coefficient estimates during estimation (Figures 6.4, 6.9 and 6.11). This coefficient determines the damping constant of the complex zeros of the system TF. Because of the significant attenuation of the TF in the frequency region of these zeros (between –10 and –25 dB with respect to the low-frequency magnitude), it is not surprising that it is difficult to estimate this coefficient accurately. A further complication is that the frequency of the mode associated with rotor oscillations is located close to the corner frequency of the TF complex zeros. Thus disturbances on the external network connected to the SMIB system produce noise (coloured) concentrated in this frequency region [14].

It is worth noting that as the real power output level of the machine decreases, the third-order field-to-terminal voltage TF of the SMIB system approaches a simple first-order TF. This is because the corner frequencies of the complex poles and zeros move together, and thus their effects on the machine TF tend to cancel. Thus for lower real power levels, it is difficult to estimate a third-order model for the SMIB system. To minimise this problem, the real power output level for the three operating conditions considered is close to the maximum obtainable output of the laboratory SMIB arrangement.

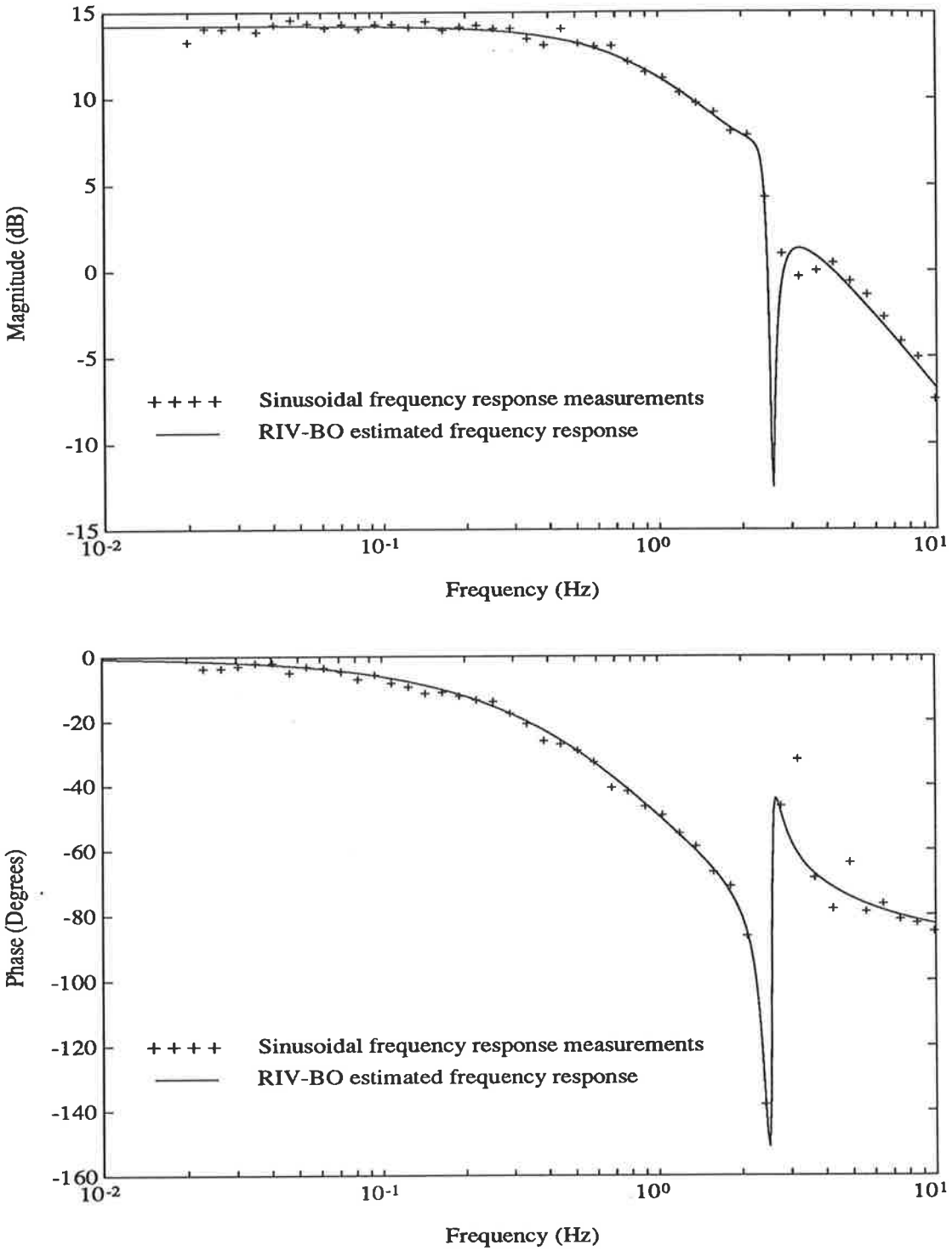

Figure 6.12: SSSFR measurement of the field-to-terminal voltage frequency response, magnitude and phase, OP3.

The three operating conditions investigated are very close together. The real output power for each condition is approximately 3.3 kW, with the reactive power varying from –80 var to 127 var. Figure 6.13 displays the Bode plots of the three estimated models, which confirms there is only a small difference between the system TF for each operating condition. Whilst the difference is small between operating conditions, there is a consistent trend in the estimated models. As the reactive power flow varies from –80 var to 127 var (as the steady-state field excitation voltage is increased), the low-frequency gain consistently decreases.

Figure 6.14 displays the three sets of SSSFR measurements for the three system operating conditions. It is clear from this figure that it would be very difficult to calculate accurate TF models of the system from these magnitude and phase measurements. In particular, there is very little information in the SSSFR results pertaining to both the complex poles and zeros of the system TF. An accurate estimate of the damping constants of these complex poles and zeros would be virtually impossible to obtain from the SSSFR measured responses. SSSFR data, however, has been used for calculating the TF of the field-to-terminal voltage TF of a synchronous machine operating online [39].

An important *practical* consideration in measuring the field-to-terminal voltage TF of the SMIB system is the time required for performing the test. Ideally the test should be performed as quickly as possible to avoid any problems due to drift in the steady-state operating condition of the SMIB system. For the purpose of RIV-BO estimation, the input-output signals are sampled for a period of 32 seconds. For the SSSFR tests performed, the magnitude and phase of the TF are measured at fifty logarithmically spaced frequency points from 0.02 Hz to 20 Hz [3]. The frequency response analyser uses three cycles of the sinusoidal excitation signal to average the response and hence the time required for testing is approximately 19 minutes [4]. From this comparison, the SSSFR testing takes approximately 36 times longer than the PRBS excitation test.

These two points, namely the relative speed of testing and accuracy of the RIV-

[3]This frequency range is comparable to that studied in [39], which covers from 0.01 Hz to 10 Hz.
[4]Using a Solartron Schlumberger 1253 gain-phase analyser.

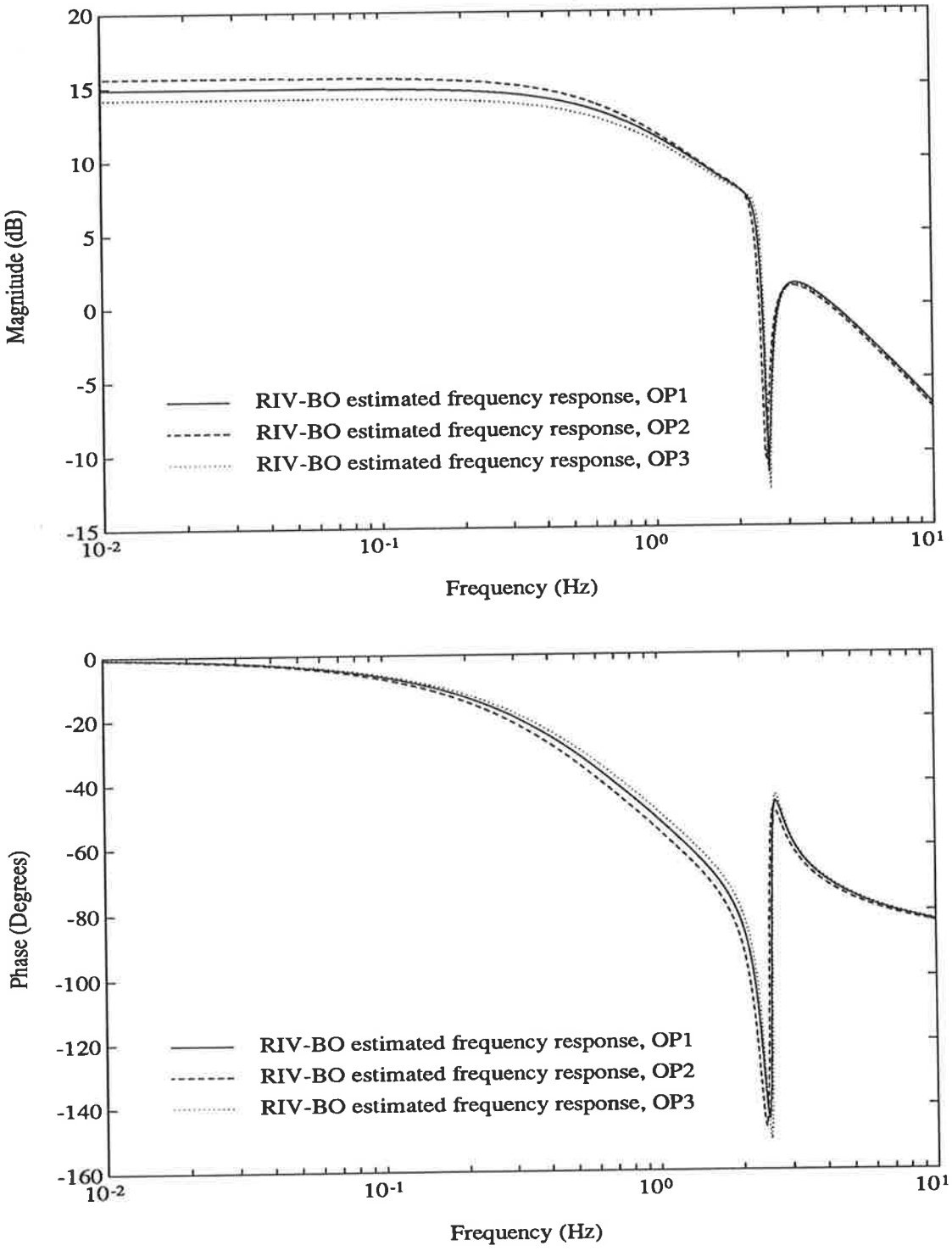

Figure 6.13: Bode plots of the three estimated field-to-terminal voltage TFs, OP1, OP2 and OP3.

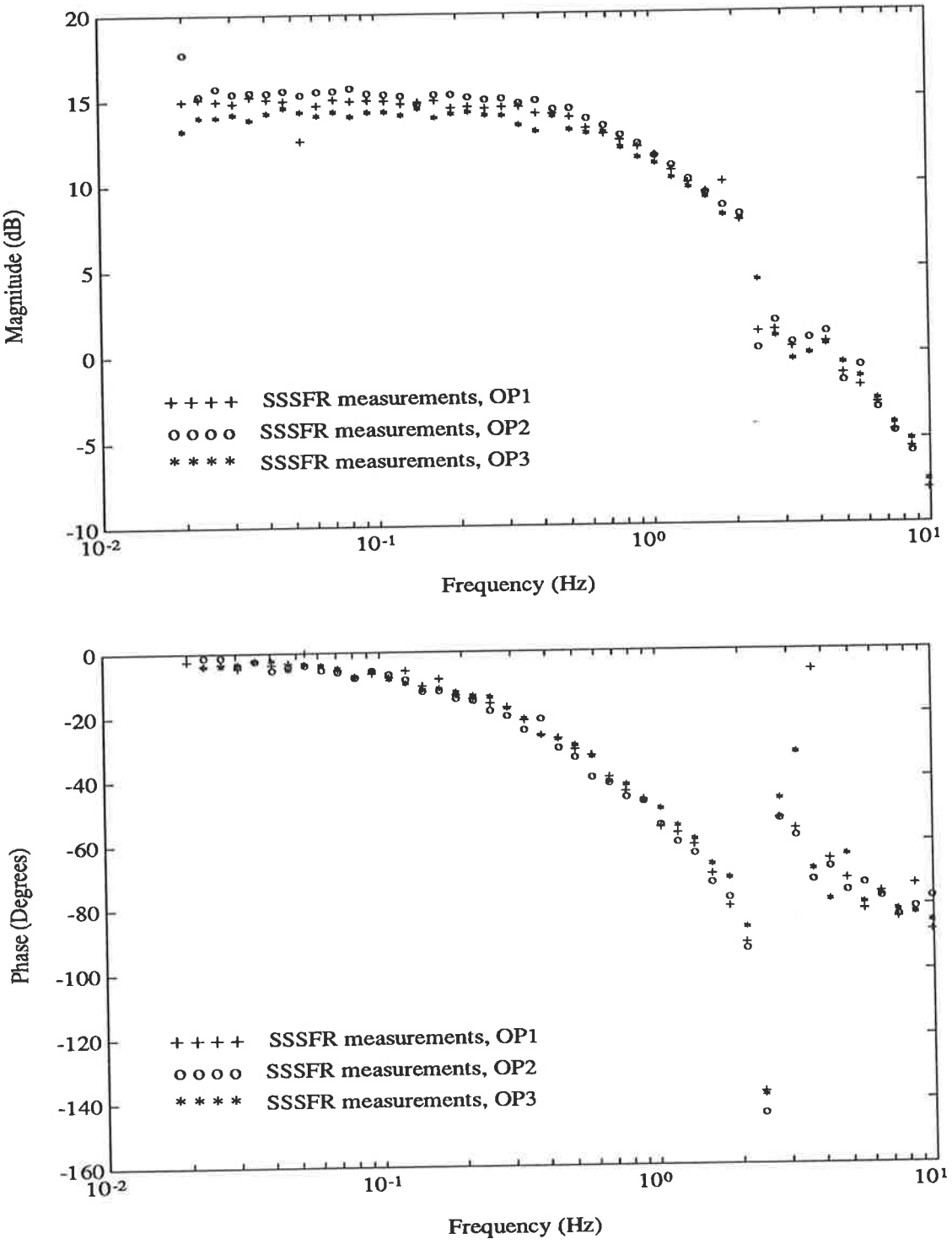

Figure 6.14: SSSFR measurement of the field-to-terminal voltage frequency response, magnitude and phase, OP1, OP2 and OP3.

BO estimation algorithm highlight its usefulness for estimating the coefficients of the small-signal field-to-terminal voltage TF of a synchronous machine operating online.

The three operating conditions (OP1 to OP3) considered in the previous sections are not the only operating conditions under which the field-to-terminal voltage TF is estimated in the experimental investigations. To demonstrate the estimation method can be applied to other online machine operating conditions, as well as open-circuit conditions, the next section contains a selection of some of the other estimation results.

6.3.6 Estimated Transfer Functions for Various Operating Conditions

Online Transfer Function

The three online operating conditions considered in the previous sections are all in close proximity of the operating condition $P_{t0} \approx 3.3$ kW, $Q_{t0} \approx 0$ var. To demonstrate that the RIV-BO estimation algorithm can estimate the coefficients of the field-to-terminal voltage TF at other operating conditions, estimation is performed at the following online operating conditions:

		OP4	OP5
P_{t0}	W	1860	2510
Q_{t0}	var	-35	-17
v_{t0}	V	413	402
v_{b0}	V	421	421

These two operating conditions represent both a relatively lightly loaded system (OP4), and an intermediate load level (OP5). The sampled input and output signals for these two operating conditions are prefiltered and used in the RIV-BO estimation algorithm to estimate third-order w-domain models for the field-to-terminal voltage TF. The model validation tests confirm that the estimated models accurately represent the response of the field-to-terminal voltage TF of the SMIB system. Figure 6.15 displays the Bode plots of the estimated models for the operating conditions OP4 and OP5, together with that calculated from the estimated w-domain model from OP1 (section 6.3.2). These plots show that the variation in the real power output of the

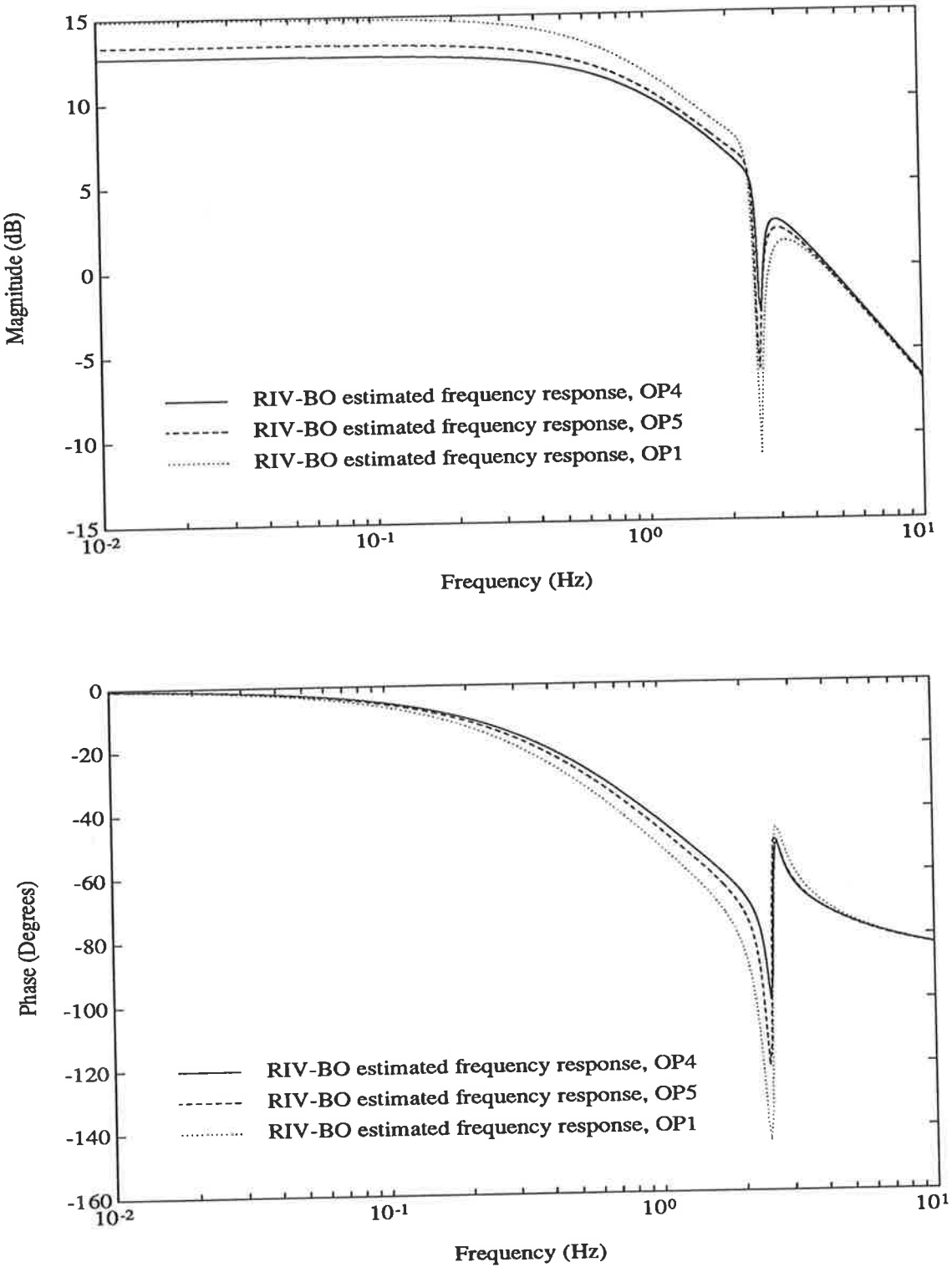

Figure 6.15: The Bode plots of the estimated w-domain models for the online operating conditions OP4, OP5 and OP1.

synchronous generator has a significant effect on the small-signal field-to-terminal voltage TF of the system. As the real power output increases from 1860 W to 3357 W, there is approximately a 2.5 dB increase in the low-frequency magnitude of the TF. Also, there is an increase in the depth of the 'notch' in the system TF, with a corresponding change in the phase response of the system. This variation is due in part to the difference between the corner frequencies of the complex poles and zeros increasing with increasing power output. Thus as the real power output increases, the effect of the complex poles and zeros becomes more pronounced on the system frequency response.

Open-Circuit Transfer Function

Another 'operating condition' under which the coefficients of the small-signal field-to-terminal voltage TF of the synchronous machine can be estimated is open-circuit operation. No modification of the transducer and filter circuitry is required for this test, which involves measurement of the field- and terminal-voltage perturbations when the machine is operating on open circuit at synchronous speed. The TF coefficients are estimated for various steady-state levels of field voltage to demonstrate the effect of saturation on the open-circuit TF. The steady-state levels considered are:

	OC1	OC2	OC3	OC4	OC5	OC6	OC7
v_{f0} V	32	30	25	20	15	10	5
v_{t0} V	415	393	356	306	247	175	89

For each of the seven steady-state open-circuit conditions, the PRBS excitation signal is applied to the machine field circuit, and measurements taken of the field and terminal voltage perturbations. The measured signals are prefiltered and used in the RIV-BO estimation algorithm to estimate the coefficients of a first-order TF. The $J(w)$ filter polynomial is selected to match closely the estimated denominator for each TF. The model validation tests confirm that the estimated first-order w-domain models provide accurate representations for the open-circuit field-to-terminal voltage response of the synchronous machine.

Figure 6.16 displays the Bode plots calculated from the estimated open-circuit models. As expected, saturation has a significant effect on the open-circuit TF. For

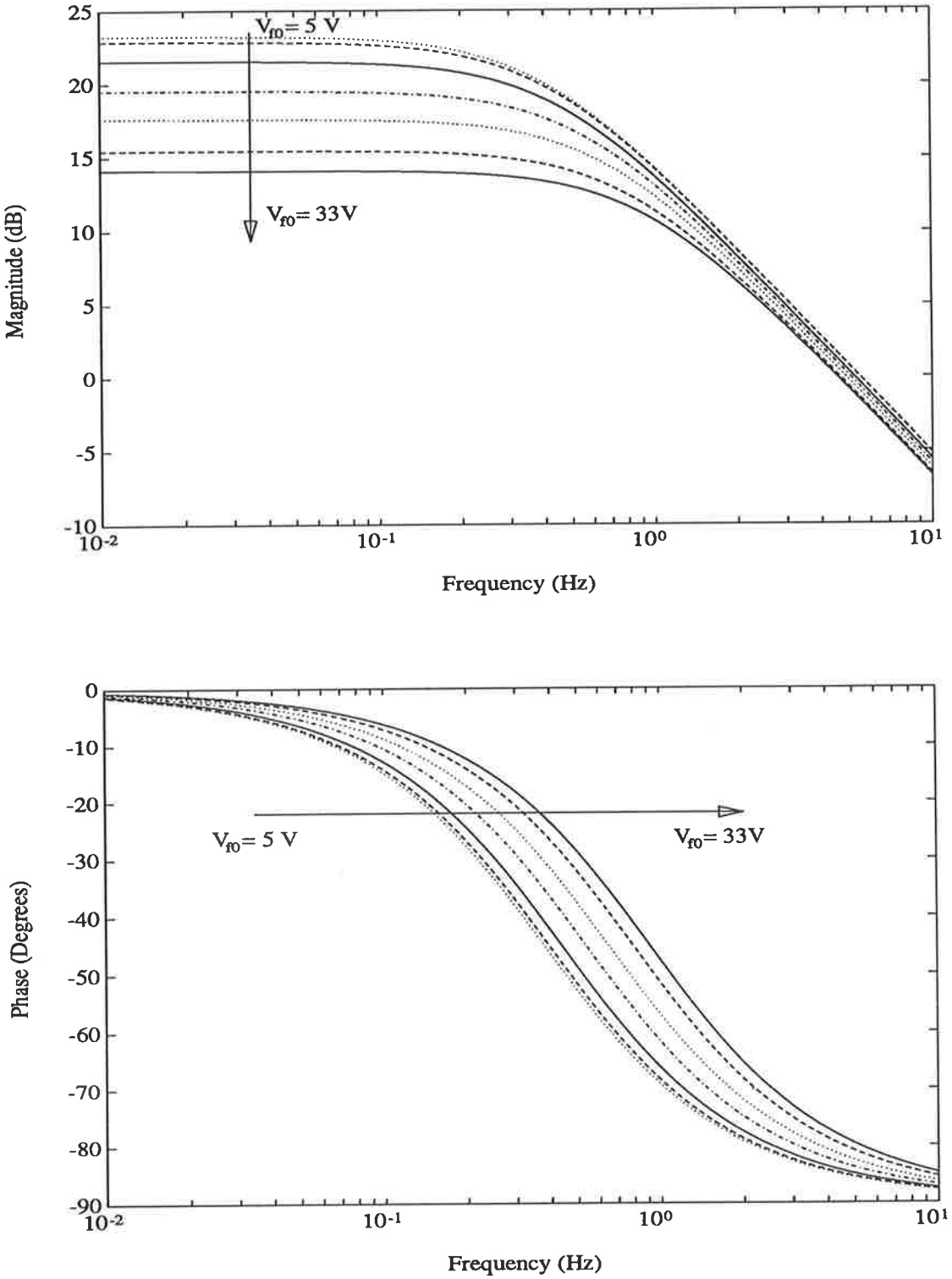

Figure 6.16: The Bode plots of the estimated models on open-circuit, for values of v_{f0} from 5 V to 33 V in approximate steps of 5 V.

relatively unsaturated conditions (v_{f0} = 5 V), the dc gain is approximately 23 dB. Increasing the steady-state field voltage v_{f0} to 33 V, which corresponds to a typical online operating value for v_f, results in the dc gain reducing to 14 dB.

In the next section, the machine parameters are calculated from the estimated coefficients of the small-signal field-to-terminal voltage TFs of the synchronous machine operating online. Only the three online operating conditions studied in detail in sections 6.3.2, 6.3.3 and 6.3.4 are considered. It is possible to evaluate several of the machine parameters from the estimated open-circuit TF coefficients. However, due to the difficulties experienced with evaluating reasonable values for the machine parameters for the online tests and the questions raised about the accuracy of the synchronous machine model, these open-circuit TFs are not considered.

6.4 Calculation of Machine Parameters from Estimated Online Transfer Functions

6.4.1 Evaluation of the Machine Parameters using the Simplified Linearised SMIB Equations

The simplified linearised set of equations describing the SMIB system at a given steady-state operating condition are given by eqns. 6.13, 6.15, 6.18, 6.19, 6.20. In section 6.2.4 it is demonstrated how these equations can be rearranged to form the third-order field-to-terminal voltage TF $\Delta v_t/\Delta v_f$ (eqn. 6.23), the six coefficients of which are complicated nonlinear functions of the SMIB parameters and the machine operating condition.

In this section, given the values of the online field-to-terminal voltage TF coefficients, the nonlinear equations are solved to calculate several of the unknown system parameters. It must be emphasised that a third-order TF, with six coefficients, allows only six unknown system parameters to be calculated.

The machine and external network parameters in the simplified linearised SMIB equations are

$$[L_{dd}, L_{qq}, L_{ff}, kM_{ff}, r_a, r_f, X_e, r_e, J, B']$$

In the laboratory SMIB system, the parameters r_a, r_f, X_e and r_e can be measured by other means, thus leaving six unknown machine parameters to be calculated, namely

$$[L_{dd}, L_{qq}, L_{ff}, kM_{ff}, J, B'] \tag{6.30}$$

These are the six parameters for which the nonlinear equations are solved.

Although the parameter J is assumed to be one of the six unknown machine parameters, its value is actually known for the laboratory SMIB system. From rundown tests performed on the synchronous machine/DC motor system, the value of J is found to be $J = 0.27$ kg m^2 (Appendix E). As the value of J is known, it provides a means of assessing whether the parameters evaluated from the estimated TF coefficients yield reasonable values.

For the laboratory SMIB system the value of X_e is known. In a practical situation however, it is unlikely this external reactance parameter X_e would be known accurately. It is however likely that the polar moment of inertia J would be known, and hence the six parameters

$$[L_{dd}, L_{qq}, L_{ff}, kM_{ff}, X_e, B']$$

would form the set of unknown parameters.

To solve the set of linearised SMIB equations, the steady-state operating condition of the SMIB system is required. Given values of $P_{t0}, Q_{t0}, v_{t0}, v_{b0}, r_e, \omega_0$ and L_q, the steady-state values of the following variables can be evaluated:

$$\delta_{t0} = \arctan\left(\frac{P_{t0}\omega_0 L_q - Q_{t0} r_a}{v_{t0}^2 + P_{t0} r_a + Q_{t0}\omega_0 L_q}\right) \tag{6.31a}$$

$$\delta_{e0} = \arctan\left(\frac{P_{t0} X_e - Q_{t0} r_e}{v_{t0}^2 - P_{t0} r_e - Q_{t0} X_e}\right) \tag{6.31b}$$

$$\delta_0 = \delta_{e0} + \delta_{t0} \tag{6.31c}$$

$$v_{d0} = v_{t0} \sin \delta_{t0} \tag{6.31d}$$

$$v_{q0} = v_{t0} \cos \delta_{t0} \tag{6.31e}$$

$$i_{d0} = (P_{t0} v_{d0} + Q_{t0} v_{q0})/v_{t0}^2 \tag{6.31f}$$

$$i_{q0} = (P_{t0} v_{q0} - Q_{t0} v_{d0})/v_{t0}^2 \tag{6.31g}$$

$$\omega_0 \psi_{q0} = -v_{d0} - i_{d0} r_a \tag{6.31h}$$

$$\omega_0 \psi_{d0} = v_{q0} + i_{q0} r_a \tag{6.31i}$$

The phasor diagram for the equations is given in Figure 6.17.

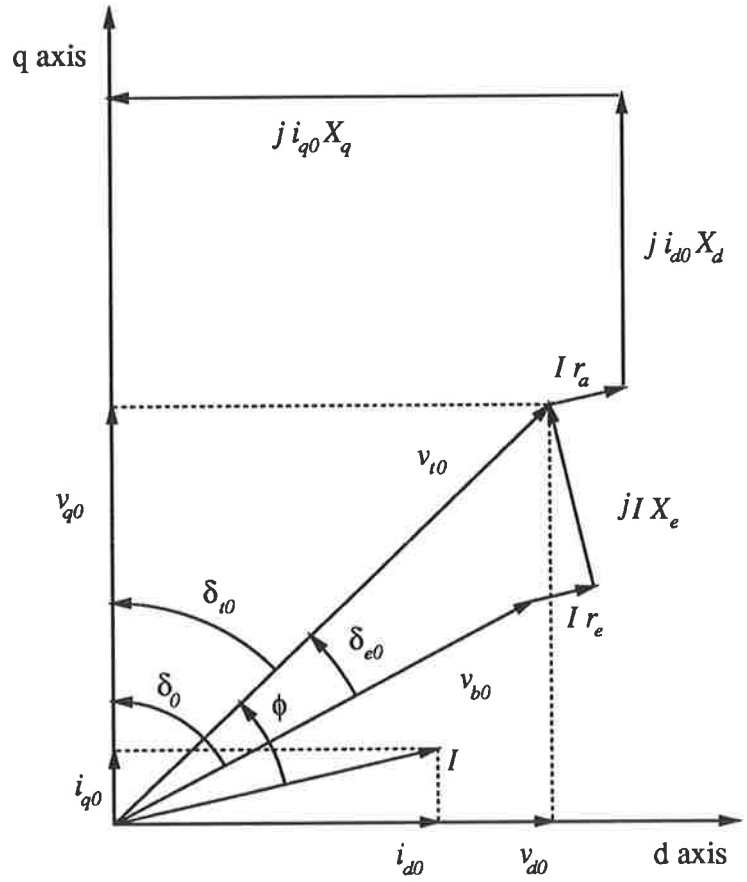

Figure 6.17: Phasor diagram for the SMIB system.

For each operating condition of the SMIB system, the steady-state conditions P_{t0}, Q_{t0}, v_{t0} and v_{b0} are measured. The value of r_e is known, and for a 50 Hz system the value of ω_0 is 100π. The parameter L_q (or $X_q = \omega_0 L_q$) however, which is required for evaluating the steady-state conditions, is still unknown. From the slip test conducted on the synchronous machine (Appendix E), an unsaturated value of X_q is calculated for the machine. Ideally the saturated value of X_q should be used for calculating the steady-state operating conditions. However, from the limited information available for the saturation of the laboratory machine q-axis, it is assumed that X_q is unlikely to saturate significantly, and thus the unsaturated value of $X_{q_{unsat}} = 11.5\Omega$ is used

for evaluating the steady-state operating conditions.

Note that it would be incorrect to use the small-signal incremental value X_{qq} for evaluating the steady-state conditions. If there is some level of saturation on the machine q-axis, it is likely X_{qq} will differ significantly from X_q. The incremental machine parameters are only representative of the synchronous machine for small perturbations about a steady-state operating condition.

It is now possible to solve for the six unknown SMIB parameters.
Given the coefficients of a third-order field-to-terminal voltage TF:

$$H(s) = \frac{b_2 s^2 + b_1 s + b_0}{s^3 + a_2 s^2 + a_1 s + a_0} \tag{6.32}$$

the measured steady-state conditions:

$$[P_{t0}, Q_{t0}, v_{t0}, v_{b0}] \tag{6.33}$$

and the known machine and external network parameters:

$$[r_a, r_f, X_q, r_e, X_e] \tag{6.34}$$

the following set of six nonlinear equations, in six unknowns, is obtained:

$$\begin{aligned}
b_2 &= f_1(L_{dd}, L_{qq}, L_{ff}, kM_{ff}, J, B') \\
b_1 &= f_2(L_{dd}, L_{qq}, L_{ff}, kM_{ff}, J, B') \\
b_0 &= f_3(L_{dd}, L_{qq}, L_{ff}, kM_{ff}, J, B') \\
a_2 &= f_4(L_{dd}, L_{qq}, L_{ff}, kM_{ff}, J, B') \\
a_1 &= f_5(L_{dd}, L_{qq}, L_{ff}, kM_{ff}, J, B') \\
a_0 &= f_6(L_{dd}, L_{qq}, L_{ff}, kM_{ff}, J, B')
\end{aligned} \tag{6.35}$$

These equations result from combining the TF form of the simplified linearised SMIB equations (eqns. 6.21, 6.22 and 6.23), and the steady-state operating condition equations (eqn. 6.31). In equations 6.35, f_1 to f_6 are nonlinear functions of the six unknown machine parameters.

This set of equations can be solved numerically for the six unknown synchronous machine parameters using any software for solving nonlinear equations. In this thesis, the equations are solved using a Fortran77 program employing an IMSL [83] nonlinear equation solving routine. Figure 6.18 displays an approximate flow chart for the Fortran77 program used for solving the set of nonlinear equations.

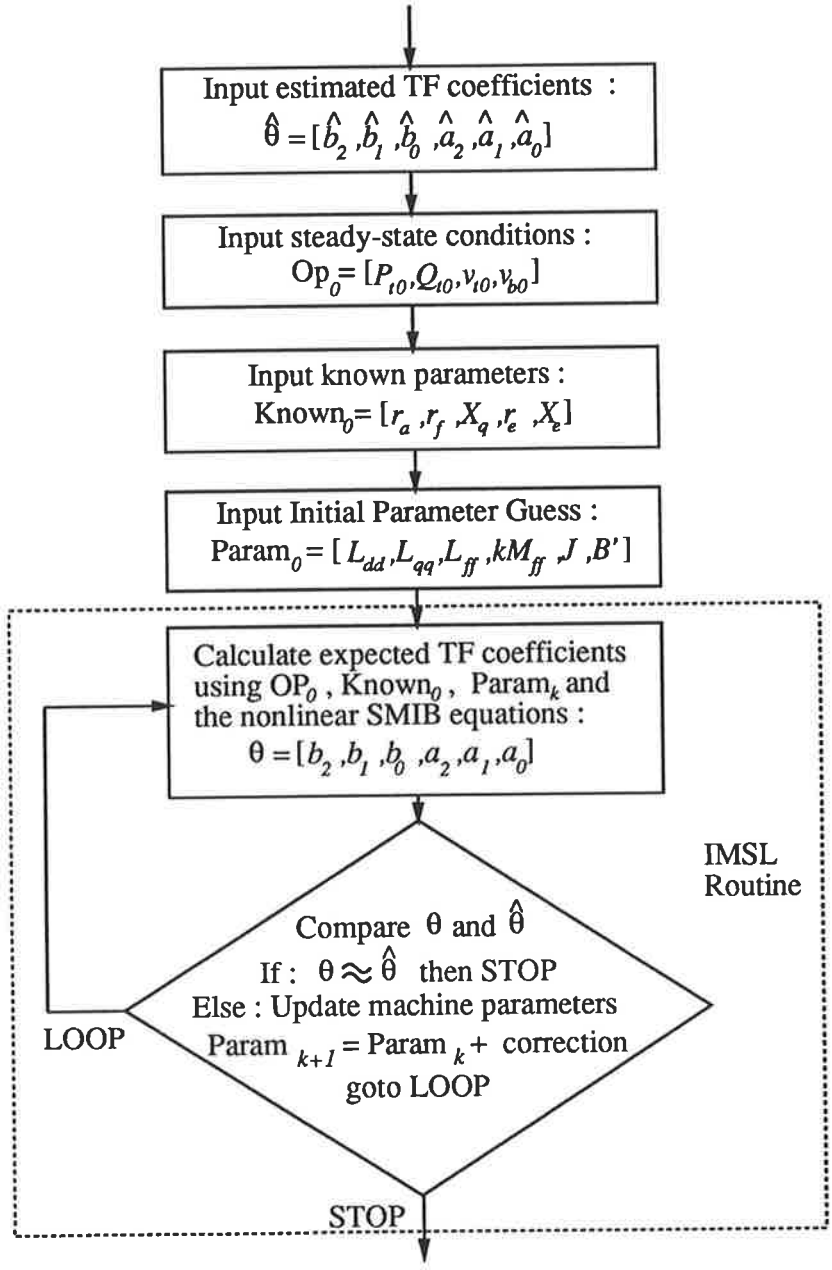

Figure 6.18: Flow chart for the evaluation of synchronous machine parameters from the estimated field-to-terminal voltage TF coefficients.

6.4.2 Machine Parameters for Operating Conditions OP1, OP2, OP3.

Table 6.2 displays the required variables to solve for the unknown machine parameters at each operating condition (see Figure 6.18). From the standstill tests of chapter 5,

		OP2	OP1	OP3
Estimated	$\hat{b}_2$	28.23	29.11	28.86
TF	$\hat{b}_1$	13.07	12.51	9.15
Coefficients	$\hat{b}_0$	6882	7401	7471
	$\hat{a}_2$	7.64	8.08	8.22
	$\hat{a}_1$	234.5	247.2	251.0
	$\hat{a}_0$	1138	1330	1453
Measured	P_{t0}	3350 W	3360 W	3330 W
Steady-	Q_{t0}	-80 var	23 var	127 var
State	v_{t0}	374 V	384 V	390
Conditions	v_{b0}	418	419	416
Known	r_a	1.12 Ω (standstill tests)		
SMIB	r_f	12.0 Ω (voltage/current measurement)		
Parameters	r_e	1.7 Ω (voltage/current measurement)		
	X_e	22.4 Ω (voltage/current measurement)		
	X_q	11.5 Ω (slip test)		

Table 6.2: Estimated TF coefficients, steady-state operating conditions, and known SMIB parameters for the laboratory SMIB system.

the value of $r_a = 1.12\Omega$ is calculated. From voltage and current measurements on the machine and external reactances, values for r_f, r_e and X_e are calculated. The value of X_q is calculated from a slip test, detailed in Appendix E.

Combining the known data for each operating point (Table 6.2) with the set of SMIB equations (eqns. 6.35) and solving, yields the following set of SMIB parameters (displayed in Table 6.3) for each operating condition.

Discussion

The machine parameters evaluated for all three operating conditions are consistent with respect to each other. The problem with the parameters is that several of their values appear to be inconsistent with the expected machine parameters. In particular:

		OP2	OP1	OP3
X_{dd}	Ω	17.1	16.7	16.4
X_{qq}	Ω	53.0	56.8	60.1
X_{ff}	Ω	720	665	643
$\omega_0 k M_{ff}$	Ω	86.2	81.7	78.5
J	kg m^2	0.14	0.13	0.13
B'	Nm/(rad/s)	0.016	0.014	0.010

Table 6.3: Evaluated small-signal machine parameters for the simplified SMIB model.

J : From rundown tests, the expected value for the polar moment of inertia is $J = 0.27$ kg m^2. The value of $J \approx 0.13$ kg m^2 evaluated for all three operating conditions is approximately half the expected value.

X_{qq} : For the laboratory synchronous machine, the q-axis is not expected to saturate significantly. Assuming no q-axis saturation, the small-signal incremental reactance X_{qq} should equal the unsaturated large-signal reactance $X_{q_{unsat}} = 11.5\Omega$. With the presence of some q-axis saturation, the reactance X_{qq} should be *less* than the value $X_{q_{unsat}} = 11.5\Omega$. The values for X_{qq} in Table 6.3 clearly disagree with this.

The other small-signal incremental reactances, namely X_{dd}, X_{ff} and $\omega_0 k M_{ff}$, are all significantly less than their values calculated from both the standstill tests of chapter 5, and the measured large-signal values in Appendix E. From finite-element analysis studies [41,79], it is known that the values of the small-signal incremental machine parameters under saturated conditions are significantly smaller than the large-signal machine parameters, as well as the small-signal standstill machine parameters. Thus the values of the machine parameters X_{dd}, X_{ff} and $\omega_0 k M_{ff}$ calculated here appear to be reasonable. The variation in these evaluated parameters between operating conditions also agrees with the expected variation. As the reactive power output varies from –80 var to 127 var (which results from an increase in the steady-state field voltage), the values of the machine parameters X_{dd}, X_{ff} and $\omega_0 k M_{ff}$ all decrease. This is expected because the increase in field voltage, and corresponding increase in machine terminal voltage, represents an increase in the machine saturation (as measured by the machine air-gap flux, which is approximately proportional

to v_{t0}, see section 6.5). This increase in saturation should result in a decrease in the machine parameters values.

Thus whilst some of the values of the evaluated small-signal machine parameters seem plausible, i.e. X_{dd}, X_{ff} and $\omega_0 k M_{ff}$, some of the other evaluated parameters, X_{qq} and J, are clearly inconsistent with their expected values. A possible explanation is that the estimated machine TF coefficients are incorrect. This appears unlikely as the model validation tests performed in section 6.3 show that the estimated w-domain models accurately represent the response of the small-signal field-to-terminal voltage machine TF. Another possibility is that the assumptions made in deriving the simplified equations for the SMIB system invalidate the model, i.e. the model is inadequate for accurately representing the small-signal behaviour of the field-to-terminal voltage TF of the SMIB system. This seems the most likely of the explanations.

In the following section, several of the assumptions used in deriving the simplified SMIB system of equations are relaxed in an attempt to derive a consistent set of parameters from the estimated field-to-terminal voltage TFs.

6.5 Relaxing Approximations in the Simplified Linearised SMIB Model

The assumptions made in section 6.2.3 for deriving the simplified SMIB model are not necessarily realistic assumptions. Assumption A1, which assumes intersaturation terms are negligible, is possibly an unrealistic assumption [81]. Unfortunately, this assumption must be retained in order to contain the number of unknown machine parameters to six. However, within the current framework for evaluating the machine parameters it is possible to relax, or partially relax, both Assumptions A2 and A3.

6.5.1 Transformer-Voltage and Speed-Variation Terms

Assumption A3 assumes both the transformer-voltage and speed-variation terms in the stator voltage equations are negligible. This is a common simplifying assumption [1]. It is possible to include these terms with the current system used for evaluating the synchronous machine parameters.

To include both transformer-voltage and speed-variation terms in the linearised SMIB model, only eqns. 6.19 and 6.20 of the simplified SMIB model must be altered. These equations become respectively

$$\begin{bmatrix} \Delta v_d \\ \Delta v_q \\ \Delta v_f \end{bmatrix} = \begin{bmatrix} -r_a - L_{dd}s & \omega_0 L_{qq} & kM_{ff}s \\ -\omega_0 L_{dd} & -r_a - L_{qq}s & \omega_0 kM_{ff} \\ -kM_{ff}s & 0 & r_f + L_{ff}s \end{bmatrix} \begin{bmatrix} \Delta i_d \\ \Delta i_q \\ \Delta i_f \end{bmatrix} + \begin{bmatrix} -\psi_{q0} \\ \psi_{d0} \\ 0 \end{bmatrix} s\Delta\delta \tag{6.36}$$

$$\begin{aligned} \Delta v_d &= (v_{b0}\cos\delta_0 - L_e i_{q0}s)\Delta\delta + (r_e + L_e s)\Delta i_d - \omega_0 L_e \Delta i_q \\ \Delta v_q &= (-v_{b0}\sin\delta_0 + L_e i_{d0}s)\Delta\delta + (r_e + L_e s)\Delta i_q + \omega_0 L_e \Delta i_d \end{aligned} \quad \text{...(Eqn. 6.14)}$$

These two linearised voltage equations, together with eqns. 6.13, 6.15 and 6.18 represent the linearised simplified SMIB model with transformer-voltage and speed-variation terms included.

Following steps similar to those performed in section 6.2.4, the linearised small-signal field-to-terminal voltage TF of the SMIB system can be expressed in the form:

$$\frac{\Delta v_t}{\Delta v_f} = \frac{B_5 s^5 + B_4 s^4 + B_3 s^3 + B_2 s^2 + B_1 s + B_0}{s^5 + A_4 s^4 + A_3 s^3 + A_2 s^2 + A_1 s + A_0} \tag{6.37}$$

The resulting SMIB TF is fifth-order, whereas the field-to-terminal voltage TFs estimated using RIV-BO estimation are only third-order. Thus this fifth-order TF is not directly compatible with the method employed for solving the set of nonlinear equations to derive the unknown machine parameters.

One method of solving this problem is to estimate fifth-order models for the machine TF. This is not a practical solution however because over the frequency range of interest, approximately 0.02 Hz to 10 Hz, the third-order model accurately represents the field-to-terminal voltage TF of the system. Estimating a fifth-order model is not possible unless the frequency range of interest is expanded to include possibly high frequency dynamics which are currently not considered. Increasing the frequency range above 10 Hz may require the synchronous machine model to be extended to explicitly model the machine damper windings, and is further complicated by the

difficulty in exciting the system response above 10 Hz, due to the long time constant of the machine field winding [14]. Thus this is currently not a practical option.

The method that is employed is to reduce the calculated fifth-order TF down to a third-order TF, which is then compatible with the estimated third-order models. Because of the location of some of the poles and zeros of the fifth-order TF, it is possible to reduce it to a third-order TF, by factorising out the high-frequency poles and zeros of the fifth-order TF. The reduced-order TF accurately represents the full fifth-order TF over the low-frequency range, up to approximately 10Hz. This procedure can easily be incorporated into the current program for solving for the machine parameters.

Figure 6.19 provides a flow chart for evaluating the machine parameters from the estimated third-order TF coefficients employing this method. Firstly, the steady-state operating conditions and known system parameters (Table 6.2), together with an initial guess of the unknown machine parameters, Param_0, are used in equations 6.13, 6.14, 6.15, 6.18, 6.36 and 6.31, to calculate the coefficients A_i, B_j for the full fifth-order machine TF (eqn. 6.37). These coefficients can be factorised to yield the poles and zeros of the fifth-order TF, from which the high-frequency poles and zeros can be discarded, and the remaining poles and zeros reformed to yield a third-order TF,

$$H(s) = \frac{b_2 s^2 + b_1 s + b_0}{s^3 + a_2 s^2 + a_1 s + a_0}.$$

These calculated coefficients, $\theta = [b_2, b_1, b_0, a_2, a_1, a_0]$, are then compared with the estimated TF coefficients, $\hat{\theta}$, from which the values of the unknown parameters Param_k can be updated, and the procedure repeated.

Machine Parameters

Using the simplified SMIB equations including transformer-voltage and speed-variation terms, and the known data for each operating condition, the set of nonlinear equations are solved to evaluate the unknown machine parameters (see Figure 6.19). Table 6.4 displays the machine parameters for the operating conditions OP1, OP2 and OP3.

A comparison of the machine parameters of Table 6.4 with those evaluated previously (Table 6.3) shows only a relatively small change in the values of the parameters

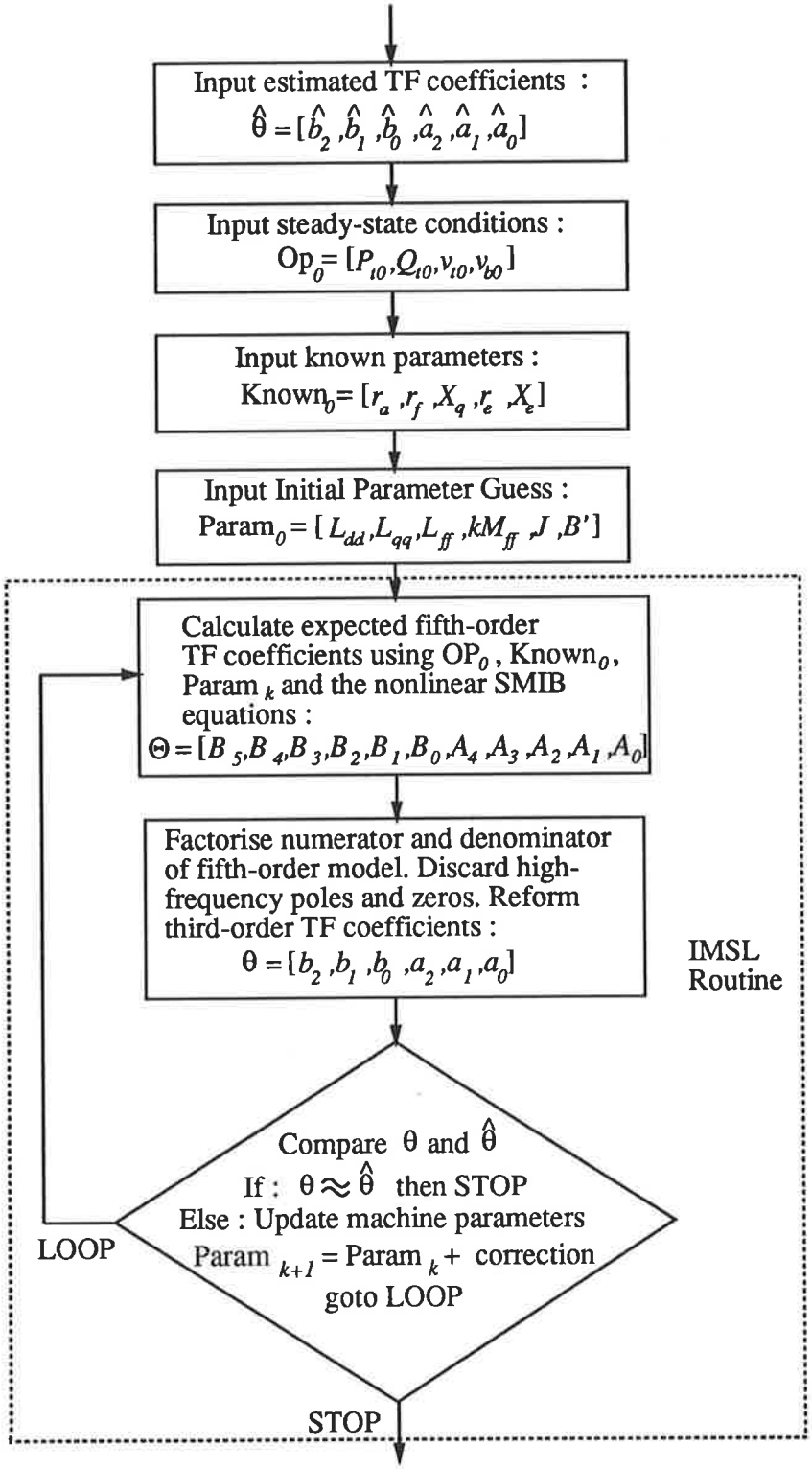

Figure 6.19: Flow chart for the evaluation of synchronous machine parameters from the estimated field-to-terminal voltage TF coefficients, with transformer-voltage and speed-variation terms included.

		OP2	OP1	OP3
X_{dd}	Ω	15.5	14.9	14.3
X_{qq}	Ω	20.3	20.7	19.5
X_{ff}	Ω	805	737	708
$\omega_0 k M_{ff}$	Ω	91.7	85.7	81.4
J	kg m^2	0.21	0.21	0.21
B'	Nm/(rad/s)	0.061	0.058	0.054

Table 6.4: Evaluated small-signal machine parameters for the simplified SMIB model, including transformer-voltage and speed-variation terms.

X_{dd}, $\omega_0 k M_{ff}$ and X_{ff}. There is a significant change in both the X_{qq} and J parameters, with values which are closer to those expected. These parameters, although an improvement from the previous case, are still inconsistent with the expected values. The polar moment of inertia J is only approximately 78% of the measured value $J = 0.27$ kg m^2, whilst $X_{qq} \approx 20\Omega$ is greater than 170% of the large-signal value of $X_{q_{unsat}} = 11.5\Omega$.

To illustrate the nature of the approximation made in reducing the machine TF from fifth- to third-order when solving for the machine parameters, the poles and zeros discarded from the fifth-order TF at operating condition OP2 are

Zeros : -1166, $-20.75 \pm j314.2$

Poles : $-26.52 \pm j314.0$

The complex poles and zeros discarded have little effect on the overall TF because they are very close in frequency, in effect canceling each other. The real zero at 1166 rad/s (186 Hz) also has little influence on the TF below 10 Hz.

For comparison with the discarded high-frequency poles and zeros, the low-frequency poles and zeros retained in the third-order TF are:

Zeros : $-0.21 \pm j15.94$

Poles : $-1.19 \pm j15.24$, -5.69

From the results of Table 6.4 the small-signal linearised SMIB equations, with both transformer-voltage and speed-variation terms included, still appear to provide a model which results in parameters which are inconsistent with the expected values.

6.5.2 Unequal kM_{fd}, kM_{df} Parameters

In Assumption A2 it is assumed that the small-signal incremental parameters kM_{fd} and kM_{df} in the linearised machine flux equations (eqn. 6.10) are equal. For lossless nonlinear inductors, this equality of the mutual inductance terms must hold [38]. However, in an actual synchronous machine it is unrealistic to assume that the machine inductors (machine windings) are lossless, unless the losses are modeled separately [84]. The losses, called core losses, are caused by the time variation of the winding flux-linkages in the iron of the machine. The synchronous machine model employed in this thesis does not separately model core losses, although the effects of the damper windings located on the rotor, and rotor core losses, are partially included in the damping term B_2 in the shaft equation of motion (eqn. 6.16). Thus, for this practical estimation task, it is unreasonable to assume the machine windings are lossless, and hence assume that the mutual inductance terms are equal.

The inclusion of separate values of kM_{fd} and kM_{df} does not alter the method for evaluating the machine parameters from the estimated TF coefficients. It does however increase the number of unknown machine parameters from six to seven. Thus for the system of equations to remain soluble, the value of one of these seven unknown parameters must be evaluated separately. The value of J has been measured for the laboratory SMIB arrangement, and should not vary between operating conditions. Thus it is assumed J is a known parameter ($J = 0.27$ kg m^2), leaving the six unknown machine parameters

$$[L_{dd}, L_{qq}, L_{ff}, kM_{fd}, kM_{df}, B']$$

The set of SMIB equations, which include the transformer-voltage and speed-variation

terms, as well as the separate kM_{fd}, kM_{df} values are given by

$$\begin{bmatrix} \Delta\psi_d \\ \Delta\psi_q \\ \Delta\psi_f \end{bmatrix} = \begin{bmatrix} -L_{dd} & 0 & kM_{df} \\ 0 & -L_{qq} & 0 \\ -kM_{fd} & 0 & L_{ff} \end{bmatrix} \begin{bmatrix} \Delta i_d \\ \Delta i_q \\ \Delta i_f \end{bmatrix} \tag{6.38}$$

$$\begin{bmatrix} \Delta v_d \\ \Delta v_q \\ \Delta v_f \end{bmatrix} = \begin{bmatrix} -r_a - L_{dd}s & \omega_0 L_{qq} & kM_{df}s \\ -\omega_0 L_{dd} & -r_a - L_{qq}s & \omega_0 kM_{df} \\ -kM_{fd}s & 0 & r_f + L_{ff}s \end{bmatrix} \begin{bmatrix} \Delta i_d \\ \Delta i_q \\ \Delta i_f \end{bmatrix} + \begin{bmatrix} -\psi_{q0} \\ \psi_{d0} \\ 0 \end{bmatrix} s\Delta\delta \tag{6.39}$$

together with eqns. 6.13, 6.14 and 6.15.

Machine Parameters

Using the simplified SMIB equations including transformer-voltage and speed-variation terms, and independent kM_{fd}, kM_{df} values (eqns. 6.13, 6.14, 6.15, 6.38, 6.39), and the known data (Table 6.2), the set of nonlinear equations are solved to evaluate the six unknown machine parameters. Table 6.5 displays the evaluated machine parameters for the operating conditions OP1, OP2 and OP3. Again comparing the

		OP2	OP1	OP3
X_{dd}	Ω	16.2	15.3	14.4
X_{qq}	Ω	8.8	8.5	8.3
X_{ff}	Ω	875	800	760
$\omega_0 kM_{fd}$	Ω	118.6	111.7	103.3
$\omega_0 kM_{df}$	Ω	94.3	87.6	82.6
B'	Nm/(rad/s)	0.081	0.080	0.072
J (Fixed)	kg m^2	0.27	0.27	0.27

Table 6.5: Evaluated small-signal machine parameters for the simplified SMIB model, including transformer-voltage and speed-variation terms and independent mutual inductance terms.

evaluated parameters with those of the previous table (Table 6.4) shows that, allowing for independent values for the small-signal incremental mutual inductance terms has a relatively small effect on the X_{dd}, X_{ff} and $\omega_0 kM_{df}$ parameters, whilst it has a significant effect on both X_{qq} and $\omega_0 kM_{fd}$.

As discussed briefly in section 6.4.2, the small-signal incremental value X_{qq} is expected to be less than the unsaturated value $X_{q_{unsat}} = 11.5\Omega$. For all three operating conditions in Table 6.5, the value of X_{qq} is $\approx 8.5\Omega$, which in comparison to the unsaturated value of X_q appears to be a reasonable value.

It is worth noting that the mutual inductance terms differ significantly. For the three operating conditions, $\omega_0 k M_{fd}$ and $\omega_0 k M_{df}$ differ by approximately 25%, with $\omega_0 k M_{fd}$ the larger of the two reactances.

Stator Core Losses

It has been assumed that the difference between the small-signal incremental mutual reactance terms $\omega_0 k M_{fd}$ and $\omega_0 k M_{df}$ in Table 6.5 accounts for losses in both the stator and rotor iron (core losses) of the machine, which are not modeled explicitly in the synchronous machine equations. This can be substantiated in part by explicitly including in the SMIB model an approximate term for the effects of core losses in the stator of the synchronous machine.

The core losses in the machine stator must be supplied by the prime mover, across the air-gap of the machine. Assume these losses are a function of both speed ω and the resultant air-gap flux, ψ_{ag}, thus

$$P_{iron} = P'_{iron}(\omega, \psi_{ag})$$

A measure of the air-gap flux online is provided by the air-gap voltage [74], given by

$$v_{ag} = \sqrt{v_{agd}^2 + v_{agq}^2} \tag{6.40}$$

where

$$v_{agd} = v_d + i_d r_a - i_q X_l \tag{6.41}$$

$$v_{agq} = v_q + i_q r_a + i_d X_l \tag{6.42}$$

and X_l is the stator leakage reactance (see Appendix E). Thus, in terms of the air-gap

voltage, the stator core losses can be written as

$$P_{iron} = P_{iron}(\omega, v_{ag}) \tag{6.43}$$

Linearising this equation yields

$$\Delta P_{iron} = \frac{\partial P_{iron}}{\partial \omega}\Delta\omega + \frac{\partial P_{iron}}{\partial v_{ag}}\Delta v_{ag} \tag{6.44}$$

where Δv_{ag} (using eqns. 6.31h, 6.31i, 6.40, 6.41 and 6.42) is

$$\begin{aligned}\Delta v_{ag} &= \left(\frac{v_{agd0}}{v_{ag0}}\right)(-\omega_0\Delta\psi_q - \psi_{q0}\Delta\omega - X_e\Delta i_q) \\ &\quad + \left(\frac{v_{agq0}}{v_{ag0}}\right)(\omega_0\Delta\psi_d + \psi_{d0}\Delta\omega + X_e\Delta i_d)\end{aligned} \tag{6.45}$$

Including the linearised stator core-loss equation (eqn. 6.44) into the shaft equation of motion (eqn. 6.15) yields

$$[\omega_0(J/4)s^2 + B''\omega_0 s]\Delta\delta = E\Delta i_q + F\Delta i_d + G\Delta\psi_d + H\Delta\psi_q \tag{6.46}$$

where

$$E = -\omega_0\psi_{d0} + \frac{\partial P_{iron}}{\partial v_{ag}}\left(\frac{v_{agd0}}{v_{ag0}}\right)X_e \tag{6.47a}$$

$$F = \omega_0\psi_{q0} - \frac{\partial P_{iron}}{\partial v_{ag}}\left(\frac{v_{agq0}}{v_{ag0}}\right)X_e \tag{6.47b}$$

$$G = -\omega_0 i_{q0} - \frac{\partial P_{iron}}{\partial v_{ag}}\left(\frac{v_{agq0}}{v_{ag0}}\right)\omega_0 \tag{6.47c}$$

$$H = \omega_0 i_{d0} + \frac{\partial P_{iron}}{\partial v_{ag}}\left(\frac{v_{agd0}}{v_{ag0}}\right)\omega_0 \tag{6.47d}$$

$$B''\omega_0 = B'\omega_0 + \frac{\partial P_{iron}}{\partial \omega} - \frac{\partial P_{iron}}{\partial v_{ag}}\left[\left(\frac{v_{agd0}}{v_{ag0}}\right)\psi_{q0} - \left(\frac{v_{agq0}}{v_{ag0}}\right)\psi_{d0}\right] \tag{6.47e}$$

Thus, modeling the stator core losses explicitly does not introduce any new terms into the the linearised equation of motion, it only modifies the terms already present.

To evaluate these stator core-loss terms in the shaft equation of motion, an approximate value for $\partial P_{iron}/\partial v_{ag}$ is required. From open-circuit tests on the machine,

an approximate value of $\partial P_{iron}/\partial v_{ag} \approx 0.54$ W/V is calculated for air-gap voltages in the vicinity of 390 V. This value of air-gap voltage is representative of the level of air-gap flux at the operating conditions OP1, OP2 and OP3. The above value of $\partial P_{iron}/\partial v_{ag}$ calculated for open-circuit conditions is only an approximate value for evaluating the losses for online conditions. In reality, the core losses for online conditions are noticeably larger than for offline conditions [74].

Including the approximate stator core losses, as well as transformer-voltage and speed-variation terms, and the independent kM_{fd} and kM_{df} parameters in the linearised SMIB equations (eqns. 6.13, 6.14, 6.38, 6.39 and 6.46), results in the machine parameters displayed in Table 6.6.

		OP2	OP1	OP3
X_{dd}	Ω	14.8	13.9	13.0
X_{qq}	Ω	9.6	9.2	9.0
X_{ff}	Ω	844	772	733
$\omega_0 kM_{fd}$	Ω	104.6	97.9	89.9
$\omega_0 kM_{df}$	Ω	91.2	84.6	79.7
B''	Nm/(rad/s)	0.083	0.082	0.074
J	kg m^2	0.27	0.27	0.27

Table 6.6: Evaluated small-signal machine parameters for the simplified SMIB model, including transformer-voltage and speed-variation terms, independent mutual inductance terms and approximate stator core losses.

From Table 6.6 it is apparent that the inclusion of the approximate stator core losses has only a relatively small effect on the majority of the parameters. However the difference between the small-signal incremental mutual reactance terms $\omega_0 kM_{fd}$ and $\omega_0 kM_{df}$ is significantly reduced. The difference in values is of the order of approximately 15%, compared to 25% without the stator core losses modeled. This tends to confirm the argument that the difference in values of the incremental mutual inductance terms is due to the synchronous machine model inadequately representing the core losses.

It is worth noting that by increasing the factor $\partial P_{iron}/\partial v_{ag}$ from 0.54 W/V to approximately 1.2 W/V, the small-signal incremental mutual reactance terms become equal, with only a small change in the other evaluated machine parameters.

Discussion

By relaxing several of the assumptions made in deriving the simplified linearised SMIB equations, machine parameters with reasonable values could be evaluated from the estimated field-to-terminal voltage TF coefficients of the SMIB system. These evaluated small-signal machine parameters differ significantly from both the conventional large-signal machine parameters evaluated from conventional machine tests (Appendix E), and the parameters evaluated from standstill tests. This difference in machine parameters is expected [41,79].

In arriving at the seemingly reasonable machine parameters, several of the common simplifying assumptions used in deriving the small-signal SMIB equations are removed. In particular, for the laboratory synchronous machine, a model including transformer-voltage and speed-variation terms, as well as some allowance for the machine stator core losses (by either allowing for unequal kM_{fd} and kM_{df} values, or explicitly modeling the losses) appears necessary. It must be pointed out that all the models considered accurately represent the field-to-terminal voltage TF of the SMIB system. Using each of the assumed model forms, and the corresponding evaluated machine parameters, the models provide an accurate representation of the field-to-terminal voltage TF. The difficulty is in employing a model form which accurately represents the physical behaviour of the system, and thus results in parameters comparable to the expected (physically realistic) machine parameters. It is not claimed that the final linearised SMIB model used for evaluating the machine parameters is necessarily an accurate representation of the true SMIB system. The exercise only highlights that the proposed estimation method provides a useful tool for examining such issues as the accurate modeling of synchronous generators.

For further work to be pursued in evaluating the parameters of a synchronous machine operating online, or in assessing the relevance or importance of currently unmodeled effects in the machine model, it appears that some sort of auxiliary measurements on the machine are required. These may allow several of the machine parameters to be evaluated independently, and thus used as a cross-reference for comparing the evaluated machine parameters. These measurements could include the independent estimation of several other online machine TFs, such as the field-

voltage to output-power, or field-voltage to shaft-speed TFs. Another alternative is to use an integrated estimation approach, considering the SMIB system as a multi-input multi-output estimation problem.

6.6 Summary and Conclusions

In this chapter, the proposed RIV-BO estimation algorithm is applied to the practical task of estimating the coefficients of the small-signal field-to-terminal voltage TF of a synchronous machine under both online and open-circuit operating conditions. The results of RIV-BO estimation for three closely spaced, online operating conditions of the SMIB arrangement are analysed in detail. Model validation tests performed on the estimated w-domain models confirm they accurately represent the small-signal response of the SMIB system. Independent small-signal sinusoidal frequency response (SSSFR) measurements also confirm the accuracy of the estimated models. The SSSFR tests are very time consuming in comparison to the PRBS perturbation tests performed for the RIV-BO estimation algorithm. The SSSFR measurements take approximately 36 times longer to perform than the PRBS test. From the SSSFR measurements it would be very difficult to calculate accurate values for the complex poles and zeros of the field-to-terminal voltage TF.

Having accurately estimated the coefficients of the field-to-terminal voltage TF of the machine under online operating conditions, the linearised equations describing the SMIB system are solved to evaluate several of the unknown machine parameters. The results show that the conventional simplified linearised SMIB equations are inadequate for accurately modeling the system. It is found that, for the laboratory synchronous machine, the model should include both the transformer-voltage and speed-variation terms, as well as some method of modeling the core losses of the machine. With these terms modeled, machine parameters with reasonable values are evaluated from the estimated TF coefficients.

The machine parameters evaluated from this small-signal type testing are small-signal incremental parameters. They are significantly less than the conventional large-signal machine parameters (approximately 60% of their equivalent unsaturated large-

signal values, which agrees with [41]), as well as being less than the values calculated from standstill tests (chapter 5). When considering the small-signal dynamic performance of synchronous machines, it is these incremental machine parameters that should be used to allow accurate modeling of the system.

From the estimation tasks conducted in this chapter, the RIV-BO estimation algorithm provides a useful tool for accurately estimating the coefficients of the small-signal field-to-terminal voltage TF of a synchronous generator. One possible disadvantage however, with employing the field-to-terminal voltage TF of the machine operating online, is that the TF contains lightly damped complex zeros. As shown in the online estimation studies, this creates difficulties in accurately estimating the TF numerator coefficient $\hat{b}_1$. Another complicating factor is that small external system disturbances, in the bus voltage or DC motor drive, produce oscillatory disturbances at the response mode associated with rotor oscillations of the machine. The frequency of this oscillatory response is close to the corner frequency of the complex zeros. To further complicate the situation, under relatively light loading conditions, the complex poles and zeros of the TF almost cancel, thus increasing the difficulty in accurately estimating them. For the online estimation task considered in this thesis, the field-to-terminal voltage TF proves sufficient for demonstrating the practicality of the proposed RIV-BO estimation algorithm, as well as enabling reasonable machine parameter values to be evaluated. However, it may be possible for the machine parameters to be evaluated more reliably and with less sensitivity over a larger range of operating conditions, if different TFs of the online synchronous machine are employed.

In a practical application of the method for evaluating the parameters of a synchronous machine, it may be best to estimate more than one of the various possible machine TFs, with the relevant TF output signals sampled simultaneously during the one test. This increases the number of unknown machine parameters that can be evaluated, as well as allowing a comparison of the values of the same parameters evaluated from different TFs. Of course, for specific machine TFs it is likely that the accuracy of certain parameters will be higher than for the same parameter evaluated from other TFs. For example, TFs which directly involve the rotor speed or electrical power output signals, which are associated with the shaft equation of motion of the

system, are likely to yield relatively more accurate values of the shaft polar moment of inertia J and damping constant B'.

The original contributions of this chapter include:

- The application of the proposed RIV-BO estimation algorithm to estimating the coefficients of the field-to-terminal voltage TF of a synchronous machine operating under both open-circuit and online operating conditions (section 6.3).
- The development of techniques for, and the evaluation of the synchronous machine parameters from the estimated coefficients of the field-to-terminal voltage TF of a laboratory synchronous machine operating online in a SMIB configuration (section 6.4).
- The experimental investigation of the validity of several common simplifying assumptions used in deriving the small-signal linearised equations of a SMIB system (section 6.5).

Chapter 7

Summary, Conclusions and Further Research

7.1 Summary and Conclusions

The original work contained in this thesis can be separated into two main categories. The first category is the development of a discrete-time, recursive estimation method for estimating, from the sampled input and output signals of a continuous-time system, the coefficients of the continuous-time system model (chapter 3). The method employs a discrete-time bilinear-operator model, the coefficients of which closely approximate those of the corresponding continuous-time system model for sampling frequencies which are high relative to the frequency range of interest of the continuous-time system. The second category is the application of the proposed estimation method to the calculation of the parameters of a synchronous machine under both standstill and online conditions. In chapter 5, the coefficients of several transfer functions of a laboratory synchronous machine are estimated with the machine at standstill; the various machine parameters are evaluated directly from the estimated transfer function coefficients. In chapter 6, the estimation method is applied to the more complex task of estimating the coefficients of the small-signal field-to-terminal voltage transfer function of a laboratory synchronous machine operating online in a single-machine infinite-bus (SMIB) configuration. By solving a set of nonlinear equations, six of the machine parameters can be evaluated.

The discrete-time bilinear-operator model is well suited to the task of estimating the coefficients of a continuous-time model. The coefficients of the bilinear-operator model provide a close approximation to those of the corresponding continuous-time model, as long as the sampling frequency is at least ten times the bandwidth or highest frequency pole or zero of the continuous-time system. This is shown in section 2.3.2. In comparison to the coefficients of the equivalent discrete-time delta-operator model, for a given sampling period, the coefficients of the bilinear-operator model provide a significantly closer approximation to those of the corresponding continuous-time model. This is clearly demonstrated in the example displayed in Figure 2.10. In Appendix A it is proved that, as the sampling period approaches zero, the discrete-time bilinear-operator TF approaches the corresponding continuous-time TF. An important benefit of employing the discrete-time bilinear-operator model is that it is numerically superior with respect to finite word-length computation than the conventional discrete-time shift-operator model. The numerical properties of the bilinear-operator model are similar to those of the delta-operator model. This is demonstrated in a numerical example in section 2.2.3.

It is worth noting that the bilinear operator is related to the shift operator by a nonlinear transformation (eqn. 2.7). In contrast, the delta operator is related by a linear transformation (eqn. 2.4). It is possible the nonlinear transformation for the bilinear operator may limit its applicability to general discrete-time signal processing and control [59]. Another consideration with the bilinear-operator model, which may be important in control applications, is that it may contain non-minimum phase sampling zeros (see the numerical example in section 2.3.2).

Two recursive estimation algorithms employing the bilinear-operator model are developed in chapter 3. The recursive least-squares estimation algorithm employing the bilinear-operator (RLS-BO) (section 3.2) is well-suited to applications in which the system output is contaminated with low-level white additive output noise. For high-level white or coloured additive output noise, the RLS-BO estimation algorithm produces biased estimates. Due to these limitations, an instrumental variable estimation algorithm (RIV-BO) is developed (section 3.3) which provides asymptotically unbiased estimates in the presence of additive output noise.

In arranging the bilinear-operator model into the regression equation form suitable for estimation, a bilinear-operator filter polynomial $J(w)$ is introduced. The coefficients of the filter polynomial $J(w)$ are selected by the user. To help explain the effects that the filter polynomial has on estimation, a frequency-domain analysis of the RLS-BO estimation algorithm is conducted in section 3.2.1. This analysis demonstrates how the selection of the $J(w)$ filter polynomial affects the distribution, across the frequency range of interest, of the modeling error between the true and estimated system models. The $J(w)$ filter polynomial can be used to weight relatively heavily the modeling error in desired frequency regions, thus improving the accuracy of the estimated model in these regions.

In chapter 4, a simulated continuous-time system is employed to assess the ability of the proposed estimation method to estimate accurately the coefficients of the continuous-time system model. Both the RLS-BO and RIV-BO estimation algorithms are investigated together with the effects of unmodeled dynamics and additive output noise on estimation. The simulation studies reveal that the proposed estimation method can accurately estimate, from sampled input and output signals, the coefficients of the continuous-time system model. The studies demonstrate that prefiltering of the sampled input and output signals with a bandpass filter is advisable for estimation. The prefilter removes dc offsets, as well as attenuating unmodeled dynamics outside the frequency range of interest. The prefilter focuses estimation on the frequency range of interest over which accurate modeling of the system is required. The simulation studies show that, as predicted in chapter 3, the RLS-BO estimation algorithm performs well in situations with low-level, white additive output noise, providing that the filter polynomial $J(w)$ is selected to approximately match the denominator of the continuous-time system model. For high-level white or coloured additive output noise the RLS-BO estimation algorithm may contain significant bias in the coefficient estimates. Under these conditions, the RIV-BO estimation algorithm should be employed. The selection of the $J(w)$ filter polynomial for RIV-BO estimation may not be as straight forward as for the RLS-BO algorithm. In some situations, selecting $J(w)$ to match the denominator of the continuous-time model may be sufficient for estimation. However, for the continuous-time system considered

in the later simulation studies (section 4.6.1), a $J(w)$ filter polynomial that weights heavily the modeling error in those regions where the magnitude of the system transfer function is small, proves the better selection.

For all simulation studies, as well as for the practical estimation examples of chapters 5 and 6, the $J(w)$ filter polynomial is selected on a trial-and-error basis. Based on prior knowledge of the system under test, a $J(w)$ polynomial is selected, and estimation performed with the sampled input and output signals. Using various model validation tests (section 5.3.1), the accuracy of the estimated model is assessed, as well as the frequency weighting effect of the selected $J(w)$ filter polynomial (section 3.2.1). If the model accuracy is unsatisfactory, another $J(w)$ polynomial is selected, and estimation re-run. Thus, whilst the proposed recursive estimation method is formulated in a form suitable for real-time online estimation, it may be difficult practically to achieve this because the user is required to select the $J(w)$ filter polynomial. In applications where the characteristics of the continuous-time system under test are relatively simple (see section 4.3.1), and the level of output noise is low, estimation may be insensitive to the selected filter polynomial $J(w)$. However, for continuous-time systems with complex characteristics and with coloured additive output noise (section 4.6.1), the selection of the $J(w)$ filter polynomial may be more critical to the success of estimation. No simple guide-lines can be provided for selection of the $J(w)$ filter polynomial.

Having investigated the ability of the proposed estimation method to estimate accurately the coefficients of the continuous-time model in the various simulation studies, the method is applied to the practical task of estimating the coefficients of certain transfer functions of a laboratory synchronous machine, under both standstill (chapter 5) and online (chapter 6) conditions.

In the standstill tests, the RLS-BO estimation algorithm is employed to estimate the coefficients of three transfer functions of the various test configurations of a laboratory synchronous machine at standstill. For both the d-axis and q-axis transfer functions, accurate third- and second-order models are estimated. Model validation tests confirm the accuracy of the estimated models. For the field-to-stator transfer function, both a second- and third-order model are estimated. Model validation

tests confirm the second-order model provides a reasonably accurate model of the machine field-to-stator response. The estimated third-order model provides a more accurate model. From the estimated transfer function coefficients, the parameters of the synchronous machine are directly evaluated. Because the standstill tests are performed with a small-amplitude excitation signal, the machine parameters calculated are small-signal values. As expected, these are significantly less than the large-signal machine parameters.

Conventionally, the method used to evaluate machine parameters under standstill conditions is to measure the standstill frequency response (SSFR) of the various machine transfer functions. In this method, a sinusoidal excitation signal is used to measure the desired frequency response at discrete frequencies across the frequency range of interest. Iterative curve fitting techniques are then employed to 'fit' a transfer function model to the measured response, from which the machine parameters are evaluated. The proposed estimation method shows considerable advantages over the conventional SSFR method. These include: (i) The coefficients of the various machine transfer functions are estimated directly from the measured input-output signals, as opposed to the sinusoidal SSFR method, which requires some form of iterative curve fitting technique to calculate the transfer function coefficients from the measured frequency response. (ii) The testing time required for the proposed estimation method is significantly less than for the sinusoidal SSFR testing. A ratio of at least 1:11 (RLS-BO to sinusoidal SSFR methods) is achieved for the practical machine tests. (iii) A general frequency-rich excitation signal is used for estimating the machine transfer function coefficients. This removes the need for a high-powered linear amplifier required for sinusoidal SSFR testing, leading to the possible use of a pulse-width modulated type excitation signal.

Standstill tests enable accurate values for the various machine parameters to be evaluated, however, these parameter values are only strictly representative of the synchronous machine under the conditions of which the test is performed. Under online operating conditions, it is likely the machine parameters are different from their standstill test values, due to both rotor rotational effects and saturation. To further demonstrate a practical application of the proposed estimation method, it is

applied to the task of estimating the coefficients of the small-signal field-to-terminal voltage transfer function of a synchronous machine operating online at load in a SMIB configuration. The SMIB configuration is an inherently nonlinear system, and thus the method is employed to estimate the coefficients of the small-signal transfer function of the system at a specified steady-state operating condition. Model validation tests confirm the estimated model accurately represents the small-signal field-to-terminal voltage response of the system. In this application, the estimation method proves much superior to the conventional small-signal sinusoidal frequency response (SSSFR) measurement method because: (i) The SSSFR measurement method is very time consuming in comparison to the testing time required for the proposed estimation method. It is particularly important for online tests that the time required for testing be short because the steady-state operating conditions may drift with time. (ii) With the limited number of measurement points considered in the SSSFR testing, it is difficult to accurately measure the system frequency response, particularly in the frequency region of the complex poles and zeros of the system transfer function (see Figure 6.14). In contrast, the proposed method provides a relatively accurate model in this frequency region.

From the estimated small-signal field-to-terminal voltage transfer function, the values of six of the machine parameters are evaluated by solving the set of linearised equations describing the SMIB system. For the laboratory system, it is found that the conventional simplified linearised SMIB model is inadequate for evaluating the values of the various machine parameters. By including both transformer-voltage and speed-variation terms in the machine model, as well as a term for modeling the stator core losses, reasonable parameters could be evaluated from the estimated transfer functions of the online machine. As has been reported elsewhere, the small-signal machine parameter values evaluated under saturated conditions are significantly less than both the large-signal machine parameter values, and the calculated standstill values. From the online estimation tests performed on the laboratory machine, the values of several of the small-signal machine parameters are approximately 60% of their unsaturated large-signal values, confirming the finite-element analysis of [41]. These online estimation tests highlight the applicability of the proposed estimation

method as a tool for investigating the modeling of synchronous machines under operating conditions.

One disadvantage with estimating the field-to-terminal voltage transfer function of the SMIB system is that it contains complex zeros with very small real components. This produces significant attenuation in the system transfer function in the vicinity of these zeros. This attenuation, in conjunction with the oscillatory disturbances at the modal frequency of the SMIB system, caused by small external system variations, make it difficult to estimate the numerator coefficient which represents the damping constant of the complex zeros. Thus, where the main aim of estimation is the evaluation of values for the parameters of a selected machine model, it may be beneficial to estimate alternative transfer functions of the SMIB system which do not contain complex zeros with small real components.

In summary, this thesis describes the development of a discrete-time recursive estimation algorithm for estimating, from the sampled input-output signals of a continuous-time system, the coefficients of the continuous-time system model. The method is successfully applied to the practical tasks of estimating the coefficients of various transfer functions of a laboratory synchronous machine under both standstill and online operating conditions.

The work pertaining to the development of the recursive estimation method and its application to standstill testing (chapters 3 and 5) is published in references [54,55]. The application of the method to estimating the coefficients of the SMIB transfer function under online operating conditions (chapter 6) is published in reference [56].

7.2 Further Research

From the simulation studies and practical estimation examples considered, the RLS-BO and RIV-BO estimation algorithms developed in this thesis provide a practical method for estimating the coefficients of a continuous-time model of a system from sampled input-output signals. However, there are some areas in which further research should be conducted, in both the development of the recursive estimation method and its application to standstill and online transfer function estimation for synchronous

machines.

Estimation Method

- Although the estimation algorithms are formulated in a recursive form, they are not suitable for use in real-time, online estimation in practice, due to the required user input on the selection of the $J(w)$ filter polynomial. Further research could investigate the online adaptive selection of the $J(w)$ filter polynomial, along lines similar to [30].

- The $J(w)$ filter polynomial is employed to 'control' the distribution of the modeling errors across the frequency range of interest. Further research into the use of higher-order $J(w)$ filter polynomials may result in greater control of the distribution of modeling errors.

- As demonstrated in Simulation Study 6 (section 4.6.1), the difference between success and failure in estimation can be only a small difference in the selection of the $J(w)$ filter polynomials. It may be beneficial to investigate various other recursive estimation algorithms (such as the extended least-squares algorithm) which may be less sensitive to the selection of the $J(w)$ filter polynomial. This may prove useful for real-time online applications, removing the possible requirement for an adaptively updated $J(w)$ filter polynomial.

- A numerical example is used to demonstrate the numerical benefits of the bilinear-operator implementation with respect to finite word-length computation (section 2.3.2). Further research could be conducted to investigate analytically the bilinear-operator numerical properties, including the conditioning of the least-square estimation which, from the studies conducted, appears to be superior to both the delta- and shift-operator implementations.

Standstill Tests

- The standstill tests performed in chapter 5 use a small-signal PRBS excitation signal. The non-strict requirement on the form of the excitation signal should allow a pulse-width modulated type signal with high voltage levels to be

employed to perform large-signal standstill tests on the synchronous machine. Large-signal standstill testing may suffer from the effects of the machine iron nonlinearity and hysteresis, however, large-signal testing is worth investigating.

- The small-signal tests are conducted about a zero steady-state flux level. It may be possible to evaluate machine parameter values that are more representative of the machine under operating conditions, by performing small-signal standstill tests with the machine iron biased at a non-zero steady-state flux level [46].

Online Tests

- The proposed estimation method is able to estimate accurately the coefficients of the small-signal field-to-terminal voltage transfer function of the SMIB system. Further research could be directed at using the proposed estimation method for estimating the coefficients of various other transfer functions of the SMIB system. The simultaneous measurement of various response signals of the SMIB system, such as terminal voltage (Δv_t), speed ($\Delta\omega$) and electrical power output (ΔP_e), for a certain field-voltage perturbation (Δv_f), may enable a single-input multi-output approach to estimation to be adopted, enabling a greater number of machine parameters to be evaluated. By increasing the number of machine parameters that can be evaluated, it may be possible to employ more complex models to accurately represent the synchronous machine.

- By improving the robustness and reliability of the recursive estimation method for real-time online estimation, it may be possible to incorporate the method into continuous-time adaptive control, or possibly online fault diagnosis.

Appendix A

Convergence Proof of w-Domain Transfer Function to Continuous-Time Transfer Function as $\Delta \to 0$

The proof follows that outlined in [6, page 101], which proves that the δ-domain TF, calculated assuming a ZOH, converges to the continuous-time TF as $\Delta \to 0$.

Continuous-Time Transfer Function

Consider the continuous-time system model, given in state-space form by

$$\frac{dx(t)}{dt} = \mathbf{A}x(t) + \mathbf{B}u(t) \tag{A.1}$$

$$y(t) = \mathbf{C}x(t) \tag{A.2}$$

Taking the Laplace transform of eqns. A.1 and A.2 assuming zero initial conditions yields

$$sX(s) = \mathbf{A}X(s) + \mathbf{B}U(s)$$

$$Y(s) = \mathbf{C}U(s)$$

which leads to the continuous-time TF

$$\frac{Y(s)}{U(s)} = \mathbf{C}(sI - \mathbf{A})^{-1}\mathbf{B}$$

w-Domain Transfer Function

Consider the continuous-time response $x(t)$ of eqn. A.1 for $t \geq k\Delta$, given that at $t = k\Delta$ the system is in the state $x(k\Delta)$ [6]

$$x(t) = e^{\mathbf{A}(t-k\Delta)}x(k\Delta) + \int_{k\Delta}^{t} e^{\mathbf{A}(t-\tau)}\mathbf{B}u(\tau)d\tau$$

At time $t = (k+1)\Delta$ the state vector is given by

$$x((k+1)\Delta) = e^{\mathbf{A}\Delta}x(k\Delta) + \int_{k\Delta}^{(k+1)\Delta} e^{\mathbf{A}((k+1)\Delta-\tau)}\mathbf{B}u(\tau)d\tau \tag{A.3}$$

Between these two sample times $k\Delta$ and $(k+1)\Delta$, the input signal $u(t)$ is assumed to obey a triangle-hold variation [57], and thus

$$u(t) = u(k\Delta) + \left(\frac{u((k+1)\Delta) - u(k\Delta)}{\Delta}\right)(t - k\Delta) \tag{A.4}$$

Substituting eqn. A.4 into eqn. A.3, and performing the change of variable $\theta = \tau - k\Delta$ yields

$$\begin{aligned} x((k+1)\Delta) &= e^{\mathbf{A}\Delta}x(k\Delta) + \left[\int_0^{\Delta} e^{\mathbf{A}(\Delta-\theta)}\mathbf{B}d\theta\right]u(k\Delta) \\ &\quad + \left[\frac{1}{\Delta}\int_0^{\Delta} e^{\mathbf{A}(\Delta-\theta)}\mathbf{B}\theta d\theta\right](u((k+1)\Delta) - u(k\Delta)) \end{aligned}$$

Taking the z transform assuming zero initial conditions yields

$$zX(z) = e^{\mathbf{A}\Delta}X(z) + (M + N(z-1))U(z) \tag{A.5}$$

where

$$M = \int_0^{\Delta} e^{\mathbf{A}(\Delta-\theta)}\mathbf{B}d\theta$$

$$N = \frac{1}{\Delta}\int_0^{\Delta} e^{\mathbf{A}(\Delta-\theta)}\mathbf{B}\theta d\theta$$

Using the substitution

$$z = \frac{2+\Delta\beta}{2-\Delta\beta}$$

to convert from z- to w-transform models, eqn. A.5 yields

$$\left(\frac{2+\Delta\beta}{2-\Delta\beta}\right)X(\beta) = e^{\mathbf{A}\Delta}X(\beta) + \left(M + N\left(\frac{2\Delta\beta}{2-\Delta\beta}\right)\right)U(\beta)$$

which rearranges to yield the discrete-time w-domain TF

$$\frac{Y(\beta)}{U(\beta)} = \mathbf{C}\left(\left(\frac{2}{\Delta}+\beta\right)I - \left(\frac{2}{\Delta}-\beta\right)e^{\mathbf{A}\Delta}\right)^{-1}(2-\Delta\beta)\left(\frac{M}{\Delta} + N\left(\frac{2\beta}{2-\Delta\beta}\right)\right) \quad \text{(A.6)}$$

Considering the terms in eqn. A.6 separately as $\Delta \to 0$:

•Term(1)

$$\lim_{\Delta\to 0}\mathbf{C} = \mathbf{C}$$

•Term(2)

$$\text{Term(2)} = \left(\left(\frac{2}{\Delta}+\beta\right)I - \left(\frac{2}{\Delta}-\beta\right)e^{\mathbf{A}\Delta}\right)^{-1}$$

Using the expansion of $e^{\mathbf{A}\Delta}$ [6],

$$\begin{aligned}
(\text{Term(2)})^{-1} &= \left(\frac{2}{\Delta}+\beta\right)I - \left(\frac{2}{\Delta}-\beta\right)\left(I + \mathbf{A}\Delta + \frac{(\mathbf{A}\Delta)^2}{2!} + \frac{(\mathbf{A}\Delta)^3}{3!} + \cdots\right) \\
&= \frac{2}{\Delta}I + \beta I - \frac{2}{\Delta}I - 2\mathbf{A} - \frac{2}{\Delta}\left(\frac{(\mathbf{A}\Delta)^2}{2!} + \frac{(\mathbf{A}\Delta)^3}{3!} + \cdots\right) \\
&\quad +\beta I + \beta\left(\mathbf{A}\Delta + \frac{(\mathbf{A}\Delta)^2}{2!} + \frac{(\mathbf{A}\Delta)^3}{3!} + \cdots\right) \\
&= 2\beta I - 2\mathbf{A} + \beta\mathbf{A}\Delta + \left(\beta - \frac{2}{\Delta}\right)\left(\frac{(\mathbf{A}\Delta)^2}{2!} + \frac{(\mathbf{A}\Delta)^3}{3!} + \cdots\right)
\end{aligned}$$

Taking the limit

$$\lim_{\Delta\to 0}(\text{Term(2)})^{-1} = 2(\beta I - \mathbf{A})$$

and thus

$$\lim_{\Delta\to 0}(\text{Term(2)}) = \frac{1}{2}(\beta I - \mathbf{A})^{-1}$$

•**Term(3)**

$$\lim_{\Delta \to 0}(2 - \Delta\beta) = 2$$

•**Term(4)**

$$\begin{aligned}
\left(\frac{M}{\Delta}\right) &= \frac{1}{\Delta}\int_0^{\Delta} e^{\mathbf{A}(\Delta-\theta)}\mathbf{B}d\theta \\
&= \mathbf{B}e^{\mathbf{A}\Delta}\frac{1}{\Delta}\int_0^{\Delta} e^{-\mathbf{A}\theta}d\theta \\
&= \mathbf{B}\left(I + \mathbf{A}\Delta + \frac{(\mathbf{A}\Delta)^2}{2!} + \frac{(\mathbf{A}\Delta)^3}{3!} + \cdots\right)\left(I - \frac{\mathbf{A}\Delta}{2!} + \frac{(\mathbf{A}\Delta)^2}{3!} - \frac{(\mathbf{A}\Delta)^3}{4!} + \cdots\right)
\end{aligned}$$

Taking the limit

$$\lim_{\Delta \to 0}\left(\frac{M}{\Delta}\right) = \mathbf{B}II = \mathbf{B}$$

•**Term(5)**

$$\begin{aligned}
N\left(\frac{2\beta}{2-\Delta\beta}\right) &= \left(\frac{2\beta}{2-\Delta\beta}\right)\frac{1}{\Delta}\int_0^{\Delta} e^{\mathbf{A}(\Delta-\theta)}\mathbf{B}\theta d\theta \\
&= \left(\frac{2\beta}{2-\Delta\beta}\right)\mathbf{B}e^{\mathbf{A}\Delta}\frac{1}{\Delta}\int_0^{\Delta} e^{-\mathbf{A}\theta}\theta d\theta \\
&= \left(\frac{2\beta}{2-\Delta\beta}\right)\mathbf{B}\left(I + \mathbf{A}\Delta + \frac{(\mathbf{A}\Delta)^2}{2!} + \cdots\right) \times \\
&\quad \Delta\left(\frac{I}{2} - \frac{\mathbf{A}\Delta}{3} + \frac{(\mathbf{A}\Delta)^2}{4\times 2!} - \frac{(\mathbf{A}\Delta)^3}{5\times 3!} + \cdots\right)
\end{aligned}$$

Taking the limit

$$\begin{aligned}
\lim_{\Delta \to 0} N\left(\frac{2\beta}{2-\Delta\beta}\right) &= \left(\frac{2\beta}{2}\right)\mathbf{B}(I)\Delta\left(\frac{I}{2}\right) \\
&= 0
\end{aligned}$$

Thus in the limit as the sampling period approaches zero, the w-domain TF becomes (collecting together the terms labelled Term(1) through Term(5))

$$\begin{aligned}
\lim_{\Delta \to 0}\frac{Y(\beta)}{U(\beta)} &= \mathbf{C}\frac{1}{2}(\beta I - \mathbf{A})^{-1}2(\mathbf{B} + 0) \\
&= \mathbf{C}(\beta I - \mathbf{A})^{-1}\mathbf{B}
\end{aligned}$$

$$= \frac{Y(s)}{U(s)} \Big|_{s=\beta}$$

Hence, as the sampling period approaches zero, the triangle-hold-equivalent discrete-time w-domain TF converges to the continuous-time TF.

Appendix B

Frequency Domain Error Criterion

In section 3.2.2, to interpret further the effects of filters and the input excitation signal on estimation, the quadratic error criterion is examined in the frequency domain.

In this appendix, the error criterion is expressed in the frequency domain. The quadratic error criterion in the time domain is given by

$$\begin{aligned} V(\hat{\theta}) &= \frac{1}{N}\sum_{k=1}^{N}(y_k - \phi_k^T\hat{\theta})^2 \\ &= \frac{1}{N}\sum_{k=1}^{N} e_k^2 \end{aligned} \tag{B.1}$$

Assuming $\{e_k\}$ is a stationary stochastic process, the autocorrelation function is given by [85]

$$R_e(\tau,\hat{\theta}) = \lim_{N\to\infty}\frac{1}{N}\sum_{k=1}^{N} e_k e_{k+\tau} \tag{B.2}$$

The power spectral density of the discrete-time signal e_k is given by [85]

$$\Phi_e(f,\hat{\theta}) = \sum_{\tau=-\infty}^{\infty} R_e(\tau,\hat{\theta})e^{-j2\pi f\Delta\tau}$$

Having introduced the autocorrelation and power spectral density functions, the error criterion can now be formulated in the frequency domain [10]. Taking the limit of

eqn. B.1 as N tends to infinity yields

$$\begin{aligned}\bar{V}(\hat{\theta}) &= \lim_{N\to\infty} V(\hat{\theta}) \\ &= \lim_{N\to\infty} \frac{1}{N}\sum_{k=1}^{N} e_k^2\end{aligned}$$

Using eqn. B.2, the quadratic error criterion becomes

$$\bar{V}(\hat{\theta}) = R_e(0,\hat{\theta})$$

The inverse Fourier transform enables the error criterion to be expressed in the frequency domain [85]

$$\bar{V}(\hat{\theta}) = R_e(0,\hat{\theta}) = \Delta \int_{\frac{-1}{2\Delta}}^{\frac{1}{2\Delta}} \Phi_e(f,\hat{\theta})df \tag{B.3}$$

Eqn. B.3 shows that minimising the quadratic error criterion, $V(\hat{\theta})$ (as $N \to \infty$), is equivalent to minimising the power spectral density of the prediction error e_k across the frequency range $-f_s/2$ to $f_s/2$, where $f_s = 1/\Delta$ is the sampling frequency.

The error power spectral density can be expanded using the prediction error signal, e_k, of the RLS-BO estimation algorithm (eqn. 3.12). From eqn. 3.12a, the prediction error is given by

$$e_k = y_k - \phi_k^T\hat{\theta} = y_k - \hat{y}_k$$

An alternative expression for $\hat{y}_k$ is given by eqn. 3.6 (with both polynomials $A(w)$ and $B(w)$ replaced with their estimates $\hat{A}(w)$ and $\hat{B}(w)$), thus e_k becomes

$$\begin{aligned}e_k &= y_k - \frac{[J(w)-\hat{A}(w)]}{J(w)}y_k - \frac{\hat{B}(w)}{J(w)}u_k \\ &= \frac{\hat{A}(w)}{J(w)}y_k - \frac{\hat{B}(w)}{J(w)}u_k\end{aligned}$$

Assuming the true system is described by eqn. 3.15, the prediction error signal rearranges to yield

$$e_k = \frac{\hat{A}(w)}{J(w)}\left\{\left[\frac{B(w)}{A(w)} - \frac{\hat{B}(w)}{\hat{A}(w)}\right]u_k + \eta_k\right\}$$

As mentioned in chapter 3, both the measured input and output signals are prefiltered prior to estimation. Assuming the prefilter has the w-domain TF Pre(β), the

prediction error becomes

$$e_k = \mathrm{Pre}(w)\frac{\hat{A}(w)}{J(w)}\left\{\left[\frac{B(w)}{A(w)} - \frac{\hat{B}(w)}{\hat{A}(w)}\right]u_k + \eta_k\right\}$$

For a discrete-time w-operator model given by

$$y(k) = \frac{C(w)}{D(w)}u(k),$$

the power spectral density relationship between the sampled input and output signals is

$$\Phi_y(f) = \left|\frac{C(\beta)}{D(\beta)}\right|^2 \Phi_u(f), \tag{B.4}$$

which can be derived directly from the corresponding shift-operator relationship [10]. Using eqn. B.4, the power spectral density of the prediction error signal thus becomes

$$\Phi_e(f,\hat{\theta}) = |\mathrm{Pre}(\beta)|^2 \left|\frac{\hat{A}(\beta)}{J(\beta)}\right|^2 \left\{\left|\frac{B(\beta)}{A(\beta)} - \frac{\hat{B}(\beta)}{\hat{A}(\beta)}\right|^2 \Phi_u(f) + \Phi_\eta(f)\right\} \tag{B.5}$$

Thus, minimising the quadratic error function, $\bar{V}(\hat{\theta})$, in the time domain, is equivalent to minimising the power spectral density of the error signal, $\Phi_e(f,\hat{\theta})$, in the frequency domain, where $\Phi_e(f,\hat{\theta})$ is given by eqn. B.5.

Appendix C

Matlab Code for the Implementation of the RLS-BO Estimation Algorithm

This appendix contains Matlab code for implementing the RLS-BO estimation algorithm for Simulation Study 2, section 4.3.2. The code consists of a main program, `main`, and two subroutines, `rls` and `updatebilins`. The code requires the simulated or measured continuous-time input and output signals, `realinputdata` and `realoutputdata`, respectively, as input for the estimation algorithm.

```
**********    main    **********

%    Performs RLS-BO estimation
%    Chapter 4, Simulation 2.
%
%  number of iterations of the RLS-BO estimation algorithm
iteration = 3000;
%
%  forgetting factor
lamda = 0.99;
%
%  sampling period
delta = 0.01;
%
%  number of iterations before updating of the coefficient
%  estimates begins
```

```
%  (produces a smoother initial variation in coefficient estimates)
purge = 10;
%
%  order of the estimated model
order=4
order=2*order;
%
%  zero the previous time-sample filtered input-output signals,
%  i.e. w^4y(k-1)/J(w), w^4u(k-1)/J(w)
yfbilins=0;
ufbilins=0;
%
%  define estimation J(w) filter polynomial
jbilin=conv([1 0.5],[1 0.5]);
jbilin=conv([1 7.5],jbilin);
jbilin=conv([1 7.5],jbilin)';
%
%  zero initial regression vector, and initialise parameter
%  estimate vector with zero a_i and b_i estimates.
bilindatas=zeros(order,1);
bilinthetas=[jbilin(2);jbilin(3);jbilin(4);jbilin(5);0;0;0;0];
%
%  initialise covariance matrix, P = cI.
bilinps=100000*eye(order);
%
%  define matrices for the recursive updating of the
%  estimation regression vector
jinv=[ jbilin'
       -delta/2 1 0 0 0
       0 -delta/2 1 0 0
       0 0 -delta/2 1 0
       0 0 0 -delta/2 1];
jinv=jinv\[1       0 0 0 0 0
           0 delta/2 1 0 0 0
           0 0 delta/2 1 0 0
           0 0 0 delta/2 1 0
           0 0 0 0 delta/2 1];
%
%  begin RLS-BO estimation
for i=1:iteration,
%
%  set y and u equal to the simulated or measured continuous-time
%  output and input signals, respectively
  y=realoutputdata(i);
  u=realinputdata(i);
%
%  update regression vector
```

```
[bilindatas,yfbilins,ufbilins]=updatebilins(bilindatas,y, ...
                                        u,yfbilins,ufbilins,jinv);
%
if i>purge,
%
%  update parameter estimates and covariance matrix
    [bilinthetas,bilinps,err]=rls(bilinthetas,bilinps, ...
                                                bilindatas,lamda,y);
  end;
%
%  remove the known J(w) polynomial coefficients and store the
%  continuous-time model coefficients (with correct sign)
bilins(:,i)=[-bilinthetas(1:order/2);bilinthetas(order/2+1:order)]...
                      +[jbilin(2:(order/2+1))',zeros(1,order/2)]';
end;

**********    rls    **********

function [theta,p,error]=rls(theta,p,data,lamda,y)
% calculates new parameter estimates and covariance matrix
% required inputs to rls(theta,p,data,lamda,y) are
% theta - past parameter estimate vector
% p - past covariance matrix
% data - regression vector
% lamda - forgetting factor
% y - current system output
% all vectors are column vectors
%
yhat=data' *theta;
num=lamda+data'*p*data;
%
%  calculate the prediction error
error=(y-yhat);
%
%  update parameter estimate vector
theta=theta+p*data*error/num;
%
%  update covariance matrix
p=(1/lamda)*(p-p*data*(data')*p/num);

**********    updatebilins    **********

function [bilindatas,yfbilins,ufbilins]=updatebilins(bilindatas, ...
                                        y,u,yfbilins,ufbilins,jinv);
%
% updates the regression vector
%
```

```
%
%                                -1
%     jinv= |1 j3  j2 j1 j0 |    | 1     0 0 0 0 0 |
%           |-del/2 1 0 0 0 |    | 0 del/2 1 0 0 0 |
%           |0 -del/2 1 0 0 |    | 0 0 del/2 1 0 0 |
%           |0 0 -del/2 1 0 |    | 0 0 0 del/2 1 0 |
%           |0 0 0 -del/2 1 |    | 0 0 0 0 del/2 1 |
%
temp=max(size(bilindatas));
%
%  section regression vector into vectors containing input
%  and output signals. include y and u, and yfbilins and
%  ufbilins.
tempy=[y;yfbilins;bilindatas(1:temp/2)];
tempu=[u;ufbilins;bilindatas(temp/2+1:temp)];
%
%  update regression vector segments
nowy=jinv*tempy;
nowu=jinv*tempu;
yfbilins=nowy(1);
ufbilins=nowu(1);
%
%  reform full regression vector
bilindatas=[nowy(2:temp/2+1);nowu(2:temp/2+1)];
```

Appendix D

Interface and Measurement Electronics for the Standstill and Online Estimation Applications

For both practical applications of the proposed estimation method, i.e. standstill TF estimation of chapter 5 and the online TF estimation of chapter 6, filter and transducer circuitry is designed and constructed. These circuits are constructed on Eurocard prototype boards, and housed in a Eurocard chassis. This appendix provides the circuit diagrams for these filters and transducers.

Standstill Test Electronics

Figure D.1 displays the circuit diagram of the signal conditioning filter which accepts the pseudo random binary sequence generated by the RTS (v_{PRBS}), and filters/scales the signal for input to the power amplifier (v_{PRBSf}, see Figure 5.4). The filter is reconfigurable as a first-order low-pass filter ($f_c \approx 1$ kHz), or a second-order Butterworth low-pass filter ($f_c \approx$10, 20 or 30 Hz).

Figure D.2 displays the circuit diagram for the two matching fifth-order Butterworth anti-aliasing filters ($f_c = 160$ Hz) employed for the standstill tests (see Figure 5.4).

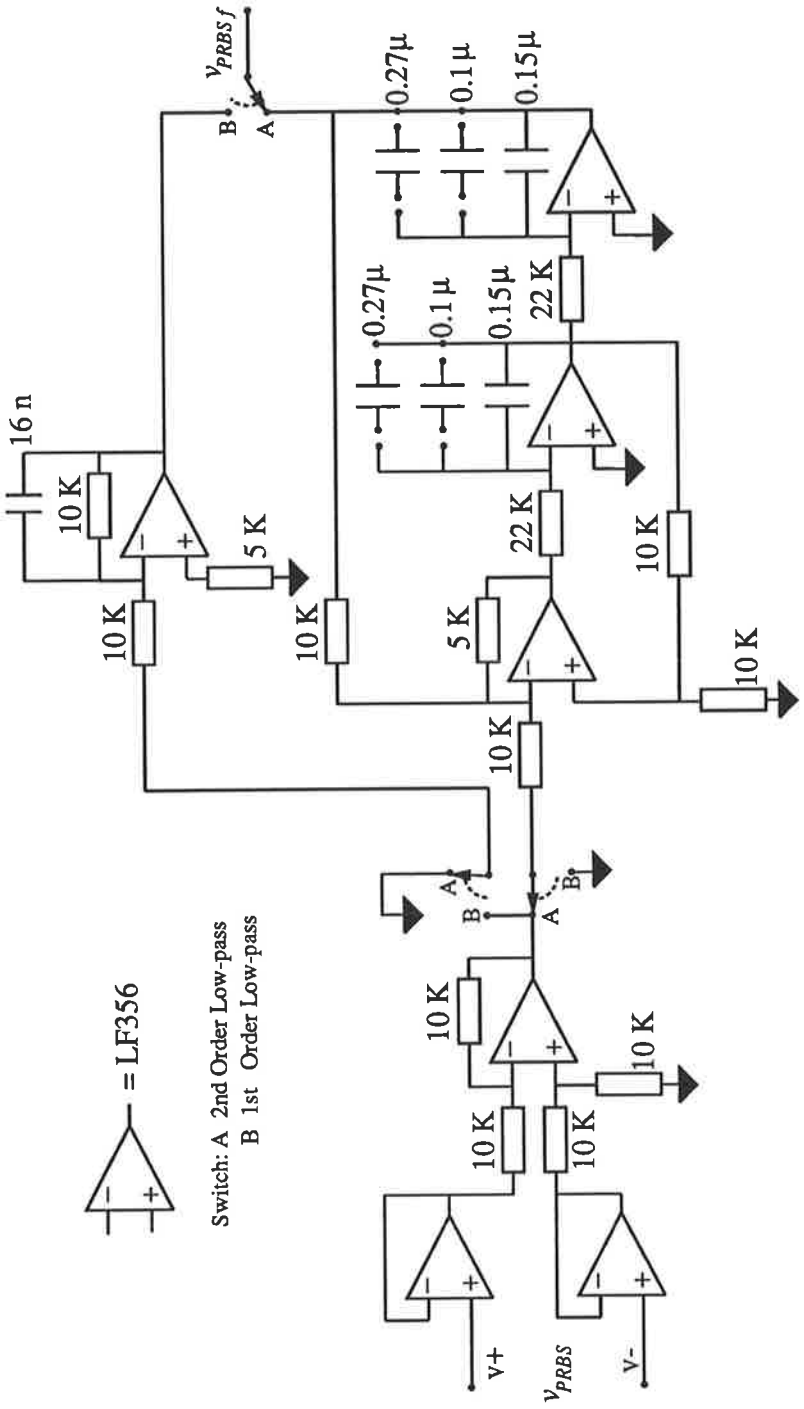

Figure D.1: Signal conditioning filter, for low-pass filtering the PRBS generated by the RTS.

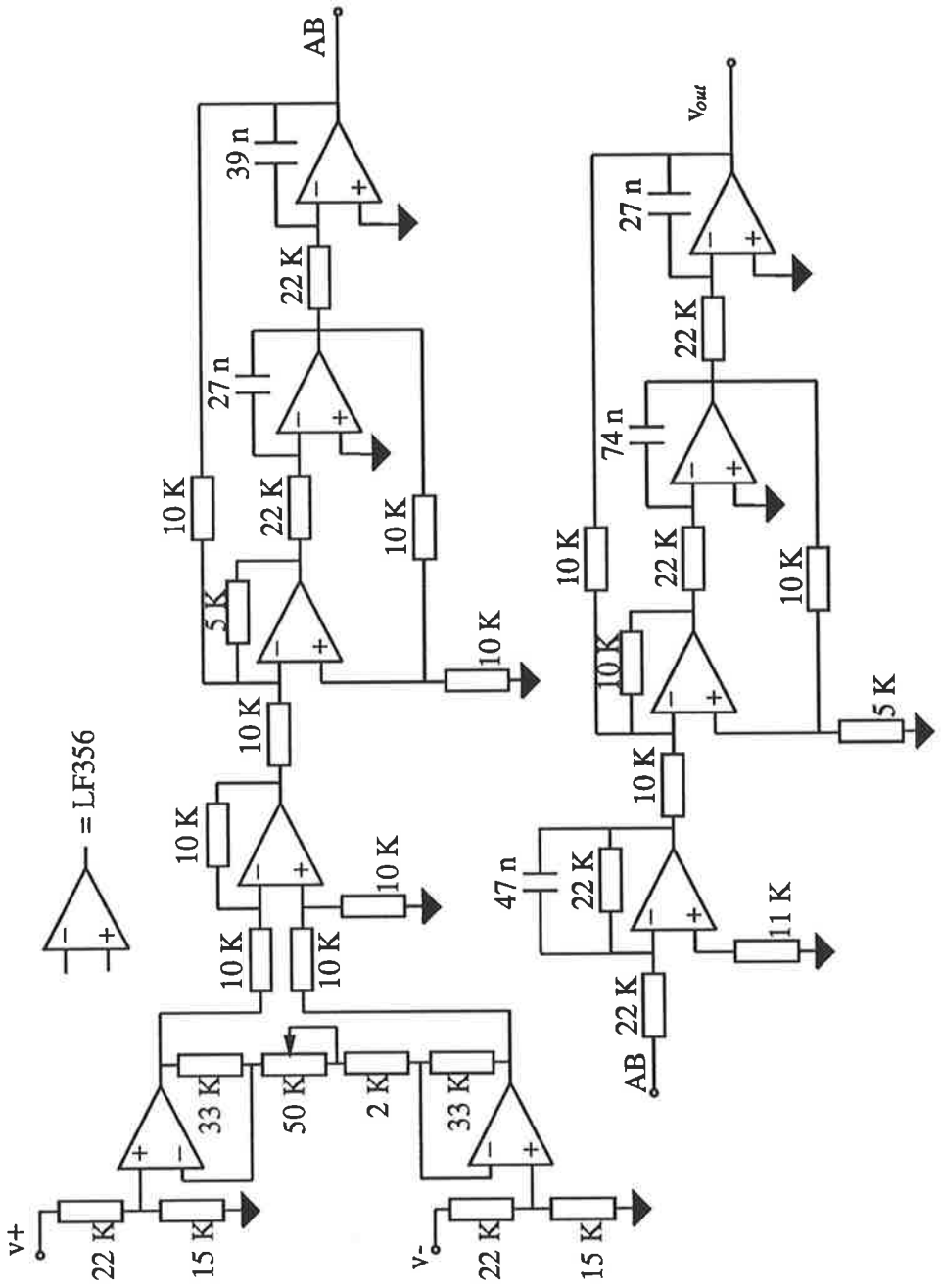

Figure D.2: Anti-aliasing filters for standstill tests.

Online Test Electronics

For the online machine tests (see Figure 6.2), transducer and filter circuitry is designed and constructed for measuring the small-signal field- and terminal-voltage perturbations. The terminal-voltage transducer circuitry consists of a precision three-phase rectifier, followed by a first-order high-pass filter ($f_c \approx 0.02$ Hz), and a fifth-order Butterworth low-pass filter ($f_c \approx 40$ Hz). The field-voltage filter circuitry essentially consists of a high-pass and low-pass filter, matching the filters of the terminal-voltage circuitry. The terminal-voltage and field-voltage circuitry are displayed in Figures D.3 and D.4, respectively. Figure D.5 displays the common high-pass and low-pass filter circuitry. As for the standstill tests, the signal conditioning filter of Figure D.1 is used to filter the PRBS generated by the RTS before being applied to the power amplifier for the field voltage supply.

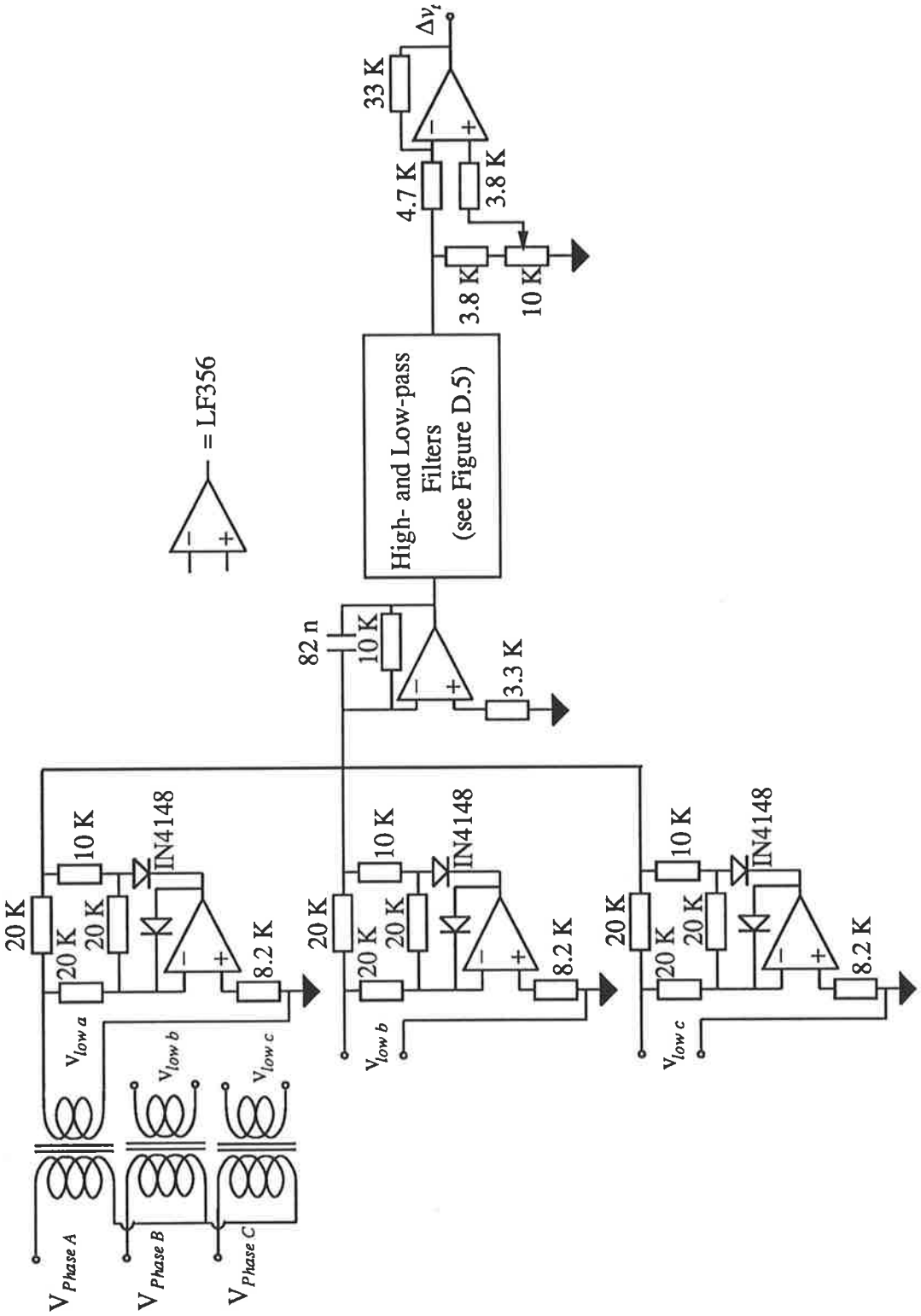

Figure D.3: Terminal-voltage transducer circuitry for small-signal online tests.

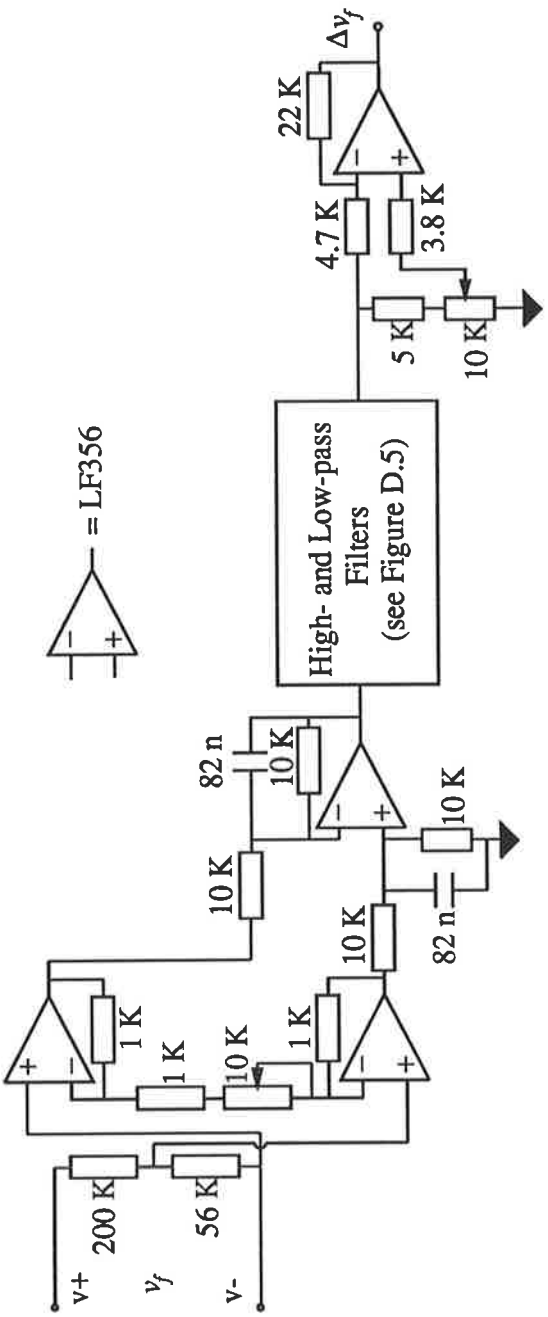

Figure D.4: Field voltage filter circuitry for small-signal online tests.

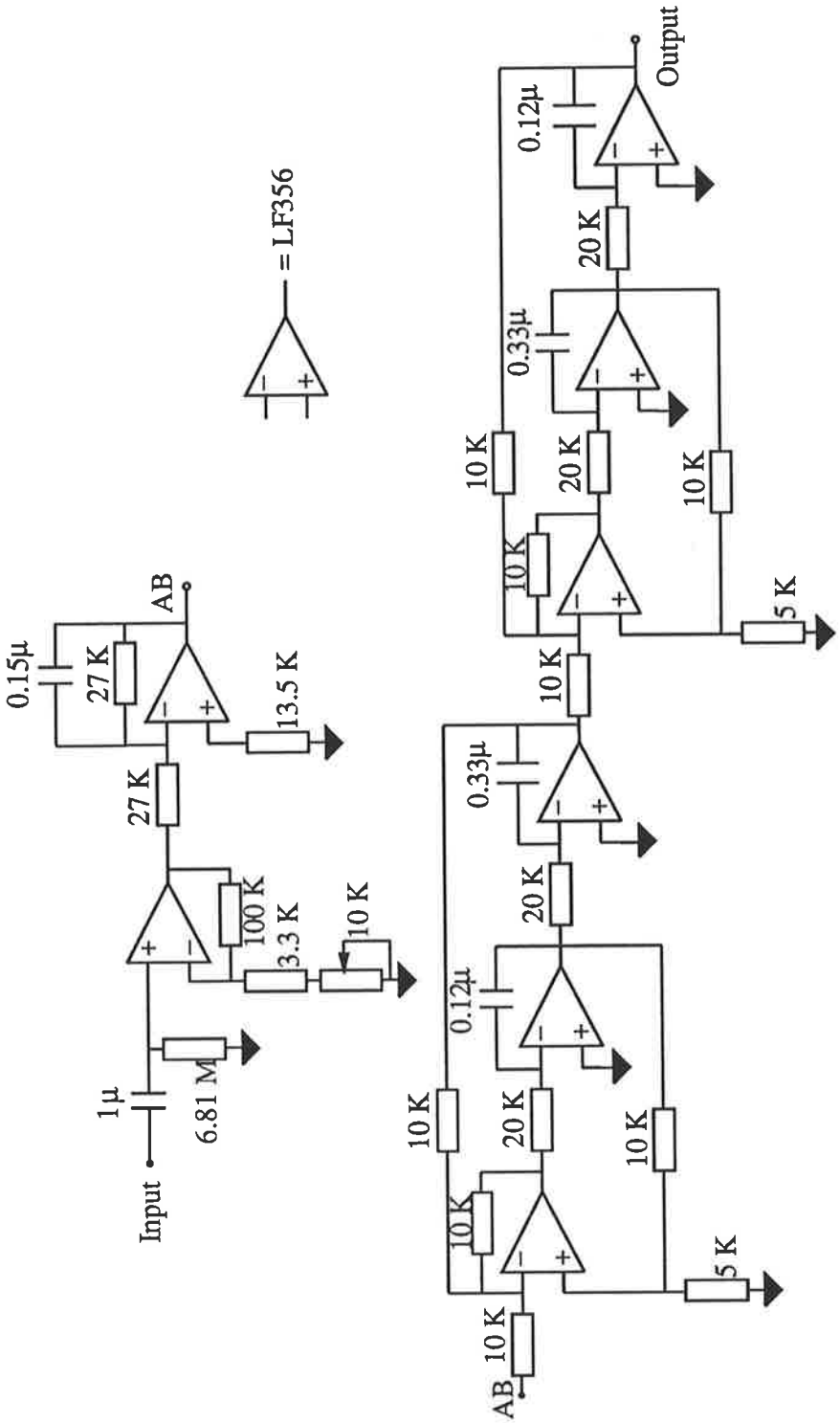

Figure D.5: The common high-pass and low-pass filters for the field- and terminal-voltage transducers (see Figures D.3 and D.4).

Appendix E

Large-Signal Machine Tests

In order to be able to assess the values of the parameters calculated from both the standstill and online tests performed in chapters 5 and 6, some conventional large-signal tests are performed on the synchronous machine and DC motor arrangement to calculate several of the system parameter values.

E.1 Open-Circuit and Short-Circuit Characteristics

The open-circuit characteristic of a synchronous machine is a plot of the machine terminal voltage versus the field excitation current, with the machine operating on open-circuit at synchronous speed. Similarly, the short-circuit characteristic is a plot of the machine terminal current versus field excitation, with the stator terminals short-circuited and the machine operating at synchronous speed. Figure E.1 displays both the open-circuit and short-circuit characteristics for the laboratory synchronous machine considered in chapters 5 and 6. From these two characteristics both the large-signal d-axis synchronous reactance, X_d, and the large-signal d-axis mutual reactance, $\omega_0 k M_f$, are calculated.

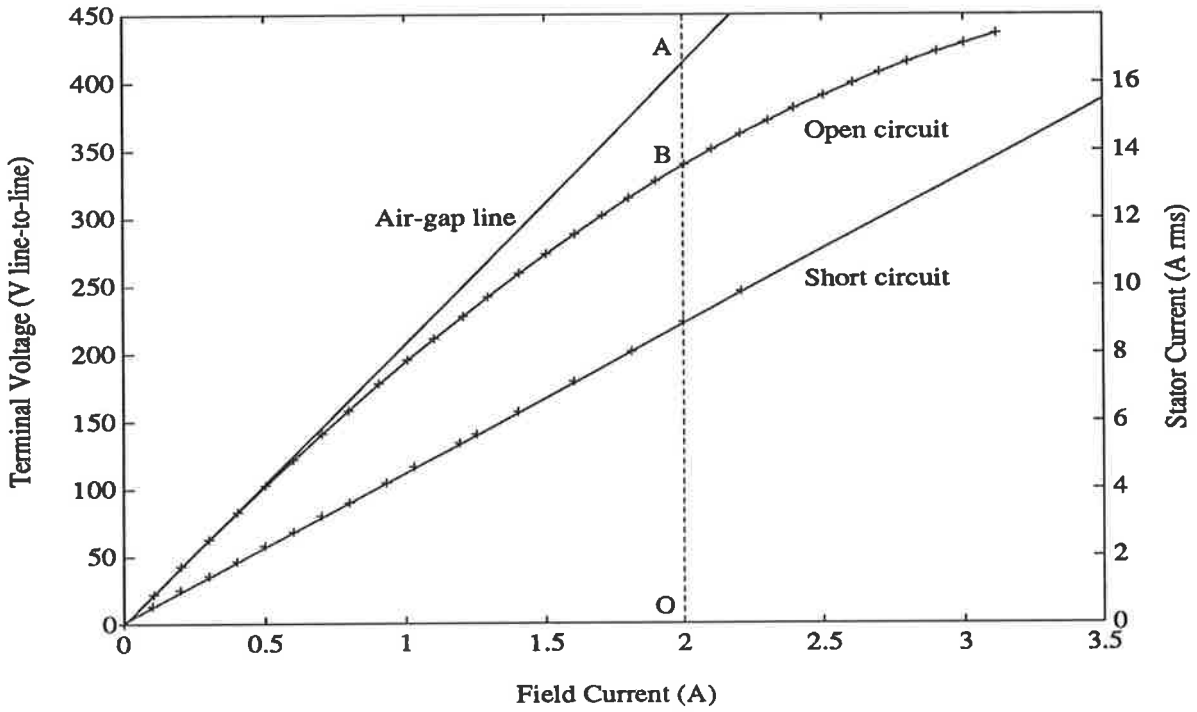

Figure E.1: Open-circuit and short-circuit characteristics of the laboratory synchronous machine.

- X_d

The unsaturated value of the synchronous reactance X_d can be calculated from the open- and short-circuit characteristics using the equation [74]

$$X_{d_{unsat}} = \frac{\text{initial slope of open-circuit characteristic}}{\text{slope of short-circuit characteristic}}$$

From Figure E.1, this yields a value of

$$X_{d_{unsat}} \approx 27\Omega$$

The open-circuit characteristic can also be used to evaluate saturated values of X_d. Assuming the d-axis leakage reactance, X_l, is known ($X_l = 2.6\Omega$, calculated in section E.2), the saturated reactance is given by [74]

$$X_d = X_l + \frac{X_{d_{unsat}} - X_l}{k} \tag{E.1}$$

where k is the saturation factor. From the open-circuit characteristic, the saturation factor k at a given field current is given by the ratio of the air-gap line voltage, to the true open-circuit terminal voltage. For example, from Figure E.1, at a field current of $i_f = 2.0$ A, the saturation factor is

$$k = \text{OA/OB} = 415/339 = 1.224$$

Using eqn. E.1, assuming $X_l = 2.6\Omega$, yields a saturated value of the d-axis synchronous reactance (corresponding to a field current of $i_f = 2.0$ A),

$$X_d \approx 2.6 + \frac{27 - 2.6}{1.224} \approx 22.5\Omega$$

The saturated value of X_d can be evaluated for other values of field current using the same procedure. Figure E.2 displays the variation in X_d with field current i_f, the values which are calculated using eqn. E.1 and the open-circuit characteristic, Figure E.1.

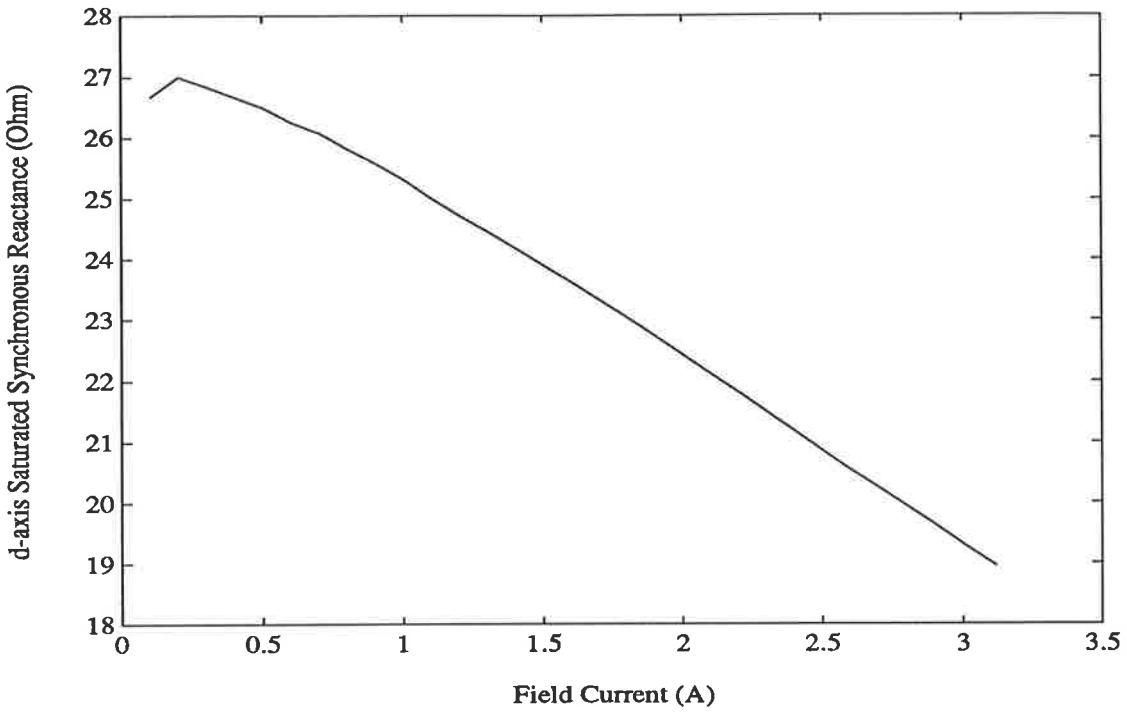

Figure E.2: Variation in X_d with field current i_f.

- $\omega_0 k M_f$

Under steady-state open-circuit conditions, the synchronous machine flux-linkage and voltage equations (eqns. 6.1, 6.2 and 6.4) yield the relationship

$$v_t = v_q = \omega_0 k M_f i_f$$

Thus the machine mutual reactance $\omega_0 k M_f$ can be directly evaluated from the machine open-circuit characteristic, which is a plot of v_t versus i_f. The unsaturated value of $\omega_0 k M_f$, evaluated from the open-circuit characteristic using $\omega_0 k M_f = v_t / i_f$ at a low level of field current yields

$$\omega_0 k M_{f_{unsat}} \approx 210\Omega$$

At a field current of $i_f = 2.0$ A, the corresponding saturated value of $\omega_0 kMf = v_t/i_f$ is

$$\omega_0 kM_f \approx 169\Omega \text{ (for } i_f = 2.0 \text{ A)}$$

Figure E.3 displays the variation in $\omega_0 kM_f$ with field current.

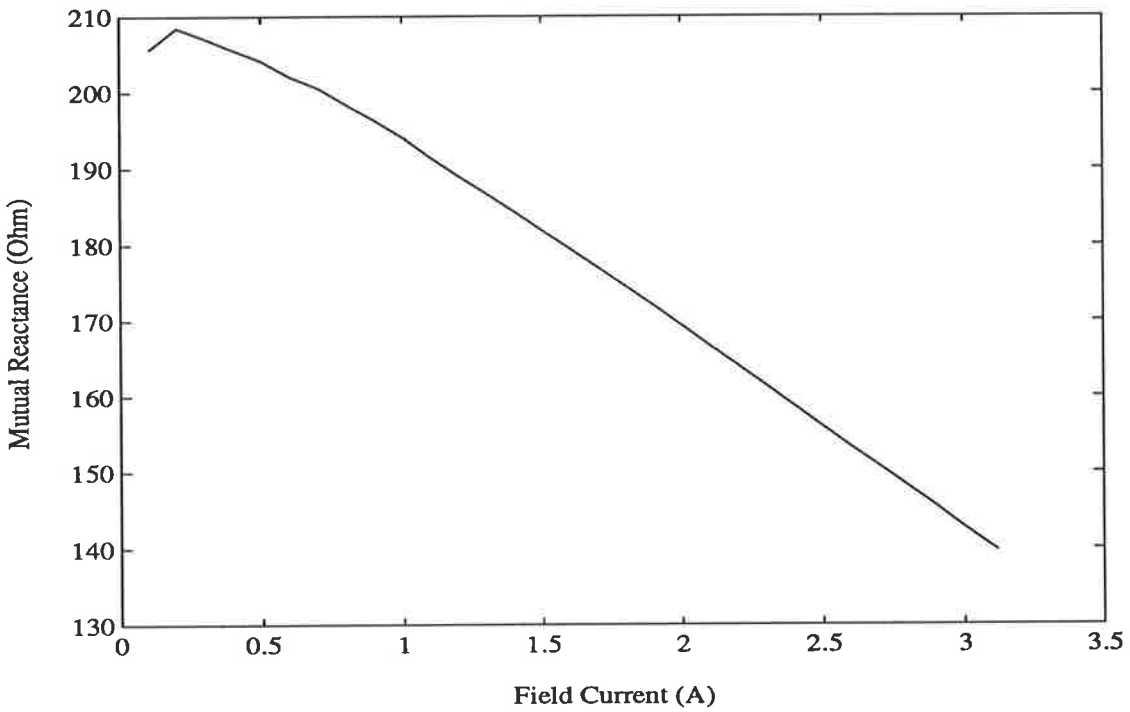

Figure E.3: Variation in $\omega_0 kM_f$ with field current i_f.

E.2 Zero-Power-Factor Characteristic

The Zero-Power-Factor (ZPF) test is employed to calculate a value for the d-axis machine leakage reactance. For the ZPF test, the synchronous machine is configured as in Figure E.4, connected to the three-phase supply through an external reactance and a three-phase auto-transformer. In this configuration, the synchronous machine is operated with zero real power output at a power factor angle of 90° lagging. Whilst keeping the machine stator current at a constant value ($I_a = 5$ A for this test), the machine field current, i_f, is varied. The ZPF characteristic is the plot of the stator

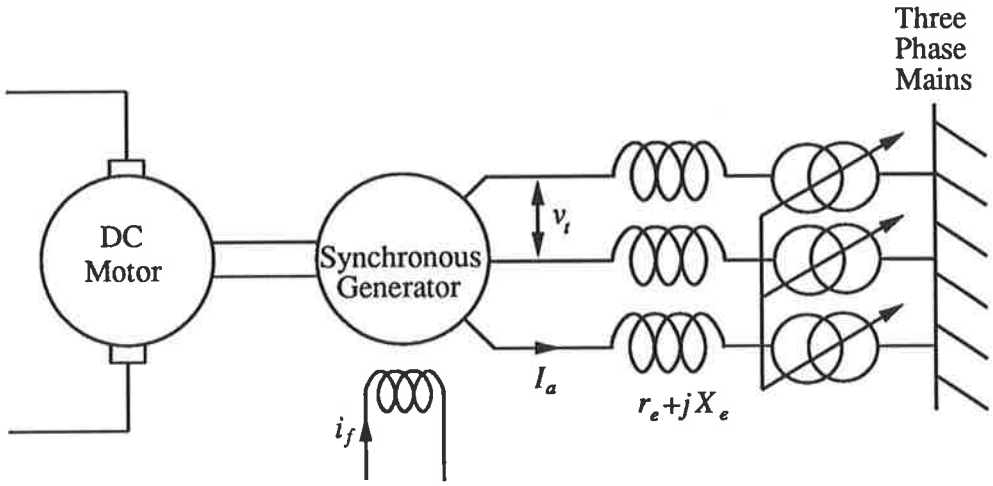

Figure E.4: Zero-power-factor test machine configuration.

voltage v_t versus field current i_f for the fixed stator current value (i.e. $I_a = 5$ A). Note that in order to ensure the constant stator current and constant power factor angle of 90° lagging, the auto-transformer output voltage must be varied whilst the field current is varied. Figure E.5 displays the ZPF characteristic for the laboratory machine for a stator current of $I_a = 5$ A. The open-circuit characteristic is also displayed. Under certain ideal conditions [74], the shape of the open-circuit and ZPF curves are identical. The ZPF curve is simply the open-circuit curve shifted downwards by an amount equal to the voltage drop across the leakage reactance, X_l, and moved across by an amount equal to the armature reaction magneto-motive-force (mmf). Thus a Poitier triangle may be fitted (triangle *abc*, Figure E.5) between the two curves [74], from which the voltage drop due to the leakage reactance may be measured. Since the machine stator current is know for the measured ZPF curve ($I_a = 5$ A), the machine leakage reactance can be calculated. For the laboratory synchronous machine, from Figure E.5, the leakage reactance is calculated as

$$X_l \approx \frac{22.5/\sqrt{3}}{5} = 2.6\Omega$$

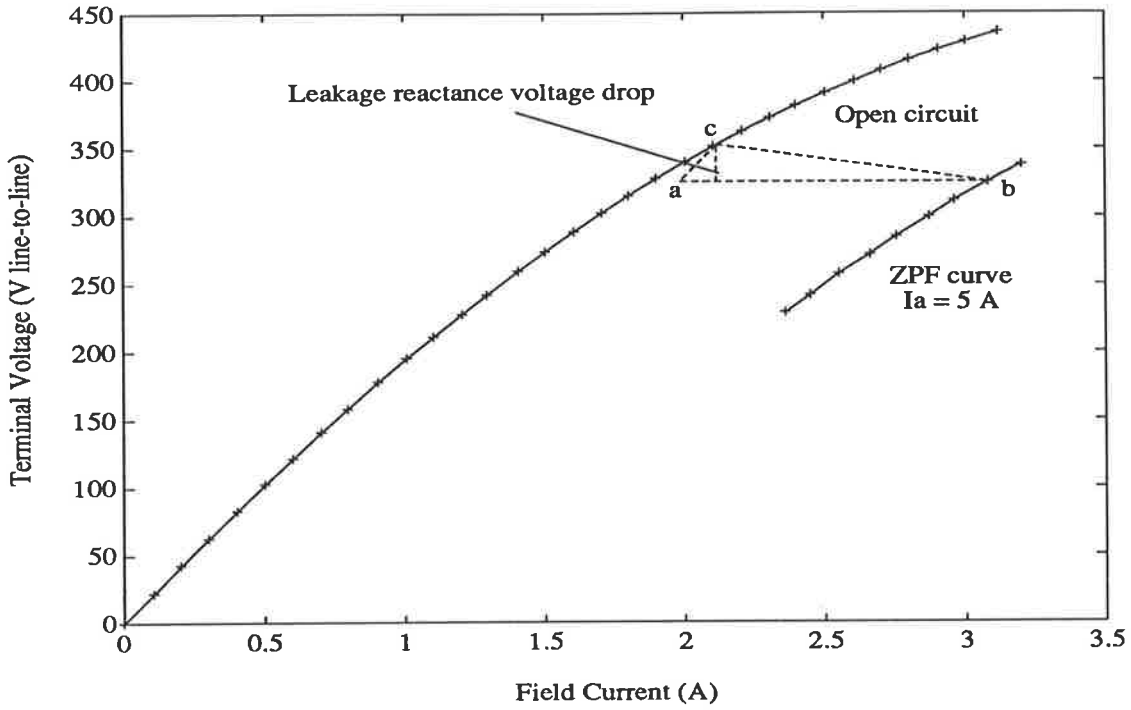

Figure E.5: Zero-power-factor characteristic, $I_a = 5$ A.

E.3 Slip Test

The slip test provides a means of calculating values for both the d- and q-axis unsaturated synchronous reactances $X_{d_{unsat}}$ and $X_{q_{unsat}}$. In the slip test the machine is driven mechanically at a speed slightly different to synchronous speed. With the field winding open-circuited, a reduced voltage three-phase supply is connected to the machine stator terminals, providing a synchronously rotating armature mmf wave. As the rotor is rotating at a speed slightly different to synchronous speed, the mmf wave slowly cycles between being aligned with the rotor d-axis and then the rotor q-axis. Figure E.6 displays the form of the terminal-voltage and stator-current waveforms measured during a typical slip test. When the terminal voltage waveform envelope is maximum, and the stator current envelope minimum, the mmf is aligned with the rotor d-axis, with $X_{d_{unsat}}$ given by the ratio of the terminal-voltage to stator-current envelope [74]. The value of $X_{q_{unsat}}$ is similarly calculated from the measured voltage and current envelopes when the voltage is minimum, and the current maximum. For

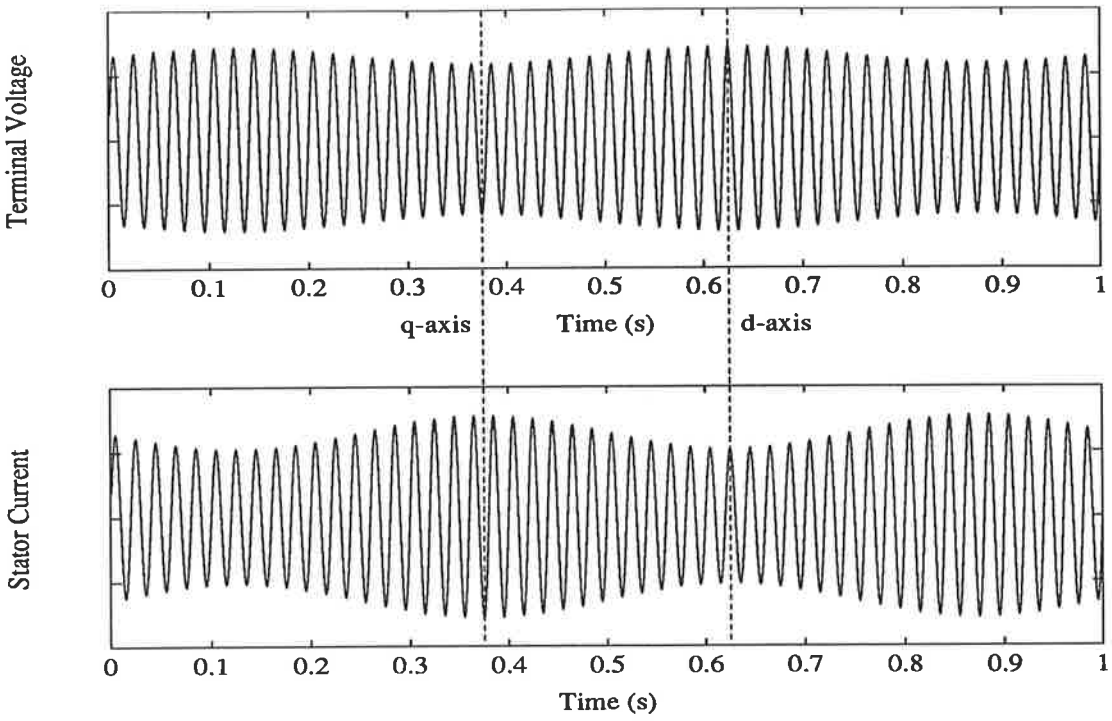

Figure E.6: Typical terminal-voltage and stator-current waveforms during a slip test.

the laboratory synchronous machine, the unsaturated reactance values are calculated as

$$X_{d_{unsat}} \approx 26.9\Omega$$

$$X_{q_{unsat}} \approx 11.5\Omega$$

E.4 Rundown Test

To calculate the polar moment of inertia J of the synchronous machine/DC motor system, rundown tests are performed. In these tests, the power required to drive the synchronous machine under open-circuit conditions with a constant field current is measured, over a large range of rotor speeds. Because there is no external mechanical load connected to the machine, the input power equals the total losses in the system, P_e, which are a function of speed and the synchronous machine field current. Disconnecting the DC motor armature circuit, whilst the synchronous machine is driven

under open circuit conditions, will cause the system rotor to decelerate, governed by the equation

$$J\omega_m \frac{d\omega_m}{dt} = -P_e,$$

where J is the rotor polar moment of inertia, ω_m is the rotor speed in mechanical radians per second, and P_e are the total losses which are measured previously. Thus, by measuring the rotor speed for a period of time after open-circuiting the DC motor armature circuit, the polar moment of inertia J of the system rotor can be calculated. For the laboratory synchronous machine and DC motor system, a consistent value of J is calculated,

$$J = 0.27 \text{ kg m}^2,$$

for various field excitation currents, over a range of speeds during the rundown test.

Bibliography

[1] P. M. Anderson and A. A. Fouad, *Power System Control and Stability.* USA: The Iowa State University Press, 1977.

[2] J. P. Norton, *An introduction to identification.* London: Academic Press, 1986.

[3] A. M. El-Serafi, A. S. Abdallah, and M. K. El-Sherbiny, "Experimental study of the saturation and the cross-magnetizing phenomenon in saturated synchronous machines," *IEEE Trans. on Energy Conversion*, vol. EC-3, pp. 815–823, Dec. 1988.

[4] R. Isermann, "Process fault detection based on modeling and estimation methods – a survey," *Automatica*, vol. 20, no. 4, pp. 387–404, 1984.

[5] H. Hägglund and K. J. Åström, "Industrial adaptive controllers based on frequency response techniques," *Automatica*, vol. 27, no. 4, pp. 599–609, 1991.

[6] R. H. Middleton and G. C. Goodwin, *Digital control and estimation.* Australia: Prentice-Hall, 1990.

[7] H. Unbehauen and G. P. Rao, "Continuous-time approaches to system identification - a survey," *Automatica*, vol. 26, no. 1, pp. 23–35, 1990.

[8] A. Patra and G. P. Rao, "Continuous-time approach to self-tuning control: algorithm, implementation and assessment," *IEE Proc. D*, vol. 136, pp. 333–340, Nov. 1989.

[9] J. J. D'Azzo and C. H. Houpis, *Linear control system analysis and design.* Singapore: McGraw-Hill, 1981.

[10] L. Ljung, *System identification: theory for the user.* New Jersey: Prentice-Hall, 1987.

[11] G. C. Goodwin and K. S. Sin, *Adaptive filtering prediction and control.* New Jersey: Prentice-Hall, 1984.

[12] T. Söderström and P. Stoica, *System identification.* UK: Prentice Hall, 1989.

[13] R. D. Lang, M. A. Hutchison, and H. Yee, "Microprocessor-based identification system applied to synchronous generators with voltage regulators," *IEE Proc. C*, vol. 130, pp. 257–265, Sept. 1983.

[14] M. E. Coultes, P. Kundur, and G. J. Rogers, "On-line frequency response tests and identification of generator models," in *Symposium on synchronous machine modeling for power system studies*, IEEE Press, 1983.

[15] N. K. Sinha, "Estimation of transfer function of continuous system from sampled data," *Proc. IEE*, vol. 119, pp. 612–614, May 1972.

[16] H. Huang, C. Chen, and Y. Chao, "Identification of mimo continuous-time models by indirect methods," *Int. J. Systems Sci.*, vol. 19, no. 7, pp. 1281–1297, 1988.

[17] P. C. Young, "Parameter estimation for continuous-time models – a survey," *Automatica*, vol. 17, no. 1, pp. 23–39, 1981.

[18] P. C. Young, "An instrumental variable method for real-time identification of a noisy process," *Automatica*, vol. 6, pp. 271–287, 1970.

[19] H. Unbehauen and G. P. Rao, *Identification of continuous systems.* Amsterdam: North-Holland, 1987.

[20] J. R. Jordan, S. A. Jalali-Naini, and R. D. L. Mackie, "System identification with hermite modulating functions," *IEE Proc. D*, vol. 137, pp. 87–93, Mar. 1990.

[21] A. H. Whitfield and N. Messali, "Integral-equation approach to system identification," *Int. J. Control*, vol. 45, no. 4, pp. 1431–1445, 1987.

[22] Y. Chao, C. Chen, and H. Huang, "Recursive parameter estimation of transfer function matrix models via simpson's integrating rules," *Int. J. Systems Sci.*, vol. 18, no. 5, pp. 901–911, 1987.

[23] C. Hwang and Y. Shih, "Parameter identification via laguerre polynomials," *Int. J. Systems Sci.*, vol. 13, no. 2, pp. 209–217, 1982.

[24] R. Chang and M. Wang, "Parameter identification via shifted legendre polynomials," *Int. J. Systems Sci.*, vol. 13, no. 10, pp. 1125–1135, 1982.

[25] G. P. Rao, *Piecewise constant orthogonal functions and their application to systems and control*, vol. 55 of *LNCIS*. Berlin: Springer-Verlag, 1983.

[26] B. Cheng and N. Hsu, "Single-input-single-output system identification via block-pulse functions," *Int. J. Systems Sci.*, vol. 13, no. 6, pp. 697–702, 1982.

[27] E. Eitelberg, "Continuous-time system representation with exact macro-difference expressions," *Int. J. Control*, vol. 47, no. 5, pp. 1207–1212, 1988.

[28] S. Sagara and Z. Zhao, "Recursive identification of transfer function matrix in continuous systems via linear integral filters," *Int. J. Control*, vol. 50, no. 2, pp. 457–477, 1989.

[29] S. Sagara and Z. Zhao, "Numerical integration approach to on-line identification of continuous-time systems," *Automatica*, vol. 26, no. 1, pp. 63–74, 1990.

[30] S. Sagara, Z. Yang, and K. Wada, "Recursive identification algorithms for continuous systems using an adaptive procedure," *Int. J. Control*, vol. 53, no. 2, pp. 391–409, 1991.

[31] S. Sagara, Z. Yang, and K. Wada, "Identification of continuous systems using digital low-pass filters," *Int. J. Systems Sci.*, vol. 22, no. 7, pp. 1159–1176, 1991.

[32] J. Arrillaga and C. P. Arnold, *Computer analysis of power systems.* England: John Wiley & Sons, 1990.

[33] P. L. Dandeno and P. Kundur, "Practical application of eigenvalue techniques in the analysis of power system dynamic stability problems," *Can. Elec. Eng. J.*, vol. 1, no. 1, pp. 35–46, 1976.

[34] J. O. Ojo and T. A. Lipo, "An improved model for saturated salient pole synchronous motors," *IEEE Trans. on Energy Conversion*, vol. EC-4, pp. 135–142, Mar. 1989.

[35] B. Adkins and R. G. Harley, *The general theory of alternating current machines: Application to practical problems.* London: Chapman and Hall, 1975.

[36] P. L. Dandeno and *et al.*, "Current usage & suggested practices in power system stability simulations for synchronous machines," *IEEE Trans. on Energy Conversion*, vol. EC-1, pp. 77–93, Mar. 1986.

[37] R. G. Harley, D. J. N. Limebeer, and E. Chirricozzi, "Comparative study of saturation methods in synchronous machine models," *IEE Proc. B*, vol. 127, pp. 1–7, Jan. 1980.

[38] J. A. Melkebeek and J. L. Willems, "Reciprocity relations for the mutual inductances between orthogonal axis windings in saturated salient-pole machines," *IEEE Trans. on Industry Applications*, vol. 26, pp. 107–114, Jan/Feb 1990.

[39] EPRI Research Project 997, *Determination of synchronous machine stability study constants*, vol. 2 (Ontario Hydro) of *EPRI Report EL-1424.* 1980.

[40] P. L. Dandeno and P. Kundur, "Stability performance of 555 mva turboalternators – digital comparisons with system operating tests," *IEEE Trans. on Power Apparatus and Systems*, vol. PAS-93, pp. 767–776, May/June 1974.

[41] T. Kamabu and J. C. Maun, *Turbine-generator models by the finite-element method*, in Modelling and simulation of Electrical Machines and Power Systems, pp. 259–266. Amsterdam: North-Holland, 1988.

[42] S. H. Minnich, M. V. K. Chari, and J. F. Berkery, "Operational inductances of turbine generators by the finite-element method," *IEEE Trans. on Power Apparatus and Systems*, vol. PAS-102, pp. 20–27, Jan. 1983.

[43] R. D. Lang, *The identification of power system dynamics by pseudo random ternary noise injection and cross correlation.* PhD thesis, University of Sydney, 1984.

[44] P. L. Dandeno and A. T. Poray, "Development of detailed turbogenerator equivalent circuits from standstill frequency response measurements," *IEEE Trans. on Power Apparatus and Systems*, vol. PAS-100, pp. 1646–1655, Apr. 1981.

[45] E. S. Boje, J. C. Balda, R. G. Harley, and R. C. Beck, "Time-domain identification of synchronous machine parameters from simple standstill tests," *IEEE Trans. on Energy Conversion*, vol. EC-5, pp. 164–170, Mar. 1990.

[46] I. Kamwa, P. Viarouge, and E. J. Dickinson, "Identification of generalised models of synchronous machines from time-domain tests," *IEE Proc. C*, vol. 138, pp. 485–498, Nov. 1991.

[47] R. Diggle and J. L. Dineley, "Generator works testing sudden-short-circuit or standstill variable-frequency-response method," *IEE Proc. C*, vol. 128, pp. 177–182, July 1981.

[48] S. H. Minnich, "Incremental permeabilities for the transient analysis of large turbine generators by the finite-element method," *J. Appl. Phys.*, vol. 52, pp. 2428–2430, Mar. 1981.

[49] P. L. Dandeno, P. Kundur, A. T. Poray, and H. M. Zein El-Din, "Adaption and validation of turbogenerator model parameters through on-line frequency response measurements," *IEEE Trans. on Power Apparatus and Systems*, vol. PAS-100, pp. 1656–1664, Apr. 1981.

[50] G. Manchur, D. C. Lee, M. E. Coultes, J. D. A. Griffin, and W. Watson, "Generator models established by frequency response test on a 555 mva machine," *IEEE Trans. on Power Apparatus and Systems*, vol. PAS-91, pp. 2077–2084, Sept./Oct. 1972.

[51] T. Sugiyama, T. Nishiwaki, S. Takeda, and S. Abe, "Measurements of synchronous machine parameters under operating conditions," *IEEE Trans. on Power Apparatus and Systems*, vol. PAS-101, pp. 895–904, Apr. 1982.

[52] M. Namba, T. Nishiwaki, S. Yokokawa, K. Ohtsuka, and Y. Ueki, "Identification of parameters for power system stability analysis using kalman filter," *IEEE Trans. on Power Apparatus and Systems*, vol. PAS-100, pp. 3304–3311, July 1981.

[53] R. E. Fairbairn and R. G. Harley, "On-line measurement of synchronous machine parameters," *IEEE Trans. on Industry Applications*, vol. 28, pp. 639–645, May/June 1992.

[54] R. W. Merchant and M. J. Gibbard, "Identification of synchronous machine parameters from standstill tests using recursive estimation with the bilinear operator," *IEE Proc. C*, vol. 139, pp. 157–165, Mar. 1992.

[55] R. W. Merchant and M. J. Gibbard, "Continuous-time transfer function estimation using the bilinear operator," in *Proceedings Australasia universities power and control engineering conference*, (Melbourne, Australia), Oct. 1991.

[56] R. W. Merchant, M. J. Gibbard, and A. M. Parker, "Identification of synchronous machine parameters online using rls estimation with the bilinear operator," in *Proceedings 27th Universities power engineering conference*, (Bath), Sept. 1992.

[57] G. F. Franklin, J. D. Powell, and M. L. Workman, *Digital control of dynamic systems.* Addison-Wesley, 2nd ed., 1990.

[58] K. J. Åström and B. Wittenmark, *Computer controlled systems : theory and design.* New Jersey: Prentice Hall, 2nd ed., 1990.

[59] G. C. Goodwin, R. H. Middleton, and H. V. Poor, "High-speed digital signal processing and control," *IEEE Proceedings*, vol. 80, pp. 240–259, Feb. 1992.

[60] T. E. Fortmann and K. L. Hitz, *An introduction to linear control systems.* New York: Marcel Dekker, 1977.

[61] R. Isermann, *Digital control systems.* New York: Springer-Verlag, 1977.

[62] F. W. Smith, "System laplace-transform estimation from sampled data," *IEEE Trans. on Automatic Control*, vol. AC-13, pp. 37–44, Feb. 1968.

[63] P. Åström, Hagander and J. Sternby, "Zeros of sampled systems," *Automatica*, vol. 20, no. 1, pp. 31–38, 1984.

[64] R. H. Middleton, *Modern, continuous and discrete, control.* PhD thesis, Dept. Electrical and Computer Engineering, University of Newcastle, 1986.

[65] R. H. Middleton, G. C. Goodwin, D. J. Hill, and D. Q. Mayne, "Design issues in adaptive control," *IEEE Trans. on Automatic Control*, vol. AC-33, pp. 50–58, Jan. 1988.

[66] P. M. Anderson, B. L. Agrawal, and J. E. Van Ness, *Subsynchronous resonance in power systems.* New York: IEEE Press, 1990.

[67] P. Stoica and T. Söderström, "Asymptotic behaviour of some bootstrap estimators," *Int. J. Control*, vol. 33, no. 3, pp. 433–454, 1981.

[68] R. Isermann, "Practical aspects of process identification," *Automatica*, vol. 16, pp. 575–587, 1980.

[69] T. Söderström and P. Stoica, "Comparison of some instrumental variable methods – consistency and accuracy aspects," *Automatica*, vol. 17, no. 1, pp. 101–115, 1981.

[70] Z. Zhao, S. Sagara, and K. Wada, "Bias-compensating least squares method for identification of continuous-time systems from sampled data," *Int. J. Control*, vol. 53, no. 2, pp. 445–461, 1991.

[71] S. Sagara, Z. Yang, and K. Wada, "Implementation of multi-rate model reference adaptive control for continuous systems via bilinear transformation based on block-pulse functions," *Int. J. Systems Sci.*, vol. 22, no. 10, pp. 1757–1774, 1991.

[72] S. Haykin, *Communication systems.* John Wiley & Sons Inc., 1983.

[73] P. Guillaume, J. Schoukens, and R. Pintelon, "Sensitivity of roots to errors in the coefficient of polynomials obtained by frequency domain estimation methods," *IEEE Trans. on Instrumentation and Measurement*, vol. IM-38, pp. 1050–1056, Dec. 1989.

[74] A. E. Fitzgerald and J. Kingsley, C., *Electric Machinery.* McGraw-Hill, 1961.

[75] M. E. Coultes and W. Watson, "Synchronous machine models by standstill frequency response tests," *IEEE Trans. on Power Apparatus and Systems*, vol. PAS-100, pp. 1480–1489, Apr. 1981.

[76] C. Moler, J. Little, and S. Bangert, *Pro-Matlab: users guide.* The Math Works, Inc., 1987.

[77] A. V. Oppenheim and R. W. Schafer, *Digital signal processing.* New Jersey: Prentice-Hall, 1975.

[78] R. G. Lawrence, "A compact 480 v 700 hp induction motor drive using darlington transistors," *IEE Conference Publication*, vol. 324, pp. 502–506, 1990.

[79] S. H. Minnich, "Small signal, large signal, and saturation in generator modeling," *IEEE Trans. on Energy Conversion*, vol. EC-1, pp. 94–102, Mar. 1986.

[80] T. J. Hammons and D. J. Winning, "Comparisons of synchronous-machine models in the study of the transient behaviour of electrical power systems," *Proc. IEE*, vol. 118, pp. 1442–1458, Oct. 1971.

[81] J. E. Brown, K. P. Kovacs, and P. Vas, "A method of including the effects of main flux path saturation in the generalized equations of a.c. machines," *IEEE Trans. on Power Apparatus and Systems*, vol. PAS-102, pp. 96–103, Jan. 1983.

[82] J. J. Schutz, "Real time computer for dynamic system identification." Student Report, University of Adelaide, Oct. 1988.

[83] IMSL Inc., *IMSL Math/Library: Users Manual*, 1977.

[84] I. Boldea and S. A. Nasar, "Unified treatment of core losses and saturation in the orthogonal-axis model of electric machines," *IEE Proceedings B*, vol. 134, pp. 355–363, Nov. 1987.

[85] L. R. Rabiner and B. Gold, *Theory and application of digital signal processing.* New Jersey: Prentice-Hall, 1975.

Addendum to PhD Thesis

Title: "Recursive Estimation Using the Bilinear Operator with Applications to Synchronous Machine Parameter Identification"

Author: Richard Merchant

A Insert on p.xi, after $v_{ag0}, v_{agd0}, v_{agq0}$ in the List of Principal Symbols:

w – Bilinear operator (not to be confused with the symbol ω for rotor speed).

B Insert on p.28, before the paragraph "To compare the numerical properties of these three state-space implementations ... ":

Note that this implementation of the bilinear-operator model is non-minimal, being a fifth-order implementation of a fourth-order system. The fifth-order implementation is employed for comparing the numerical properties of the three models as it closely resembles the form of the δ-operator implementation. For completeness, the fourth-order bilinear-operator implementation is

$$\begin{aligned} Nx_{k+1} &= Mx_k + \frac{\Delta}{2}\begin{bmatrix}1\\0\\0\\0\end{bmatrix}(u_k - u_{k+1}) \\ y_k &= [-B_4''A_3'' + B_3'', -B_4''A_2'' + B_2'', -B_4''A_1'' + B_1'', -B_4''A_0'' + B_0'']x_k + B_4''u_k \end{aligned}$$

where

$$N = \begin{bmatrix} 1 + \frac{\Delta}{2}A_3'' & \frac{\Delta}{2}A_2'' & \frac{\Delta}{2}A_1'' & \frac{\Delta}{2}A_0'' \\ -\Delta/2 & 1 & 0 & 0 \\ 0 & -\Delta/2 & 1 & 0 \\ 0 & 0 & -\Delta/2 & 1 \end{bmatrix}$$

$$M = \begin{bmatrix} 1 - \frac{\Delta}{2}A_3'' & -\frac{\Delta}{2}A_2'' & -\frac{\Delta}{2}A_1'' & -\frac{\Delta}{2}A_0'' \\ \Delta/2 & 1 & 0 & 0 \\ 0 & \Delta/2 & 1 & 0 \\ 0 & 0 & \Delta/2 & 1 \end{bmatrix}$$

$$x_k^T = \left[\ \frac{w^3 u_k}{A''(w)} \quad \frac{w^2 u_k}{A''(w)} \quad \frac{w u_k}{A''(w)} \quad \frac{u_k}{A''(w)}\right]$$

C Insert on p.55, after " ... estimator, and its sensitivity due to noise.":

A forgetting factor is employed in the estimation algorithm because its intended application is in continuous estimation of time-varying systems. For one-shot type estimation, alternative modifications of the algorithm may be employed.

D Insert on p.64, starting a new paragraph after " ... may be used to minimise this problem (see Simulation Study 6, section 4.6.1).":

The separation and 'allocation' of the effects of both the prefilter and the term $\hat{A}(w)/J(w)$ on estimation provide a logical basis for the design and selection of the prefilter and $J(w)$ filter polynomial. However, from the way the prefilter and the term $\hat{A}(w)/J(w)$ enter into the error function (eqn. 3.23), they can affect estimation in the same way. For example, using a prefilter of the form $1/M(w)$ and a $J(w)$ filter polynomial $J(w) = N(w)$ is equivalent to using a prefilter $1/N(w)$ with a $J(w)$ filter polynomial $J(w) = M(w)$. This can be shown following a similar argument to that used in expanding eqn. 3.48.

The main difference between the prefilter and the term $\hat{A}(w)/J(w)$ is that for the prefilter the poles, zeros and order are selectable by the user, offering full control of the response of the prefilter. With the term $\hat{A}/J(w)$, only the poles are selectable; both the zeros and the order of the $J(w)$ filter polynomial are determined by the estimated polynomial $\hat{A}(w)$.

E Insert on p.121, second paragraph, after " ... for most cases, the effect on the coefficient estimates is minimal.":

This is consistent with eqn. 3.23 because, providing the prefilter bandwidth covers the frequency range of interest, and outside this frequency range unmodeled dynamics, noise and dc offset are heavily attenuated, prefiltering should have little effect on estimation.

F Insert on p.125, bottom of the page:

The estimation algorithm becomes unstable when the $J(w)$ filter polynomial is selected to match approximately the denominator of the continuous-time TF.

G The denominators of eqns. 5.5 and 5.7, p.133, should read:

$$(1 + sT'_{d0})(1 + sT''_{d0})$$

H Insert on p.138, directly after eqn. 5.45:

where $\theta = \omega t + \theta_0$ is the angle between the axis of phase 'a' of the stator windings and the direct axis of the field winding (electrical radians): θ_0 is an initial angle. [Note θ as defined above is used only on p.138-139 to introduce the well-known Park's Transform. The transform is described in detail in references [1,35]. The variable θ is also used to define a vector of parameters (see p.53).]

I Insert on p.143, as a new paragraph after " ... are used to assess the accuracy of the estimated model.":

A useful area of further research would be the application of statistical methods to the assessment of the accuracy of the coefficient estimates [2].

This may also provide the basis for assessing the accuracy of the machine parameters evaluated in later chapters. This statistical analysis is outside the objectives and scope of the thesis.

J Insert on p.162, before the last paragraph "Although the third-order stator-to-field model ...":

It is possible that the third-order model may account for effects such as hysteresis and iron losses, or iron and brush non-linearities. These effects are not considered when deriving the second-order field-to-stator model.

K Insert on p.177, after " ... the rotor speed in electrical radians per second.":

Note that a somewhat loose notation has been employed, with a lower-case symbol representing both the time signal and its corresponding Laplace transform. The correct interpretation of the symbol is clear from the context of the equation in which it appears.

L Insert on p.181, after " ... used as the prime mover in the laboratory SMIB system (see section 6.3.1).":

This coefficient results because the DC motor, with constant supply voltage and constant flux per pole, inherently has a linear torque/speed characteristic.

M Assumption 2 on p.181-182, the incremental mutual inductance equation should read:

$$kM_{fd} = -\frac{\partial \psi_f}{\partial i_d} = kM_{df} = \frac{\partial \psi_d}{\partial i_f}$$

N On p.212, the steady-state field voltage, v_{f0}, in the table should read 33 V for condition OC1, not 32 V.

O Insert on p.214, after " ... results in the dc gain reducing to 14 dB.":

As well as a reduction in dc gain, there is also a significant variation in the corner frequency of the TF pole with excitation; the variation is from approximately 2.4 rad/s ($v_{f0} = 5$ V) to approximately 5.7 rad/s ($v_{f0} = 33$ V).